ROLLING CONTACT FATIGUE OF THERMAL SPRAY COATINGS

By

Rehan Ahmed
BEng(Hons) MSc AMIMechE

A Thesis submitted for the degree of

Doctor of Philosophy

Department of Mechanical Engineering
Brunel University
February 1998

786

Dedicated to my parents

Preface

This thesis is submitted to the degree of Doctor of Philosophy in the Department of Mechanical Engineering, Brunel University. To the best of my knowledge the submitted work is original, except where references has been made to others. The research was carried out by myself in the period September 1994 to August 1997 under the supervision of Dr. Mark Hadfield in the Department of Mechanical Engineering, Brunel University.

No part of this thesis , or any similar to it, has been, or is currently being, submitted for any degree or any other qualification. This thesis is less than 50,000 words.

Rehan Ahmed
Brunel University
United Kingdom
February 1998

ABSTRACT

The practical advantages of thermal spray coatings like high deposition rates, low cost and tribological properties of high wear resistance have enabled these coatings to become an integral part of aircraft and automobile industry. Recent advancements in thermal spraying techniques like high particle speed and temperature call for new applications for these coatings. This experimental study addresses the Rolling Contact Fatigue performance of thermal spray coatings deposited by a variety of techniques like High Velocity Oxy-Fuel (HVOF), Detonation Gun (D-Gun) and Plasma spraying.

RCF tests were conducted using a modified four ball machine in conventional steel ball bearing and hybrid ceramic bearing configurations. Tribological conditions during the RCF tests were varied by changing the test lubricant and the lubrication mechanism, contact load and shape of the drive coated rolling element to vary the roll/slip ratio. RCF tests were analyzed on the basis of the performance, coating failures using surface and subsurface observations, and residual stress studies. Experimental and theoretical studies of the ball kinematics have also been included.

These tests revealed that the performance of the coated rolling elements was dependent upon the coating and the substrate properties. The coating thickness, substrate hardness, tribological conditions during the test, coating and substrate material as well as the coating process and the substrate preparation significantly affect the coating performance and the failure modes. Three different failure modes of these coatings have been discussed along with the changes in the near surface residual stress behaviour of the coated rolling elements.

PUBLICATIONS RESULTING FROM THESIS

1: R. Ahmed & M. Hadfield

Rolling contact fatigue behaviour of thermally sprayed rolling elements. Jr Surface & Coatings Technology, **82**, 176-186, 1996.

2: R. Ahmed & M. Hadfield

Rolling contact fatigue performance of detonation gun coated elements. Jr Tribology International, **30(2)**, 129-137, 1997.

3: R. Ahmed & M. Hadfield

Wear of HVOF coated cones in rolling contact. Jr Wear, **203-204**, 98-106, 1997.

4: R. Ahmed & M. Hadfield

Experimental measurement of the residual stress field within thermally sprayed rolling elements. Jr Wear, **209**, 84-95, 1997.

5: R. Ahmed & M. Hadfield

Fatigue behaviour of HVOF coated M-50 steel rolling elements. Jr Materials & Manufacturing processes, Special issue on thermal spraying, accepted March 97, In print.

6: R. Ahmed & M. Hadfield

Rolling contact fatigue performance of HVOF coated elements. Advances in Surface Engineering, **1**, ISBN 0-85404-747-6, 229-237, 1997.

7: R. Ahmed, M. Hadfield & S. Tobe

Residual stress analysis in thermal spray coated rolling elements. National thermal spray conference, USA, ISBN 0-87170-583-4, 875-883, 1996.

8: R. Ahmed & M. Hadfield

Rolling contact fatigue performance of plasma sprayed coatings. Paper presented in World Tribology Congress, United Kingdom, submitted to Wear, 1997.

9: M. Hadfield, R. Ahmed & S. Tobe

Rolling contact fatigue of thermal spray coated cones. International thermal spray conference, Kobe, Japan, 1097-1102, 1995.

ACKNOWLEDGEMENTS

I am grateful to a number of people who have encouraged and supported me during the course of my research

First of all, my supervisor Dr. Mark Hadfield who has always inspired, and guided me and our discussions on the planning and progress of the project enabled the timely completion of my thesis.

Professor Shogo Tobe of the Ashikaga university, Japan, not only helped in liaising with the Japanese industry for the preparation of the test samples but also allowed me to perform the residual stress studies at his institute.

Support by the Experimental Technique Centre for the use of the equipment and the time of their technical staff, especially Jennifer is greatly appreciated.

Bob Webb (Departmental superintendent) and several technicians helped me with the test rig modifications including Keith Withers, Len F Soans, Clive Barrett.

Lastly but not leastly this task would not have been accomplished without the support of my family, friends and colleagues especially my parents, my aunt Razia and my wife Shabnam who has always been a source of encouragement.

CONTENTS

NOMENCLATURE

The following notation is used in the finite element model, chapter three.

E_1 = Coating Young's modulus (GPa)
E_2 = Substrate Young's modulus (GPa)
{F} = Force matrix
{K} = Stiffness matrix
{U} = Displacement matrix
ν_1 = Coatings Poisson's ratio
ν_2 = Substrate Poisson's ratio
t = Coating thickness (μm)
a = Contact radius (μm)

The following notation is used in the mathematical model of the contact kinematics, chapter three.

N = Speed of the drive shaft (rpm).
R1 = Radius of the upper drive ball (mm).
R2 = Radius of the lower planetary ball (mm).
R3 = Radius of the wear track on the upper drive ball (mm).
R4 = External radios of the cup (mm).
R5 = Radius of the cup (mm).
ω = Angular velocity of the upper drive ball about the spindle axis MN (rad/sec).
ω_P = Angular velocity of the planetary ball about the axis MN (rad/sec).
ω_s = Spin angular velocity of the planetary ball about the axis inclined at an angle β to the spindle axis MN (rad/sec).
θ = Angle between the axis of the driving shaft and the connecting line of centres of the driver and the driven ball.
β = Angle between the axis of the driving shaft and the axis of spin of the planetary balls.
δ = Angle between the spin axis of rotation of the planetary ball and the connecting line of the conjunctions formed between the planetary balls and the cup.
Z = Number of planetary balls.

The following notation is used in the X-ray diffraction measurements, chapter four.

n = Positive integral number indicating the order of diffraction
λ= X-ray wave length
d = Inter-planar spacing in the crystal
θ = Diffraction angle
ψ = Angle between the normal of the sample and the normal of the crystal plane
ϵ = Strain
θ_d = Diffraction angle in a stress free condition.
σ = Stress
K = Elastic constant for the X-ray stress measurement
M = Gradient of the data regression line

The following notation is used in the theoretical film lubrication regime calculations, Appendix E.

η_o = viscosity at atmospheric pressure (Ns/m^2)
μ = mean surface velocity in the direction of motion (m/s)
E^* = effective elastic modulus (GPa)
R_x = effective radius in x direction (m)
R_y = effective radius in y direction (m)
ξ = pressure viscosity coefficient (m^2/N)
F = normal load (N)
R^2_{qd} = RMS surface roughness of the drive rolling element
R^2_{qp} = RMS surface roughness of the planetary ball
λ= ratio of film thickness to average surface roughness

ABBREVIATIONS

APS	Air Plasma Spraying
BEI	Back-scattered Electron Image
D-Gun	Detonation Gun
DLC	Diamond Like Carbon
EHL	Elastohydrodynamic Lubrication
EPMA	Electron Probe Microscopy Analysis
FEM	Finite Element Modelling
HIP	Hot Isostatic Pressing
HRC	Hardness Rockwell C
HVOF	High Velocity Oxy-Fuel
HVAF	High Velocity Air Fuel
H_v	Micro Vickers Hardness
RCF	Rolling Contact Fatigue
RMS	Root Mean Square
SEI	Secondary Electron Image
SEM	Scanning Electron Microscopy
WC-Co	Tungsten Carbide Cobalt Coating

Chapter 1
INTRODUCTION

1.1 General Background

The quest for improving the performance (higher load, speed, and low friction), and reliability (fatigue life) of rolling element bearings demands new approaches towards material selection and the optimization process. Overlay coatings, like thermal spraying, have the versatility of coating any material (provided it does not decompose during melting) on any substrate (if it can withstand coating temperatures), with the added advantage of high deposition rates and low production costs. It is possible that rolling element bearings can benefit from the advantages of high particle speed and temperature due to the developments in the thermal spraying processes. These coatings have already become an integral part of the aircraft and automobile industry (Arata, 1995). Coating properties, like high hardness, and resistance to sliding and abrasive wear in hostile environments can be attractive to the rolling element bearing industry. However, the investigations on the lubricated rolling contact fatigue performance of these coatings have been limited. Research is therefore required to understand the Rolling Contact Fatigue (RCF) performance and failure mechanisms of these coatings before consideration of their use in rolling element bearing design. It may also be possible to reach the full potential of hybrid ceramic bearings and improve the performance of conventional steel bearings using the coated steel races. Other applications can include rolling mills, crank and cam shaft and gear applications etc.

An experimental investigation of the RCF performance and observation of the failure modes of these thermal spray coatings can enable a better understanding of their behaviour in the rolling contact. The numerical approach, like modelling to access the RCF life of thermal spray coatings, makes the problem complex and expensive to solve. This is mainly due to the anisotropy of thermal spray coatings and the complex lamella microstructure of thermal spray coatings. Investigation tools like microhardness, residual stress, microslip, contact stress analysis, elasto-

hydrodynamic lubrication film theory, surface and subsurface observation, and finite element modelling support the experimental work of this thesis.

A modified four ball machine described in appendix A is used to investigate the RCF resistance of thermally sprayed rolling elements. A configuration of deep groove ball bearing can be simulated by contacting the three lower planetary balls which are free to rotate and driven by the fourth upper ball. Hence, many more stress cycles can be achieved in a fixed contact area on the upper ball thereby reducing the fatigue testing time. The contact of the upper drive ball and the lower planetary balls differ from the contact of the inner race and the rolling elements due to non-conforming contact.

Although the correlation between the fatigue properties of the rolling contact devices, like four ball machines, etc, and entire bearing units has not yet been satisfactorily accomplished (Harris, 1984) the four ball machine gives a rapid screening of the rolling contact fatigue resistance of the materials and an appreciation of the failure modes before full scale testing. In the present studies the driving rolling elements in the shape of 12.5 mm diameter ball and 14.5 mm diameter cones are used to vary the roll/slip conditions in type II configuration (Tourret, 1977). The RCF tests conducted are not intended to be used for statistical fatigue life prediction, but to give an appreciation of the rolling contact fatigue performance of thermal spray coatings.

1.2 Thermal Spray Coatings

Thermal spraying is generally classified as a molten or semi-molten state coating process (Mathews, 1993), and can be defined as a process in which thermal energy is used to deposit finely divided material in molten, semi-molten or plasticised conditions on to a prepared substrate (Fauchis, 1993). The thermal energy can be provided from a combustion process, electric arc, gas plasma, laser (photons) etc, and the coating material can be in the form of a powder or a wire. The method of heat generation thus provides a basis for the general classification of thermal spray

coatings in two groups, ie. 1) combustible gases as the heat source and, 2) electrical power as the heat source. Group 2 can be further classified into wire arc processes or plasma assisted alternating current (AC) or direct current (DC) processes. A general classification & description of some of the coating processes has been included in appendix B.

During a thermal spraying process individual particles land (splat) on to the surface and solidify thereby giving a lamella structure. In most cases the particles lands on an already solidified lamella due to quick cooling of the lamellae (Fauchis. 1993), resulting in quenching stresses. The lamellar structure of these coatings not only depend upon the thermal spraying process and the process parameters, but also upon the wettability, velocity and temperature of the impacting particle and the surface conditions (mainly roughness and temperature) of the underlying substrate or lamella. These coatings have an anisotropy in the coating microstructure (Nakahira et. al. 1992). The coating properties like Young's modulus, and also the coating behaviour in residual stress measurements, etc. can vary significantly depending not only upon the coating process and the parameters controlled during the coating process, but also on the method of measurement (Kawase et. al. 1990). Developments in the thermal spraying techniques have made it possible to obtain particle velocities in excess of 750 m/s (Pawlowski, 1995) and particle temperatures in excess of 3000°C. Kreye, (1991) has described the comparative average particle speeds and temperatures of WC-Co particles for some of the thermal spraying processes as indicated in appendix B. However, the exact speed and temperatures can vary depending upon the coating process parameters, location of individual particle in the flame, spraying distance etc. The work carried out in this thesis involves the coatings produced by super D-Gun (SDG 2040), High Velocity Oxy-Fuel (HVOF) and Air Plasma Spraying (APS, Gator Gard) processes. These processes are explained in appendix B. The coating material in most of the cases considered was WC-Co. The selection of the coating material was made because of the high wear resistance and high hardness of WC-Co coatings and their high resistance to sliding wear, abrasive wear specially in corrosive erosive environments

(Vuoristo et. al. 1993). Preliminary testing of WC-Co and Al_2O_3 coatings were then carried out in which WC-Co coatings performed better.

1.3 Objectives and Scope of the Research Work

The main objective of the study presented in this thesis was to experimentally investigate the performance and failure modes of thermal spray coatings produced by D-Gun, HVOF and APS processes using a model contact. The scope of this research includes the following:

a) The effect of coating thickness on the performance and failure modes of the thermal spray coatings.
b) The influence of substrate hardness on the performance and failure modes of the coatings.
c) To investigate the affect of RCF tests on the near surface residual stress of thermal spray coatings.

The influence of variation in tribological conditions of lubrication and contact stress at an ambient room temperature with coating/steel and coating/ceramic contact and the variation in roll slip ratio by varying the sample geometry are also studied.

1.4 Thesis Outline

In chapter one, the general background information and previous experimental work related to the fatigue performance of thermal spray coatings in rolling or rolling/sliding contact have been presented. Chapter two describes the sample polishing and experimental test procedures adapted to perform the RCF tests. Experimental rig modifications have also been included in this chapter. Chapter three describes the results of analytical investigations of the contact stresses. The kinematic analysis have also been included in this chapter. Chapter four gives a brief explanation of the experimental techniques used to measure the residual stress using X-ray diffraction technique, subsurface cracks using dye penetrant and surface roughness investigations of the coated rolling elements.

Experimental test results are described in chapter five. Section one describes the case of D-gun coated balls and section two explains the case of HVOF coated rolling element cones on mild steel substrate. Section three describes the case of HVOF coated balls on M-50 steel substrate. Section four of this chapter explains the case of plasma sprayed coatings and finally, section five of chapter five describes with the case of HVOF coatings on the bearing steel (440-C) substrate. Chapter six represents the analysis and interpretation of the experimental test results described in chapter five. Chapter seven gives a description of the conclusions and recommendations of the future work.

1.5 Literature Survey

The RCF behaviour of thermally sprayed coatings was initially studied by Tobe et. al. (1988). They studied plasma sprayed ceramic and metallic coatings on a steel substrate using a two roller type rolling fatigue test machine. They observed that the roller design to assist the coating at the edges of the contact area can improve the coating fatigue life, and that it also influences the crack initiation and propagation. Moreover, surface roughness of the rollers was also significant on the fatigue performance. When the coating was not supported at the edges (roller type A), the fatigue life time reduced and the cracks initiated at the edges of the roller, leading to severe delamination. It is possible that these cracks initiated in mode I, due to the tensile stresses at the edges of the contact area. Although the mode of failure for the roller design which support the coating at the roller edges (roller type B), still resulted in the coating delamination, the failure was initiated at the middle of the contact area. This not only reduced the delamination debris size but also, the scatter in the fatigue results was reduced. The depth of maximum shear stress did not correspond with the depth of failure, hence these cracks could be related to the peak compressive Hertz stress. Although there was no description of the rolling speed during the test conditions, it is appreciated that these tests were conducted in boundary lubrication owing to high R_a (average surface roughness) values of the roller surfaces, thereby providing an asperity contact between the coating and the roller, which has a significant effect on the fatigue performance. In all the cases the

coatings delaminated at the interface, representing a poor adhesive strength of the coatings. The bond coat in the ceramic coatings acting at an interface layer did not provide the necessary adhesion between the coating and the substrate, which represents a mismatch between the properties of the coating and the substrate material. This can impose high residual stress at the interface. A solution could be to change the material of the interface layer, or perhaps the functional grading of the coating can provide improved adhesion. The substrate preheat temperature and its surface roughness and cleanliness also effects the adhesive strength between the coating and the substrate. Poor adhesion can also result from unmelted particles (lamellae) of Alumina within the spray stream due to the high melting temperature required for melting and also due to their oxidation during thermal spraying process.

Later studies by Tobe et. al. (1990) using the same type of fatigue test equipment but on an aluminium alloy substrate revealed that compressive strength of the coating and the shear stress between the coating and the substrate were the most important factors in the RCF performance of the coatings. These tests were conducted using the modified roller design to support the coating edges and improved surface finish of the coatings. The coatings showed an increase in the RCF life of the aluminium alloy. Although the failure mechanism remained as delamination, it was reported to be caused by the generation of blisters at the interface for metallic coatings, and at the interface of bond coat and substrate for ceramic coatings. These results showed that variation in tribological conditions alter the failure mechanism of thermal spray coatings. This also revealed that the future coatings need to improve the adhesive strength of the coatings for any more improvement in the RCF life. An important result of this study was the understanding that significant residual stress can be generated within the coating microstructure during the rolling contact fatigue tests, thereby indicating plastic deformation of coatings. Another reason for the low adhesive strength of these coatings might be the presence of oxide film on the surface of the aluminium substrate which has a high affinity for oxygen.

Another attempt to study the RCF behaviour of thermally sprayed coatings was made by Makela et. al. (1994). Their experimental approach using a three roller type RCF test machine and a two roller type test machine on WC-12%Co coated steel rollers using HVOF and D-Gun processes in unlubricated conditions concluded that the behaviour of coatings in rolling contact not only depend upon the Hertz contact stress but also on the tribological conditions and vibrations during the test. The need to investigate the surface finish and hardness of not only the coated roller but also the contacting roller was addressed during the study. An important result of their study was that the WC-12%Co coatings were failing at the interface, thereby following the same trend as reported by Tobe et al. (1988, 1990). The authors anticipated that hard cermet coatings like WC-12%Co do not plastically deform in ductile behaviour at the cracks and micropits present in the coating microstructure thereby leading to high stress concentration, resulting in crack propagation and ultimately delamination.

Sahoo, (1993) studied the rolling contact fatigue resistance of WC-Co coatings in the slat and flap track areas of the airplanes wing under high loads. He reported that the cracks initiated from the surface and progressed through the coating thickness. However, delamination occurred just above the coating substrate interface. One possible explanation of the surface crack initiation can be the tribological conditions during the rolling contact eg high friction and sliding action can cause the crack initiation at the surface in shear mode (mode II). The change in delamination behaviour can be attributed to strong mechanical interlock and the nature of residual stress at the interface to resist delamination.

Yoshida et. al. (1995) performed a study on the fatigue performance of WC-Cr-Ni coatings under pure rolling and rolling/sliding contact conditions. They addressed the effect of coating thickness, substrate hardness and slip ratio on the performance of these coatings produced on a carburized steel rollers using a two roller type test machine. Their studies indicated that when the substrate material was not blasted the coatings failed at initial stages of the test and the coating failure was at the coating

substrate interface. However, when the coatings were produced on a blasted substrate, it not only improved the coating performance but also the coatings failed from within the coating microstructure. This behaviour was different from the previous studies by Tobe et. al. (1988, 1990), Ichimura et. al. (1991) and Makela et. al. (1994) etc. which showed that the coatings normally fail at the interface or just above the interface. It can be appreciated that the coating design and tribological conditions can effect the coating failure mechanism. Yoshida et. al. (1995) also indicated that thicker coatings (90 μm) performed better than thinner coatings (20 μm) under the given test conditions. However, there was a significant scatter in their test results eg. tests B-5,6 C-1,2 and D-2,3 etc. (Yoshida et. al. (1995)), do not support this conclusion and it is possible that these differences could have been caused due to complex microstructure of thermal spray coatings leading to poor reproducibility of test results. The most significant result of their study was the effect of slip ratio on the coating performance. They indicated that when the coated roller was placed on the slower side (slip ratio = -14.8%) the coatings failed more quickly than pure rolling conditions and the effect was reversed when the coated roller was placed on the faster side (slip ratio = +12.8%). This revealed that the failure of thermal spray coatings under rolling/sliding conditions is determined not only by the magnitude of the tangential force but also its direction. They indicated that the friction was largest in the initial stages of the test gradually dropping to a steady level. This can be attributed to the running in of the coating at the initial stages of the test. Moreover, they indicated that the flaking occurred at early stages of the test when the subsurface hardness was low thereby indicating the plastic deformation of the substrate. Thus it is appreciated that the substrate should support the coating under the contact load. In most cases the coating flaking occurred at the edges of the contact area and crowning of the roller resisted this failure. This is consistent with the studies by Tobe et. al. (1988, 1990) when the coating failure was at the edges of the contact area and the roller design was shown to effect the coating performance.

Nieminen et. al. (1995) have also carried out similar tests on the two roller type test

machine under dry and non-sliding conditions and compared the performance of WC-12%Co coatings produced by the APS, and the HVOF process at the Hertzian contact stress of 420~600 MPa. They indicated that the performance was reduced in the case of APS coatings due to the porous microstructure and the subsurface cracks were initiated at the approximate depth of maximum shear stress. However, the trend was not consistent and subsurface cracks at a much shallower depth were observed in the case of HVOF coatings.

In another study (Keshavan et. al. (1993)), the WC-Co coatings deposited by super D-Gun process were subjected to full scale testing for radial bearing sleeves and thrust bearing sleeves. Although the contact configuration does not simulate a pure rolling contact it is interesting to appreciate that the coatings were failing by catastrophic delamination. However, conformal clad coatings fused in furnace improved the life time of the bearings.

Although other coating processes like gaseous state process, eg. Physical Vapour Deposition (PVD), etc. have a different coating microstructure and coating thickness from thermal spray coatings, extensive data are available on the RCF performance of these coatings. Two important conclusions from the studies of PVD coatings can also be considered important for the RCF performance of thermally sprayed coatings. Firstly, the substrate hardness should not deteriorate during the coating process, and secondly the coating thickness should be optimised for any improvement in the RCF life of coatings, since a change in coating thickness can actually degrade the RCF life times.

1.6 State of the Art from Literature Survey

Although there has been limited studies on the RCF performance of thermally sprayed coatings, the results appreciated can be helpful in designing the future coatings for the rolling contact applications. In all the cases reported the coatings delaminated either at the interface, just above the interface or from within the coating microstructure. Thus representing poor adhesive and cohesive strength of

the coatings. The blasting of the substrate material prior to the coating process also had a pronounced affect on the failure mechanism of coatings. The coating failure was effected by the tribological conditions during the test and also the substrate shape and material to support the coating was seen to effect the coating life time. Thus there remains a need to experimentally investigate the effect of variation in coating thickness for different coating processes for the rolling contact applications. Moreover, the effect of substrate hardness and residual stresses can be significant. The multiple cause diagram shown below as figure 1.1 represents some of the important parameters which can be influential on the RCF performance of thermal spray coatings. This figure only represents the key areas and some factors have been omitted to simplify the presentation of the diagram. Although a thorough investigation of all the parameters indicated in the multiple cause diagram is beyond the scope of this research programme, effort has been made in this thesis to address some of the key elements.

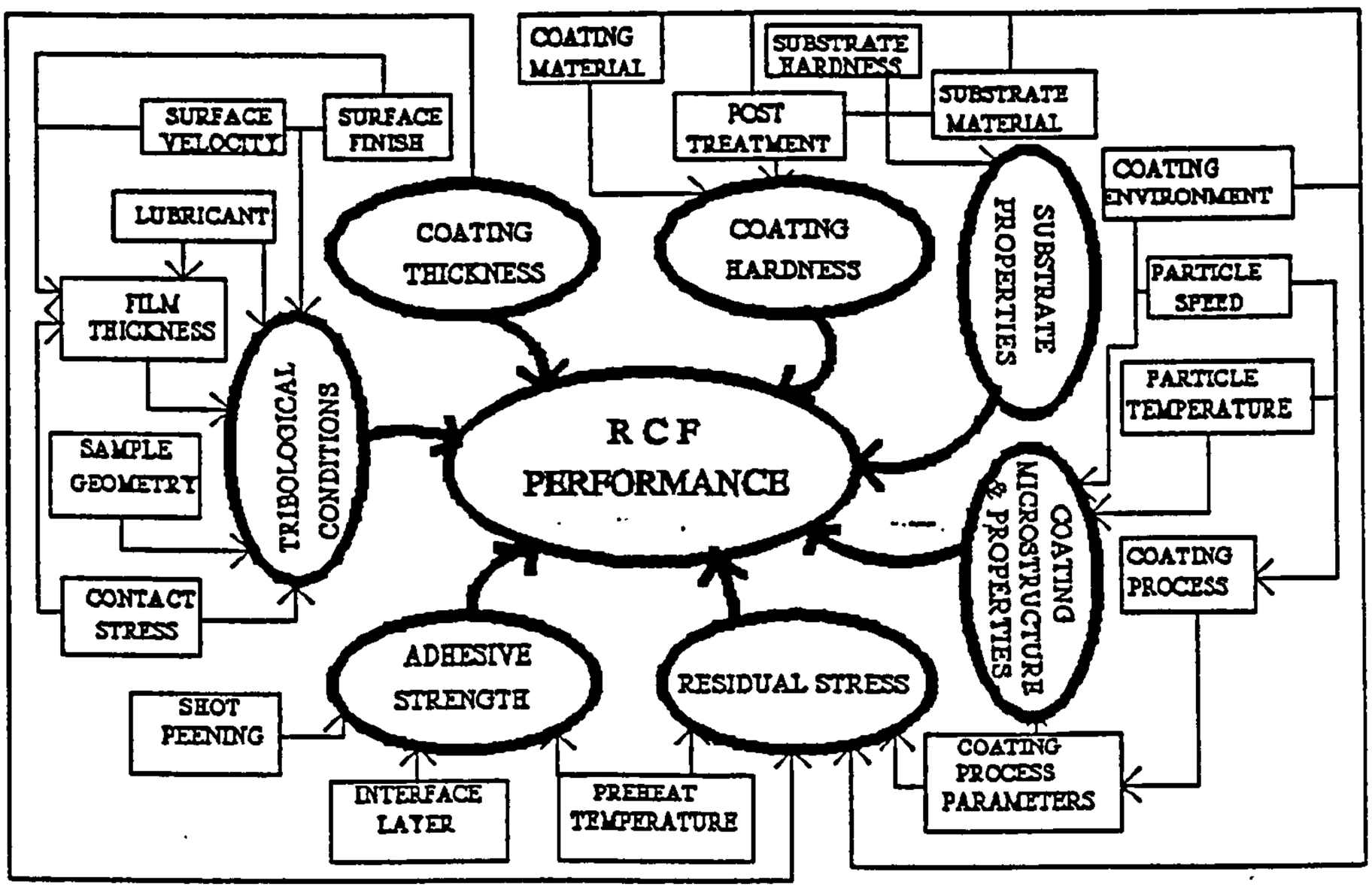

Figure 1.1, Multiple cause diagram

Chapter 2

ROLLING ELEMENT POLISHING AND EXPERIMENTAL TEST PROCEDURES

2.1 Introduction

This chapter presents the background work prior to the Rolling Contact Fatigue (RCF) testing in which the rolling elements were polished using the modified four ball machine. Experimental test rig modifications to alter the lubrication system to splash the lubricant at the inlet to the contact area, ball kinematics during the RCF test to experimentally measure the speed of the drive rolling element and the average orbital speed of the plenary balls under the given test conditions and the experimental arrangement used to measure frictional torque in the four ball assembly has been included. The experimental test procedure to conduct the RCF tests has also been described.

2.2 Sample Polishing

The surface roughness of the contacting bodies under the given lubrication conditions (ie. boundary, hydrodynamic, elasto-hydro-dynamic) influence the extent of the asperity contact and can thus alter the failure mechanism under the given tribological conditions. Achieving a high surface finish on the rolling elements is always a desirable factor since it affects the lubrication conditions.

2.2.1 Context of the problem

After the rolling elements in the shape of 12.7 mm diameter half coated ball and 14 mm diameter cones having an apex angles of 109.4° and 90° were sprayed, machining and grinding of these rolling elements was necessary. This was done using conventional machine tools. The conical specimens were then ground on a universal type grinding machine using a diamond particle grinding wheel to attain the best possible surface finish. Conventional water based grinding lubricant was used for grinding. The grinding of the 12.7 mm diameter half coated balls could not be performed because of specialized tooling required. This resulted in the typical surface roughness value (R_q) of 1.5 ± 0.3 μm for the rolling element balls and

1.0±0.2 μm for the conical rolling elements measured at a cut-off of 0.8 mm using a Gaussian roughness filter. These values are two orders of magnitude higher than the lower bearing steel and silicon nitride ceramic rolling element planetary balls which were commercially available and measured to have the R_q values of 0.015 μm and 0.012 μm respectively using the same filter and cut-off. Polishing of these samples was thus necessary to obtain a better surface finish which was closer to the values of lower planetary balls. Designs were considered to construct a new machine to fulfil the above requirements and at the same time possibilities of modifying the four ball machine to polish the samples were explored.

2.2.2 Proposed design

The proposed design was very simple in construction and involved the rotation of the rolling element in a female cup containing abrasive particles. This design was selected after some careful assessment of a variety of solutions on the basis of experimental observations. The female cup had exactly the same geometry as that of the rolling element ball or cone and different grades of abrasive particles were used for progressive polishing. A schematic of the design is shown in figure 2.1. The rolling element ball or cone to be polished was held in the spindle of the four ball machine via a collet and rotated at the desired speed. The female cup was held in the cup holder of the four ball machine and the normal load was applied by putting the dead load at the end of lever arm. The female cup was initially made from mild steel and aluminium and it was thought that the hard abrasive particles would become embedded in the soft steel or aluminium surface. Thus polishing the rolling elements by two body abrasion between the hard particles on the surface of female cup. Experimental trials were conducted using this technique and it was observed that polishing was only marginal and the female cups were wearing out. Moreover, the heat generated was high. It is possible that this behaviour was due to three body abrasion, in which case the hard abrasive particles were not embedding on the surface of soft steel or aluminium cup. This problem was overcome by placing a polishing cloth between the surface of female cup and rolling element ball or cone to hold the abrasive particles. This not only stopped any damage to the cup but also a better polish could be achieved.

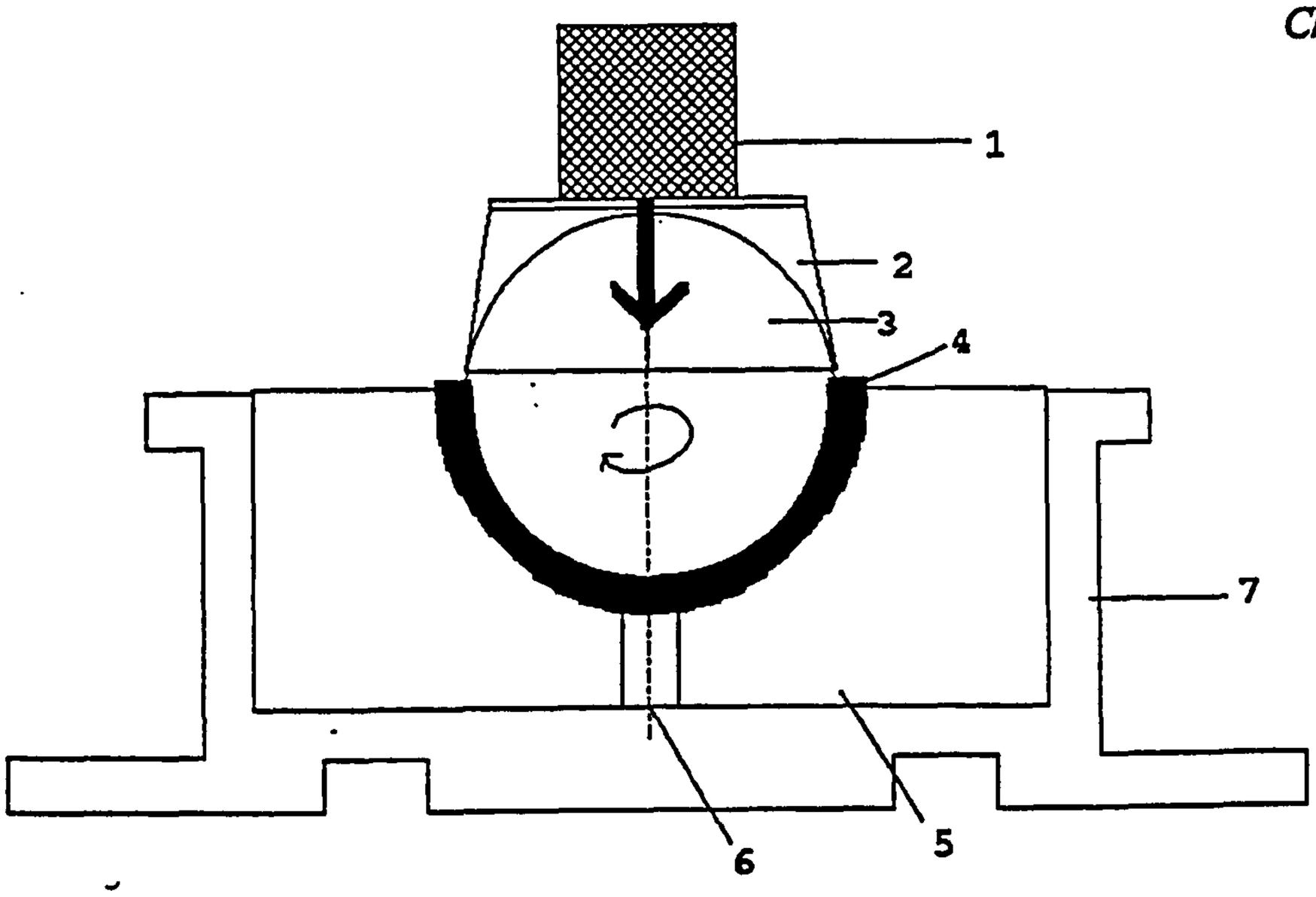

Figure 2.1, Schematic of the design

(1; Applied load, 2; Collet, 3; Sample for polishing, 4; Polishing cloth, 5; Female cup, 6; Hole for debris)

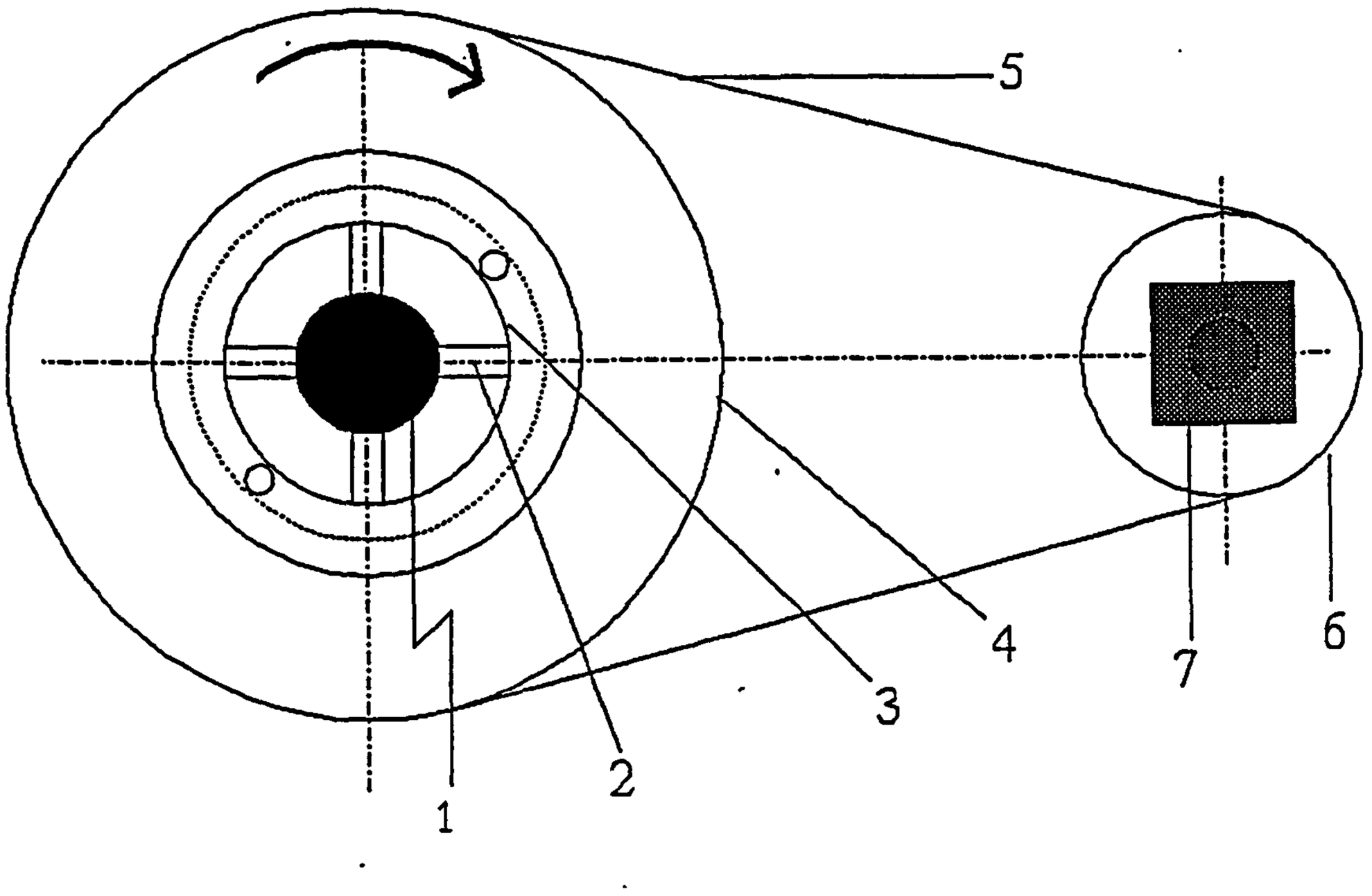

Figure 2.2, Schematic of the sample polishing method

(1; Female cup, 2; Slot, 3; Cup holder, 4; Pulley, 5; Belt, 6; Pulley, 7; Motor)

However, there was still a problem of machining these female cups to the high level of precision required. This problem was solved by moulding these female cups. The moulding material was selected as Backelite (Phenolic) because of reduced cost and a readily available backelite moulding machine. Further investigations revealed that by putting horizontal slots in the female cup and also by rotating it in the opposite direction to that of the spindle gave the best results using this technique. A motor was used to rotate the female cup with the help of a belt and pulley arrangement. The schematic of the finalized design is shown in figure 2.2.

2.2.3 Polishing procedure

Initial tests were conducted using silicon carbide and diamond particles as the abrasive medium to polish the WC-Co coatings. The selection of diamond particles as the abrasive medium was then made on the basis of these studies due to better surface finish results. Different types and grades of polishing cloths were also studied and it was observed that a soft cotton cloth gives the best results, especially in the final stages of polishing. This was thought to be the case due to the ability of this cloth to easily conform with the contour in the female cup due to its softness and less thickness. Repeated tests at a variety of loads and speed using different grades of diamond abrasive particles showed that the polishing time not only varied for thermal spray coatings produced by different spraying processes but it also depended upon the surface finish after grinding of the rolling elements. This was mainly because different coating processes use different process parameters and spray powder size which result in varying fine microstructure etc. Similarly if the grinding was poor it was difficult to achieve a good polish on these samples.

A general procedure which incorporated progressive polishing was consistently followed to polish the rolling elements. During this procedure the initial polishing was done using a 25 μm diamond slurry at spindle speed of 200$\pm$20 rpm and cup speed of 150$\pm$20 rpm in the direction opposite to the spindle rotation. Slurry was added to the female cup every 20 to 30 seconds by lowering and spraying it manually with a pipet. This procedure randomized the abrasive particles and washed the debris. The lever arm load was generally kept at 0.1 kg at a 20:1 ratio. The

same procedure was followed to progressively polish the samples in 14 μm, 6 μm and 1 μm diamond slurry. The final polishing was done using 0.25 μm diamond paste in polishing lubricant. The diamond slurries were oil based and of commercial brand. Care was required to avoid debris accumulation in the female cup and to maintain the cleanliness of the cup and the rolling elements to avoid any contamination of diamond particles between the different stages of progressive polishing. Tests at other loads resulted in poor polishing.

This polishing technique resulted in the surface roughness values of 0.075 ± 0.05 μm (R_q) for coatings deposited by different thermal spraying techniques. Although, these values were still high in comparison to the values of the lower rolling element balls they were more than an order of magnitude better than the ground surface finish. These improvements in surface roughness values were considered reasonable and no attempts were therefore made to either refine this technique or to manufacture a new polishing machine. The surface roughness results obtained after polishing of the coatings deposited by different spraying techniques will be discussed in detail in chapter 5.

2.3 Rolling Contact Fatigue (RCF) Tests

The following section describes the methodology adopted to perform the RCF tests using the modified four ball machine.

2.3.1 Test preparation

Periodic checks were made to maintain the belt tension in the high speed driving belt of the modified four ball machine and the accuracy of the proximity sensors. The driving belt tension was adjusted to give an extension in the belt length of 2.5% which corresponded to an increase in the centre distances of the driving and driven pulleys of 5 mm as indicated by the machine supplier. When a new belt was fitted these checks were made after every 20 hours and then less frequently. This was necessary to avoid slippage of the belt and avoid unnecessary forces on the spindle bearing. This also effected the spindle eccentricity. Proximity sensors were checked for the correct registration of the shaft speed by the tachometer reading which was

confirmed by the stroboscope readings. Spindle run-out was also checked by the dial indicator and the deviation due to spindle eccentricity and its surface roughness was found to be 0.02 mm. The deviation in the ball when the ball collet assembly was fitted to the spindle was found to be 7 nm. These readings were just within the tolerance limits of the machine manufacturer. The values changed as the belt was tightened. The electric mains switch was then turned on and vibration trip mode was selected as a method for the test termination. The vibration mode was checked by the illumination of the green LED by pressing the vibration test switch.

Consistent cleaning and degreasing procedures were adopted to prepare the rolling elements and the cup assembly before each RCF test. The driving rolling element & collet, the driven balls, the cup, the cup holder and the cup holder plate were initially cleaned in an immersed acetone bath in the ultrasonic cleaner for five minutes. The surfaces were then cleaned and dried with paper sheet and cotton. The components of the cup assembly were then dried with a fan heater for five minutes and allowed to cool down. The steel lower race and the rolling element balls were then inspected for any damage under light microscope. New steel lower balls were used for each test. However, the lower race was used for a number of tests until appreciable damage was observed on its surface. Tests were conducted with bearing steel or silicon nitride ceramic planetary balls of the specifications shown in table 2.1.

The lower race was then pressed in to the cup holder using a special fixture and the surfaces were again cleaned in an acetone bath in an ultrasonic cleaner for five minutes. The surfaces were then dried using the fan heater for five minutes. The three grub screws at the base of the cup holder were then placed in position to avoid any oil leakage from the base of the cup during the test. The driving spindle was then cleaned with acetone and dried using the fan heater. The counter balance of the loading lever arm was adjusted in its position to give a 20:1 ratio on the lever arm. The lever arm was then locked in the inclined position with the help of a locking lever.

Lower ball	Supplier	Nominal Diameter (mm)	R_a (μm)	R_q (μm)	Vicker's Hardness (H_v)
Bearing Steel	SKF	12.7	0.012	0.015	820
Silicon Nitride Ceramic	NORTON	12.7	0.010	0.013	1580

Table 2.1

2.3.2 Test procedure

The driving ball and collet were assembled to the machine spindle and pressed in to ensure no relative motion. The lower planetary balls were put in the cup and the cup holder lid placed in position with the help of the two screws. Test lubricant was put in the cup assembly until the planetary balls were completely immersed in the lubricant. The cup assembly was then placed on the heater pad which rested on the locator pins. The cup assembly and the heater pad were then placed on the piston with the help of the arm provided. The loading piston was then raised by disengaging the locking lever and the lever arm levelled with the help of the spirit level. Necessary adjustments in the piston height were made with the help of the adjusting nut at the base of the piston. The piston was then lowered by raising the lever arm and the lever arm was then locked in its inclined position with the help of the locking lever. Only a small fraction of the total load was placed on the end of the lever arm and thermocouple connections were made to record the oil bulk temperature during the test.

The motor speed controller was then set to zero and the tachometer scale set to the X1 position. Motor enable switch was then selected and the spindle speed gradually increased to 1000 rpm. The locking lever was disengaged and the lever arm was gradually lowered until the lower rolling elements came in to contact with the upper drive rolling element. The machine was checked for any unnecessary vibration. The spindle speed was then gradually increased to the required speed. The required load to the cup assembly was then applied to the cup assembly by gradually increasing the load at the end of the lever arm. Spindle speed was then readjusted and the timer

and counter switch selected to mark the start of the test. The date, time and, the oil bulk temperature were then recorded and any unnecessary vibration noted. Vibration sensitivity was then increased by the potentiometer adjustment until the green Light Emitting Diode (LED) just illuminated. The vibration sensitivity was then slightly decreased and this initial level of sensitivity was then noted. During the initial phase of the test the oil bulk temperature increased due to the heat generation caused by the elastic hysteresis, microslip and other frictional effects. This temperature increased to an equilibrium stage after a certain amount of time when the frictional heat generation became equal to the heat dissipation. This temperature depended upon the lubricant type, the load and the speed of the test. A typical temperature variation curve for a test at a spindle speed of 4000 rpm and lever arm load of 10 Kg is shown in figure 2.3. The lubricant was Hitec-174 and the balls material was bearing steel. This temperature increase caused viscosity variation and the test speed varied during this phase of the test. The spindle speed was thus readjusted to the required speed until the temperature equilibrium was reached. Vibration sensitivity was again checked and readjusted if required.

The lubricating oil was replenished for long duration tests. But this lubricant loss was marginal and the machine was left running overnight for long duration tests. If any of the rolling elements in the cup assembly failed the vibration level tended to increase the preset value which caused the green LED to illuminate. If the LED was illuminated for more than two seconds the vibration trip switch cut off the drive motor marking the test termination. In some cases when no failure occurred for a longer period of the time the test was suspended after a certain number of stress cycles (50~60 million). After the test termination or suspension the timer, revolution and temperature readings were recorded. The piston was lowered by locking the lever arm in the inclined position and the cup assembly removed. The upper rolling element was inspected while in the spindle for any visible failure. In case of failure the rolling element was removed from the spindle and cleaned in acetone in the ultrasonic bath for detailed inspections at a later stage. The lower balls were removed from the cup assembly and cleaned in acetone and prepared for microscopic analysis. The test lubricant was filtered through hardened ashless, grade

541 filter paper in to a Buchner flask. The filter paper was then stored in a desiccator for further examinations. The cup was removed from the cup holder, cleaned in acetone and analyzed for any surface damage.

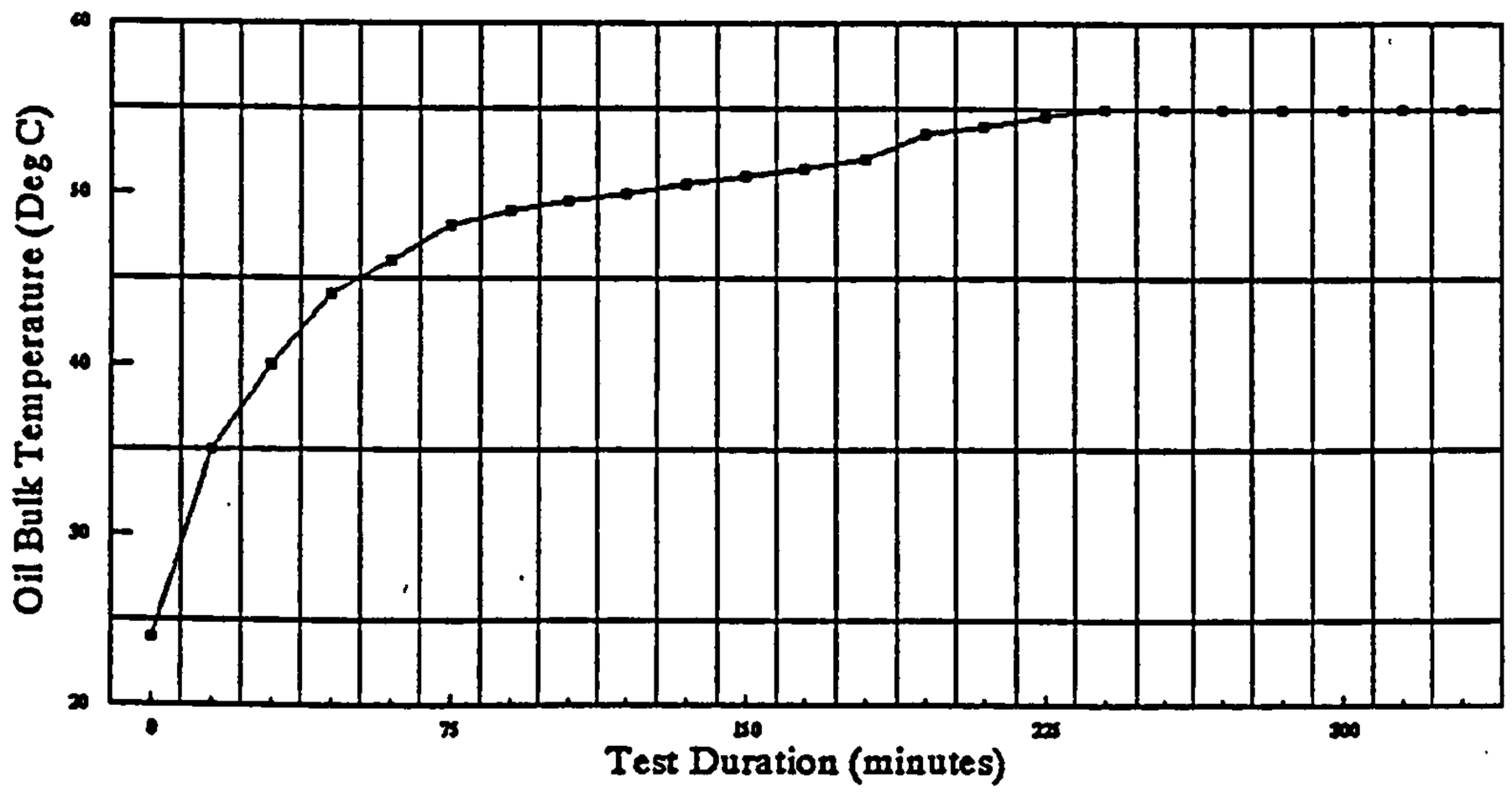

Figure 2.3, Temperature profile during a test

2.3.3 Test verification

The IP300, which is a standard test of the Institute of Petroleum to study the effect of lubricant properties on fatigue failure, was used to assess the correct operation of the machine at regular intervals. The test procedures described above were followed and the shaft speed was set to 1450±10 rpm at a contact load of 600 Kg. SKF steel balls and a base lubricant Talpa-20 was used in these tests. Time to failure was observed to vary from 20 to 35 minutes which was within the limits prescribed by IP300 (user manual, four ball machine, 1980).

2.3.4 Test lubricants

Three test lubricants were used to study their effect on the lifetime and fatigue failure mode of thermal spray coatings. Some of the properties of these lubricants are summarized in table 2.2. Talpa-20 is a hydrocarbon oil (used as a base oil) extracted from the mineral petroleum. Exxon-2389 is a commercially available synthetic oil used in turbine propelled engines, etc. This lubricant contains chains of alternating silicon and oxygen atoms. Silicones are superior to hydrocarbons

because of their non-flammability. Hitec-174 is high viscosity hydrocarbon oil containing oxygen atoms attached to it. This lubricant has increased attraction force for metal surfaces. This lubricant was not commercially available. In addition to the lubricants described in table 2.2, tests were also conducted in corrosive environments by ultrasonically mixing distilled water and conventional automobile brake fluid in equal proportions by volume. This lubricant was used with splash feed lubrication system as described in section 2.4. In addition to this, dry tests at atmospheric pressure were also conducted. For most of these lubricants, data on the pressure viscosity coefficient was not available which is an important property when evaluating the lubricant film thickness due to Elasto-Hydrodynamic Lubrication (EHL). These values were thus approximated as shown in appendix E.

Lubricant Type	Specific Gravity (15°C)	Flash Point (°C)	Pour Point (°C)	Kinematic Viscosity (c.s. °C)	
				40 °C	100 °C
Talpa-20	0.899	216	-33	94.6	8.8
Exxon 2389	0.955	220	-65	12.46	3.19
Hitec 174	0.95	255	-20	200.0	40

Table 2.2

2.4 Splash Feed Lubrication System

Tribological behaviour of the lubricated contacting surfaces can not only be affected by the properties of the lubricant and the mechanism of the fluid film formation but also by the mechanism through which the lubricant is supplied at the point of contact. This is not only because of the variations in the lubricant properties, ie. viscosity etc. and the increase in oil and contacting surface temperature during a tribological process, but also because the behaviour of the debris can be influenced by the lubrication mechanism. Four ball machine tests are conventionally performed under the immersed lubrication conditions during which the oil bulk temperature increases due to frictional effects, etc. Generally, negligible amount of surface wear

debris are produced before the fatigue failure occurs in the modified four ball tests but with certain lubricants the asperity contact can cause problems of excessive debris generation. The debris accumulate within the lubricant and can thus alter the tribological behaviour during the test. A splash feed lubrication system shown as figure 2.4, was designed to modify the immersed lubrication system.

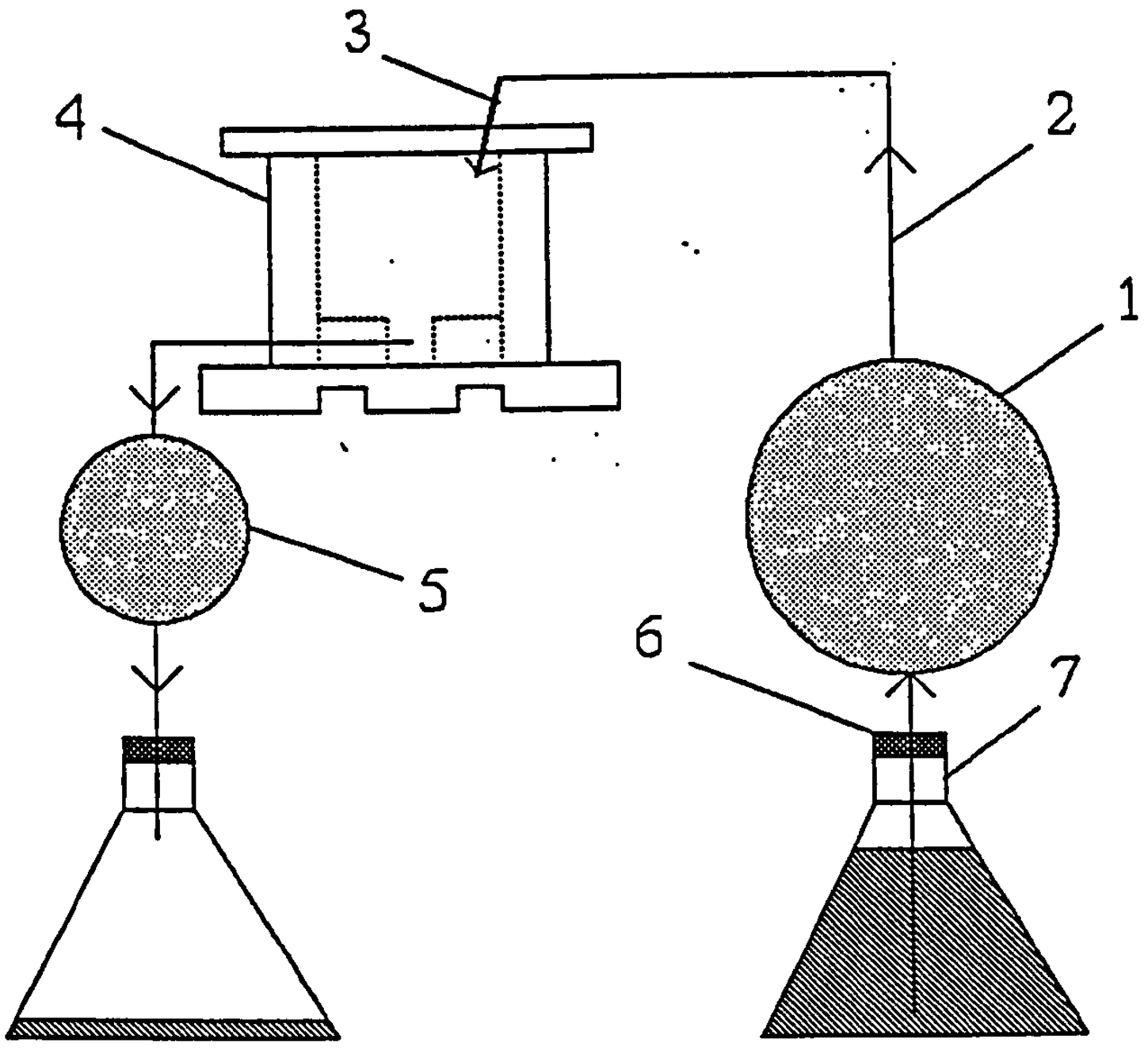

Figure 2.4, Schematic of the Splash Feed Lubrication System
(1; Micro pump, 2; Flexible tubing, 3; Injector syringe, 4; Cup assembly, 5; Valve, 6; Seal, 7; Flask)

There were the following two main objectives for this modification:

a) To avoid viscosity variation of the lubricant at the inlet to the contact area during the test.

b) To remove the contaminant lubricant from the contact region.

The basic design feature for such a modification relies on a regulated supply of non-contaminated lubricant of constant temperature at the inlet to the contact area. Also,

a mechanism is required to remove the contaminated lubricant from the four ball assembly. A micro pump (type 4.1) supplied by Prominent was thus selected to feed the lubricant. This pump had a stainless steel chamber to resist corrosion which was important for the tribological testing with the water based (corrosive) lubricants. The pump operated from a diaphragm and swash plate which allowed both the stroke volume and the stroke rate to be adjusted giving a flexibility in the control of volume flow rate. The pump feed rate had a range from 1170 cc/hr to 1.2 cc/hr. The requirement of splashing this lubricant at the inlet to the contact area was met by using a hypodermic syringe which was connected to the discharge side of the pump via a 6 mm flexible tubing. The syringe was carefully positioned to rest in an angular hole in the cover plate of the cup holder which assisted in the correct positioning of the splash of the lubricant at the inlet to the contact area (in the direction of rotation of the spindle) between the driving rolling element and the plenary balls. The provision of removing the contaminant lubricant from the cup assembly was provided by a modified cup holder which was designed to assist the gravity drain of the contaminated lubricant with the help of a right angled hole at the base of the cup holder.

2.5 Planetary Ball Speed in the Four Ball System

Analytical studies to calculate the speed of the lower planetary balls under a given shaft speed and configuration of the modified four ball system are generally made under the assumption of pure rolling conditions in the four ball assembly. However, depending upon the tribological conditions, ie. friction and lubricant behaviour, etc. the actual speeds can be different from the theoretically calculated speeds. Hence, experimental investigation of the orbital speed of the lower planetary balls can not only reveal whether the motion was pure rolling or a combination of rolling and sliding, but can also estimate the amount of sliding in the four ball system by comparing the results of experimental investigations with the theoretical calculations. It was for this reason that efforts were made to experimentally measure the speed of the planetary balls.

Initial studies to measure the speed of the drive ball and the lower planetary balls

were conducted by means of a stroboscope. These studies showed that although it was possible to measure the orbital speed under a variety of conditions the method suffers from low accuracy and difficulty in measurements for non-translucent lubricants. Another technique was thus developed in which the vibration signal from the cup assembly was used to accurately track the speed of the drive shaft and the lower planetary balls. In this technique the AQ type piezoelectric accelerometer was attached to the body of the cup by means of a stud screw. One accelerometer was connected along and another perpendicular to the axis of the drive shaft. The accelerometer had a resonant frequency of approximately 53 kHz. Later studies showed that only one accelerometer was necessary either in the horizontal or vertical plane. Figure 2.5 represents a schematic of the method used. The signal from the accelerometer was sent in to an amplifier. The amplified signal was fed in to a Schlumburger 1200 signal processor. This signal processor was used to convert the vibration amplified signal from time domain to frequency domain. This process is generally termed the Fast Fourier Transformation (FFT) of the vibration signal.

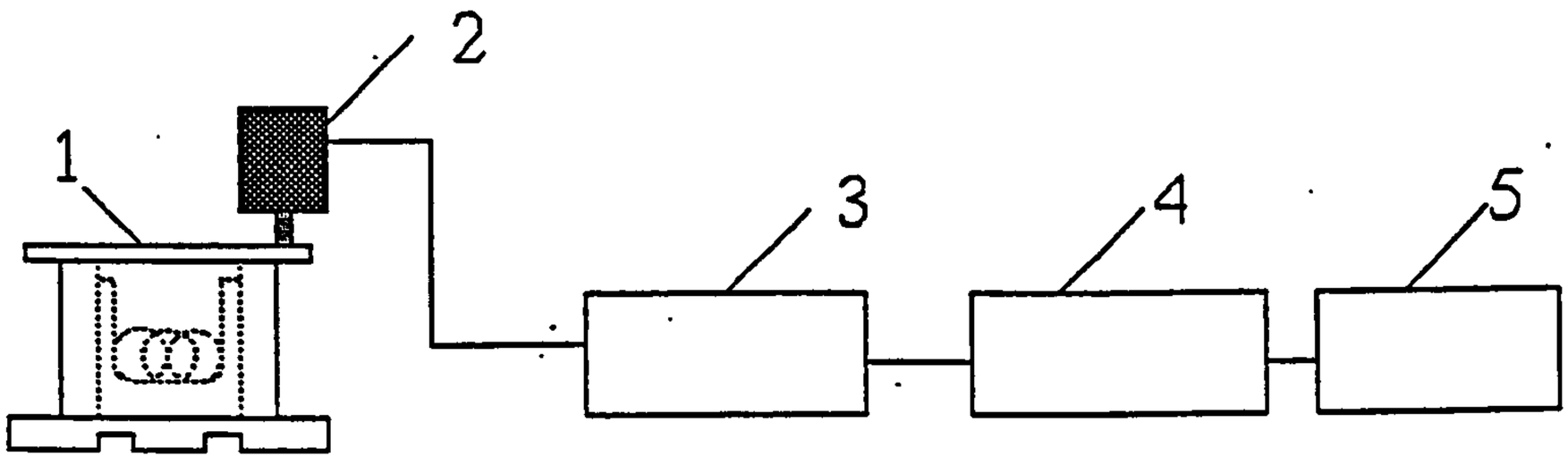

Figure 2.5, Schematic of the vibration monitoring system

(1; Cup assembly, 2; Accelerometer, 3; Amplifier, 4; Signal processor, 5; Printer)

The technique enabled the precise measurement of the drive shaft speed and average speed of the planetary balls to an accuracy of ± 0.1 Hz. Figure 2.6 shows a result recorded at a shaft speed of 4000 rpm (66.6 Hz) and the average speed of the planetary balls can be measured as 976 rpm. These speeds were then used to evaluate the amount of sliding between the drive rolling element and lower planetary balls as explained in chapter 3.

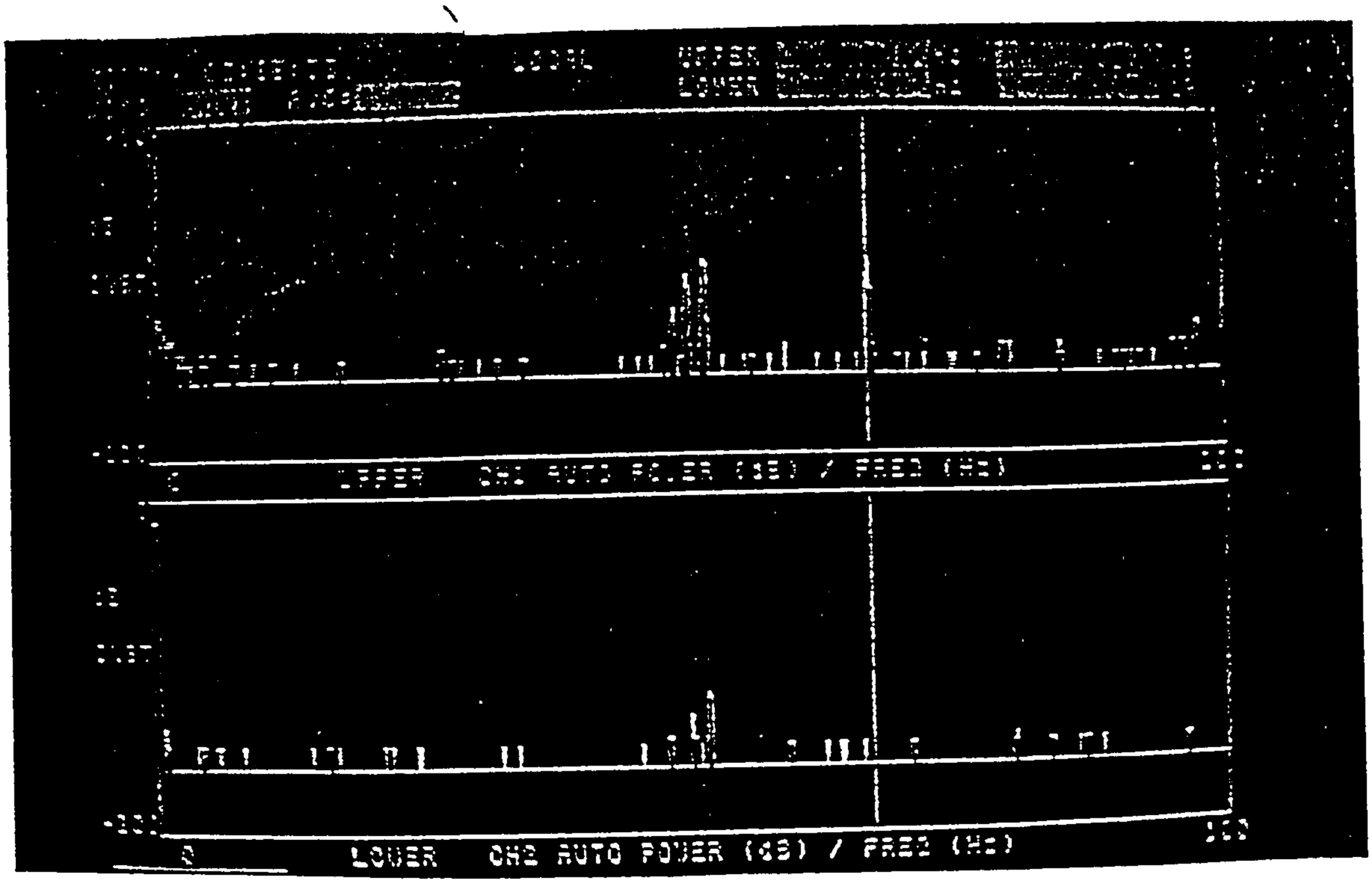

Figure 2.6, Vibration Signal after FFT

2.6 Frictional Torque Measurements

The first scientific study to understand the phenomenon of rolling friction was considered by Coulomb (in 1785). Later studies were then made by Morin and Depuit in the early nineteenth century and then by Reynolds towards the end of the 19th century. Similarly, Palmgren (1945), Tabor (1955), have attributed rolling resistance to inelastic properties of the bulk material and have provided a qualitative experimental evidence that the extent of microslip in free rolling is small (Bidwell, 1962). All these studies successively provided a better understanding of the mechanism of rolling friction. Frictional forces effect the stress distribution of the rolling bodies and can thus effect the failures. Frictional forces in rolling contacts can be regarded as a combination of different factors which behave in a complex way. Some of these factors which can contribute to over all rolling friction can be categorized as follows:

* Microslip and overall interfacial sliding effects. Frictional forces can arise from any overall interfacial sliding between the rolling bodies. Even when there is no sliding present microslip between the bodies in the rolling contact

contributes to the rolling friction.

* Contacting bodies are not perfectly elastic and the elastic hysteresis in the contacting bodies dissipate energy which leads to rolling friction.
* The surface roughness, affects the real area of contact ratio as well as, dissipates energy in surmounting the irregularities. These factors contribute to rolling friction. As a general rule it is known that the higher the surface roughness the higher is the frictional force and vice versa.
* Most of the bodies in rolling contact use some form of lubrication. The lubricant film can not only affect the stress distribution but also dissipate energy in overcoming the viscous forces which can contribute to frictional effects.

All of these factors can contribute to the rolling friction in the four ball assembly. Although it was virtually impossible to calculate the exact value of the coefficient of rolling friction between the drive and the driven rolling elements, frictional torque measurements were experimentally performed in the four ball assembly for comparative studies. Figure 2.7 shows the schematic of the arrangement used to measure the total frictional torque in the modified four ball assembly. The arrangement consisted of a torque arm protruding from the base of the cup assembly which contacted a force transducer at the other end in a horizontal plane. The transducer was calibrated before the measurements and measured the frictional force acting at the end of the lever arm. The output signal from the force transducer was sent to a digital display and then to a printer. The cup assembly rested on a rolling element thrust bearing. The frictional torque measured represented the sum of the frictional torque in the four ball cup assembly and the frictional torque due to the rolling element thrust bearing through which the load is applied to the cup assembly. Table 2.3 shows typical results of the frictional torque measurements made under the immersed lubrication conditions using Hitec-174 as the test lubricant, with steel drive and driven balls. These measurements were made at a contact load of 40 N, 160 N, and 400 N applied to the cup assembly at a variety of the drive shaft speeds. The frictional torque measurement results shown in table 2.3 indicate that under the given test conditions the results were sensitive to the variations in the contact load

in the range of 40~160 N. Similarly, the effect of the speed of the upper drive ball was critical to the frictional torque results in the range of 1000~2000 rpm.

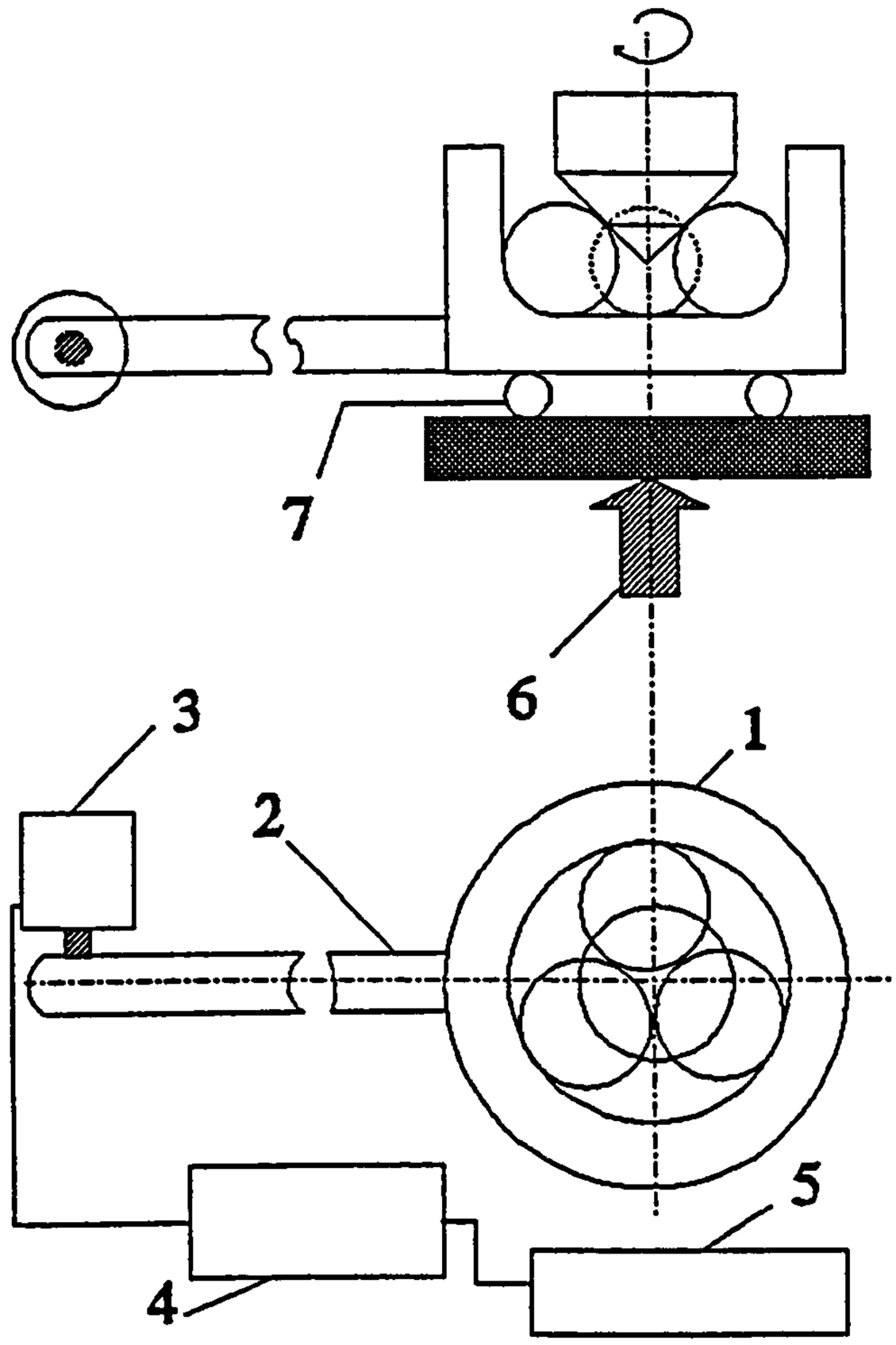

Figure 2.7, Schematic of frictional torque measurement arrangement (1; Cup assembly, 2; Torque arm, 3; Force transducer, 4; Digital readout display, 5; Printer, 6; Applied load, 7; Rolling element thrust bearing)

In general, steady state values were achieved at shaft speeds greater then 2000 rpm and at contact load in excess of 40 N applied to the cup assembly. The steady state values of the frictional torque for this case of uncoated rolling element balls were in the range of 0.02~0.03 Nm. A similar trend was observed with the Exxon-2389 lubricant with slightly higher values of the frictional torque in the four ball assembly.

Speed (rpm)	Frictional Torque Measurements		
	Contact Load 40 N	Contact Load 160 N	Contact Load 400 N
1000	0.009 Nm	0.015 Nm	0.02 Nm
2000	0.019 Nm	0.028 Nm	0.027 Nm
4000	0.019 Nm	0.028 Nm	0.027 Nm
8000	0.019 Nm	0.03 Nm	0.031 Nm

Table 2.3, Frictional torque measurements (lubricant Hitec-174)

2.7 Discussion

The polishing technique used was progressively developed and based on an iterative refinement of the design. The technique used may not be the optimum to polish these samples but it was selected because of its simplicity and a reasonable improvement in the surface roughness of the rolling elements. The polishing times and surface finish after polishing depended upon the surface finish after grinding and the coating microstructure eg. porosity, secondary phase particles, etc. However, this technique may not be suitable for mass production, for which other arrangements and designs can be considered. The speed and load etc. parameters used to polish the samples were based on the experimental observation of the author and were thought to be best suited for the arrangement used. However, other combinations of these parameters might also have been possible. The mechanism of polishing can be thought of mainly as abrasion caused by the diamond particles which were either embedded or held on the cloth used for polishing. The debris produced were either absorbed by the cloth or carried away by the polishing oil into the slots of the cup when fresh slurry was sprayed. No attempts were made to study the size or shape of the debris produced during polishing.

The test procedures described briefly outline the methodology used for the RCF

testing. Parameters selected such as the spindle speed, load on the four ball assembly, lubrication conditions, etc. during the RCF testing will be discussed in chapter 5. The arrangement used to study the ball kinematics enabled the experimental measurement of the speed of the drive shaft and orbital speed of the planetary balls. These results of the orbital speed measurement can be beneficial in studying the sliding in the four ball assembly as shown in chapter 3. However, no attempts were made to measure the magnitude of spin in the lower planetary balls.

The splash feed lubrication system enabled a constant supply of non-contaminated lubricant at the inlet to the contact area and also served the purpose of the removal of contaminated lubricant from the cup assembly. The versatility in design enabled the selection of a variety of lubricants for a range of volume flow rates. The design can also be used to recycle the lubricant after filtering the debris. The debris can then also be analyzed for further investigations.

The frictional torque measurements gave a comparison of the results for different contact configurations of the four ball machine. However, it represented the friction component arising from the contact between the lower balls and the cup as well as the friction forces due to the thrust bearing. It was for this reason that the frictional torque measurements were used for the comparative studies only. The results for the case of conventional steel ball bearing configuration can be compared with the case of coated configurations as shown in chapter 5 of the thesis.

Chapter 3
ANALYTICAL INVESTIGATIONS

3.1 Introduction

The stress fields in coated elements are studied to develop an understanding of the relationship between the stress fields and the coating failures. A finite element approach is used to develop the contact model which represents the case of a coated upper ball in contact with an uncoated lower ball of the modified four ball machine. The results are presented for various coating types and different coating thicknesses. The ball kinematics of the modified four ball machine are also studied along with the slip analysis due to contact conformity within the contact region. The analytical slip results are compared with the experimental observations.

3.2 Finite Element Model (FEM)

3.2.1 Background and objectives

It is well established that conventional contact mechanics approaches based on homogenous materials cannot be directly applied to find solutions to layered surfaces. The possibility that there may be defects in the multilayer and that the contact stress can lie in the elastic range of one material and plastic range of the other material, makes the analytical analysis complex. Initial studies to evaluate the contact stress in a layered elastic surface were performed by Chen et. al. (1971) & Gupta et. al. (1974). They performed a mathematical formulation of the problem using the integral transfer technique and indicated that the actual pressure distribution in a layered surface is quite similar to the Hertzian distribution for modulus ratios less than or equal to four. Cole et. al. (1992) have used a similar approach and included the effect of coating surface asperities. Later studies by Djabella et. al. (1992, 1993a, 1993b, 1993c, 1994), Lee et.al. (1992a, 1992b), Schwarzer et. al. (1995), Sun et. al. (1995), and Kapoor et. al. (1996) have used a finite element modelling (FEM) approach to evaluate the contact stress in layered surfaces subjected to rolling or rolling/sliding contacts. Laborious numerical techniques and complex analytical equations were thus avoided using the computer codes along with the flexibility of analyzing complex functionally graded systems

not only in elastic but also in elastic/plastic models of varying geometries. Some of these studies addressed static frictionless contact which can be a simulation of rolling frictionless contacts as indicated by (Djabella et. al. 1992) and some involved normal and tangential loading including frictional effects thereby representing a sliding case for layered surfaces.

Initial studies by Djabella et. al. (1992) on an elastic monolayer coating substrate system subjected to normal loading used a prescribed pressure distribution approach for cylindrical and spherical contacts using plane strain and an axisymmetric FEM approach respectively. They investigated the effect of coating thickness and the Young's modulus ratio of the coating and substrate materials on the stress fields and indicated that these parameters affect the in-plane tensile, and compressive stress and interfacial shear stress in a complicated fashion. They concluded that the stresses within the outer layer of the coating and at the coating/substrate interface which can be responsible for cohesive and adhesive failure respectively cannot be simultaneously minimized by an appropriate choice of these two variables. Their studies on double and multi-layered coating/substrate systems (1993a, 1994) indicated that for a given coating thickness and ratio of outer coating layer to substrate Young's modulus, a system with two or more intermediate layers was preferred to a coating with a sharp interface. They indicated that the functional grading of the coatings can not only enable less severe stress distribution at the interface but also allow thicker coatings to be deposited. Studies by Djabella et. al. (1993b, 1993c) on elastic coating substrate systems subjected to normal and tangential loading including frictional effects indicated that the maximum tensile stress at the surface and the shear stress at the interface increases very significantly with an increasing coefficient of friction. However, the increase in interfacial shear stress becomes less marked as the coating thickness increases. They reported that functionally graded, thick double layered coating systems with decreasing modulus from surface to the substrate are more resistant to surface tensile failure and interfacial delamination, and are preferred in high friction conditions then thinner coatings. These studies revealed that the coating's failure at the interface and at the surface was a complex function of coating thickness, Young's modulus and friction

coefficients. The role of residual stresses and coating defects can make the failure predictions more complex. Functional grading can thus be helpful in resisting interfacial delamination. Hence it can be appreciated that it is beneficial to target the coating failure resistance based on some experimental studies relating to the coating failures eg. for a given coating thickness in single or multiple layer system. This can be helpful in combating the failures within the coating whereas functional grading can strengthen the resistance to interfacial delamination. As it was not usually possible to provide high surface and interfacial failure resistance by a suitable selection of parameters for a given system of the coating thickness and modulus ratio in a single layer system it would be practical to strengthen one or the other, based on the coating applications and experimental evidence of the failures. Recent studies by Djabella et. al. (1995) indicated that both analytical and FEM approaches can be used to investigate the elastic contact stress in coating substrate systems. However, the FEM approach can be easily extended to perform elastic plastic analysis in the layered systems and thus provide a better understanding of the coating failure mechanisms.

Sun et. al. (1995) have reported studies on plastic deformation behaviour and thus studied some of the possible coating failure modes for TiN coatings on various substrates subjected to normal loading. They indicated that the plastic deformation is initiated in the substrate at the coating substrate interface and the plastic deformation in the coating does not initiated until a large plastic zone has been developed in the substrate. However, when thick coatings (coating thickness > 9μm) were deposited on relatively strong substrate (high speed steel) yielding initiated in the coating at a certain distance from the interface. Once initiated the plastic zone in these coatings grew more rapidly in the coating, yet at the interface the substrate yields before the coating does such that the two distinct plastic zones are formed. Similarly, for thin coatings on a strong substrate once the plastic zone initiated at the interface just below the contact centre the plastic zone grew towards the surface faster around the contact edge region than it did in the contact region. This showed the detrimental effect of the thin coating on a hard substrate. Hence, the substrate strength and the coating thickness can be significant to the coating

failure. In general, it can be appreciated from the elastic and elastic/plastic FEM studies that the coating failure is a complex phenomenon which is significantly affected by the coating and substrate material properties, coating thickness, functional grading, frictional effects, etc. Moreover, none of these studies included the effect of the residual stress caused during the deposition process and almost all studies assumed that a homogeneous isotropic coating which was perfectly adhered to the substrate. These assumptions can make the actual stress field in the layered structure different from the predicted, and a thorough understanding is thus required to reflect the real problem. Lee et. al. (1992) has addressed one of these assumptions by modelling (FEM) the subsurface crack at the interface of the coated material under the effect of a moving compressive load incorporating frictional effects at the crack surface. They considered various crack configurations and concluded that the stress intensity factor for the subsurface crack at the interface of a coated material becomes smaller as the stiffness of the coating layer becomes larger. Similarly, Kapoor et. al. (1996) have considered the effects of coating anisotropy in their analysis and similar approaches can be used to develop further models with some experimental studies. In general, further studies are required before a complete understanding of the coating's failure can be developed.

The present study represents a static frictionless elastic contact model in which a coated rolling element ball contacts with another uncoated ball. In this model the coated ball represents the upper drive ball of the modified four ball machine which contacts the lower ball. The stress fields are calculated for the configurations of a conventional steel ball bearing (steel lower ball) and hybrid ceramic bearing (ceramic lower ball). The objectives of the work were two fold:

1) To evaluate the effect of coating thickness on the contact stress fields.
2) To evaluate the effect of changes in Young's modulus of the coating material on the contact stress fields.

3.2.2 Model description

The FEM is an approximate displacement method which involves discretion of a physical problem into *elements* which are solved analytically. These subregions or

elements are represented by a function much simpler than that required for the entire region which are then joined together to give an approximate solution. A commercially available finite element code (PAFEC) was used during this investigation which uses a strain energy and stiffness matrix to calculate the stress fields. The general form of equation used to evaluate the stress fields can be written as:

$$\{F\} = \{K\}\ \{U\} \text{ ----------(1)}$$

where F is the force matrix, K the stiffness matrix and U the displacement matrix. Equation 1 is initially applied to calculate the displacements at local nodes within each element, and these displacements are then combined together with a piecewise continuous function to give the global force displacement equations. Castigliano's theorem is used to calculate the force at individual and global nodes by differentiating the strain energy with respect to displacement.

Figure 3.1 shows the static elastic contact model of a coated upper ball contacting a lower steel or ceramic ball. The model represents the actual dimensions of 12.7 mm diameter balls. This is an axisymmetric model which reduces the cost of the model by simplifying the geometric requirements to one plane. The axis of symmetry is the X-axis and the load is also applied along this axis. The applied load is calculated after considering the contact angle and the lever arm load and represents the contact force between the balls. The contact model is restrained along the load axis of symmetry in the perpendicular direction and the lower ball is also restrained along the perpendicular axis in the load axis direction. The model simulates a static contact between the contacting elements subjected to normal loading and the following assumptions were made:

a) Contact is dry and frictionless.

b) The material is homogenous and isotropic.

c) Fluid film does not effect the stress distribution.

d) The material behaves completely elastically under the given loading conditions.

e) The coating is perfectly adhered to the substrate and there are no residual

stresses or coating defects.

f) Surface roughness does not effect the stress distribution.

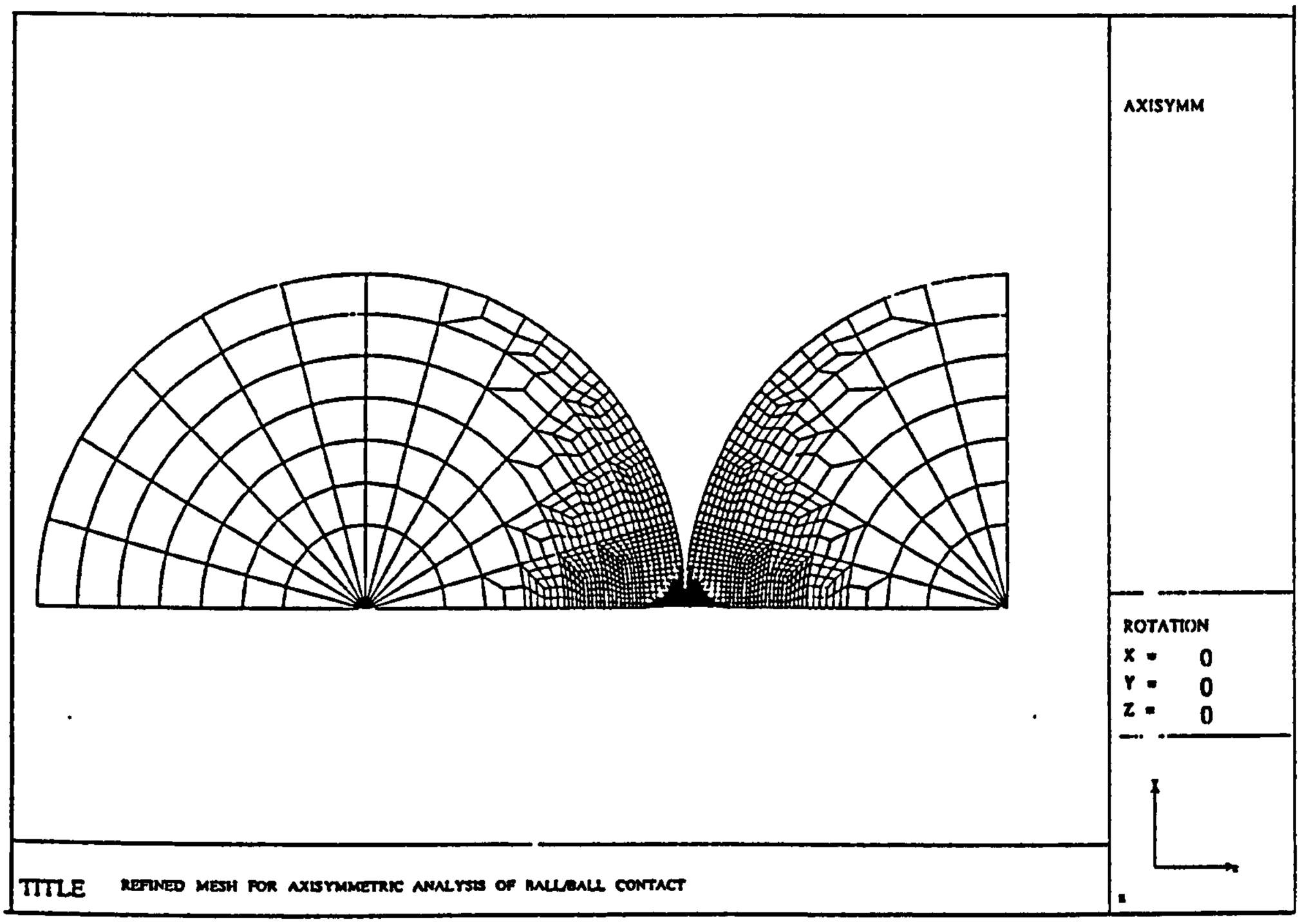

Figure 3.1, Finite element contact model

Although the ceramic and steel materials in this analysis can be assumed to be homogenous and isotropic, unfortunately the thermal spray coatings do not have the homogeneity or isotropy. It is for this reason that the values of Young's modulus are varied for a given coating thickness and the results are thought to be indicative of the stress fields only. It should be appreciated that owing to the porosity and secondary phase particles in the coating material the stress values will vary accordingly depending upon their shape and size, which can lead to stress concentrations. This behaviour was not studied during this analysis.

The model shown in figure 3.1 consists of 2856 isoparametric curvilinear quadrilateral eight noded elements and 18 isoparametric curvilinear triangular six noded elements for axisymmetric analysis. Both element types have mid side nodes to allow for reasonable distortions in the element shape. There are 8863 nodes in the model. The model initially considers the balls contacting each other at a point.

The nodes are then joined with each other allowing the material elastic deformation and thereby resulting in the contact circle. The number of nodes assigned is typical of the contact loading and contacting material, and represents the radius of the contact circle. Appendix D gives a brief description of the modules used to create the data file.

3.2.3 Model validation

The element's aspect ratios and the mesh density plays an important role for the accurate evaluation of the contact pressure distribution and analyses of the stress fields in the highly stressed areas. Figure 3.2 shows the mesh density and element's aspect ratios for the contact model. It can be seen that the mesh density decreases away from the contact zone, so as to reduce the computing cost of the model. Similarly, the element's aspect ratios in the contact zone is approximately unity whereas it varies away from the contact region. Each element in the contact region represents approximately 15 μm along the X-axis and Y-axis. Hence the coating thickness can be varied in multiples of 15 μm.

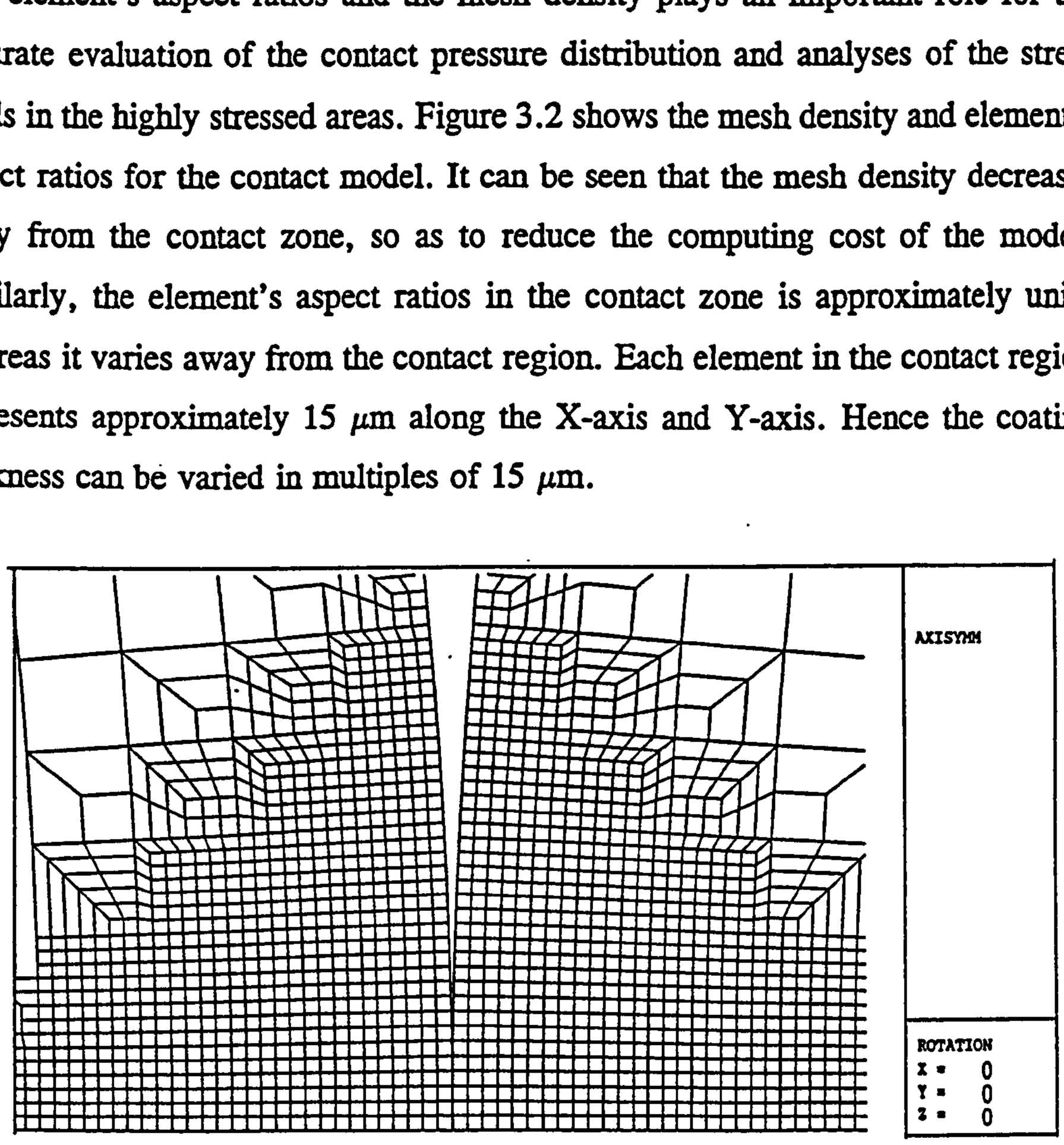

Figure 3.2, Mesh density in the contact zone

The accuracy of the FEM used in the analysis was evaluated by comparing the FEM results for an uncoated substrate model for ceramic/ceramic, steel/steel and steel/ceramic contacts with the analytical solutions of the Hertzian analysis.

Comparisons were made on the basis of the contact width, peak compressive stress, maximum shear stress and maximum principal stress for four different contact loads. The stress values from analytical and FEM results were within 5% of each other. A coarse mesh was also considered and it was seen that the results of the methods converged even with the coarse mesh. However, the stress fields were not well defined and the coating thickness could only be varied in the multiples of 80 μm. Hence a finer mesh shown in figure 3.2 was considered necessary for more accurate analysis. The suitability of the mesh in the FEM for the given loading was also be judged from the strain energy density which was found to vary uniformly away from the contact zone.

3.3 Result Analysis of Typical Load Cases

Although there can be numerous ways of analyzing the results of FEM for various coating thickness and Young's modulus. In order to reduce the number of results, the discussion in this thesis is restricted to the effects of these variables on the maximum shear stress, maximum orthogonal shear stress, maximum tensile stress and Von-Mises stress only. This is mainly because in rolling contact, the fatigue failure modes are generally associated with these stresses, the stress fields at the interface are also considered. The coating thicknesses considered in the present analysis are 30 μm and, 60 μm. Four different ratios of the modulus of the coating to the substrate were considered for all the coating thicknesses considered by varying the Young's modulus of the coated layer. The Young's modulus of the substrate material was kept constant at 207 GPa, which is consistent with the experimental studies on the steel substrate performed during this work. The Poison's ratio values were also varied accordingly with the Young's modulus values and approximations were made for the cases where the value was not available. It should be appreciated that the effect of the coating's Poison ratio on the stress fields is generally insignificant in the range 0.20-0.30 as indicated in the studies by Djabella et. al. (1992). Table 3.1 shows the typical values of Young's modulus and Poisson's ratio used in the analysis. The coating thickness ratio is approximated on the basis of the applied load of 400 N, for a coated ball in contact with the steel lower ball where, 't' is the coating thickness and 'a' is the contact radius (200 μm at 400 N

contact load) for the uncoated case for comparison of values in nondimensional numbers.

Type of coating	Modulus ratio (E_1/E_2)	Poisson's ratio variations (ν_1/ν_2)	Coating thickness ratios (t/a)
C1	220/207	0.28/0.3	0.15, 0.3
C2	400/207	0.23/0.3	0.15, 0.3
C3	524/207	0.22/0.3	0.15, 0.3
C4	700/207	0.17/0.3	0.15, 0.3

* Subscripts 1 and 2 refer to the coating and the substrate respectively.
Table 3.1

3.3.1 Analysis of 60μm thick coatings

Figure 3.3 shows the contact stress results for the 60 μm (t/a=0.3) thick coatings in contact with the steel and ceramic lower balls. It can be seen from the figure that the stress values for the case of ceramic lower balls are slightly higher than the case of the steel lower balls. This is mainly due to the smaller contact area and higher value of Young's modulus for the ceramic lower balls. As the modulus ratio increases the magnitude of Von-Mises and maximum shear stress increases more sharply than the orthogonal shear stress and the peak compressive stress.

Figure 3.4 shows the maximum shear stress contours for the C2 type coating. The left hand side contours represent the stress distribution in the coated ball. The stress contours have a similar pattern for the two stresses and their maximum magnitude is situated at the coating substrate interface. The coating substrate interface shows sharp changes in the stress values which can be significant to coating delamination at the interface. Figure 3.5 shows the orthogonal shear stress contours for the C2 coating in contact with ceramic lower balls. It can be seen that the maximum value lies within the coating material and the stress contours do not indicate sharp changes in the stress values at the interface. This could imply that the coating delamination from within the coating microstructure can be a result of orthogonal shear stress reversal within the coating microstructure at a depth of approximately 40 μm.

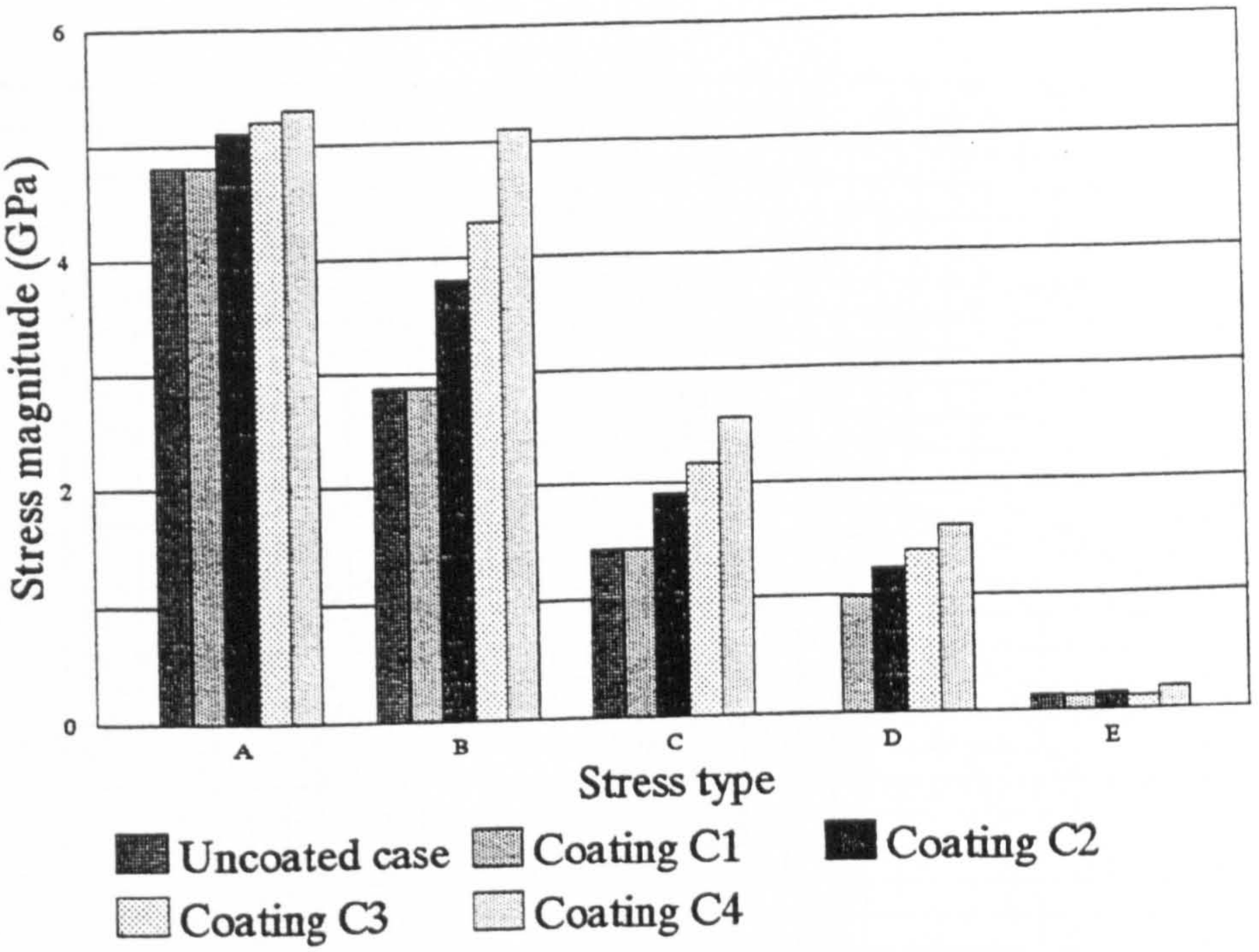

(a), steel lower balls

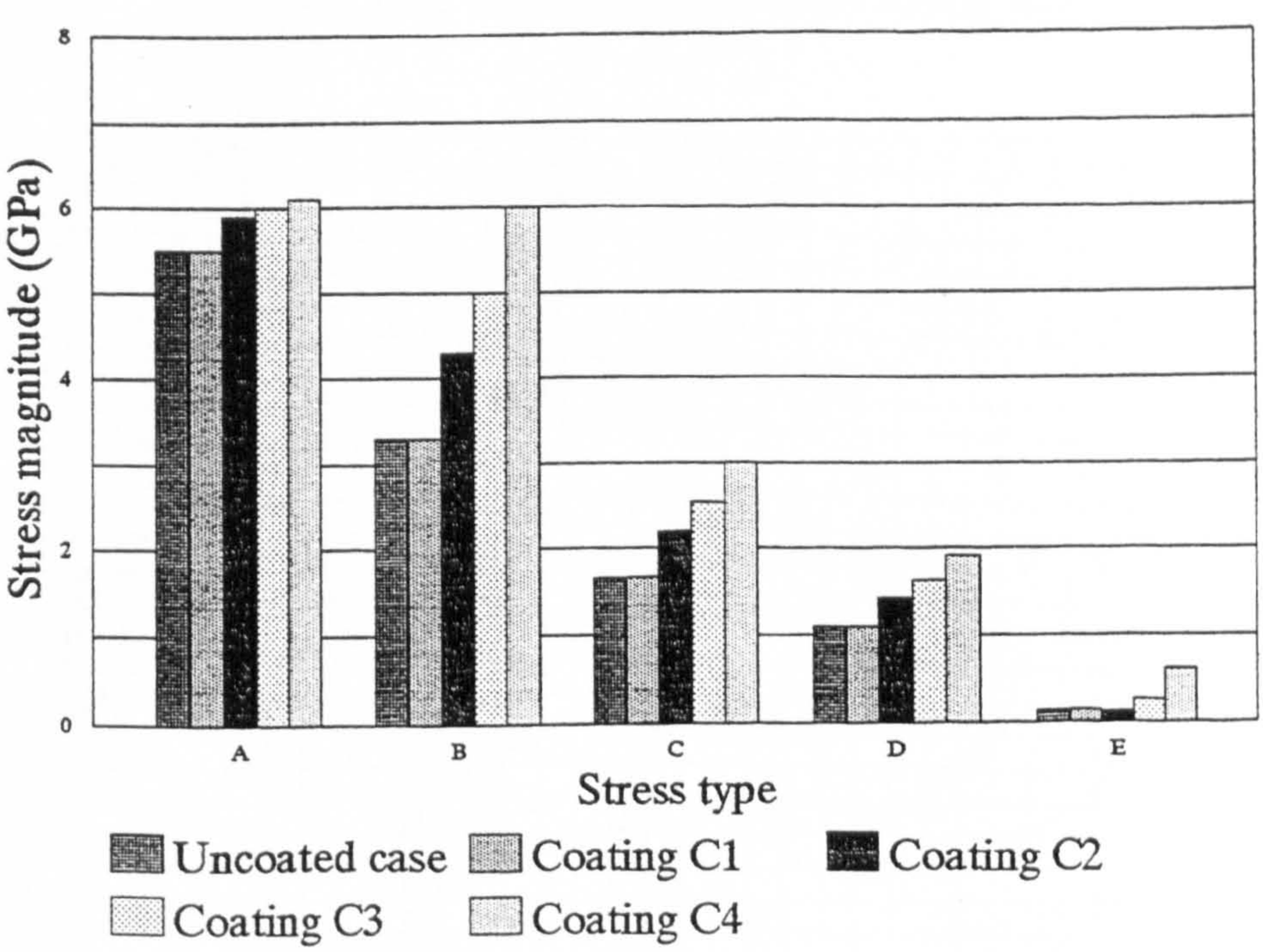

(b), ceramic lower balls

Figure 3.3, Contact stress results for 60 μm (t/a=0.3) thick coating.
(A:Maximum compressive stress, B:Von-Mises stress, C:Maximum shear stress, D:Orthogonal shear stress, E:Maximum tensile stress)

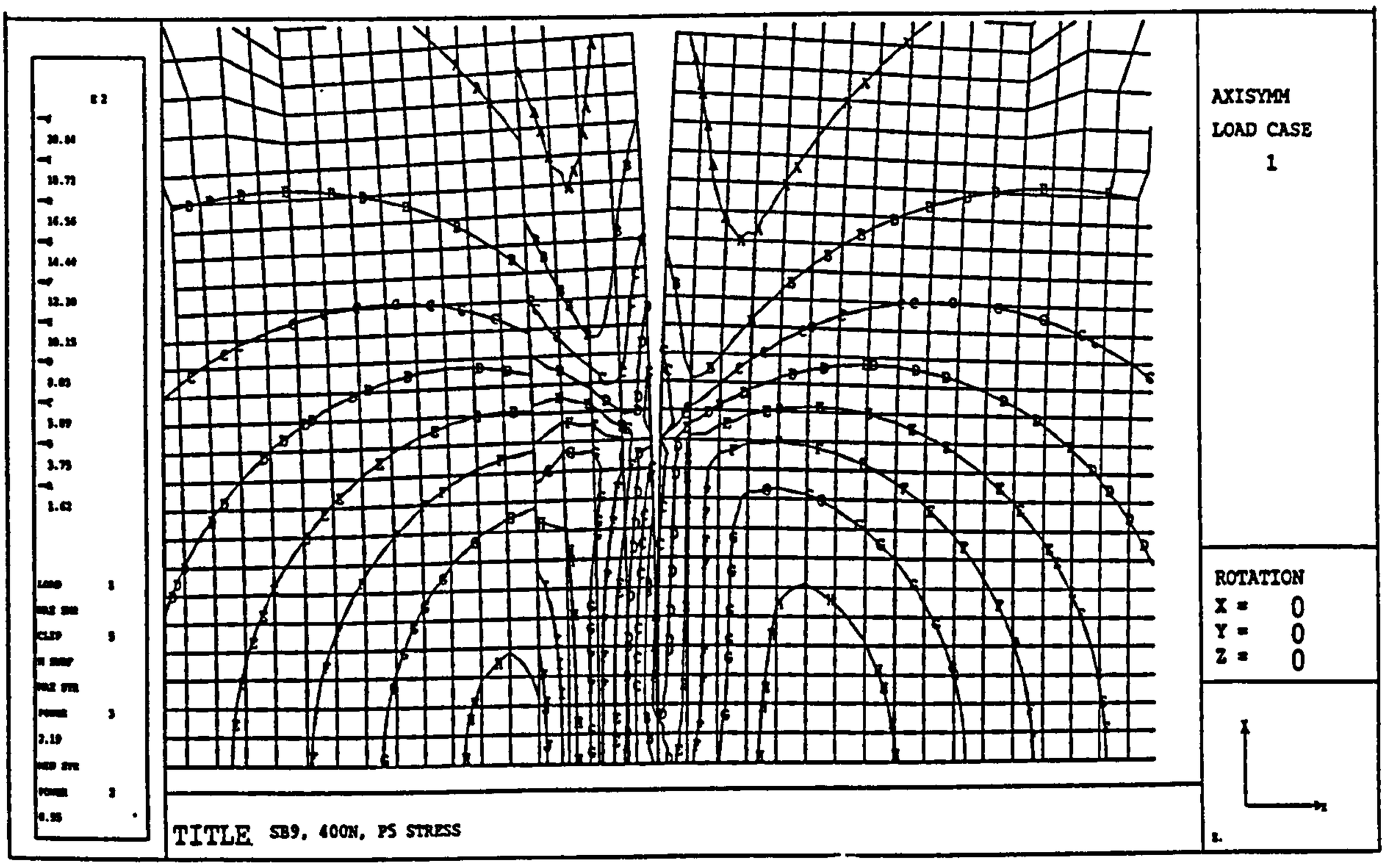

Figure 3.4, Maximum shear stress contours for C2 type (t/a=0.3) coating
(left hand sided represent coated rolling element)

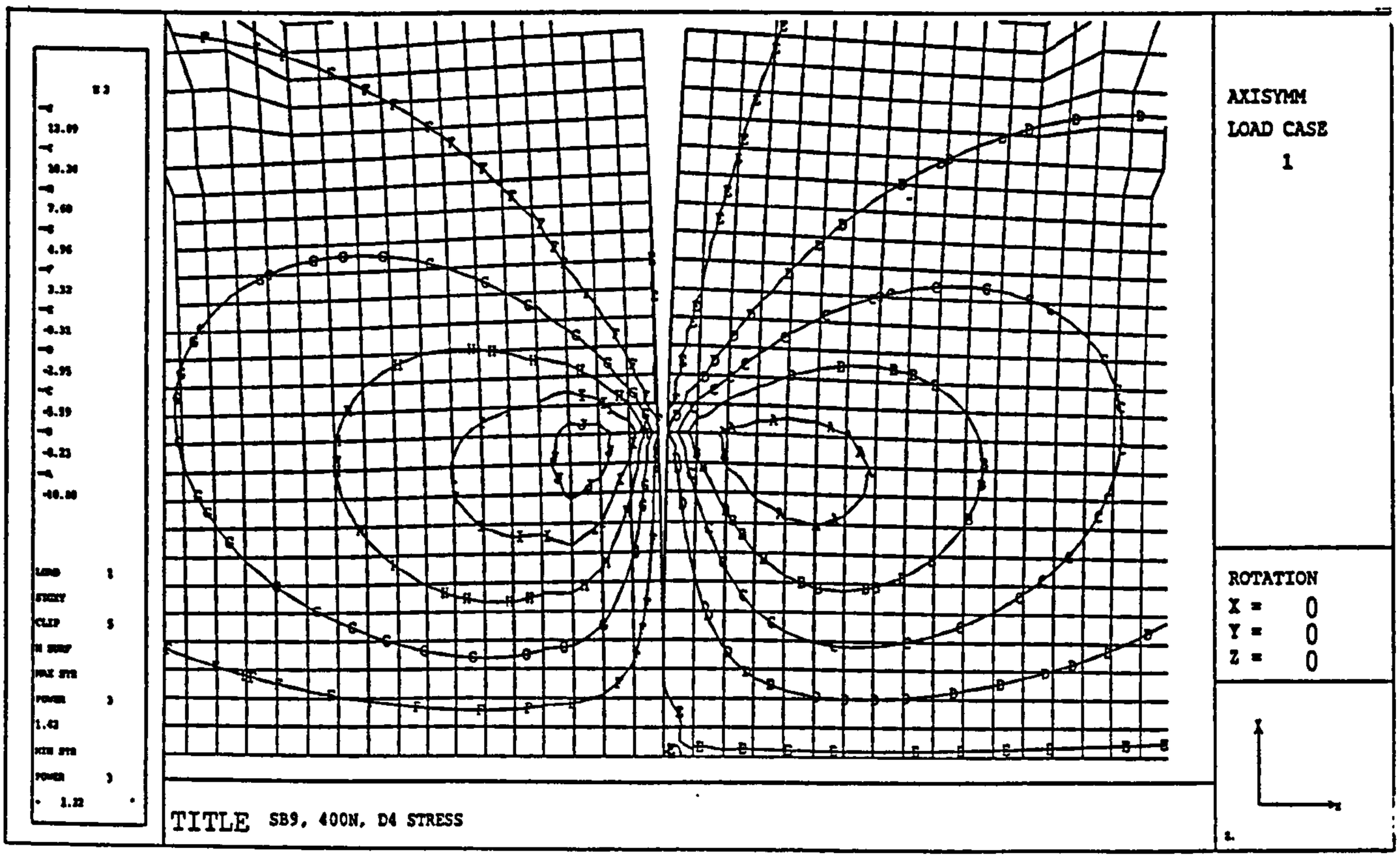

Figure 3.5, Orthogonal shear stress contours for C2 type (t/a=0.3) coating
(left hand sided represent coated rolling element)

3.3.2 Analysis of 30μm thick coating

Figure 3.6 shows the contact stress for the 30 μm (t/a=0.15) thick coatings in contact with the ceramic lower balls. It can be appreciated that the stress values are lower for the case of a 30 μm (t/a=0.15) thick coating in comparison to a 60 μm (t/a=0.3) thick coating. This indicates that the effect of coating Young's modulus is more prominent for thicker coatings. Moreover the Von-Mises and shear stress values do not increase sharply with the increase in modulus ratio which can be due to the location of these values in the substrate material for 30 μm (t/a=0.15) thick coatings.

Figures 3.7 shows the shear stress contours for a C2 type 30 μm coating in contact with ceramic lower balls. It can be appreciated that the maximum value of these stresses is situated in the substrate material. The coating substrate interface shows changes in the stress values but the stress values are not as sharp as were seen in the case of 60 μm thick coatings. Figure 3.8 shows the orthogonal shear stress contours for the C2 type coating in contact with ceramic lower balls. These contours indicate that the maximum value of orthogonal shear stress is concentrated in a region of coating and substrate material with sharp stress changes at the interface. This can affect the coating failure not only from within the coating microstructure but also at the interface. However, the magnitude of stress is lower for 30 μm thick coating.

In general it can be appreciated that as the coating thickness increases the magnitude of stress increases and the location of shear stress moves towards the interface. However, the changes in stress magnitude are not as rapid as the changes in the location of maximum stress values. For 30 μm thick coatings the orthogonal shear stress can be responsible for the interfacial delamination or the delamination from within the coating microstructure. However, for the 60 μm thick coating maximum shear stress occurs at the interface and the orthogonal shear stress can be responsible for the coating delamination from within the coating microstructure.

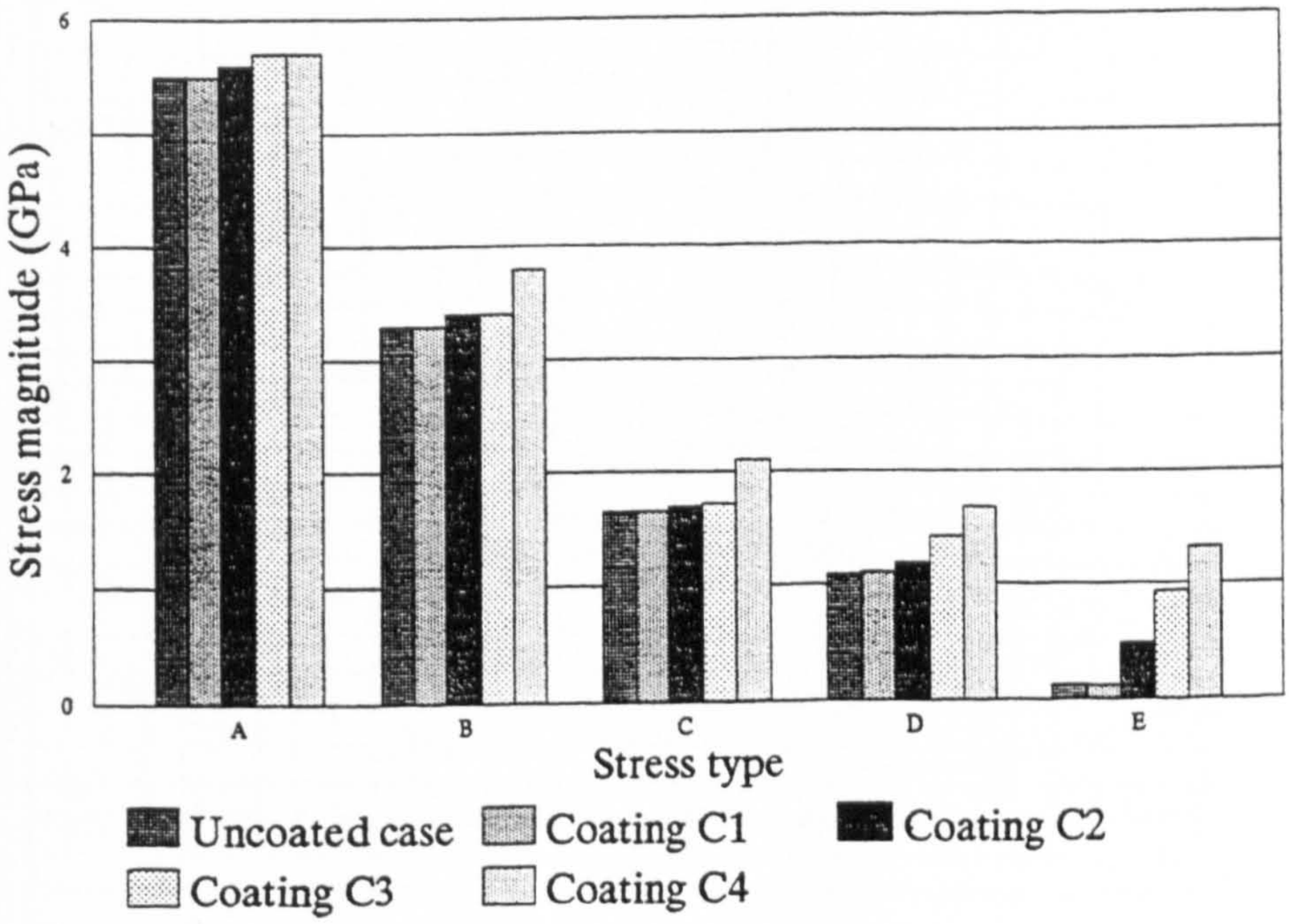

(b), ceramic lower balls

Figure 3.6, Contact stress results for 30 μm (t/a=0.15) thick coating.
(A:Maximum compressive stress, B:Von-Mises stress, C:Maximum shear stress,
D:Orthogonal shear stress, E:Maximum tensile stress)

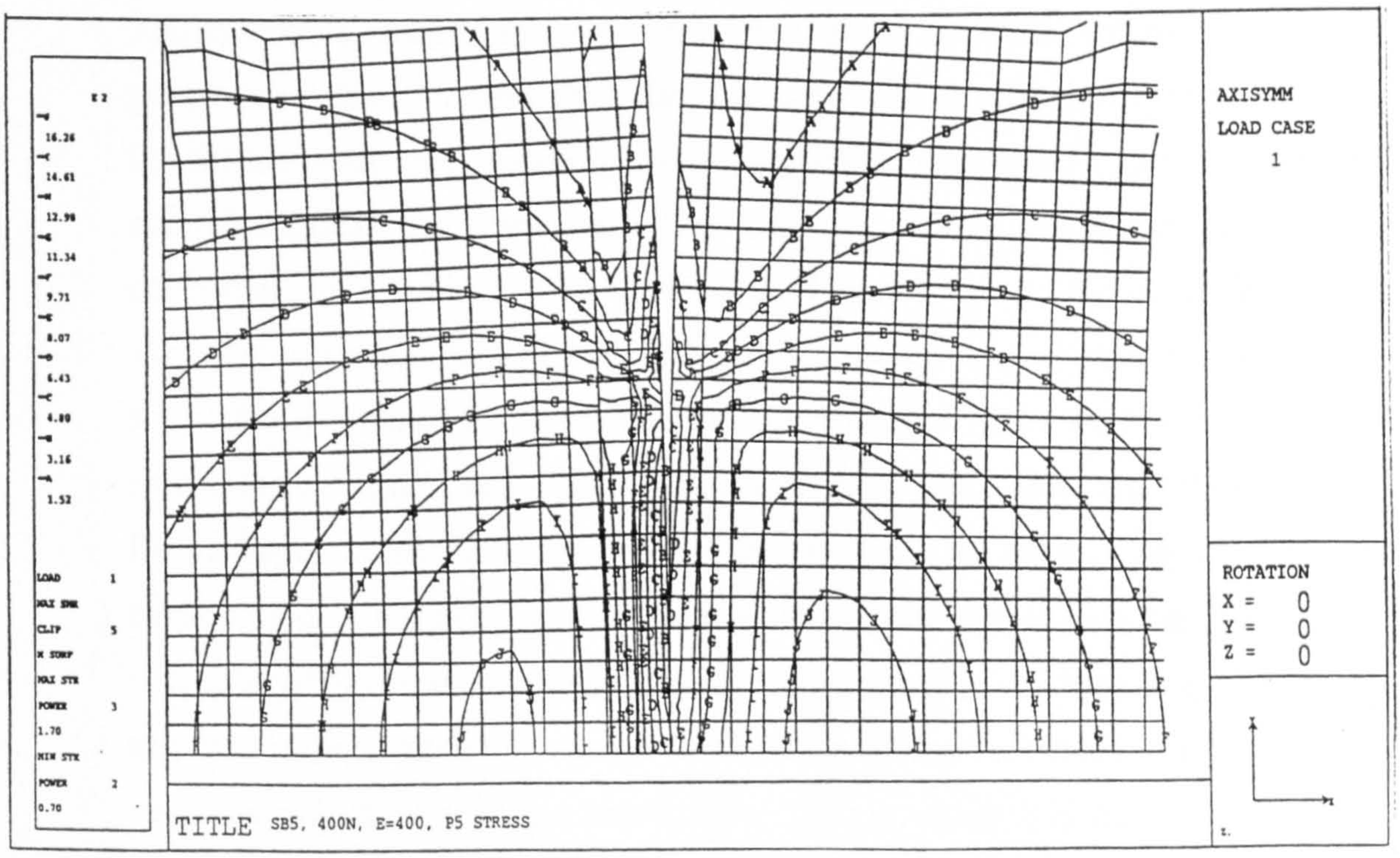

Figure 3.7, Maximum shear stress contours for C2 type (t/a=0.15) coating
(left hand sided represent coated rolling element)

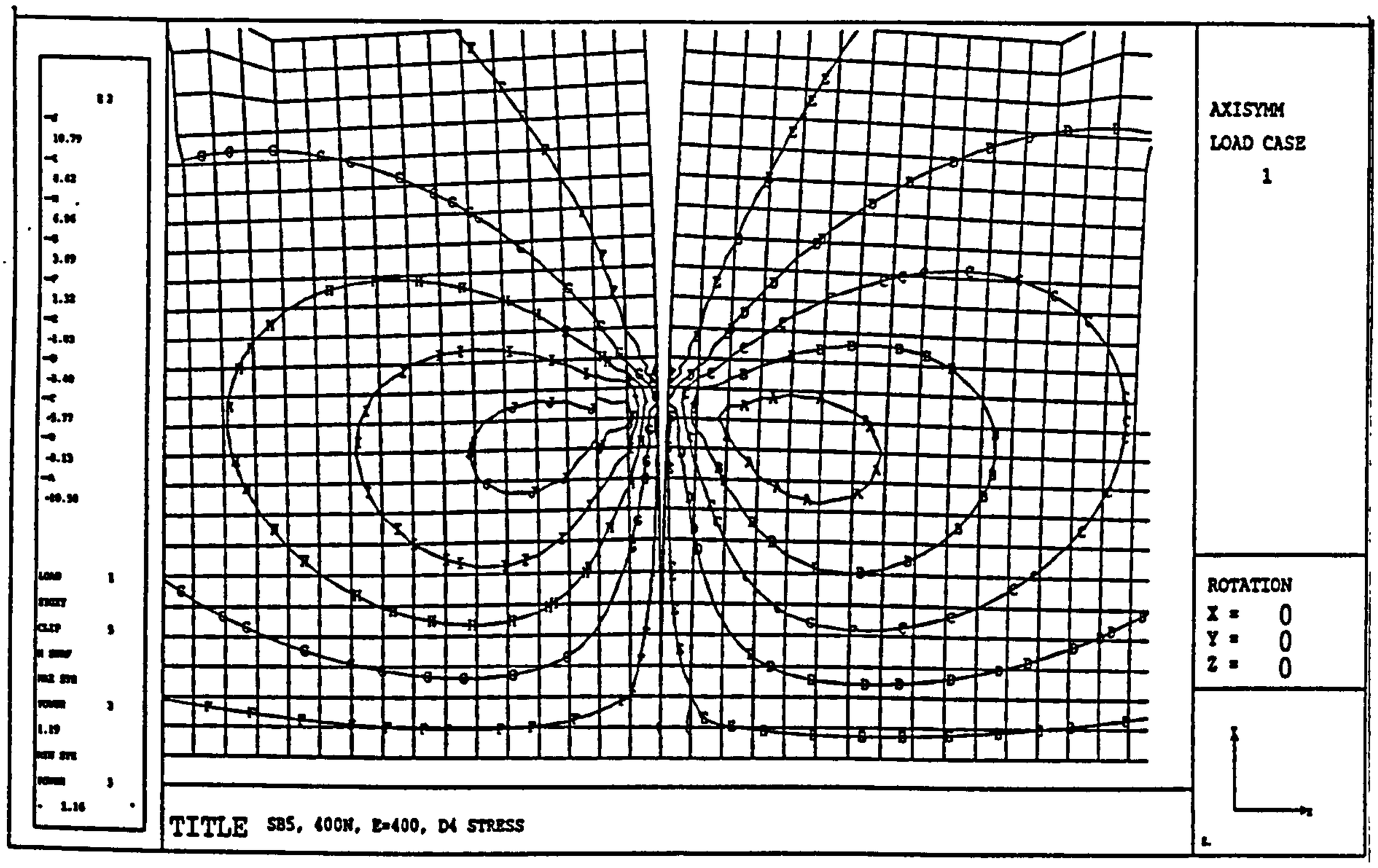

Figure 3.8, Orthogonal shear stress contours for C2 type (t/a=0.15) coating (left hand sided represent coated rolling element)

3.4 Ball Kinematics

The kinematic analysis in the cup assembly of the modified four ball machine can enable a better understanding of the fatigue mechanisms by providing an insight to the surface velocities, microslip and sliding within the contact region. In lubricated rolling contacts the phenomena like microslip within the contact area of the contacting bodies either due to material deformation or due to differences in Young's modulus, lubricant traction, sliding and heat generation etc. can be significantly affected by the kinematics. The objective of the work presented was to calculate the angular and linear velocities of the driver and driven rolling elements for the different contact geometries and then evaluate the microslip due to the elastic deformation of the material. This was performed by considering the instantaneous velocities of the driver and driven rolling elements of the modified four ball machine and then incorporating the material deformation effects calculated on the basis of the contact width of the Hertzian contact area. The equations were then used to evaluate the overall sliding in the four ball assembly by using the experimentally measured velocities using the technique described in chapter 2 of the thesis (section 2.5).

3.4.1 Ball velocity

The kinematics of the modified four ball machine shows an example in which the rolling motion is associated with the spin. The three planetary balls orbit about the axis of rotation of the shaft (or driving ball) and at the same time have a spin component of the velocity the angle of which is inclined to the shaft axis. Consider figure 3.9 in which the upper drive ball rotating at the shaft speed contacts the planetary ball at point 'a'. The lower planetary ball contacts the cup at point 'c', and the three wear radius are formed on the driver and driven balls as shown by the thick lines in figure 3.9.

Lets suppose that:

N = Speed of the drive shaft (rpm).

R1 = Radius of the upper drive ball (mm).

R2 = Radius of the lower planetary ball (mm).

R3 = Radius of the wear track on the upper drive ball (mm).

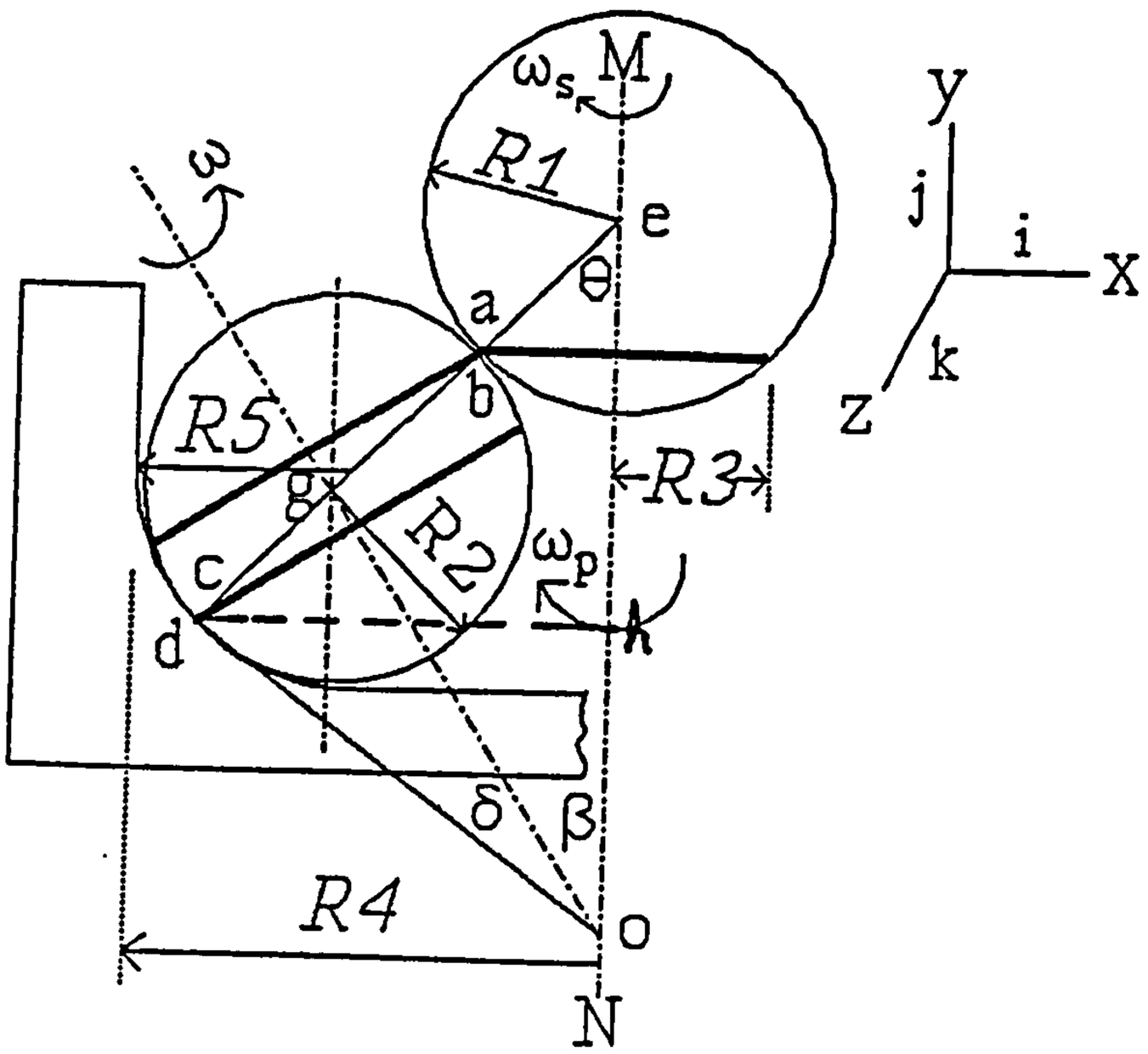

Figure 3.9, Geometry of type II configuration

R4 = External radius of the cup (mm).

R5 = Radius of the cup (mm).

ω_s = Angular velocity of the upper drive ball about the spindle axis MN (rad/sec).

ω_p = Angular velocity of the planetary ball about the axis MN (rad/sec).

ω = Spin angular velocity of the planetary ball about the axis inclined at an angle β to the spindle axis MN (rad/sec).

θ = Angle between the axis of the driving shaft and the connecting line of centres of the driver and the driven ball.

β = Angle between the axis of the driving shaft and the axis of spin of the planetary balls.

δ = Angle between the spin axis of rotation of the planetary ball and the connecting line of the conjunctions formed between the planetary balls and the cup.

Z = Number of planetary balls.

Consider the triangle oce, it can be seen that

$$\beta+\theta+\delta = 90^{o} \quad \ldots\ldots\ldots\ldots\ldots\ldots\ldots\ldots \quad (3.1)$$

where

θ = arcSin{(R4-R5)/(2R2+R1-R5)}

δ = arcTan{R2/(2R2+R1)Tanθ}

β = 90-($\theta+\delta$)

Also

$$\omega = (2\pi N)/60$$

The instantaneous velocity of the drive ball at point a (Va) can be given as:

$$Va = \omega_s \times \mathbf{R3} = -(\omega_s \times R1\ Sin\theta)k \quad \ldots\ldots\ldots\ldots\ldots\ldots\ldots\ldots(3.2)$$

Consider the instantaneous motion of the planetary ball at point b. This motion can be divided into two components i.e. about the vertical axis MN and about an axis inclined at an angle β to the vertical. The instantaneous velocity of the planetary ball at point b (Vb) can be given as:

$$Vb = \omega_p \times R3 + \omega \times r_{gb} \quad \text{..... (3.3)}$$

Also

$$\omega = \omega_x i + \omega_y j + \omega_z k$$

and

$$r_{gb} = R2\ Sin\theta\ i + R2\ Cos\theta\ j$$

$$\omega \times r_{gb} = \begin{bmatrix} i & j & k \\ \omega_x & \omega_y & \omega_z \\ -R_2Sin\theta & -R_2Cos\theta & 0 \end{bmatrix}$$

$$\omega \times r_{gb} = i(-\omega_z\ R2\ Cos\theta) + j(\omega_z\ R2\ Sin\theta) + k(\omega_x\ R2\ Cos\theta - \omega_y\ R2\ Sin\theta)$$

Putting this value in equation (3.3):

$$Vb = -(\omega_p \times R1\ Sin\theta)k + (\omega_x \times R2\ Cos\theta - \omega_y \times R2\ Sin\theta)k - (\omega_z \times R2\ Cos\theta)i + (\omega_z \times R2\ Sin\theta)j \quad \text{..... (3.4)}$$

Assuming no slip at the contact of the driver and driven ball

$$Va = Vb$$

Equating equations 3.2 & 3.4, we have:

$$-(\omega_s \times R1\ Sin\theta)k = -(\omega_p \times R1\ Sin\theta - \omega_x\ R2\ Cos\theta + \omega_y\ R2\ Sin\theta)k \quad \text{...(3.5)}$$

Also at point b

$\omega_x = -\omega\ Sin\beta$

$\omega_y = +\omega\ Cos\beta$

Putting the value of ω_x & ω_y in equation 3.5, and replacing the value of $\beta+\theta$ from

equation 3.1

$$\omega_s \times R1\ Sin\theta = \omega_p \times R1\ Sin\theta + \omega\ R2\ Cos\delta \quad \ldots\ldots\ldots\ldots\ldots\ldots\ (3.6)$$

Consider the motion of the planetary ball at point C. The instantaneous velocity at point C (Vc) is given as:

$$Vc = \omega_p \times r_{ch} + \omega \times r_{gc}$$

$$\omega_p \times r_{ch} = +\{\omega_p \times (R1+2R2)\ Sin\theta\}k$$

$$\omega \times r_{gc} = \begin{bmatrix} i & j & k \\ \omega_x & \omega_y & \omega_z \\ R_2Sin\theta & R_2Cos\theta & 0 \end{bmatrix}$$

$$\omega \times r_{gc} = (\omega_z \times R2\ Cos\theta)i - (\omega_z \times R2\ Sin\theta)j + (-\omega_x \times R2\ Cos\theta + \omega_y \times R2\ Sin\theta)k$$

Hence

$$Vc = (\omega_p \times (R1+2R2)\ Sin\theta - \omega_x \times R2\ Cos\theta + \omega_y \times R2\ Sin\theta)$$

Also at point c

$$\omega_x = \omega\ Sin\beta$$

$$\omega_y = -\omega\ Cos\beta$$

$$Vc = \omega_p\ (R1+2R2)\ Sin\theta - \omega\ R2\ Cos\delta$$

Assuming no slip between the planetary ball and the cup at point c,d

$$Vc = Vd$$

But $Vd = 0$

Hence

$$\omega_p\ (R1+2R2)\ Sin\theta - \omega\ R2\ Cos\delta = 0 \quad \ldots\ldots\ldots\ldots\ldots\ldots\ (3.7)$$

$$(\omega/\omega_p) = \{(R1+2R2)\ Sin\theta\ /\ R2\ Cos\delta\} \quad \ldots\ldots\ldots\ldots\ldots\ldots\ (3.8)$$

Adding equations 3.6 & 3.7

$$(\omega_s/\omega_p)= \{2(R1+R2) / R1\} \ldots\ldots\ldots\ldots\ldots\ldots\ldots \quad (3.9)$$

Dividing equation 3.9 by 3.8

$$(\omega/\omega_s) = [\{(R1/2R2) + 1\}\{(R1/(R1+R2)\}\{Sin\theta / Cos\delta\}] \ldots\ldots\ldots\ldots \quad (3.10)$$

The number of stress cycles per revolution of the shaft can be calculated as:

Number of stress cycles / revolution = $Z(\omega_s - \omega_p)/\omega_s$

Putting the values of ω_s & ω_p

$$\text{Stress cycle factor} = Z\{(R1+2R2)/2(R1+R2)\} \ldots\ldots\ldots(3.11)$$

3.4.2 Slip analysis due to contact conformity (Heathcote slip)

The applied load changes the initial point contact in to a well defined contact area which can be obtained from the Hertz contact analysis. Within this contact region some points may have different tangential velocities for the contacting elements. This results in sliding between the contacting bodies within the contact area and the effect will be maximum at the edges of the contact area. This was analyzed at the edges of the major axis of the contact area (a). The micro slip for any point within the contact area due to conformity can be calculated as:

$$\text{Microslip} = 1 - (Va/Vb) \ldots\ldots\ldots\ldots\ldots\ldots\ldots\ldots \quad (3.12)$$

Hence at the lower edge of the contact area the equation 3.12 can be written as:

Micro slip $= 1 - [(\omega_s \times R1\ Sin\theta - a\ Cos\theta)/\{\omega_p\ R1\ (Sin\theta - a\ Cos\theta) + \omega\ (R2\ Cos\delta + a\ Sin\theta)\}]$..... (3.13)

Inserting the values of variables for the test conditions the variations in microslip for various loads for different contact geometries and configurations can be summarised in figure 3.10.

It should be appreciated that the negative slip shown in figure 3.10 represents the case of a pure rolling motion between the driver and the driven balls. Similarly, the

contact area used for the slip analysis has been calculated for the uncoated case of rolling elements which can change for different coatings. Techniques like FEM can be used to evaluate these differences in the contact dimensions in the coated and uncoated case of contacting bodies. Some of these cases have been discussed in section 3.3 of the thesis. Also, there can be appreciable sliding between the driver and the driven balls under the given test conditions which can effect the friction, microslip and in general performance of the rolling elements by making the contact rolling/sliding. The magnitude and direction of this sliding will now be analyzed on the basis of experimental observations.

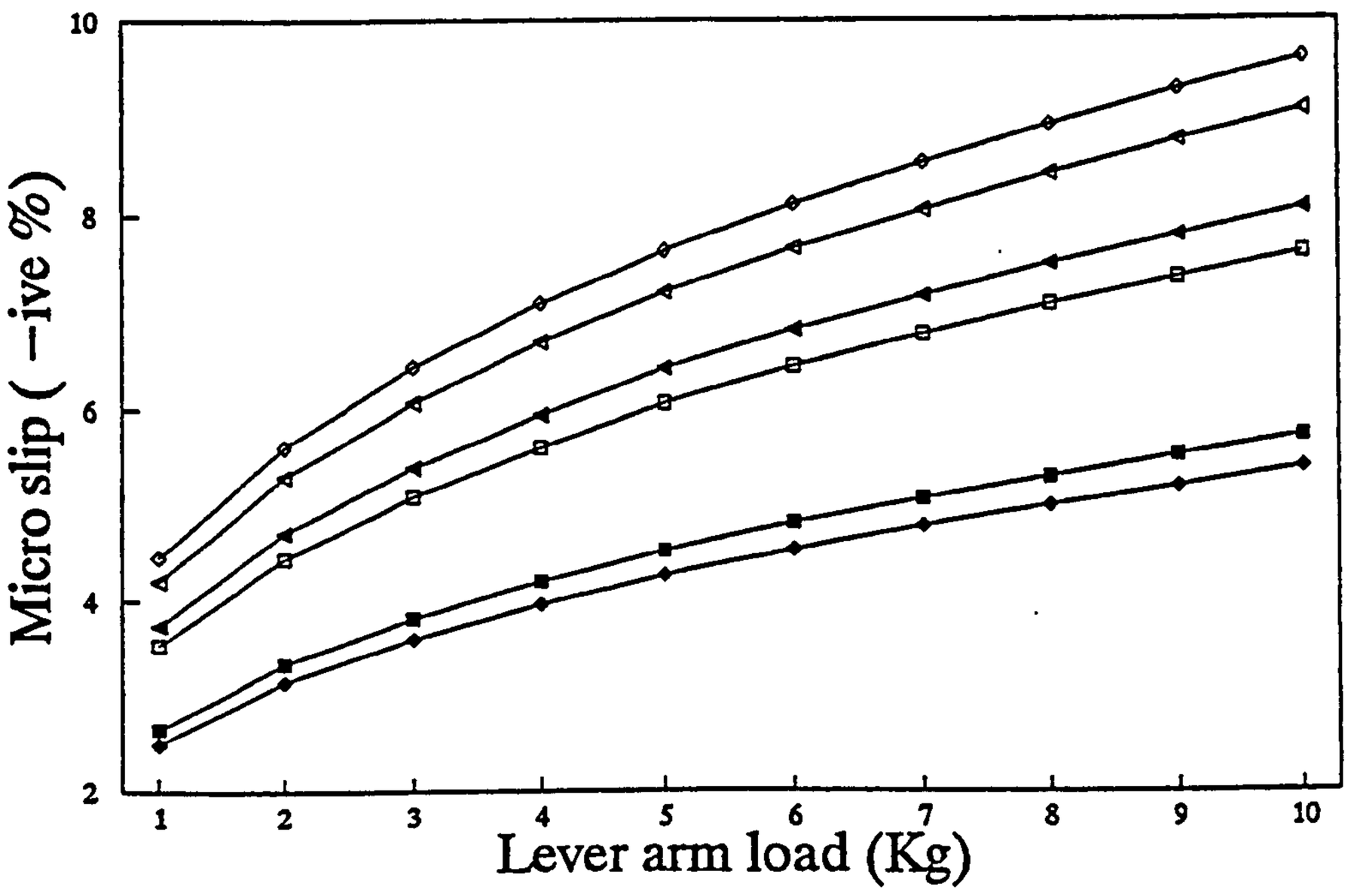

Figure 3.10, Negative slip due to contact conformity

The experimental investigation of sliding between the rolling elements in the four ball cup assembly requires a knowledge of ω & ω_p under the given ω_s. As indicated in chapter 2 (section 2.5), it was possible to measure ω_p under the given ω_s. If the value of ω was calculated from equation 3.8, it was possible to evaluate the experimental sliding using equation 3.12. Experiments investigations were then

made under the range of shaft speed, contact load and lubricant to evaluate the amount of sliding in the four ball system . Typical results for the case of uncoated steel balls are shown in figure 3.11. These results give an appreciation of the magnitude and direction of sliding in the four ball system under the given test conditions. The sign convention used to describe the direction of sliding in this thesis can be defined as " when the drive rolling element was on the faster side of the rolling sliding contact the +ive sign was used and vice versa". This was consistent with the analogy used by Soda et. al. (1981).

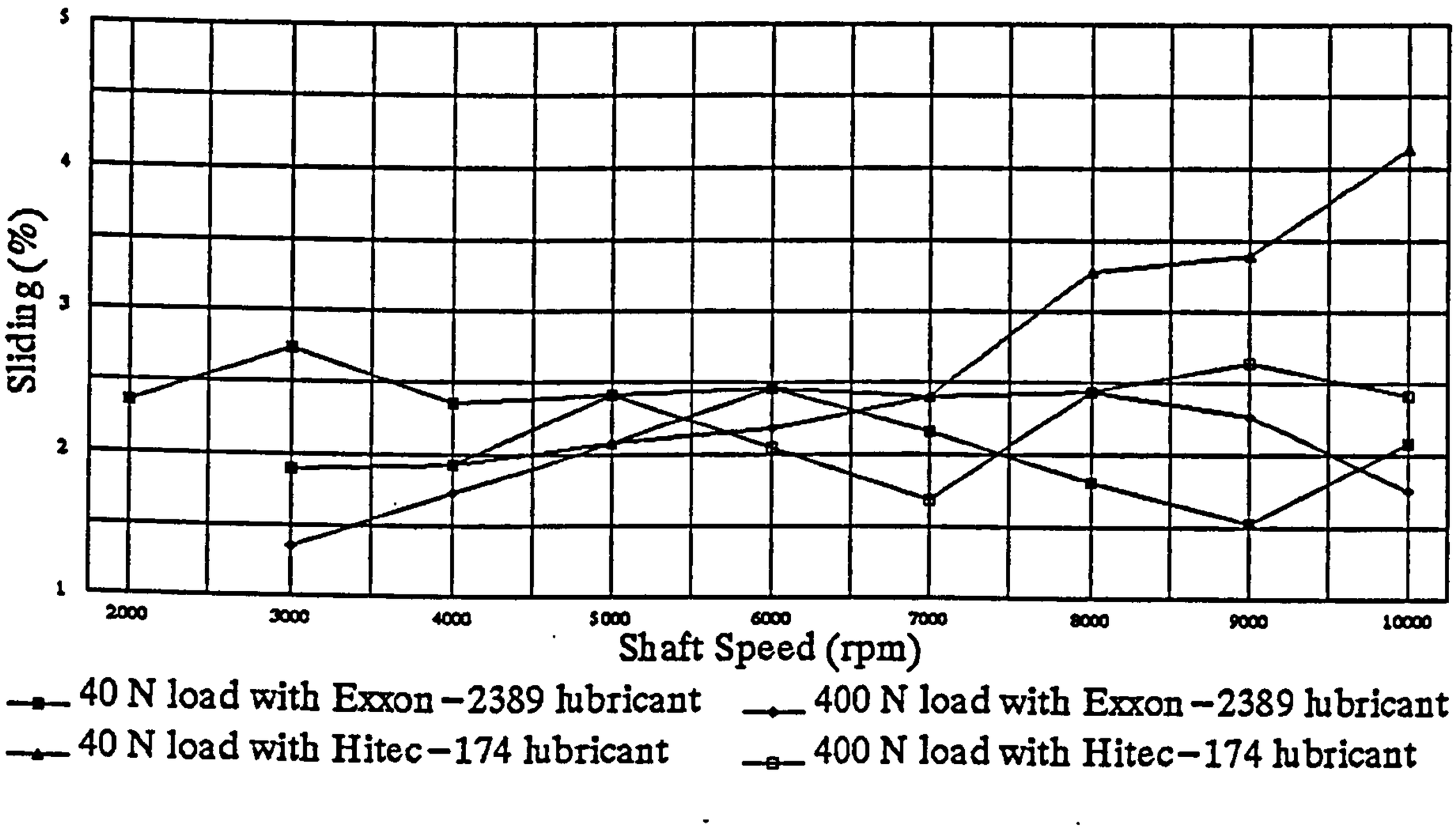

Figure 3.11, Effect of load, lubricant and speed on the sliding

3.5 Discussion

The FE results gave an appreciation of the effect of coating thickness and the coating Young's modulus on the stress distribution within the coated rolling element in contact with steel or ceramic lower ball for a pure rolling condition. It should be appreciated that these results should only be used as a precedent solution since the actual stress field will be different due to the coating anisotropy and the coating defects. The case of the 110 μm thick coating and functionally graded coatings will be discussed in later chapters of the thesis. The kinematic analysis represented the

surface and angular velocities in pure rolling conditions. These results were then compared with experimentally measured velocities to establish the amount of sliding in the four ball cup assembly. It can be seen that these values of overall sliding in the four ball system were within a narrow band for the shaft speed in the range of 3000~7000 rpm, for both the test lubricants at a variety of contact loads. Below this range of speed the vibration signal was too weak to establish any values of the velocities. Similarly, above this range of shaft speed the inertia and centrifugal effects resulted in the scatter of the results. These results were presented to give an appreciation of the overall sliding for the uncoated case of the rolling elements. The case of coated rolling elements in contact with steel and ceramic lower balls will be discussed in chapter 5 of this thesis.

Chapter 4
EXPERIMENTAL INVESTIGATIONS

4.1 Introduction

This chapter deals with a brief description of the experimental techniques used to investigate the behaviour of thermally sprayed coated rolling elements before or after the Rolling Contact Fatigue (RCF) tests. These techniques included residual stress studies, dye penetrant investigations, and surface roughness measurements.

4.2 Residual Stresses Studies

4.2.1 Background

The specific nature of the thermal spraying process results in the generation of residual stresses within the coating microstructure. The magnitude and direction of these stresses depends upon the coating process and the parameters controlled during the coating process. The magnitude of these residual stress values can range up to several hundreds of Megapascals (MPa). They can be critical to the performance of these coatings, where used for engineering applications involving mechanical or thermal loading. Coated rolling element bearings was no exception to this phenomenon. Previous studies on the surface and subsurface residual stress fields in conventional steel ball bearing have shown that compressive residual stresses can significantly improve the bearing life (Clark et. al. 1985). Moreover, the studies by Bush et. al. (1962), Zaretsky et. al. (1969), Pomeroy et. al. (1969), Muro et. al. (1973) and Chen et. al. (1988) indicate that the generation of residual stress in rolling contact can be critical to the RCF performance and the stress field depends upon the tribological conditions. These studies indicate that maximum compressive residual stress can occur at the location of the maximum orthogonal shear stress, maximum shear stress or on the surface. The residual stress investigations can thus provide an improved understanding of the rolling contact fatigue behaviour of thermal spray coatings. This experimental research addresses the nature and magnitude of surface residual stresses which were measured using the x-ray diffraction technique within tungsten carbide cobalt (WC-Co) coatings, which are developed not only during the coating process but also after these coatings have

been subjected to Rolling Contact Fatigue (RCF) tests.

4.2.2 Previous experimental studies

Previous studies related to the magnitude and orientation of residual stress induced in WC-Co coatings deposited by a variety of processes, ie. HVOF, Air Plasma Spraying (APS), Jet-Kote (JGun) and, Continuous Detonation Spraying (CDS) etc, reveal different results.

Provot et. al. (1993), in their experimental study of residual stress in WC-Co coatings on Ti6Al4V substrate deposited by APS and CDS processes, reported a gradient of the residual stress magnitude throughout the coating thickness. These measurements were achieved by using a step by step hole drilling technique. These stresses were of tensile nature with the values much higher for APS coatings in comparison to CDS coating method. A similar behaviour was observed by Grevinge et. al. (1994a), when they discovered that WC-Co coatings deposited by the HVOF process on Ti6Al4V substrate can induce residual stresses of tensile or compressive nature or a combination of both within the coating thickness.

Knight et al. (1993) in their study applied a different approach using an Almen test strip methodology for the measurement of the residual stress in WC-Co coatings deposited by JGun (JP5000). They reported significant changes in the stress values by varying the parameters controlled during the coating process. Morishita et. al. (1992), in their study of residual stress using the drilling technique, revealed that the stress induced by plasma spray WC-Co coatings on an aluminium substrate are of tensile nature whereas JGun coatings produce compressive stress in these coatings. Similarly, Brandt (1995) during his study of residual stress in WC-Co coatings on an aluminium substrate found that the magnitude of these stresses increases with an increase of the coating thickness.

In general it has been observed that the magnitude and orientation of these residual stresses depends not only upon the coating techniques and the parameters during the coating process, but also on the measurement method.

4.2.3 The generation of residual stresses in thermal spray coatings

The thermal spraying technique involves a process in which a stream of high speed particles, in a molten or semi-molten state, lands on an underlying lamella or substrate which is usually sand blasted. The nature of the coating process, thermal and mechanical properties of the substrate and the coating material, the preheat temperature of the substrate, and the particle speed are the major factors which affect the generation of the residual stress field (figure 4.1).

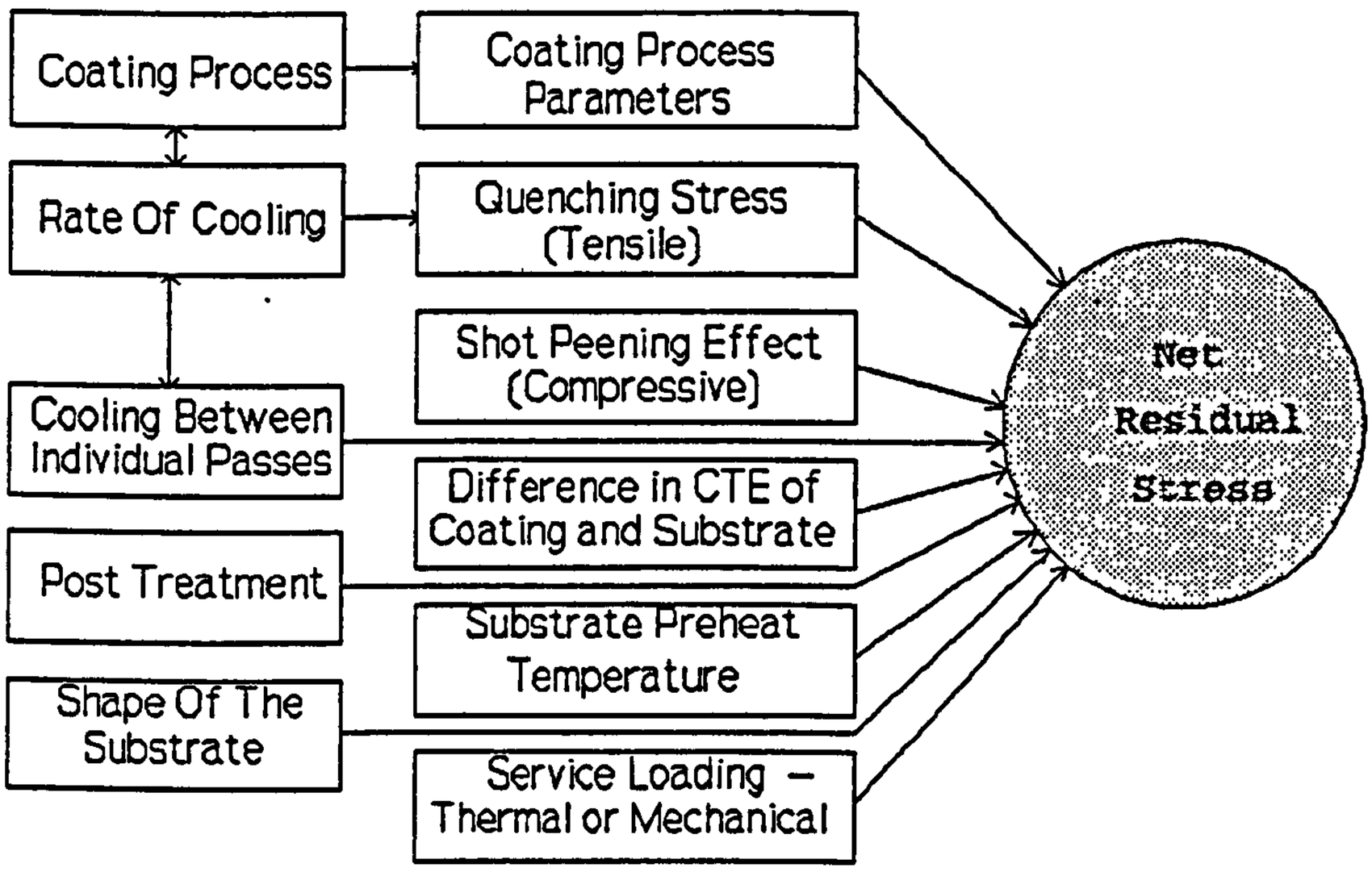

Figure 4.1, Generation of residual stress in thermal spray coatings

It has been established that during the thermal spraying process each molten-lamella lands on an already solidified lamella resulting in macro stresses of tensile nature commonly known as the quenching stress within the individual splats (Kuroda et. al. 1992). This is because of an inelastic behaviour of the deposited splat since its contraction is constrained by the underlying lamella . This also results in the generation of the micro stresses at the interface of the lamellae. Gill (1993) described a variety of phenomena which explain the relaxation of these stresses by interfacial sliding, micro-cracking, etc. With the advancements of high velocity processes, particle speeds up to 750 m/s are achieved which cause a shot-peening effect on the underlying lamella and, as a result, macro stresses of compressive

nature are generated in the coatings. The rate at which these coatings cool, especially between the individual passes of spraying can also affect the generation of these stresses. During the thermal spraying process the substrate temperature increases, whereas the temperature of the deposited lamellae decreases because of their heat conduction into the substrate, and heat convection and radiation into the immediate environment.

After the thermal spraying process an equilibrium is reached when the coating bulk temperature equals the substrate temperature. Then the substrate and coating cool until the bulk temperature reaches the atmospheric equilibrium temperature. During this cooling process, both the coating and the substrate contract at a rate which depends upon their individual coefficient of thermal expansion. This difference in the coefficient of thermal expansion creates residual stresses of compressive or tensile nature in the coating and the substrate. Post treatment of the coating eg. heat treatment, hot isostatic pressing or grinding will also affect the residual stress field.

The overall stress value within a coating can vary significantly throughout the coating thickness, depending upon the combination of significant local factors at particular locations. The behaviour is more complicated for substrate shapes of varying geometry, since the rate of heat transfer and the cooling intensity will vary. Moreover, the anisotropy of thermally sprayed coatings causes variations in the magnitude and orientation of these stresses, not only in the as-sprayed conditions but also during the service conditions involving mechanical or thermal loading. The case is worst for a cyclic loading process because individual passes of load can cause plastic deformation within the coating microstructure which result in the generation of residual stresses. The process of plastic deformation can continue until the shakedown limit is reached (Wong et. al. 1995) and (Kapoor et.al 1996).

4.2.4 Experimental techniques of residual stress measurement

There are many techniques available to measure the residual stresses in engineering materials some of which are destructive and some non-destructive. The anisotropy of thermally sprayed coatings (Nakahira et. al. 1992) makes it difficult to provide

a measurement of the stress distribution prevailing within the coating microstructure. X-ray diffraction is a non-destructive technique which can be employed to measure the residual stress field on the surface of the component. This method can enable the measurement of the generation of these stresses not only due to the thermal spraying process but also due to service loading. This technique can however suffer from low penetration depth for certain materials, and the technique of layer removal makes this method destructive. Bending tests have also been used for the measurement of residual stresses in thermal spray coatings, but this technique only gives an overall value of macro stresses in a coating substrate combination, and tells little about the distribution of stresses within the coating. Moreover, no information is provided about the micro stresses.

The deep hole drilling technique is useful in determining the stress distribution in a coating but the process is destructive and assumes that the coating is homogenous. This technique requires a knowledge of the values of physical properties like the Poisson's ratio and modulus of elasticity. Unfortunately, the values of modulus of elasticity and Poisson's ratio vary significantly for different coating processes and there is poor agreement between the values obtained from different measuring techniques (Kawase et. al. 1990). Techniques like the Almen strip method (Knight et al. 1993) need to be fully developed before any meaningful results can be obtained. Computer models using numerical techniques can be helpful, but need to consider a variety of factors some of which are shown in figure 4.1. This makes the problem complex and expensive to solve.

4.2.5 X-ray diffraction technique of residual stress measurement

The X-ray diffraction technique has the capacity to accurately measure the magnitude and orientation of both macro and micro residual stresses by non-destructive analysis. These features can enable the investigation of the generation of residual stress due to the coating process and the RCF tests. The work presented in this thesis is, however, limited to macrostresses. This technique measures a change of a diffraction peak caused by the change in lattice spacing. A knowledge of the elasticity modulus (E) and Poisson's ratio (ν) can enable the measurement of

residual stress. The $\sin^2\psi$ technique of X-ray diffraction was used for residual stress measurements. Residual strain was calculated using Bragg's equation:

$$n\lambda = 2d \sin\theta \quad \ldots\ldots\ldots\ldots\ldots\ldots (4.1)$$

$$\epsilon = \frac{\Delta d}{d} = \cot\theta_d \, \Delta\theta \quad \ldots\ldots\ldots\ldots\ldots\ldots (4.2)$$

where n is the positive integral number indicating the order of diffraction, λ is the X-ray wave length, d is the inter-planar spacing in the crystal, θ is the diffraction angle, ϵ is the magnitude of strain and, θ_d is the diffraction angle in a stress free condition. The stress(σ) on the surface is then calculated from the following expression:

$$\sigma = \frac{E}{1+\nu} \frac{\partial(\epsilon)}{\partial(\sin^2\psi)} = -\frac{E \cot\theta_d}{2(1+\nu)} \frac{\partial(\theta)}{\partial(\sin^2\psi)} \quad \ldots\ldots (4.3)$$

where ψ is the angle between the sample normal and diffraction-plane normal. The above equation may be expressed as a product of constant 'K' and gradient 'M' using the equation:

$$\sigma = KM \quad \ldots\ldots\ldots\ldots\ldots\ldots (4.4)$$

where $K = -\frac{E \cot\theta_d}{2(1+\nu)}$ ..... (4.5)

and $M = \frac{\partial(\theta)}{\partial(\sin^2\psi)}$ ..... (4.6)

In equation (4.4) above, K is an elastic constant for the X-ray stress measurement and M is the gradient of the data regression line representing the stress results for various ψ angles, typically from 0^0 to 40^0. A more detailed description of residual stress measurement by X-ray diffraction can be found in Farrahi et. al. (1991). The value of K in the above equation was measured using conventional insitu four point bending test equipment subjected to a known stress within the elastic range. The details of the method have been described by Cullity (1978) and the measured value was -466 MPa/deg.

The penetration depth of X-rays for residual stress measurements varies for different sources of X-rays and the properties of material to be analyzed. Hadfield et. al. (1993) in their study of residual stresses described the penetration depths for different sources of X-rays. Most of the coatings suffer from the drawback of low penetration depths and hence require layer removal techniques like electrolytic polishing for the measurements at a greater depth, making the technique destructive and time consuming. This is specifically true of WC-Co coatings; moreover, electrolytic polishing of hard coatings like WC-Co is difficult.

4.2.6 Method of residual stress measurements

Residual stress measurements using a X-rays diffraction, $\sin^2\psi$ technique, were performed on Rigaku RINT 2000 equipment. Figure 4.2 is a schematic representation of the configuration used for the measurements. This equipment had a special residual stress attachment with a maximum capacity of 18 kw at 300 mA current and 60 kv voltage. The residual stress measurements, during this study, were performed at 40 kv (voltage) and 200 mA (current). The X-rays diffraction results of residual stress in coatings were sensitive to the selection of the diffraction peak, elastic modulus, shape of the sample, time of measurement, surface roughness, and the orientation of the sample. The initial selection of the potential diffraction peaks for the residual stress measurements was made on the basis of the results of the X-rays diffraction pattern of the coating microstructure, using a wide angle goniometer. The diffraction results revealed the potential peaks for the residual stress measurements. Experimental analysis of the residual stress on the selected peaks led to the selection of the optimum peak, i.e. the peak which gives the most accurate statistical results at the maximum possible 2θ angle. These tests revealed that a 2θ angle of 125^0 for a Cr-kα X-rays source gives maximum statistical confidence in the results. The selection of modulus of elasticity and Poisson's ratio values was made on the basis of previously obtained results using X-rays diffraction technique for an in-situ four point bending test using the same equipment.

As the samples to be measured have the geometrical shapes of a ball and cone, the

measurement areas were kept very small to minimize the effect of the curvature of the samples. This was done using small size collimators, ie. 0.3 mm and 0.5 mm diameter. This requires a longer time for stress measurement. The results for other collimator sizes did not produce statistically confident results. A position Sensitive Proportional Counter (PSPC) of 24^0 and step angle of 0.05^0 was used for the experimental analysis.

The orientation of the sample was found to have an influence on the stress results. For this purpose, an optical microscope was used to position the sample for each measurement. Considering the shape of the specimen and the anisotropy of the thermally sprayed coatings, residual stress measurements were made in three different directions. This enabled the investigation of the effect of measurement direction on the residual stress results. The residual stress measurements were made at 0^0 (Fa), 45^0 (Fb) and, 90^0 (Fc) to the direction of rolling. An attempt was also made to measure the through thickness residual stress field of the coating cross section but the diffraction profile was not significant enough to provide a statistical confidence in the residual stress results.

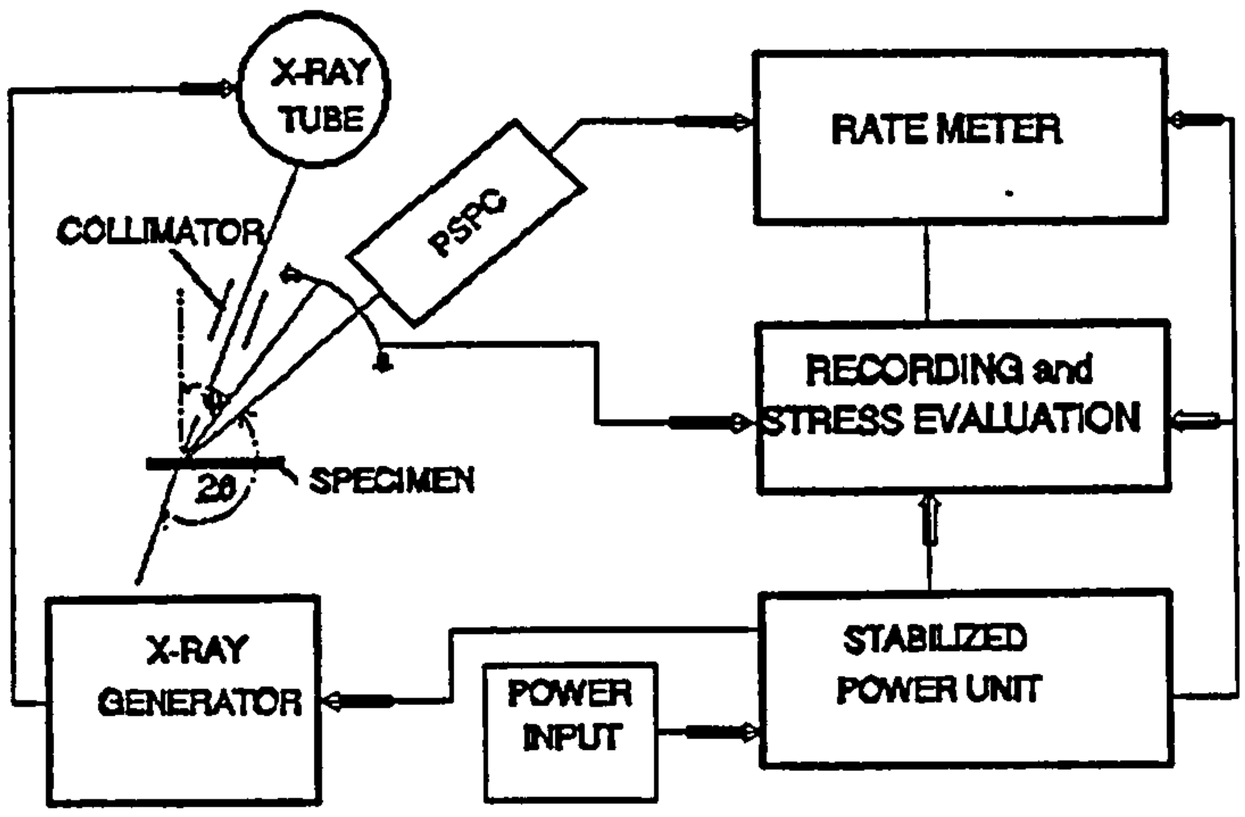

Figure 4.2, Schematic of the X-rays measurement

As the residual stress measurements were sensitive to the orientation of the

specimen, a special technique was developed to rotate the samples at the prescribed angle to change the orientation of the sample, while keeping the measurement point. For this purpose an arrangement shown in figure 4.3 was used. In this arrangement the sample had two axial motions, ie. along the x-axis and y-axis, coupled with a rotational motion about the z-axis. The distance of the sample from the collimator was kept constant by flushing the sample in a jig which was clamped at the centre of rotating mechanism. The first measurement was performed at 0^0 rotation, then the sample was rotated at 45^0 using the rotation about z-axis, while the measurement point was constantly kept at a reference point using optical microscope and x-y axis motion of the sample for adjustments. The vernier divisions along the x and y axis gave an accurate measurement of 30 μm, while the degrees scale was marked at 0.1 degree for accurate rotation.

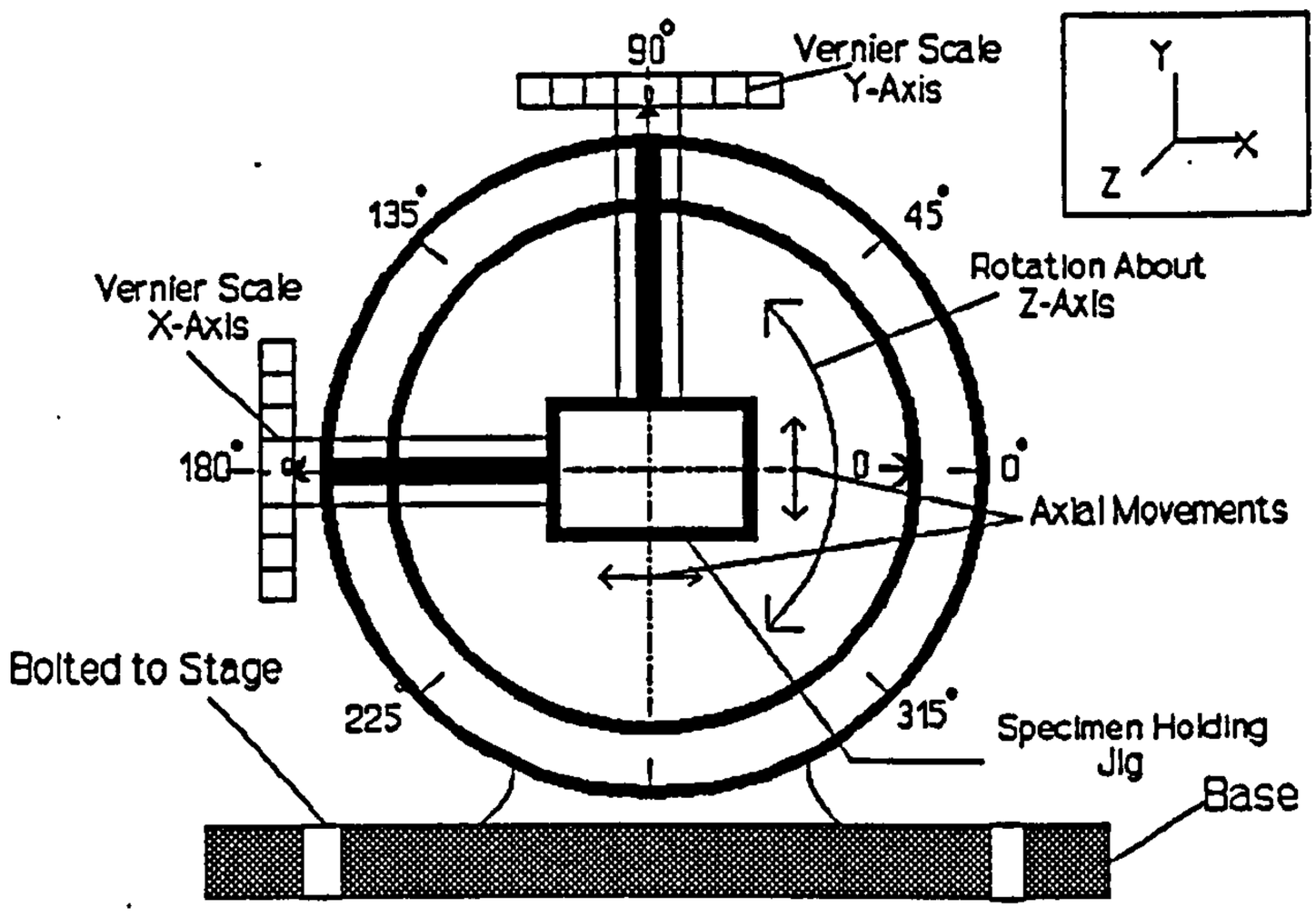

Figure 4.3, Schematic of the sample rotation mechanism

4.3 Dye Penetrant Investigations

In the present study, subsurface cracks were investigated by sectioning (grinding) of the rolling element along the axis of the rolling element cone after the RCF tests. The brittle and lamellar microstructure of thermal spray coatings made it difficult to section the rolling elements without generating cracks during the sectioning process, either within the coating microstructure or at the coating substrate interface using conventional sectioning techniques with a diamond saw. To minimize the

generation of cracks during the preparation process the sectioning was not carried out using a diamond saw but the rolling elements were ground at the location of the wear track using silicon carbide paper along the axis of the cone. This was a slower but gentler process than the conventional diamond saw sectioning process and therefore the coating was less prone to cracking during the grinding process. This technique also had the advantage of removing very thin layers of material which would have been extremely difficult with the diamond saw technique. However, even with this gentle process there was no guarantee that the grinding of the rolling element cones would not alter the subsurface cracks. To overcome this problem and to confirm that the subsurface cracks were generated during the rolling contact and not due to the grinding of the rolling elements the rolling elements were examined for subsurface cracks using the dye penetrant technique. The dye penetrant technique relies on the penetration of the fluorescent dye in the subsurface cracks which are open to the surface. The fluorescent dye has a pigment which glows under ultraviolet light and thus the subsurface cracks can be investigated after the sectioning of the specimen.

The actual method of surface and subsurface crack investigation using the dye penetrant technique varies for different materials and a careful selection of parameters was required before any results can be achieved. Among these parameters the time for which the sample is immersed in the dye and the time for which the sample is immersed in the remover were very critical. The remover serves the purpose of removing the excessive dye before examining in the microscope. The cleaning procedures and a careful handling of the sample during preparation are also critical and results are critical to the skill of the researcher. Hadfield et. al, (1993) used a similar technique to reveal the subsurface cracks in ceramic rolling element balls and has shown that if the technique is carefully used it can reveal significant results. This technique is also commonly used to reveal cracks in welds of pressure vessels in a slightly different way. A general method used during the subsurface investigations of the coated rolling elements have been described below.

After surface observations, the coated rolling elements were thoroughly cleaned in acetone in an ultrasonic bath for five minutes and dried with fan heater. These rolling elements were then ultrasonically cleaned in petroleum spirit for five minutes and dried with the fan heater. This was done to ensure that any residues of the test lubricant were removed from the sample. The coated rolling element was then immersed in the fluorescent dye for a certain number of hours ranging from one hour to 24 hours to allow sufficient time for the fluorescent dye to penetrate in the cracks. The coated rolling element was then immersed in a remover for a time ranging from few seconds to few minutes. Again this time was critical to ensure that only the excess dye was removed and the remover should not penetrate deep into the cracks. The coated rolling elements were then rushed to be cleaned in distilled water to clean the remover as it was water based. The test samples were then dried with the fan heater and cold mounted using the Buehler Ultramount Kit. Other resins and epoxies were also tried but the Ultramount was found to give better results. After the mould was cured, grinding was carried out along the axis of the cone to reveal the subsurface cracks under the ultraviolet light. The microscope was also modified to provide a facility of mixing the ultraviolet light with white light for improved results.

4.4 Surface Roughness Measurements

The surface roughness measurements during this study were performed on a Rank Taylor Hobson talysurf (stylus profilometer) machine with a stepper motor. Unlike the techniques like Atomic Force Microscopy (AFM) this technique relies on the physical contact of a stylus with the surface. In this technique the stylus was dragged smoothly over the surface under examination. As the stylus travels it rises and falls to give vertical displacements in accordance with the profile of the intact surface. These displacements are then converted in to an electrical signal which is then amplified to give the surface profile. Although there are a number of surface roughness parameters available to define the profile of the surface the results in this thesis are limited to R_q, which is defined as the (root mean square) RMS parameter corresponding to R_a, where R_a is defined as the arithematic mean of the absolute departures of the roughness profile from the mean line. The machine was used in

its standard configuration with the option of incorporating different roughness filters, cut-off lengths and form options to the raw data obtained from the measurement of coated rolling elements. Surface roughness measurements were made after cleaning the sample in acetone in the directions across the wear track. The machine was calibrated before the measurements in accordance with the machine manual.

4.5 Discussion

The equipment used for the residual stress measurement studies had the advantage of high power for reduced measurement times and good diffraction peaks. However, the technique had low penetration depth and studies were limited to near surface analysis. New approaches are therefore required to measure these stresses to a much deeper layers to provide a detailed analysis of the stress distribution within the coating. These approaches can include neutron diffraction and ultrasonic methods.

The technique of subsurface investigations of the cracks using the dye penetrant was improved and optimized for the specific case of coated rolling elements after repeated tedious trials. The method was specific to the coating material and may need optimization for other materials. The exact times of immersion and the brand of chemicals used have not been included in the above description due to confidentiality reasons. However, it is emphasized that whatever may be the nature of chemicals or the amount of time of immersion the operator skills had to be developed before any results can be obtained. However, this technique was limited to surface breaking cracks and methods like acoustic imaging can be used for non-surface breaking cracks.

The surface roughness measurement results were sensitive to the cut-off length and type of roughness filter used. In this thesis the surface roughness measurement conditions were kept consistent for a cut-off length of 0.8 mm and using a Gaussian filter with a minimum number of cut-offs as six for comparative studies. It is however emphasized that three dimensional roughness parameters need to be designed for an improved representation of the surface roughness.

Chapter 5

EXPERIMENTAL TEST RESULTS AND ANALYSIS

5.1 Introduction

This chapter deals with the Rolling Contact Fatigue (RCF) test results of the coated rolling elements. The surface and subsurface observations of the coated rolling elements before and after the RCF tests using Scanning Electron Microscope (SEM), talysurf analysis, microhardness measurements, dye penetrant investigations and residual stress analysis are described. Each coating case has been dealt in the individual section of this chapter.

5.2 Detonation Gun Coated Balls on Bearing Steel Substrate

5.2.1 Introduction

Metal carbide coatings represent a family of coatings which are used to improve the wear resistance of components. Among this family, D-Gun sprayed tungsten carbide coatings are known to possess extremely high resistance against sliding wear, hammer wear, abrasion and fretting (Vuoristo et. al. 1993). This study represents the RCF performance of thermally sprayed Tungsten carbide (WC-15%Co) coatings produced by the Detonation Gun (D-Gun) process, on the surface of the bearing steel rolling element balls.

5.2.2 Coated ball rolling elements

A super D-Gun (SDG-2040) was used to spray the tungsten carbide cobalt (WC-15%Co) coatings on the surface of 12.7 mm diameter bearing steel (440-C) balls. Only half of the ball was required to be coated for the RCF tests. The material composition of the coating can be summarised as Co-15%, C-03% and WC-82% (manufacturer's data). The substrate material was sand blasted prior to coating process so as to assist a strong bonding by mechanical interlock between the coating and the substrate and preheated to a temperature of approximately 150°C. The as-sprayed coating thickness of the rolling element balls was approximately 100 μm. The rolling element were then ground and polished using the technique described in chapter 2 of the thesis (article 2.2.3) to attain an average coating thickness of

60±10 μm. The surface roughness (R_q) of the rolling elements in the as-sprayed, ground and polished conditions was 5.5±0.5 μm, 2.0±0.5 and, 0.08±0.02 respectively. The surface roughness values were measured in the direction perpendicular to the direction of rolling at a cut-off length of 0.8 mm using a Gaussian roughness filter.

5.2.3 Test conditions and experimental test results

The test lubricant used in this study was B.P. Hitec-174. Exxon-2389 was also used but not in all the test configurations. RCF tests were conducted at spindle speed of 4000±5 rpm at a load of 160 N, 400 N, and 570 N load applied to the cup assembly. RCF tests were conducted under immersed lubrication conditions at an ambient temperature of approximately 24°C in conventional steel ball bearing (steel lower balls) and hybrid ceramic bearing configurations (ceramic lower balls). Experimental test procedures described in chapter 2 (article 2.3) were followed. The ratio (λ) of the minimum film thickness to the average surface roughness under the given test conditions was approximated as $\lambda>3$ and $\lambda<2$ for the Hitec-174 and Exxon-2389 test lubricants, the details of which can be seen from appendix E. Table 5.1 gives an appreciation of the RCF performance of the coated rolling elements under the given tribological conditions. The RCF test results are represented in terms of the contact configuration, lubricant and the time to failure. The details of the magnitude and location of these stresses can be seen from appendix D.

The RCF test results given in table 5.1, indicate that the coated rolling element balls did not perform well during the RCF tests. Similarly, the tests with ceramic planetary balls had significantly reduced fatigue life than the tests with steel planetary balls.

5.2.4 Surface observations

Figure 5.2.1 shows Scanning Electron Microscope (SEM) observations of failed tungsten carbide coated balls against ceramic balls (test DG3). Figure 5.2.1(a) shows the failed area for the 400 N test.

Test No:	Contact Load (N)	Average coating thickness (μm)	Lower balls	Contact stress* (GPa)	Contact width (mm) (a)	Depth of max: shear (μm) (0.5a)	Maximum shear stress (GPa)	Lubricant	Final Lubricant Temperature (°C)	No: of stress cycles (10^6)	Time to Failure (minutes)
DG1	160	60	ceramic	3.8	0.14	70	1.35	Hitec-174	32	0.783	87
DG2	160	60	steel	3.4	0.15	75	1.20	Hitec-174	36	2.961	329
DG3	400	60	ceramic	5.2	0.19	95	1.83	Hitec-174	25	0.099	11
DG4	400	60	steel	4.6	0.20	101	1.63	Hitec-174	39	0.720	80
DG5	560	60	ceramic	5.8	0.21	107	2.05	Hitec-174	23	0.004	0.5
DG6	560	60	steel	5.2	0.23	114	1.82	Hitec-174	41	0.405	45
DG7	160	60	steel	3.4	0.15	75	1.20	Exxon-2389	24	0.081	09

* UNCOATED CASE

Table 5.1, Rolling contact fatigue test results for D-Gun coated rolling element balls.

The detail of this failure can be appreciated from figure 5.2.1(b), which shows that there are cracks visible not only on the edge of wear track but also within the coating microstructure and the propagation of cracks is also visible. The depth of failure can be approximated as 40 μm. The Electron Probe Microscopy Analysis (EPMA) results showed the presence of a tungsten (W) and cobalt (Co) peak only at the failed surfaces thereby confirming that the coatings did not fail at the coating substrate interface. The mode of failure in these results was observed to be coating delamination from within the coating microstructure. Figure 5.2.1(c) shows some shallow pits and deformations in the middle of the wear track which might have been caused during the RCF test or by the action of debris produced due to the coating delamination. Some cracks were also observed with in the wear track as shown in figure 5.2.1(d).

Surface observations for the tests in which coated balls were tested against steel planetary balls indicated similar failures as shown for the case of ceramic lower balls. Surface observations of the coated rolling element ball tested in Exxon-2389 as the test lubricant (test DG7) have been presented in figure 5.2.2. Figure 5.2.2(a) shows the overall view of the failed area for this test at 160 N contact load. The rolling direction was from left to the right of figure. Figure 5.2.2(b) shows the detail of failed area. The depth of failure in both the cases can be approximated as approximately 40 μm. The EPMA results confirm that the failure was through the coating itself and not at the coating substrate interface. Figure 5.2.2(c) shows the wear track cross section at the location of failure. The figure shows the delamination crack within the coating microstructure whereas, no subsurface cracks were visible at the coating substrate interface. The coating can be seen adhered to the substrate at an approximate depth of 20 μm below the depth of delamination crack. Figure 5.2.2(d) shows a Backscattered Electron Image (BEI) of the wear track cross section at another location and deformations within the coating microstructure can be seen with the appearance of microcracks under the wear track after the RCF tests.

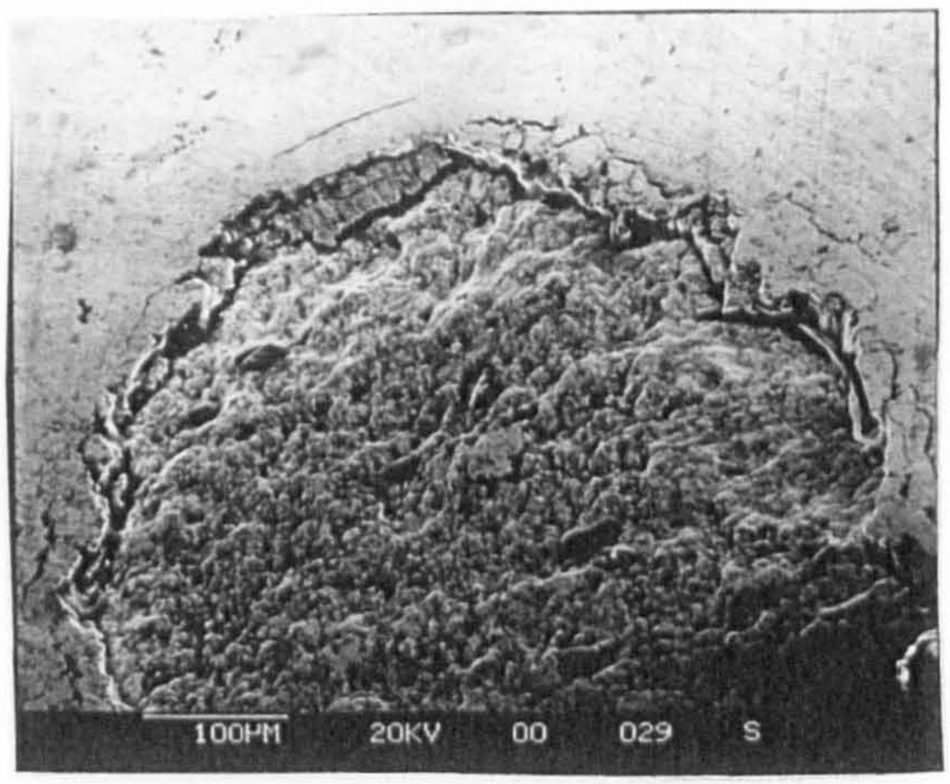

(a) failed area (SEI)

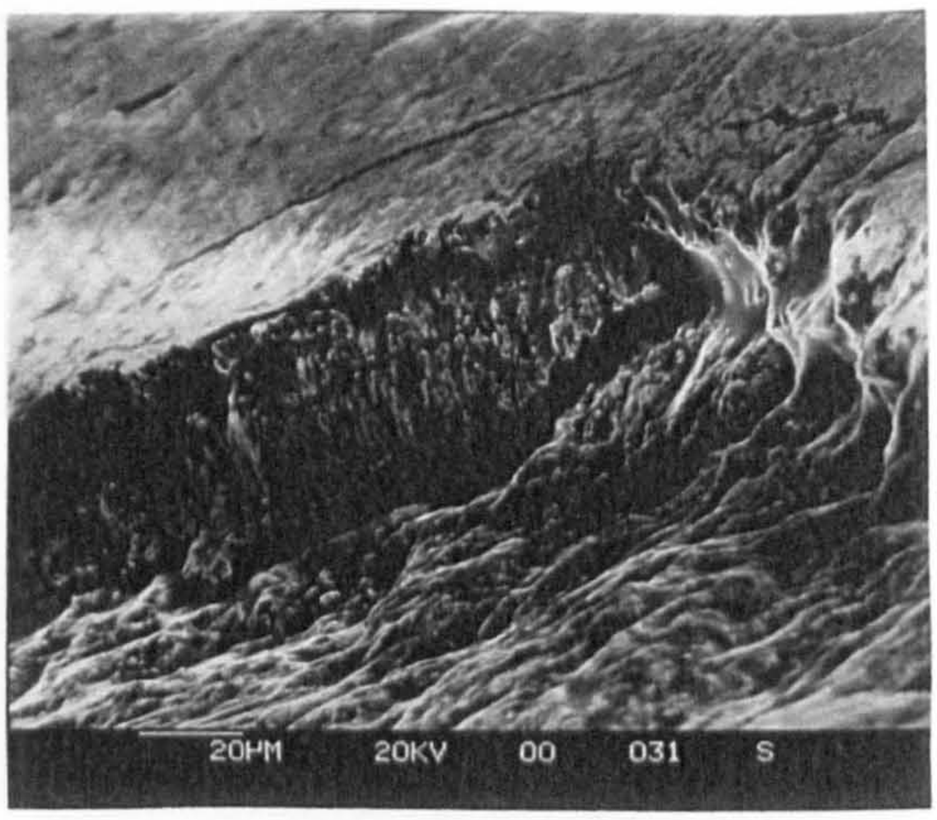

(b) cliff edge (SEI)

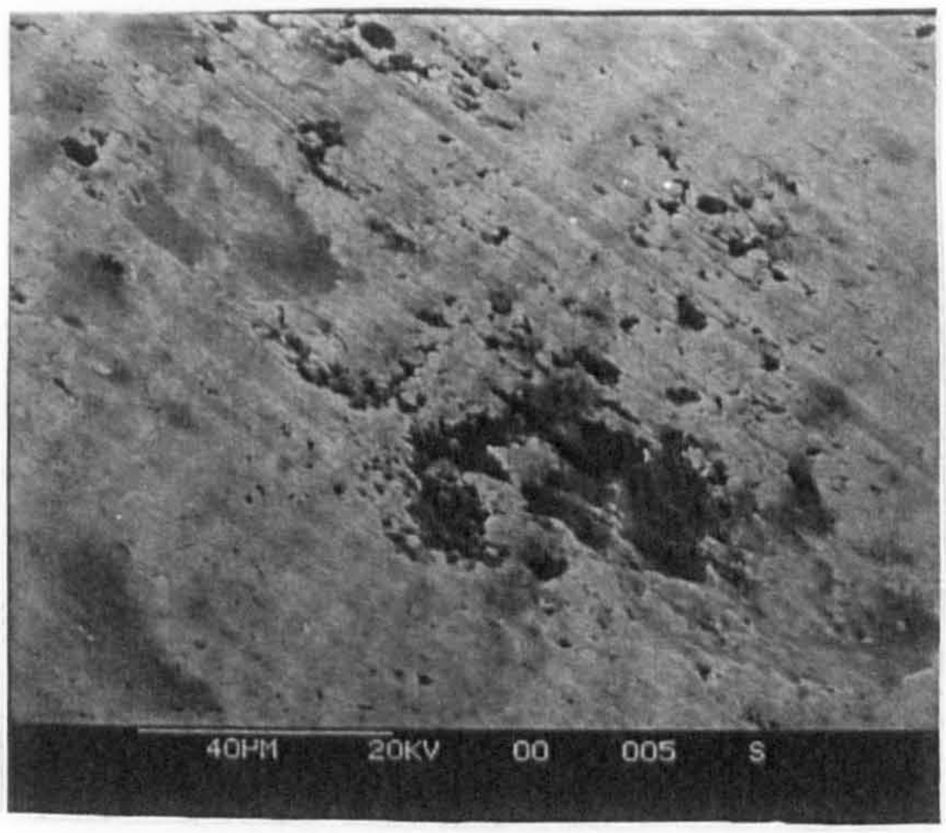

(c) pits in the wear track (SEI)

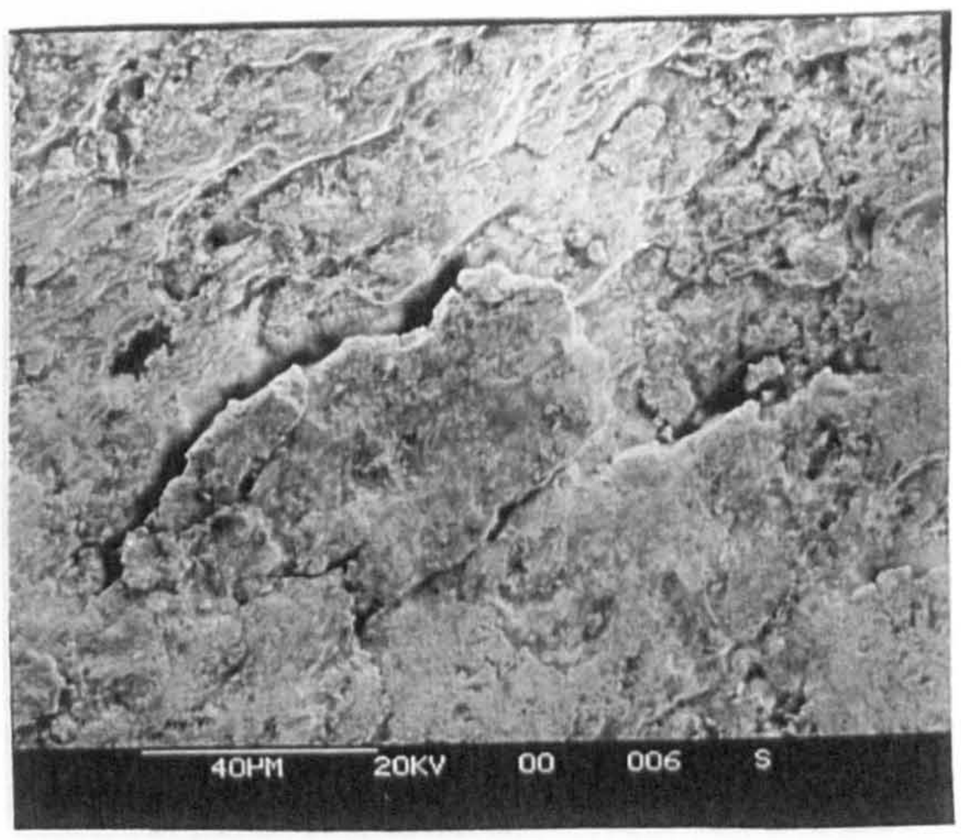

(d) cracks and loose debris (SEI)

Figure 5.2.1, Surface observations of the rolling element ball DG3

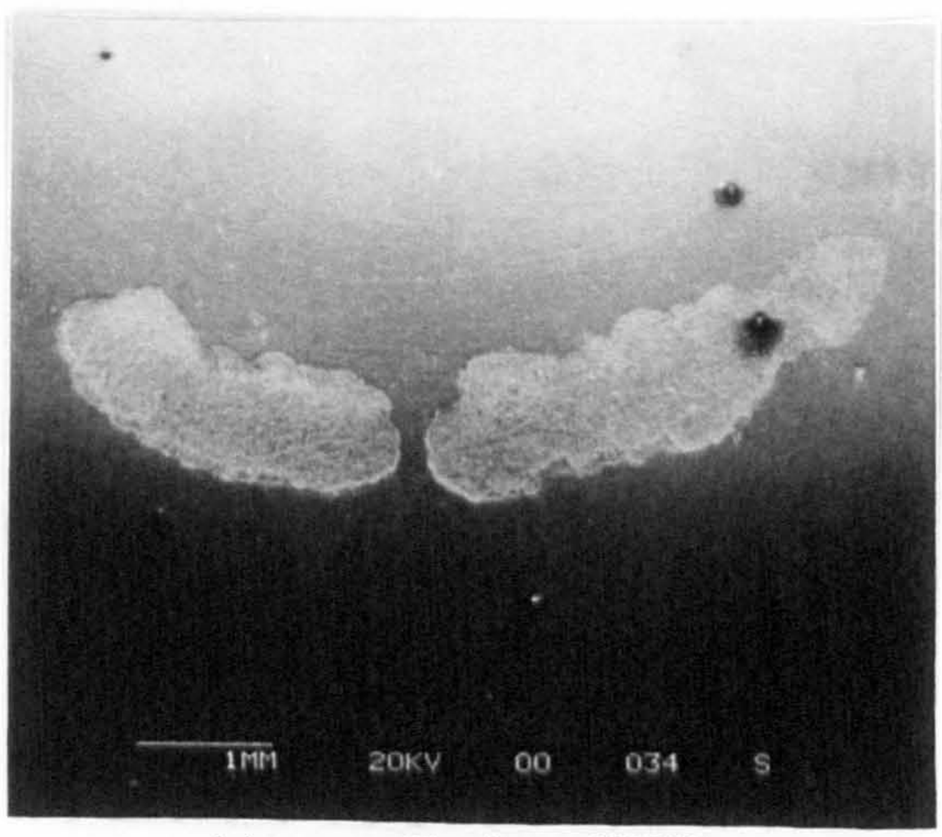

(a) overall view (SEI)

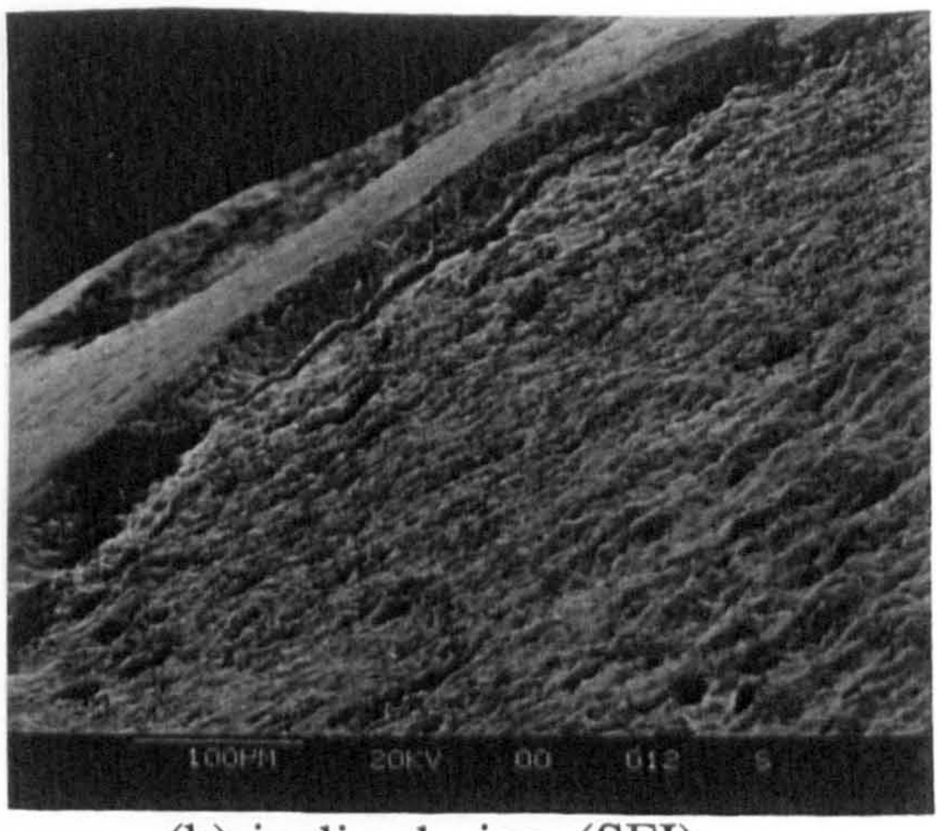

(b) inclined view (SEI)

Figure 5.2.2, Surface observations of the rolling element ball DG7

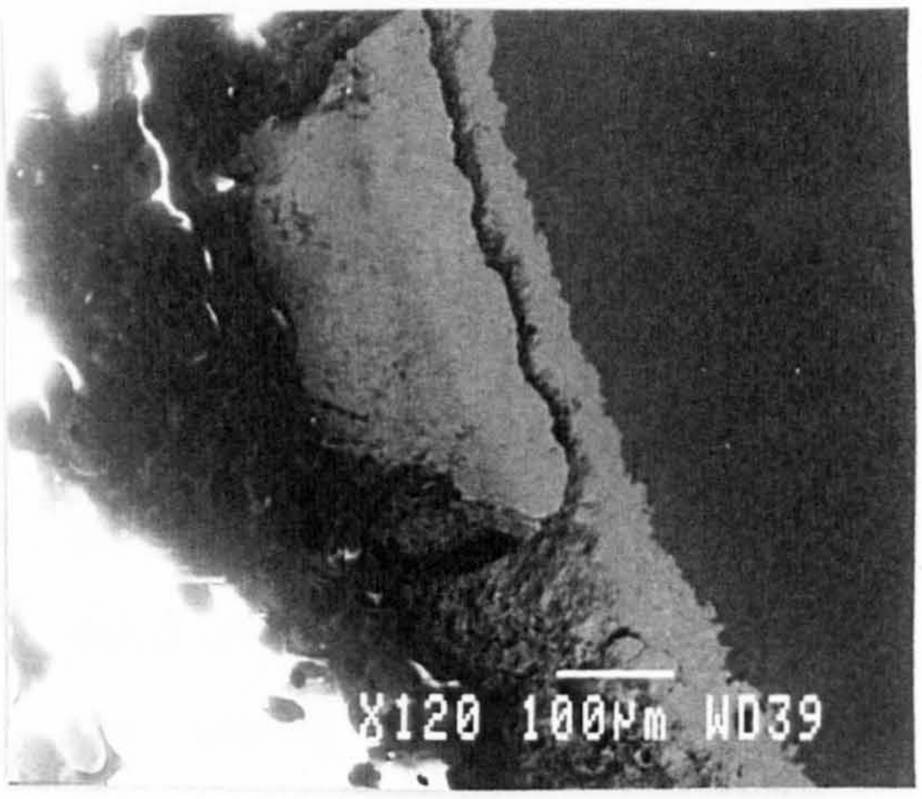

(c) wear track cross section (SEI)

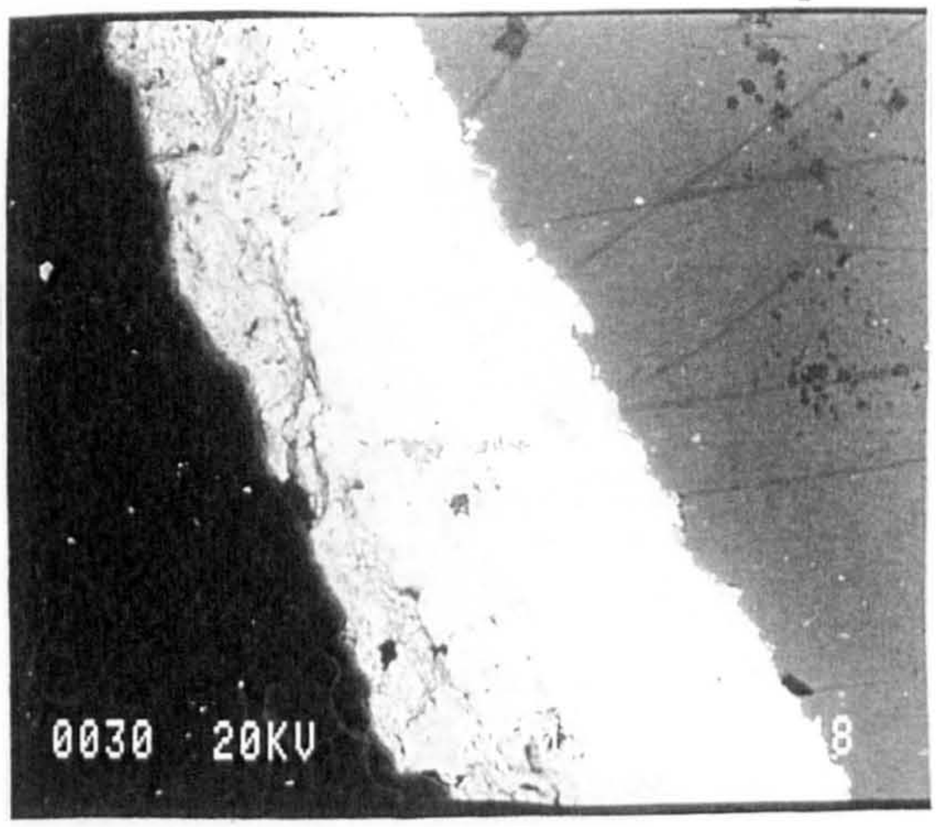

(d) subsurface microcracks (BEI)

Figure 5.2.2, Surface observations of the rolling element ball DG7 (continued)

5.2.5 Microhardness measurements

Leitz miniload 2, Vickers, knoop and scratch hardness tester was used to measure the micro-hardness of the coating and substrate. Measurements on a typical ball at a load of 300 p and 100 p revealed an average microhardness of the coating and substrate as 1200 Hv_{300} and 600 Hv_{100} respectively.

The microhardness values were averaged after neglecting the maximum and minimum values. The major objective of this analysis was to investigate the variation in hardness of the coating and the substrate. The tests revealed that the hardness of the coating varied from 1100 Hv to 1500 Hv, while that of the substrate varies from 560 Hv to 680 Hv. The variation in the microhardness of the coating was mainly due to the lamella structure and coating defects. Higher hardness values like 1500 Hv were mainly due to the presence of secondary phase particles like W_2C, etc. This is consistent with the hardness analysis presented by Wira et. al. (1995). Microhardness results also indicated that the substrate microhardness increased near the interface which could be mainly due to the temperature prevailing during the coating process and the sand blasting prior to the coating process which could impose residual stresses in the substrate material.

5.2.6 Coating microstructure

Tungsten carbide (WC-Co) coatings, consist of tungsten carbide particles held in a

cobalt matrix. The WC particles provide hardness whereas, the Co matrix provides toughness to the coating microstructure. Figure 5.2.3(a) represents a high magnification SEM image of the coating microstructure, whereas figure 5.2.3(b) represents the Backscattered Electron Image (BEI) of the coating at the same location. Highly illuminated particles represent high atomic number element whereas the tungsten carbide particles are also visible embedded in cobalt matrix. The microstructure showed that there were secondary phase particles and micropores in the coating microstructure which was typical of the D-Gun process. Some microcracks were also visible within the sprayed coatings within the angular tungsten carbide particles as shown in figure 5.2.3(c) in SEI whereas, figure 5.2.3(d) shows the same image in BEI.

5.2.7 Finite element modelling

The Finite Element Model (FEM) of the 60 μm thick coating which represents the case of the coated rolling element balls under consideration have already been described in chapter 3 (article 3.3.1) . The results for that specific case can thus be directly applied to the current section. Those results are not described here to avoid repeatability and the reader is referred to section 3.3.1 of the thesis. The results would however be used to aid the discussion of results and failure mechanism.

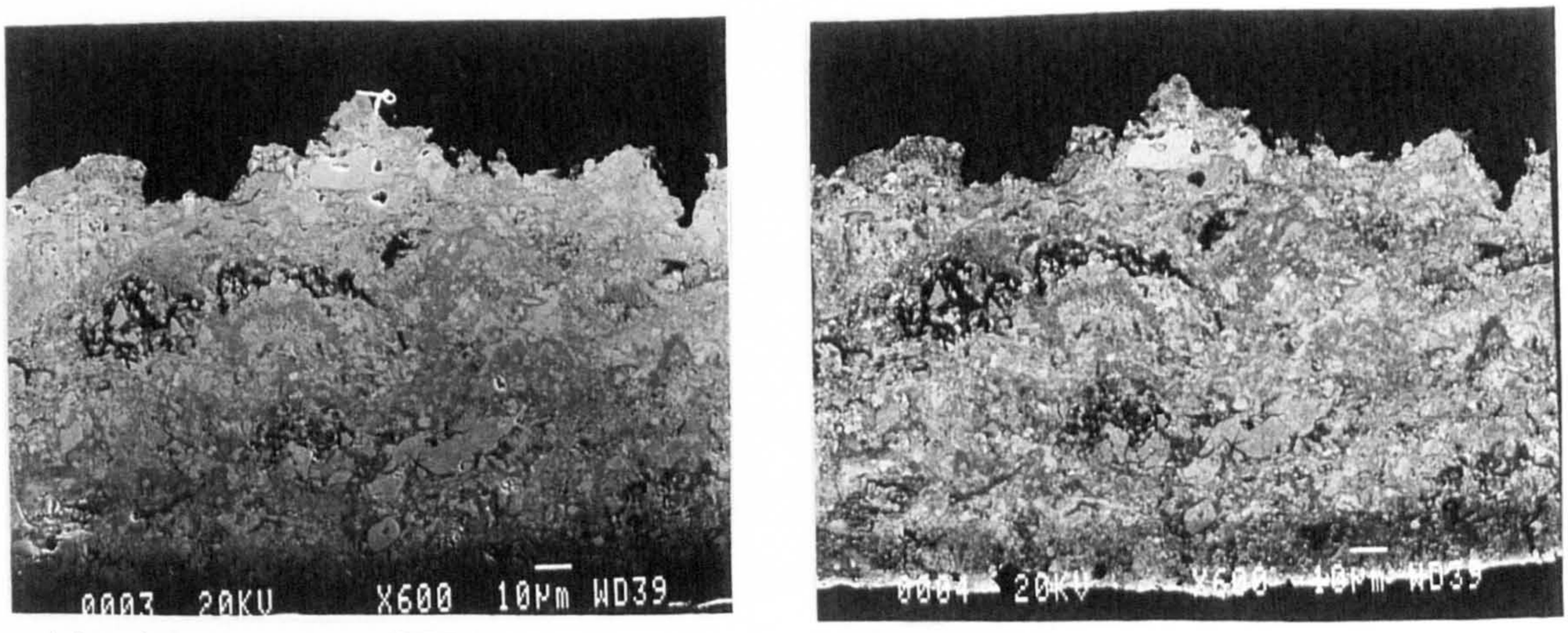

(a) microstructure (SEI) (b) microstructure (BEI)

Figure 5.2.3, Coating microstructure

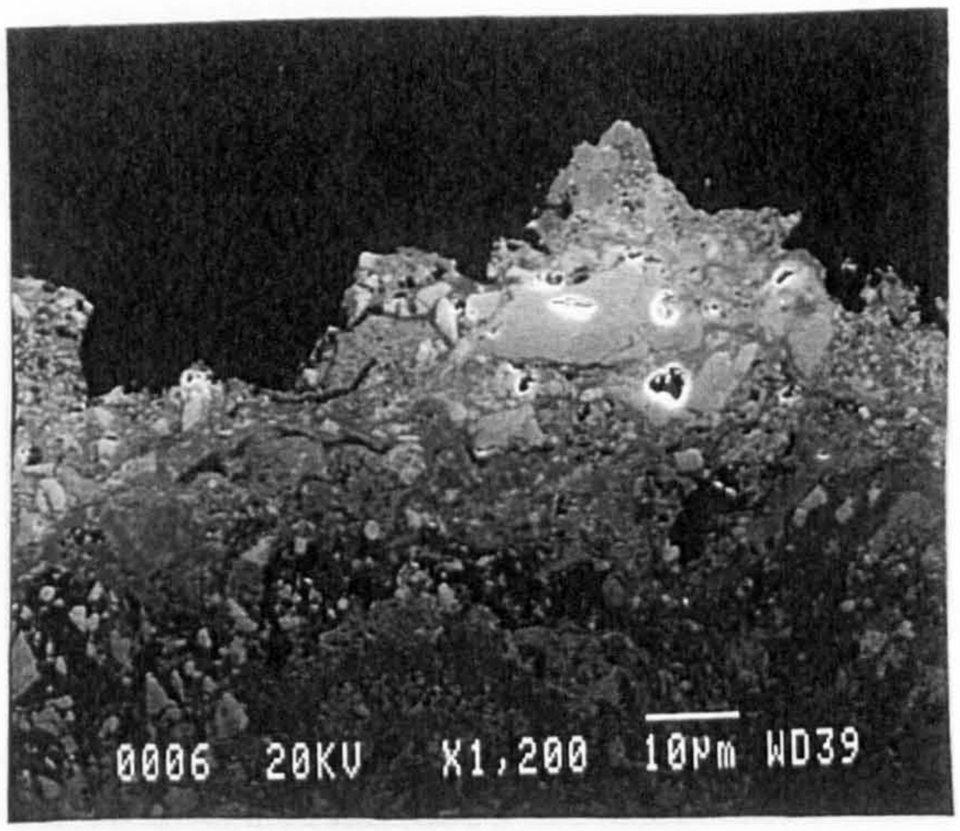

(c) higher magnification (SEI)

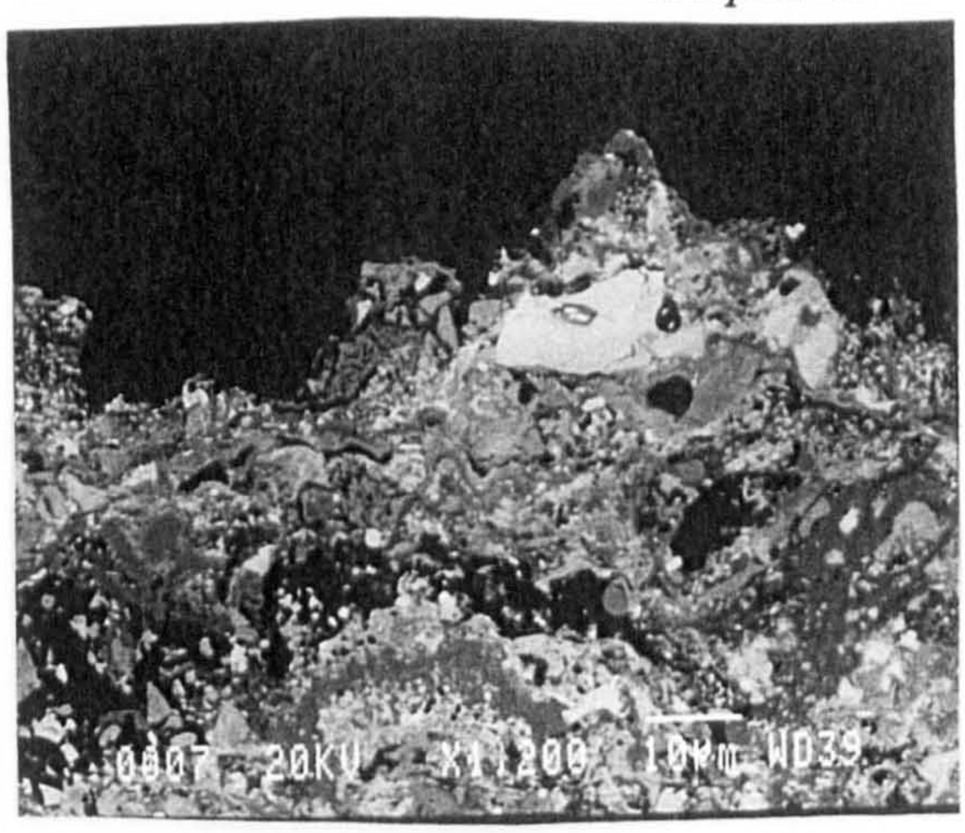

(d) higher magnification (BEI)

Figure 5.2.3, Coating microstructure (continued)

5.2.8 Residual stress measurements

Figure 5.2.4 represents the location and orientation of some typical residual stress measurements on D-Gun coated balls before and after the RCF tests. The numerical values of stress relating to these individual measurement points in three different directions can be appreciated from table 5.2. Figure 5.2.4(a), represents the location of stress measurements before the RCF tests at two points, ie. point 1, which was halfway between the wear track and crown of the ball while measurement point 2, was at a position on which the wear track will be formed during the RCF test. Figure 5.2.4(b) represents the location of measurement point 3, which was in the middle of the wear track on a ball subjected to test DG4. Figure 5.2.4(c), represents the location of three measurement points on the ball subjected to test DG3. The first set of measurements at point 4 were made in the middle of wear track, whereas the measurement point 5 represent the measurements at the edge of wear track. Measurement point 6 was located in the middle of the failed area within the wear track. The SEM observation at the residual stress measurement point in the failed area for the ball subjected to test DG3 can be appreciated from figure 5.2.1. Figure 5.2.4(d) represents the location of measurement points 7 and 8 on the ball subjected to test DG2. Point 7 was situated in the middle of the wear track, whereas point 8 was located at the edge of the wear track in the failed area. In some cases it was difficult to measure accurate diffraction peak shifts in the middle of the wear track, especially in the failed areas, mainly because of the poor surface roughness.

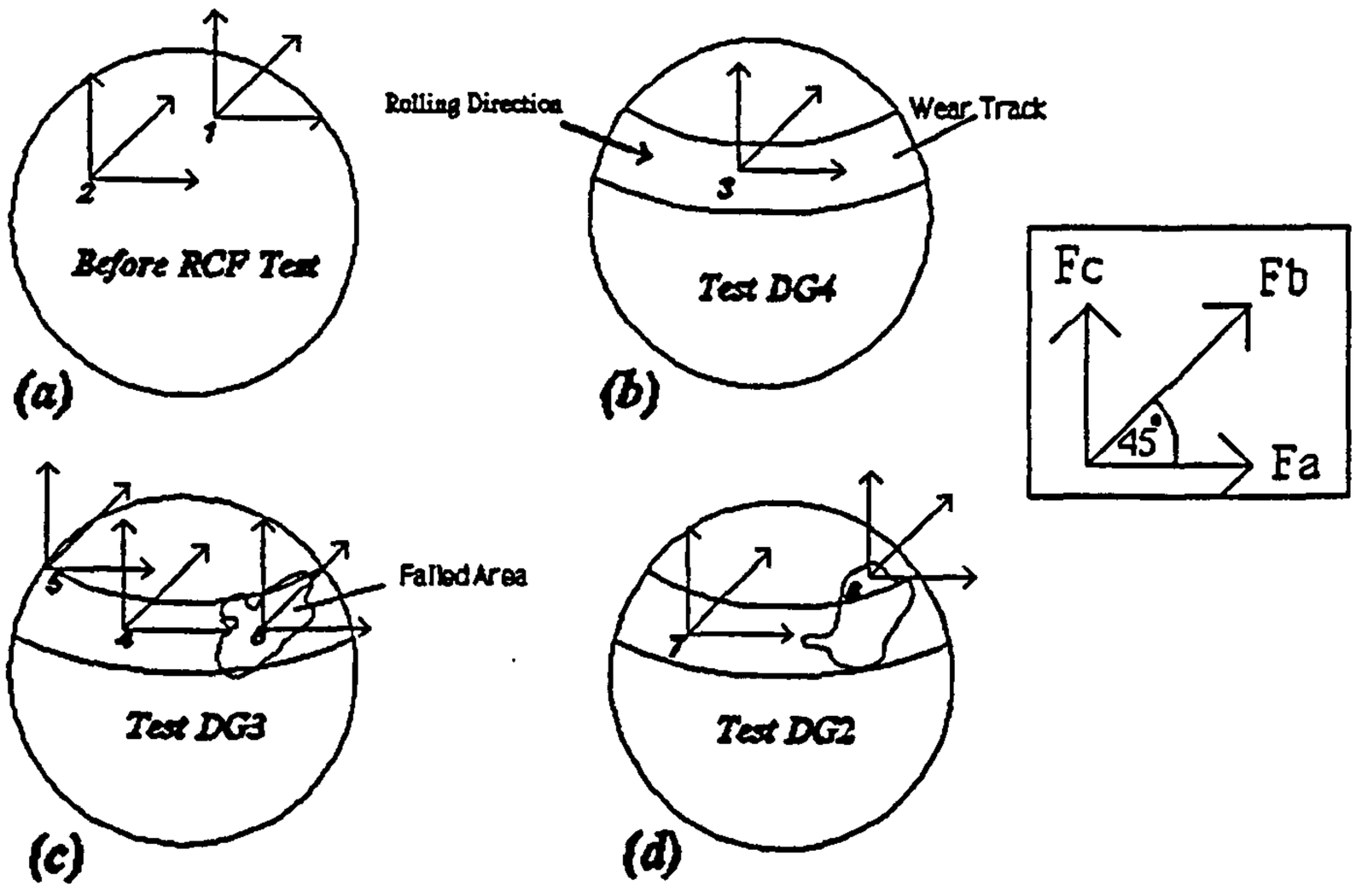

Figure 5.2.4, Residual stress measurement points

Point No:	Test	Collimator Size (mm)	Time (min)	Residual Stress Values (MPa)		
				Fa (0 deg)	Fb (45 deg)	Fc (90 deg)
1	Untested	0.5	167	-296 ± 61	-336 ± 77	-440 ± 73
2	Untested	0.5	167	-515 ± 69	-394 ± 95	-685 ± 61
3	DG4	0.5	167	-243 ± 48	-500 ±97	-336 ± 141
4	DG3	0.5	167	-220 ± 73	*	-240± 96
5	DG3	0.5	167	-117 ± 58	-372 ± 112	-301 ± 50
6	DG3	0.5	167	-302 ± 61	*	-250 ± 42
7	DG2	0.5	167	-121 ± 91	*	-329 ± 50
8	DG2	0.5	167	-382 ± 96	*	-347 ± 79

* Value not available

Table 5.2, Residual stress measurement results of D-Gun balls

5.3 High Velocity Oxy-Fuel Coated Cones on Mild Steel Substrate

5.3.1 Introduction

Tungsten carbide cobalt (WC-Co) coatings deposited by high velocity thermal spraying processes are well known for their resistance against sliding wear, hammer wear, abrasion wear and fretting. This coating process use higher velocities of the impact particles (typically 750 m/s) in comparison to the conventional plasma spraying process, which results in a dense and compact coating microstructure. This section addresses an investigation in which the performance of thermally sprayed WC-Co coatings deposited by the High Velocity Oxy-Fuel (HVOF) process on the surface of the mild steel cones were investigated in rolling contact under the various tribological conditions of lubrication and contact configuration for different coating thicknesses. The main objective of this work was to investigate the affect of substrate hardness on the performance and failure modes of the coated rolling elements.

5.3.2 Coated cone rolling elements.

Thermally sprayed tungsten carbide cobalt (WC-12%Co) coatings produced by the HVOF process were deposited on the surface of the mild steel cones. The substrate material was selected to study the affect of hardness of the substrate steel on the RCF performance of thermal spray coatings. The rolling element cone was of 14.5 mm diameter having an apex angle of 109.2^0. The substrate material was sand blasted prior to the coating process and preheated to a temperature of approximately 150°C. The spraying powder had a particle size of approximately $15\sim50\mu$m (manufacturers data). The rolling elements were coated in three thickness of 200μm, 100μm and 75μm in the as-sprayed conditions by several passes of the spraying in a direction perpendicular to the cone axis. The rolling elements were then ground and polished to give an average coating thickness of $150\pm10\mu$m, $50\pm10\mu$m and $20\pm5\mu$m. The surface roughness (R_q) of the coated rolling elements in the as-sprayed conditions and after polishing were measured to be $6\pm0.5\mu$m and $0.075\pm0.025\mu$m respectively at a cutoff of 0.8 mm.

5.3.3 Test conditions and experimental test results.

In order to access the performance of thermal spray coatings under various tribological conditions three lubricants were considered during the testing programme. In addition to the Hitec-174 and Exxon-2389 as the test lubricant a third test lubricant was also used which was a mixture of distilled water (H_2O) and Brake Fluid (BF) in equal proportions by volume which were thoroughly mixed in an ultrasonic bath. This lubricant was used to access the performance of these coatings in hostile environments by making the fluid corrosive. This mixture ($BF+H_2O$) was measured to have an average kinematic viscosity of 9.06 cst at room temperature of 24^0C using a Redwood viscometer. The RCF tests with the test lubricants Hitec-174 and Exxon-2389 were conducted in immersed lubrication conditions. This is consistent with the other studies in this work, where these lubricants did not suffer from contamination or high viscosity variations under the given test conditions. However, preliminary studies indicated that this lubrication system was inadequate for the test lubricant ($BF+H_2O$), due to water evaporation owing to the flash temperature between the rolling elements and high contamination by the debris. A splash feed lubrication as described in chapter 2 (article 2.4), was used to conduct RCF tests with this lubricant ($BF+H_2O$).

The RCF tests were conducted at an ambient temperature of approximately 24^0C. The spindle speed was set to $4{,}000\pm5$ rpm using a high speed drive. The RCF tests were conducted at a contact load of 40 N and 160 N applied to the cup assembly. The ratio (λ) of the approximate value of the Elasto-Hydrodynamic Lubrication (EHL) film thickness to the average surface roughness for the test lubricants Hitec-174 & Exxon-2389 under the given test conditions were calculated to be $\lambda>3$ and $\lambda<1.5$ respectively. The EHL results for the test lubricant ($BF+H_2O$) could not be included due to the lack of technical data like pressure viscosity coefficient etc. However, it was estimated that the λ value was less than unity under the given test conditions (for a range of pressure viscosity coefficient), this could imply that boundary lubrication existed.

The total frictional torque in the modified four ball assembly was measured using

the technique described in chapter 2 (article 2.6). Only one rolling element cone was used for these measurements, and the frictional torque measurements were conducted under the test conditions of contact stress (1.7 GPa) and spindle speed (4000$\pm$5 rpm) in contact with the steel planetary balls. The average frictional torque measured for the test lubricants Hitec-174, Exxon-2389 and (BF+H_2O) was measured to be 0.043 N-m, 0.041 N-m & 0.05 N-m respectively. These friction values were low and comparable with the values of uncoated rolling elements as shown in Chapter 2.

The experimental test procedures described in chapter 2 (article 2.3) were followed to perform the RCF tests. Table 5.3 summarises the experimental test results in terms of contact stress, test configuration and test duration. The contact stress and contact area shown in table 5.3, represents the calculations based upon the assumption of uncoated contact configuration. It can be appreciated from appendix D that the depth of maximum shear stress and orthogonal shear stress for the given test conditions was approximately 50 μm and 30 μm respectively at 40 N contact load and approximately 90 μm and 40 μm respectively at 160 N contact load tests.

5.3.4 Surface observations of the rolling elements

Figure 5.3.1 shows the SEM observations of the failed WC-Co coated rolling element subjected to the test conditions described for the RCF test HVMS4. The figure shows the different stages of the crack propagation leading to the coating delamination. Figure 5.3.1(a) shows the crack initiation within the wear track as well as at the edges of the wear track of the test cone. Figure 5.3.1(b) shows the crack propagation at an advanced stage within the wear track and an appreciation of the occurrence of the edge cracks which were much more pronounced than the cracks within the wear track. Figure 5.3.1(c) shows an inclined view of the cracks shown in figure 5.3.1(b) and represents the initial stage of coating delamination at the edge of the wear track. Figure 5.3.1(d) shows the failed surface after the coating delamination. Further analysis of the failed coating revealed that the depth of the delamination failure in the middle of the wear track was approximately 80 μm which corresponds to the approximate depth of maximum shear stress.

Test No	Contact Load (N)	Average coating thickness (μm)	Lower balls	Contact stress* (GPa)	Contact width (mm) (b)	Depth of max: shear (0.65b) (μm)	Maximum shear stress (Gpa)	Lubricant	No: of stress cycles (10^6)	Time to Failure (minutes)
HVMS1	40	150	steel	1.73	0.08	50	0.6	Hitec-174	19.062	2118
HVMS2	40	150	steel	1.73	0.08	50	0.6	Exxon	2.637	293**
HVMS3	160	150	steel	2.75	0.13	80	0.96	Hitec-174	0.144	16
HVMS4	160	150	steel	2.75	0.13	80	0.96	Exxon	0.126	14
HVMS5	40	50	steel	1.73	0.08	50	0.6	Hitec-174	30.78	3420
HVMS6	40	50	steel	1.73	0.08	50	0.6	Exxon	15.66	1740
HVMS7	160	50	steel	2.75	0.13	80	0.96	Hitec-174	0.126	14
HVMS8	160	50	steel	2.75	0.13	80	0.96	Exxon	0.144	16
HVMS9	40	50	steel	1.73	0.08	50	0.6	(BF+H_2O)	1.458	162
HVMS10	40	50	ceramic	1.94	0.07	50	0.6	(BF+H_2O)	0.162	18
HVMS11	40	20	steel	1.73	0.08	50	0.6	Hitec-174	68.58	7620**
HVMS12	40	20	steel	1.73	0.08	50	0.6	Exxon	8.208	912
HVMS13	40	20	steel	1.73	0.08	50	0.6	(BF+H_2O)	5.76	640
HVMS14	40	20	ceramic	1.94	0.07	50	0.6	(BF+H_2O)	3.051	339

* UNCOATED CASE ** Suspended test

Table 5.3, Rolling contact fatigue test results for HVOF coated cones on mild steel substrate

The Electron Probe Microscopy (EPMA) analysis of the failed coating showed that the coating failure was from within the coating microstructure and not at the coating substrate interface. This type of delamination failure from within the coating microstructure was seen in all the tests conducted with 150 μm thick coatings with some failures at a depth of 40 μm.

Figure 5.3.2 shows the SEM observations of the 50 μm coated cones. Figure 5.3.2(a) shows the Back-scattered Electron Image (BEI) of the failed cone subjected to test HVMS7. The figure shows that the coating failure was within the wear track with no edge cracks. The figure also gives an appreciation of the three stages of the coating delamination from the left to the right of the figure. The BEI of the failed coating shows that the coating initially fails just above the coating substrate interface as seen by the left hand side failure in the figure. The EPMA analysis also confirmed the presence of coating in this failure. The figure indicates that the coating failure initially took place just above the coating substrate interface and it is possible that the debris produced during the RCF test caused a three body abrasion, to wear away the intact thin layer of coating as the test progressed. This behaviour can be seen by the dark and bright portions of the delaminated coating area as seen on the right hand side failure in figure 5.3.2(a). Figure 5.3.2(b) shows the failed coating for the cone subjected to test HVMS8. The figure shows that the cracks are initiated in the middle of the wear track but, the coating did not fail in the middle of the wear track. It is appreciated that the plastic flow of the substrate from underneath the surface to the edges of the wear track took place due to the ductile behaviour of the mild steel substrate under high compressive stress of 2.7 GPa on a soft steel substrate. The coating failure takes place at the edge of the wear track. This behaviour is more evident in figure 5.3.2(c), which shows an inclined BEI of the delaminated edge. The EPMA analysis confirms that the migration of the steel substrate takes place at the edges of the wear track. Figure 5.3.2(d) represents the detail of cracks shown in figure 5.5.2(b). It can be clearly seen that the cracks travel around the boundaries of the WC particles. The plastic deformation of substrate material due to compressive stress is thought to be a major factor for the initiation of these cracks in the middle of the wear track.

Figure 5.3.3 represents the surface observations of the failed coated rolling element subjected to the test conditions described for HVMS10. Figure 5.3.3(a) shows the inclined view of the delaminated edge. The delamination at the coating substrate interface can be appreciated from this figure in which the coating had de-bonded catastrophically forming a cavity of approximately 10 μm deep at the interface as shown at a higher magnification in figure 5.3.3(b). The depth of delamination can also be approximated as 40 μm. In general, the surface observations of the failed coated rolling elements of 150 μm and 50 μm thick coatings indicated that these coatings failed due to the delamination of coating within the coating microstructure for 150 μm thick coatings and at or just above the coating substrate interface for 50 μm thick coated rolling elements under the given RCF test conditions.

Figure 5.3.4(a) shows the SEM observations of a 20 μm thick coating tested in Hitec-174 lubricant with steel lower balls (test HVMS11). The test was suspended after 60 million stress cycles. Small pits can be seen on the surface of the wear track however subsurface observations indicated that no delamination cracks were present underneath the wear track. Figure 5.3.4(b) shows a typical talysurf observation of the wear track of this rolling element after the RCF test. Figure 5.3.5(b) indicate that there may be some coating deformation at the edge of the wear track which was also observed during the surface observations of the failed rolling element HVMS8 (figure 5.3.2(c)). Figure 5.3.4(c) shows the BEI of the surface of the rolling element cone tested in lubricant (BF+H_2O) in contact with the ceramic lower balls (test HVMS14). It can be seen that the coating is still intact with the substrate however an appreciable amount of surface wear can be seen on the wear track. The presence of coating at the bright portions was confirmed by EPMA analysis. It can be seen that the coating failure is from the substrate material. This behaviour is more evident in the Figure 5.3.4(d) which shows the cross section of the wear track. This Figure (5.3.4(d)) also shows the plastic deformation and the cracks in the substrate material.

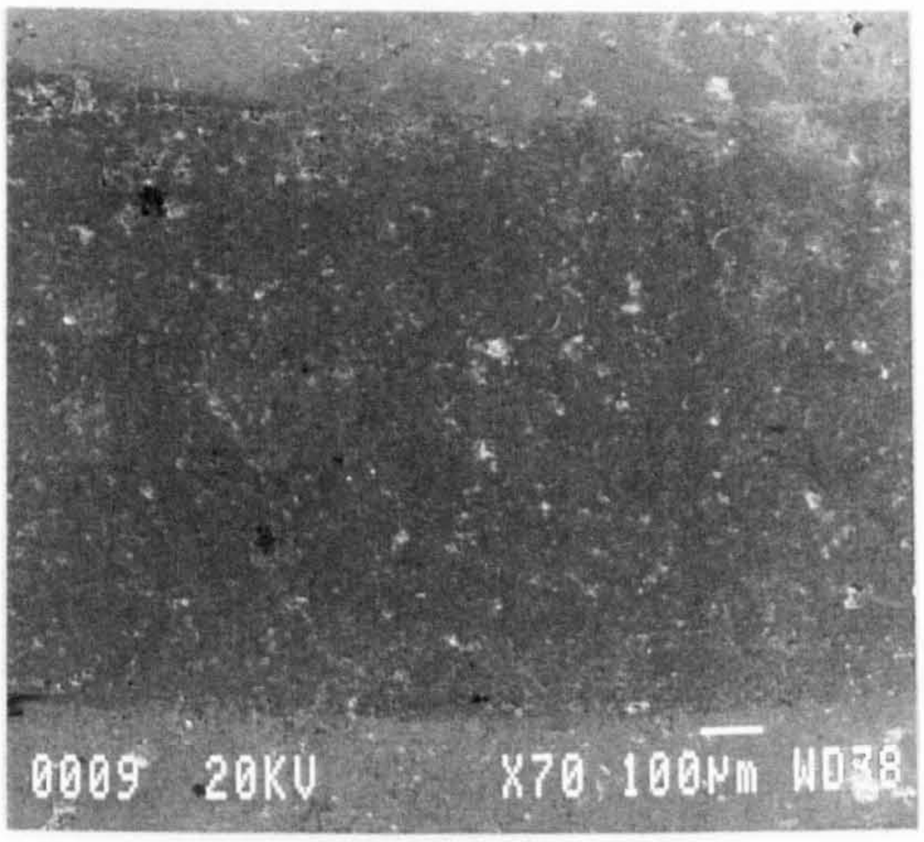

(a) initial cracks (SEI)

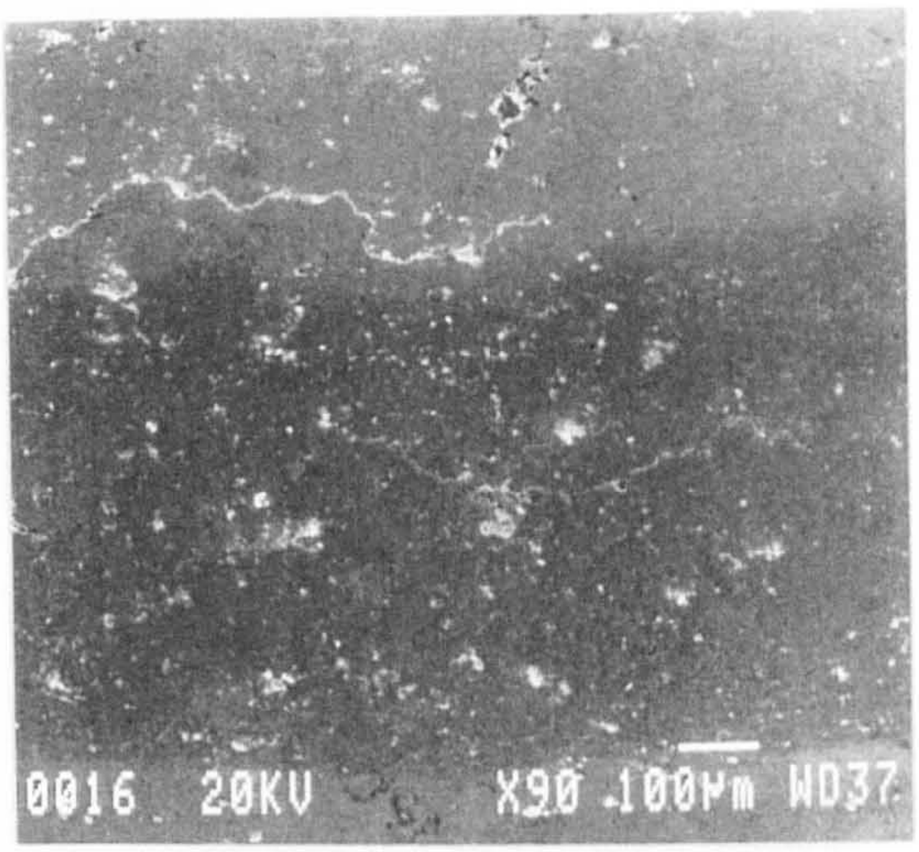

(b) crack propagation (SEI)

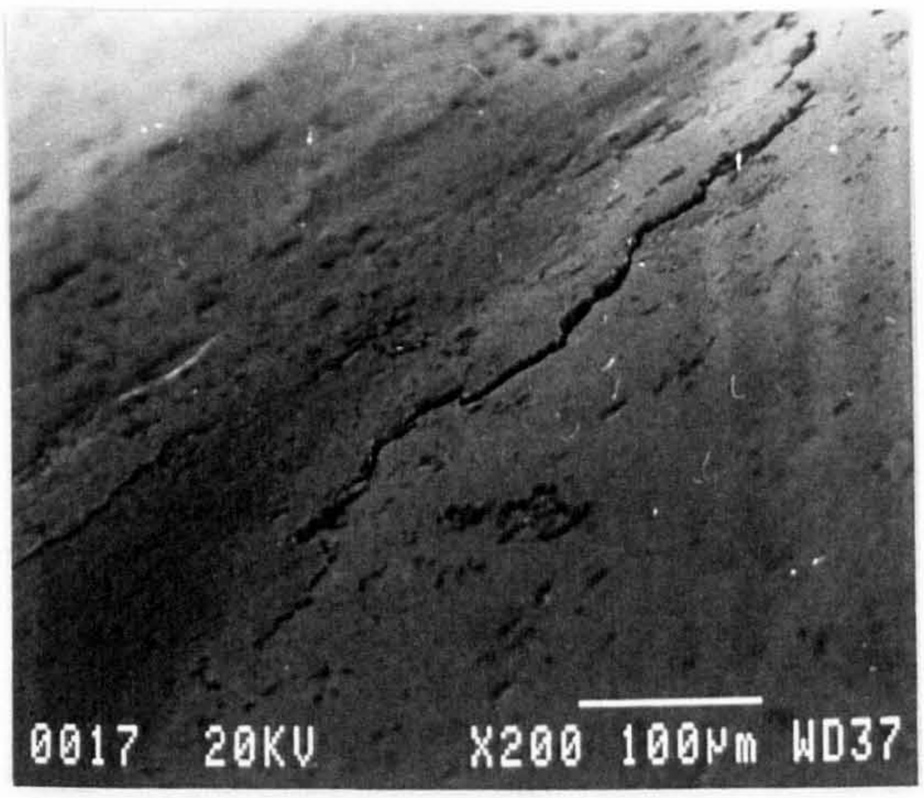

(c) inclined view (SEI)

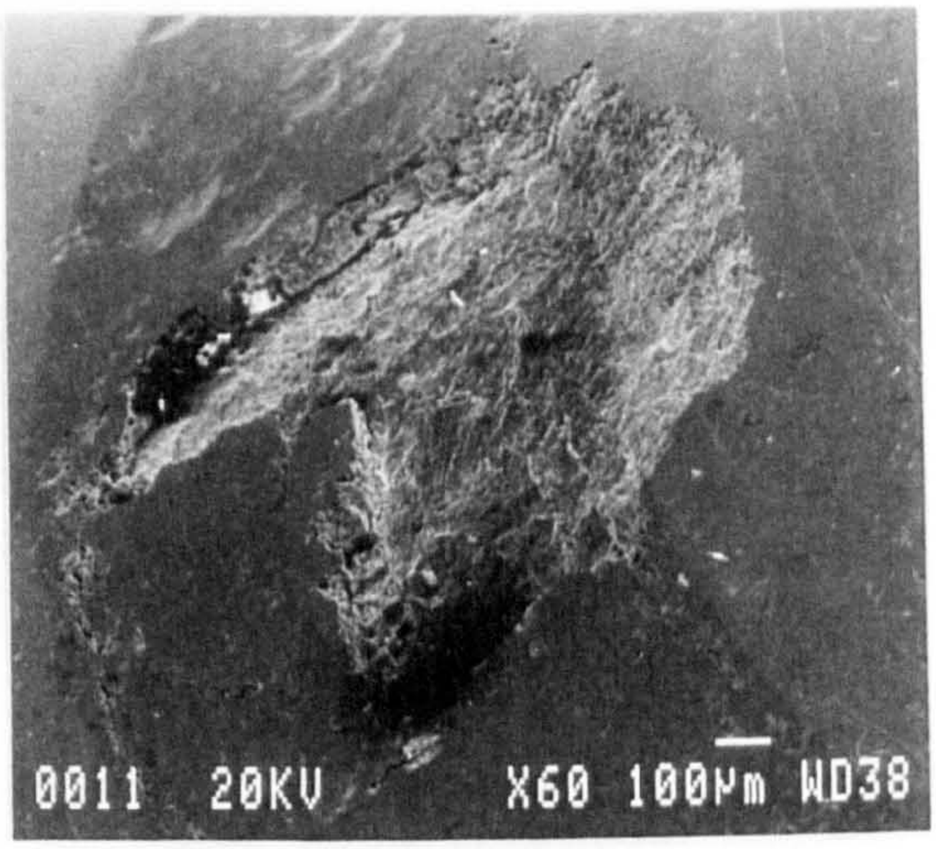

(d) coating delamination (SEI)

Figure 5.3.1, Surface observations of the rolling element cone HVMS4

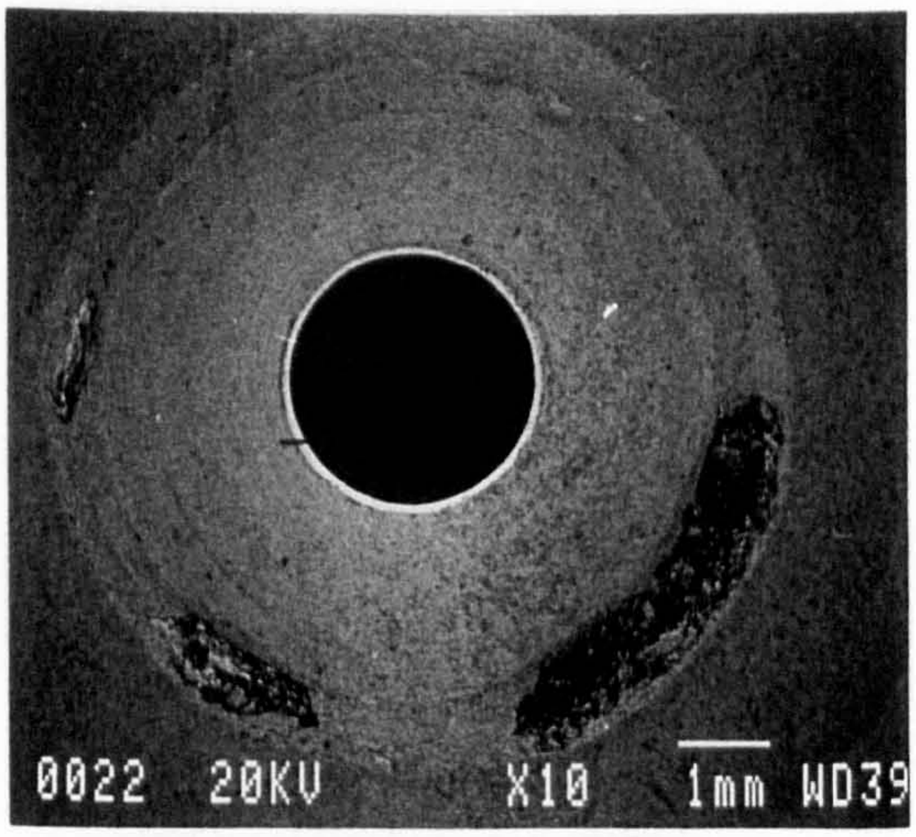

(a) overall view (BEI)

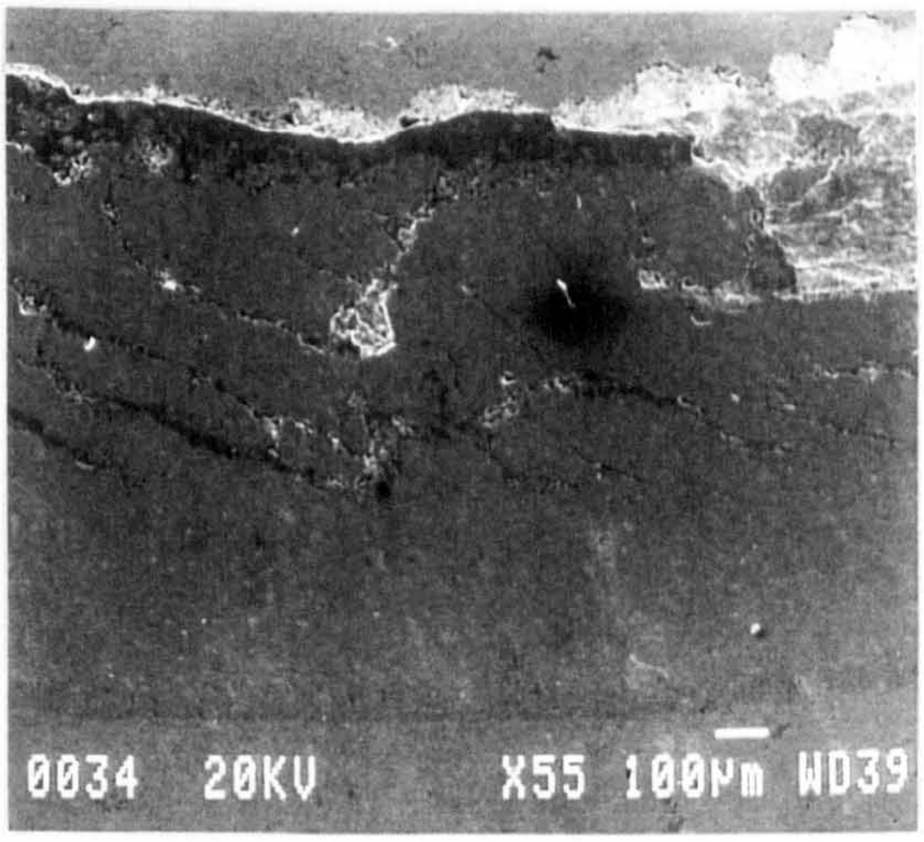

(b) wear track (SEI)

Figure 5.3.2, Surface observations of the rolling element HVMS7 & HVMS8

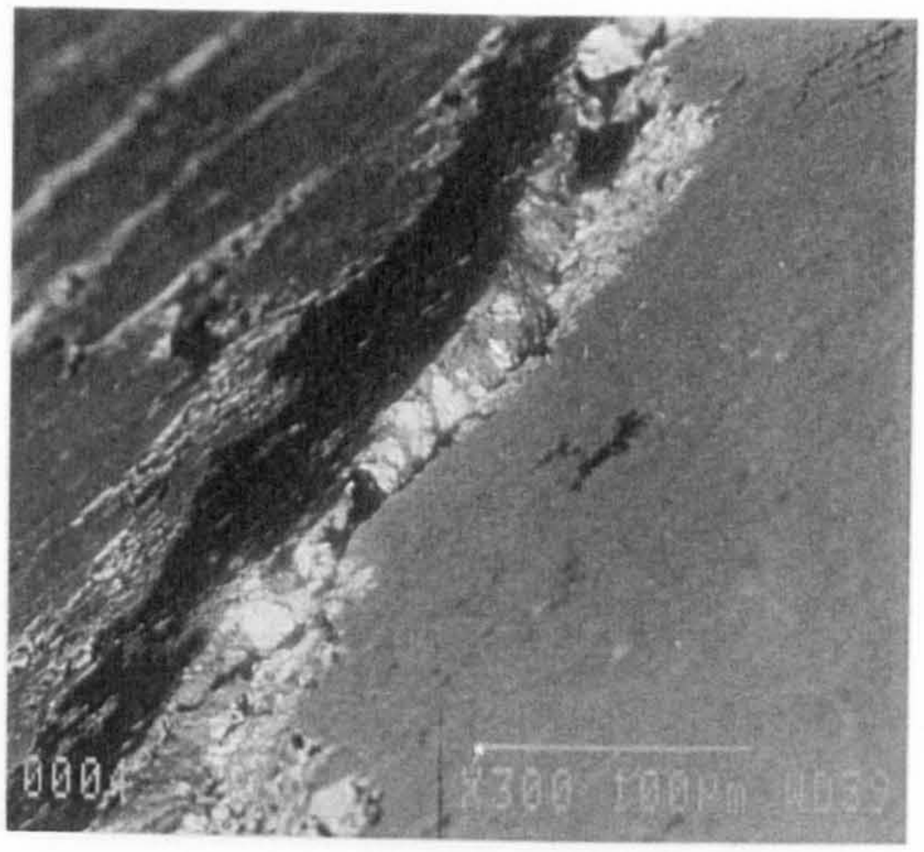

(c) inclined view (SEI)

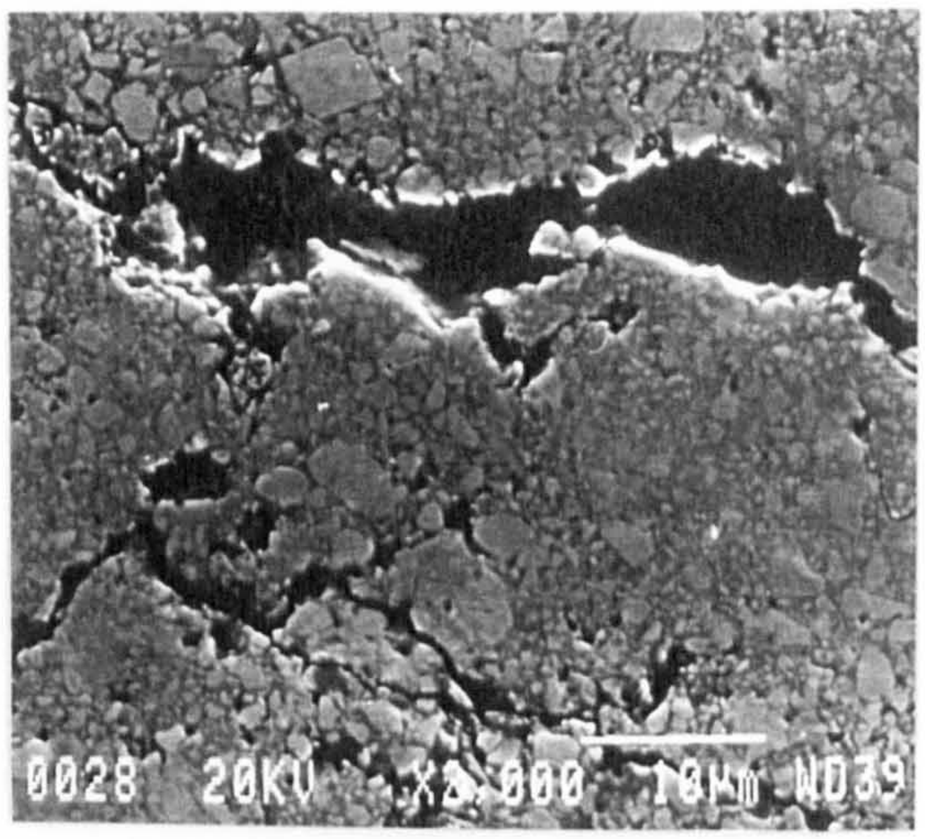

(d) cracks (middle of wear track)

Figure 5.3.2, Surface observations HVMS7 & HVMS8 (continued)

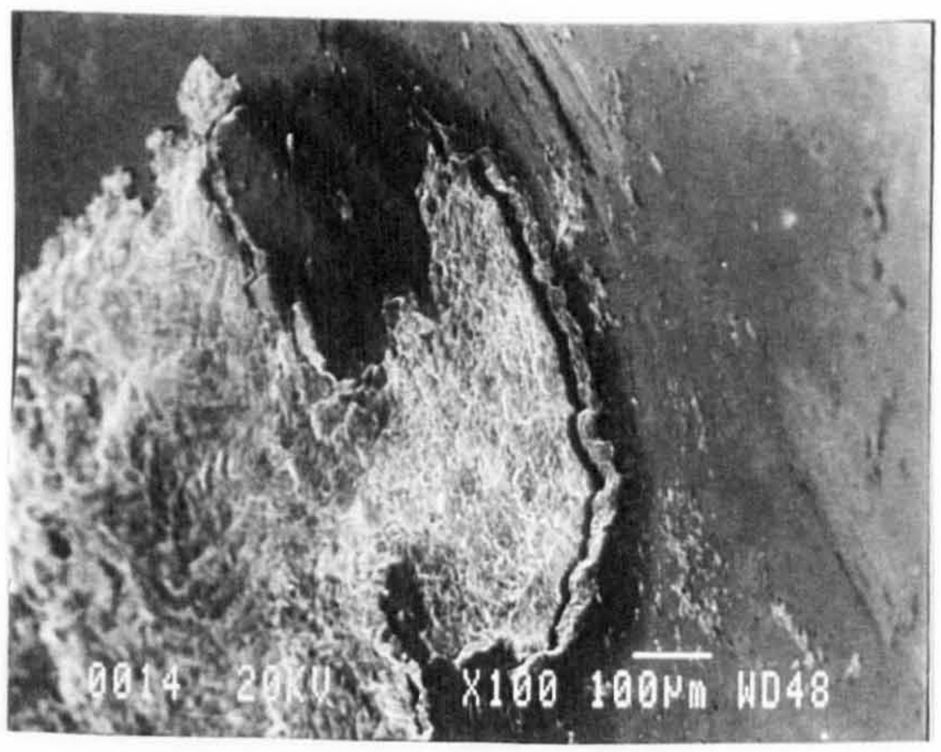

(a) inclined view (SEI)

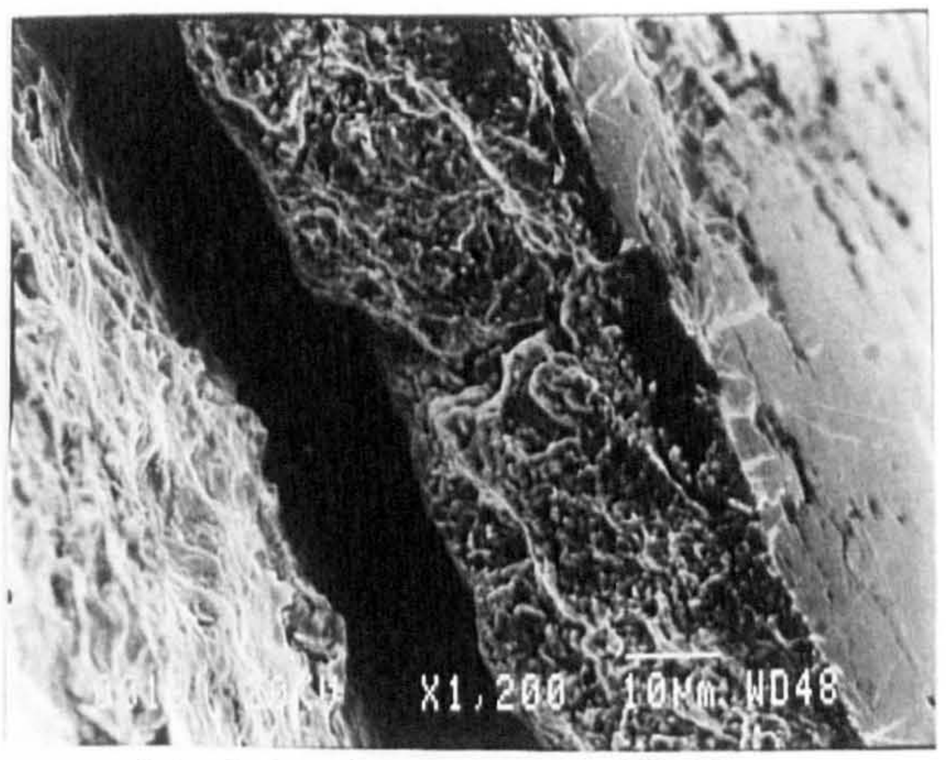

(b) delaminated area (SEI)

Figure 5.3.3, Surface observations of the rolling element cone HVMS10

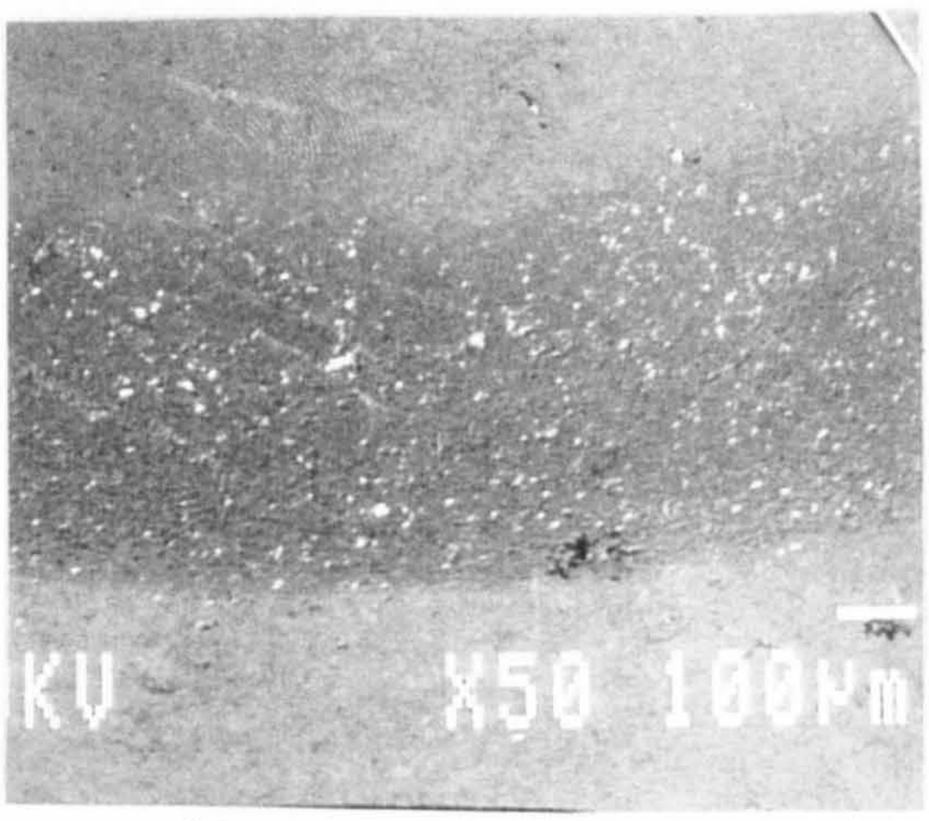

(a) wear track (SEI)

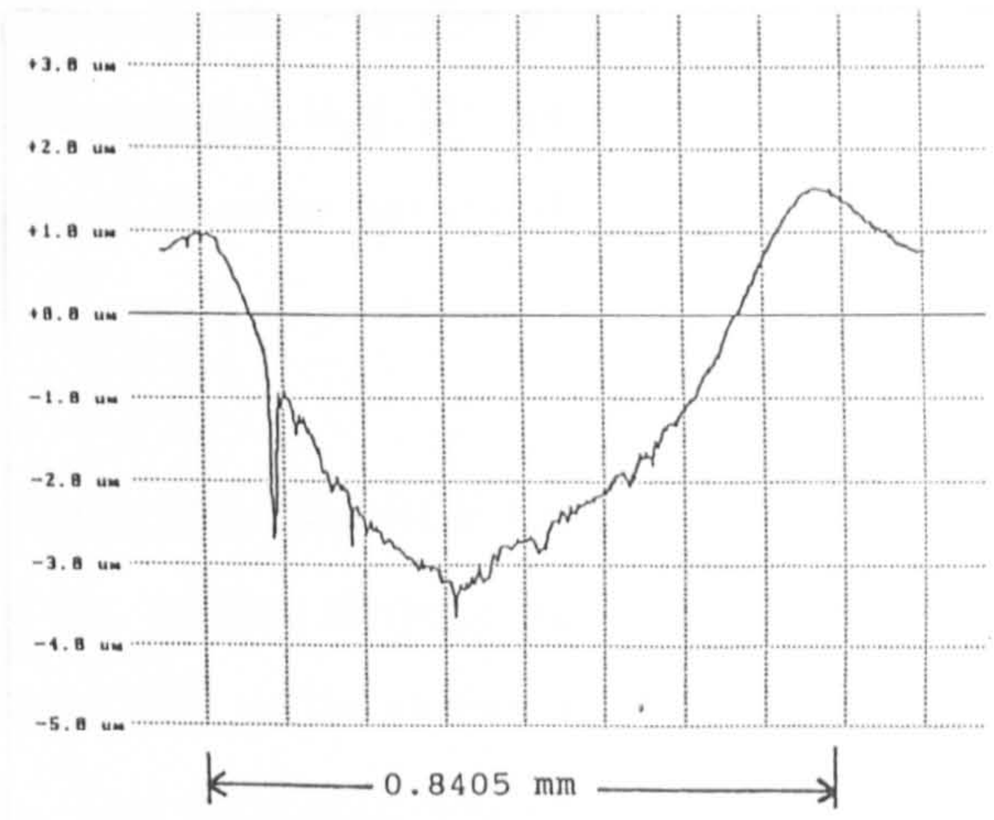

(b) wear track analysis

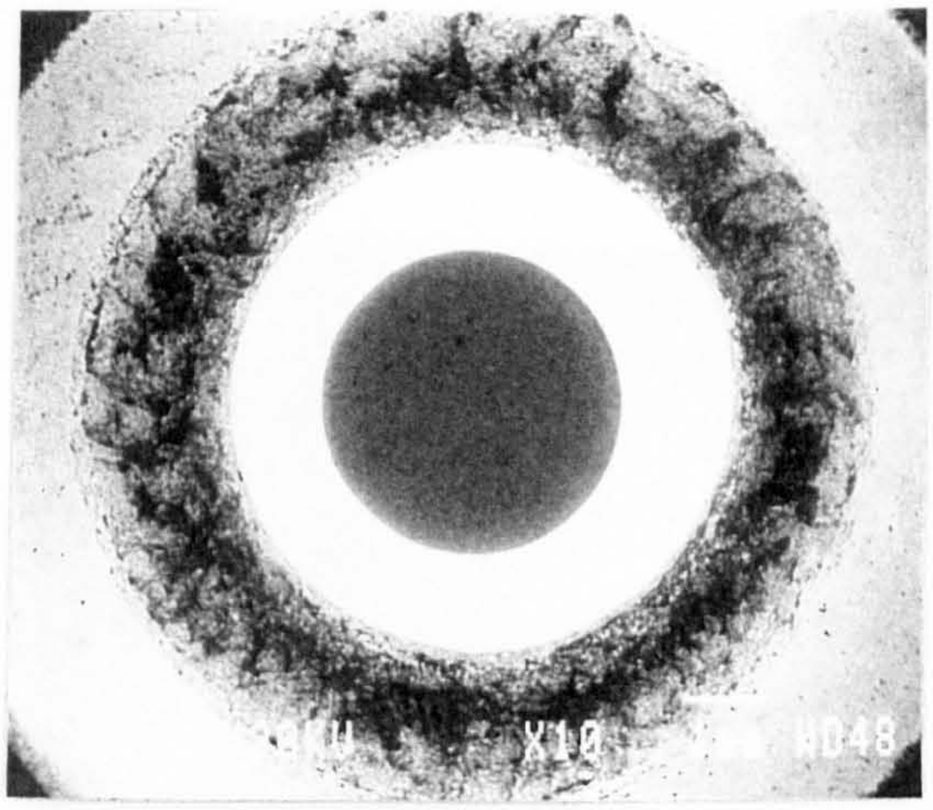

(c) overall view (BEI)

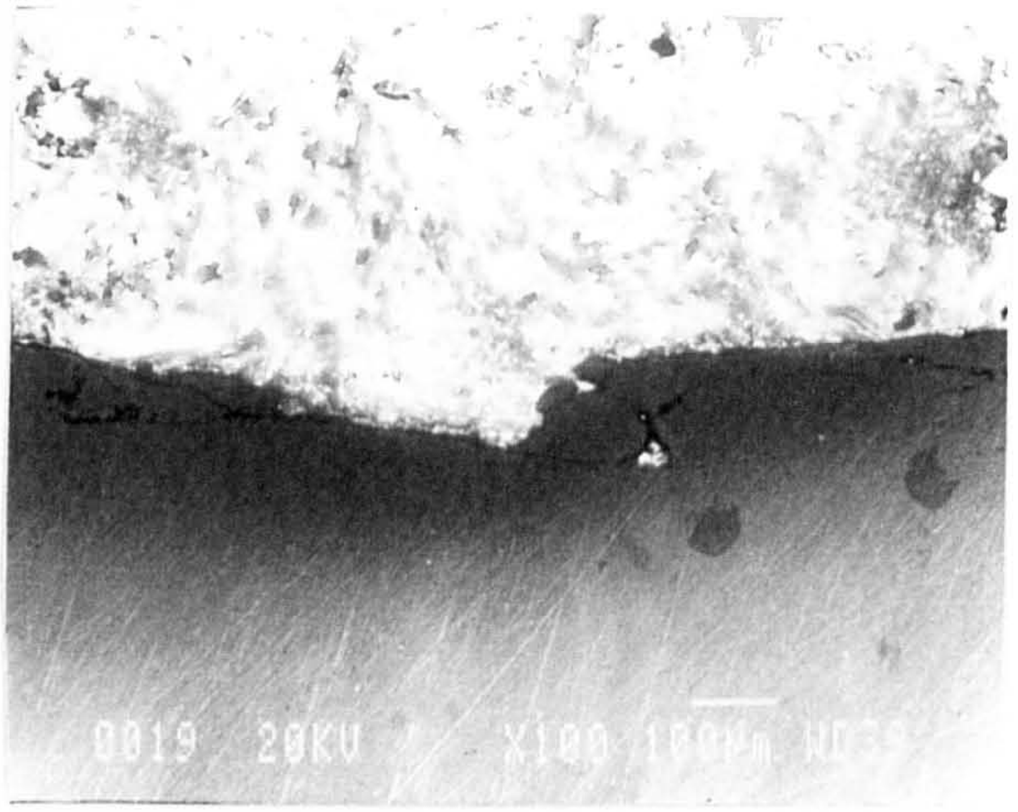

(d) wear track cross section (SEI)

Figure 5.3.4, Surface observations of the rolling elements HVMS11 & HVMS14

5.3.5 Debris analysis

Figure 5.3.5 shows the debris collected from the test lubricant (Hitec-174) used for the RCF test HVMS3. Figure 5.3.5(b) shows the delaminated surface of the debris. Numerous cracks were seen on delaminated side of coating debris. The thickness of these debris was in the range of 30 ~ 40 μm as shown in figure 5.3.5(b). Figure 5.3.5(c) shows the SEM surface observations of failed coating debris particle for a 150 μm thick coated rolling element tested in Exxon-2389 lubricant (HVMS4), at an inclined angle and gives an appreciation of its thickness. This debris size was rare in the test lubricants. In general, the debris for 150 μm and 50 μm thick coatings collected from different test lubricants were similar to the debris shown in figure 5.3.5(b). The debris for the tests conducted with 20 μm thick coatings were much smaller in size and in the form of powder having dimensions of a few micrometre.

Surface observations of the planetary balls after the RCF tests indicate that WC debris were present on the surface of the rolling element balls. Figure 5.3.5(d) shows a typical result which shows debris (BEI) on the surface of the steel planetary balls tested in the lubricant ($BF+H_2O$). This behaviour was commonly seen in the tests conducted with lubricant ($BF+H_2O$). A rare occurrence of embedded WC

debris particles on the steel lower balls was also seen for the tests conducted in lubricant Hitec-174 and Exxon-2389. No debris were seen on the surface of ceramic balls.

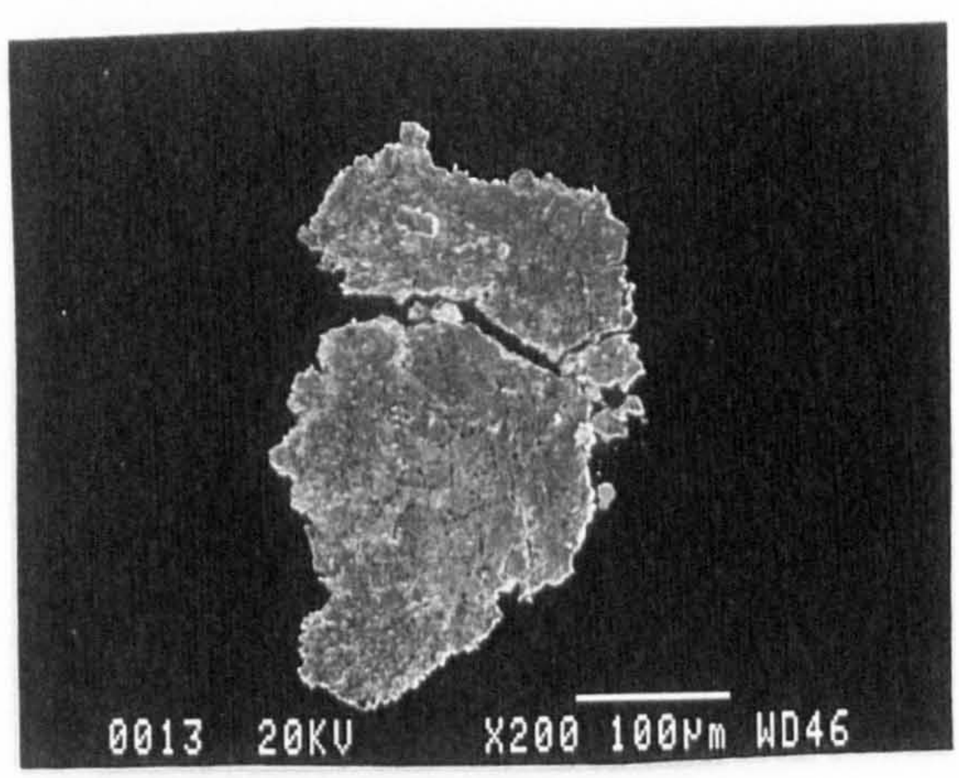

(a) delaminated surface (SEI)

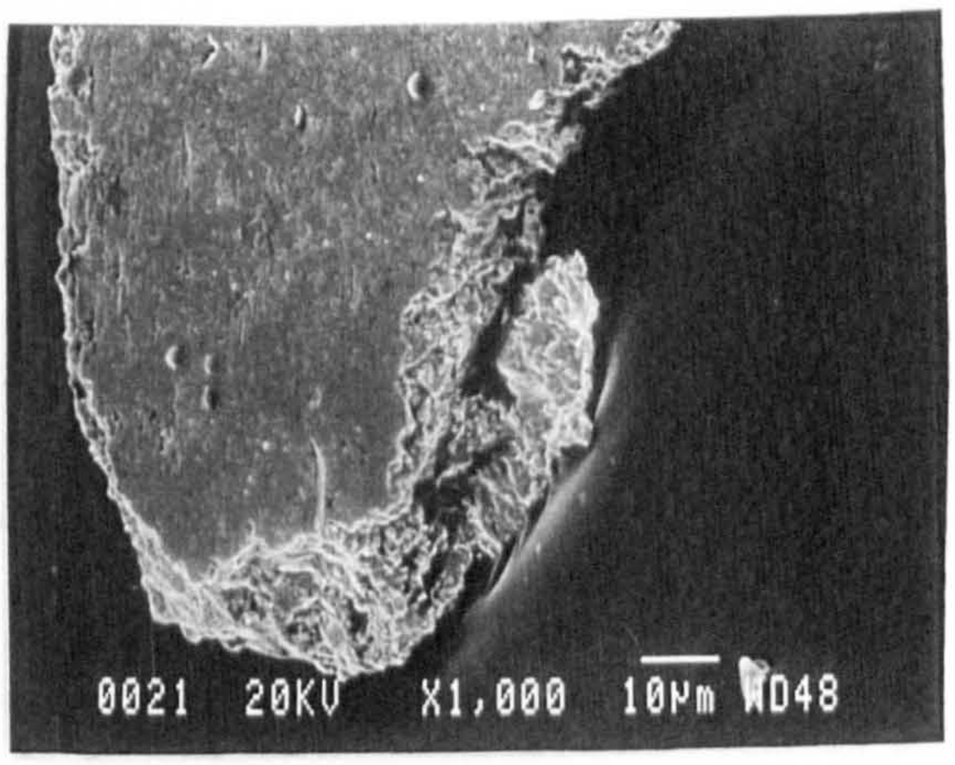

(d) inclined view (SEI)

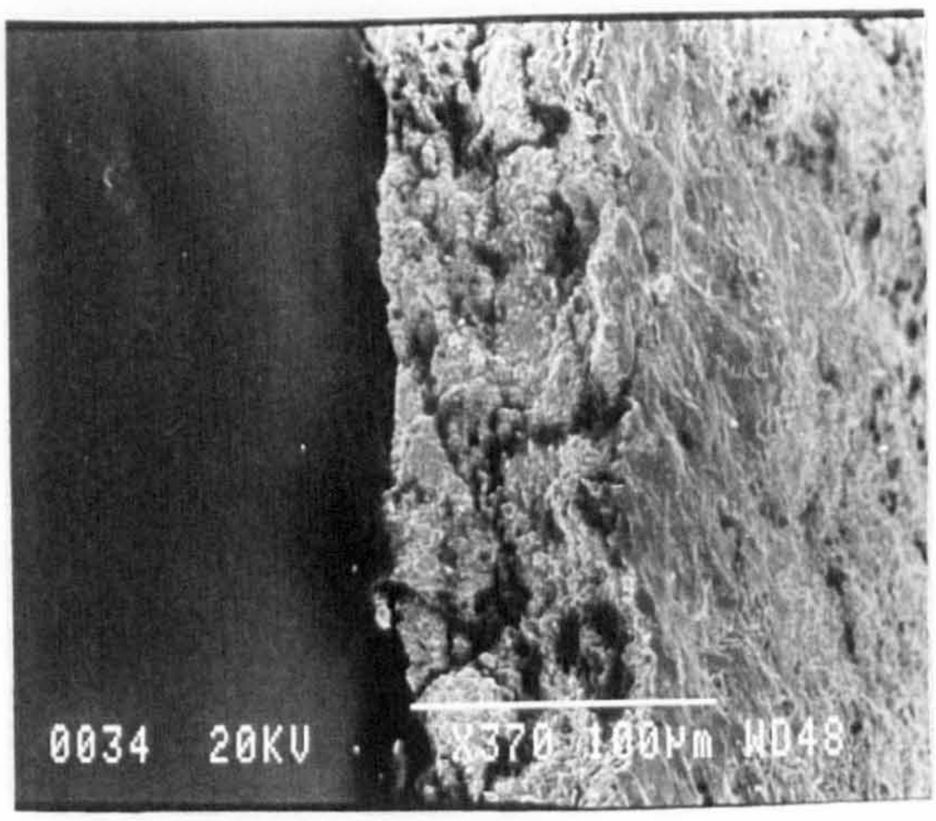

(c) inclined view (SEI)

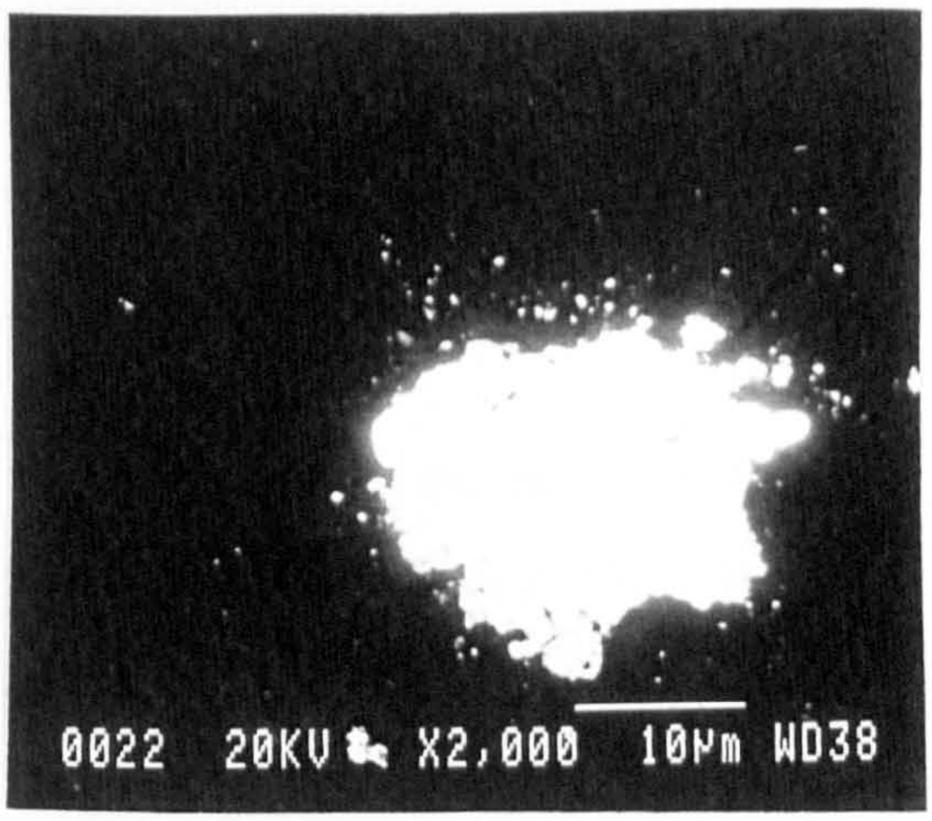

(d) debris on the steel ball

Figure 5.3.5, Debris

5.3.6 Coating microstructure

Figure 5.3.6 shows a typical microstructure of the coating cross section. The Secondary Electron Image (SEI) is shown in Figure 5.3.6(a) whereas Figure 5.3.6(b) shows the Back Scattered Electron Image (BEI). The comparison of the two images shows that the amount of retained WC particles was high which is typical of the HVOF process. The X-ray diffraction analysis of the microstructure confirmed that the amount of retained WC particles was high with small quantities

of W_2C particles. This is consistent with the work done by Harvey et. al. (1995), and is indicative of the high wear resistance of the coatings. The secondary phase particles were not common in the coating microstructure, however, numerous pores and microcracks were evident in the coating microstructure.

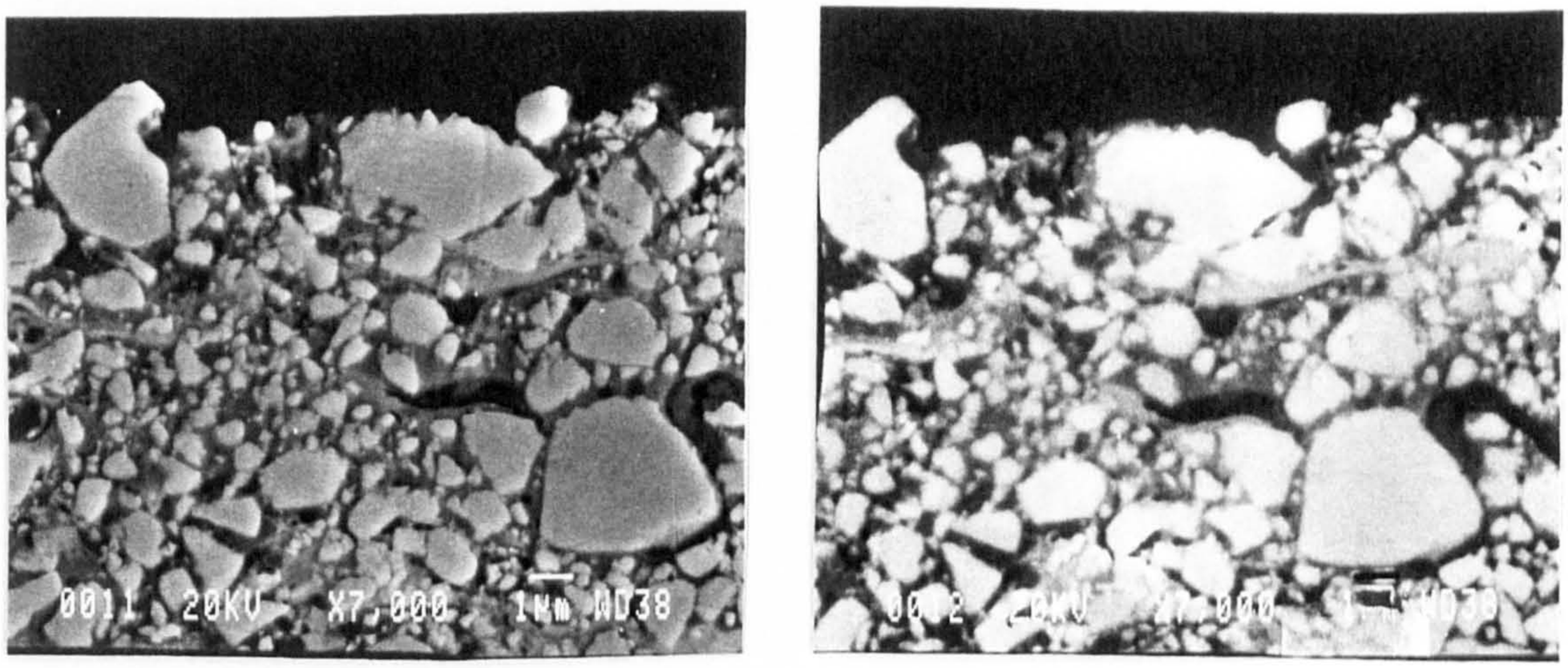

(a) coating microstructure (SEI) (b) coating microstructure (BEI)

Figure 5.3.6, Coating microstructure

5.3.7 Microhardness measurements

A Knoop and scratch hardness tester was used to measure the microhardness of thermal spray coatings. These results indicated that the microhardness of these coatings varies from 1097 Hv_{300} to 1390 Hv_{300} with an average value of 1318 Hv. The studies of the steel substrate microhardness indicate an average value of 218 Hv_{100}. Studies were also made to investigate any difference in the values of microhardness on the coating surface and through the coating cross section, due to the lamellar structure and anisotropy. The results indicate that the average surface microhardness of these coatings was approximately the same as the through thickness microhardness at an indentation load of 300p. During these measurements it was found that the coating can crack at certain locations at low indentation load of 100p whereas at other sections the coating does not crack even at a higher indentation load of 300p. This behaviour was evident on the surface as well as through thickness measurements. A typical result is shown in Figure 5.3.7(a) in which the crack propagated at a load of 100p. There was no definite trend in this

anisotropic behaviour of the coating and it was appreciated that the fracture toughness of the lamella structure of the coating was different within the microstructure.

The weakness in the coating microstructure was also seen in a simple compression test in the four ball machine. The coated rolling element cone was loaded at a Hertz contact stress of approximately 6 GPa in a clean, dry contact with the stationary planetary steel balls of the four ball machine. The load was removed and it was observed that the surface of the rolling element cone peeled as shown in Figure 5.3.7 (b). The coating particles adhered to the ball surface. This shows that the deformation resistance of the coating substrate combination was low. Moreover, the cohesive strength between the lamellas is low and the coating is prone to peeling in the absence of shear force. This can indicate the weakness and brittleness of the coating microstructure. The cracks can also be seen on the edge of the contact area due to the tensile stress.

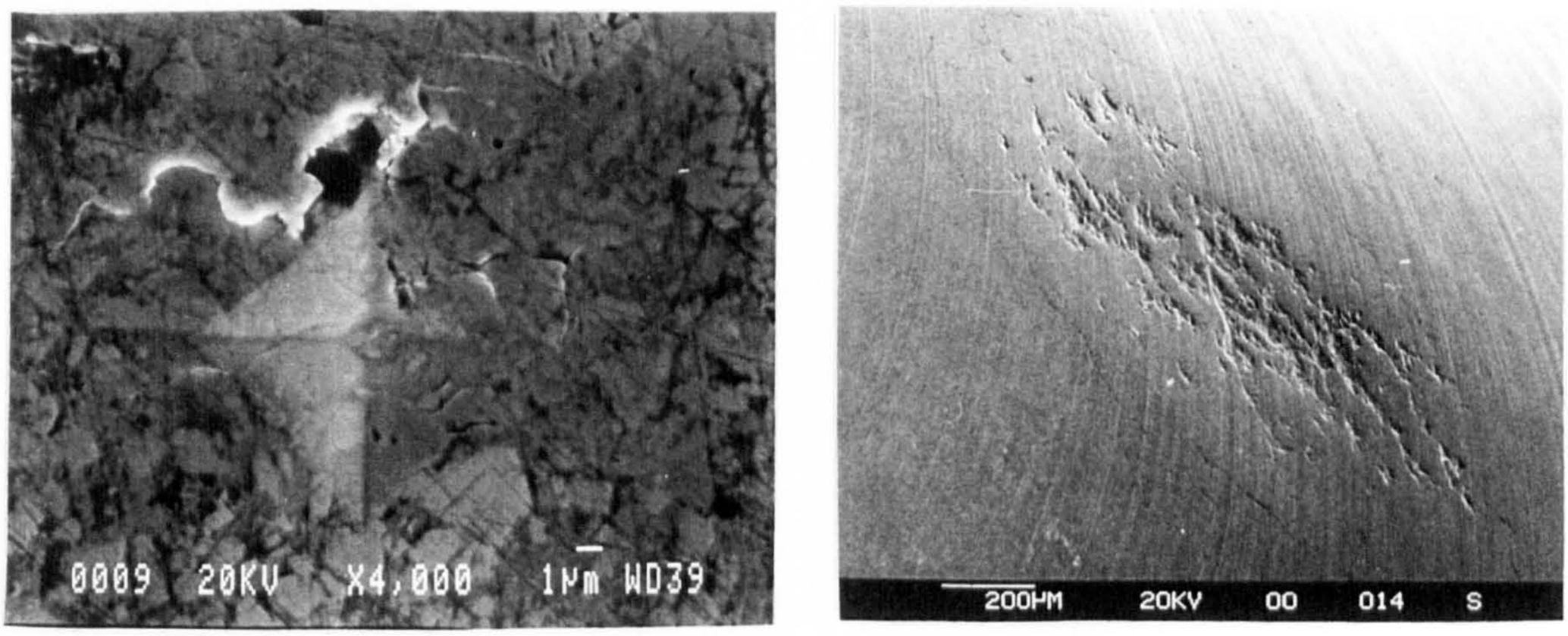

(a) indentation (100p) (b) coating peeling

Figure 5.3.7, Microhardness indentations

5.3.8 Residual stress measurements

Figure 5.3.8 represents the orientation and location of some measurements made on HVOF coated cones. The numerical values of stress relating to these individual measurement points in three different directions can be appreciated from table 5.4.

Figure 5.3.8(a), represents the stress measurement point for a 200 μm thick coated cone in as-sprayed condition. Measurement point 9 is approximately at the location at which the wear track will be formed during the RCF test. Measurement point 10 in figure 5.3.8(b) represents the same for a 100 μm thick coated cone, whereas figure 5.3.8(c) represents the measurement point 11 on a flat plate in as-sprayed conditions.

Residual stress measurement point 12 on a cone subjected to test HVMS4 can be appreciated from figure 5.3.8(d). This point is some distance from the wear track and located towards the cone apex, whereas measurement point 13 is at the edge of the wear track. Measurement point 14 is in the middle of the wear track within the failed area. Stress measurement points for the cone subjected to test HVMS8 can be seen from figure 5.3.8(e). These measurements are made away from the wear track, and in the middle of the failed area. The SEM observations at the residual stress measurement points after the RCF tests HVMS4 and HVMS8 can be appreciated from figures 5.3.1 and 5.3.2 respectively.

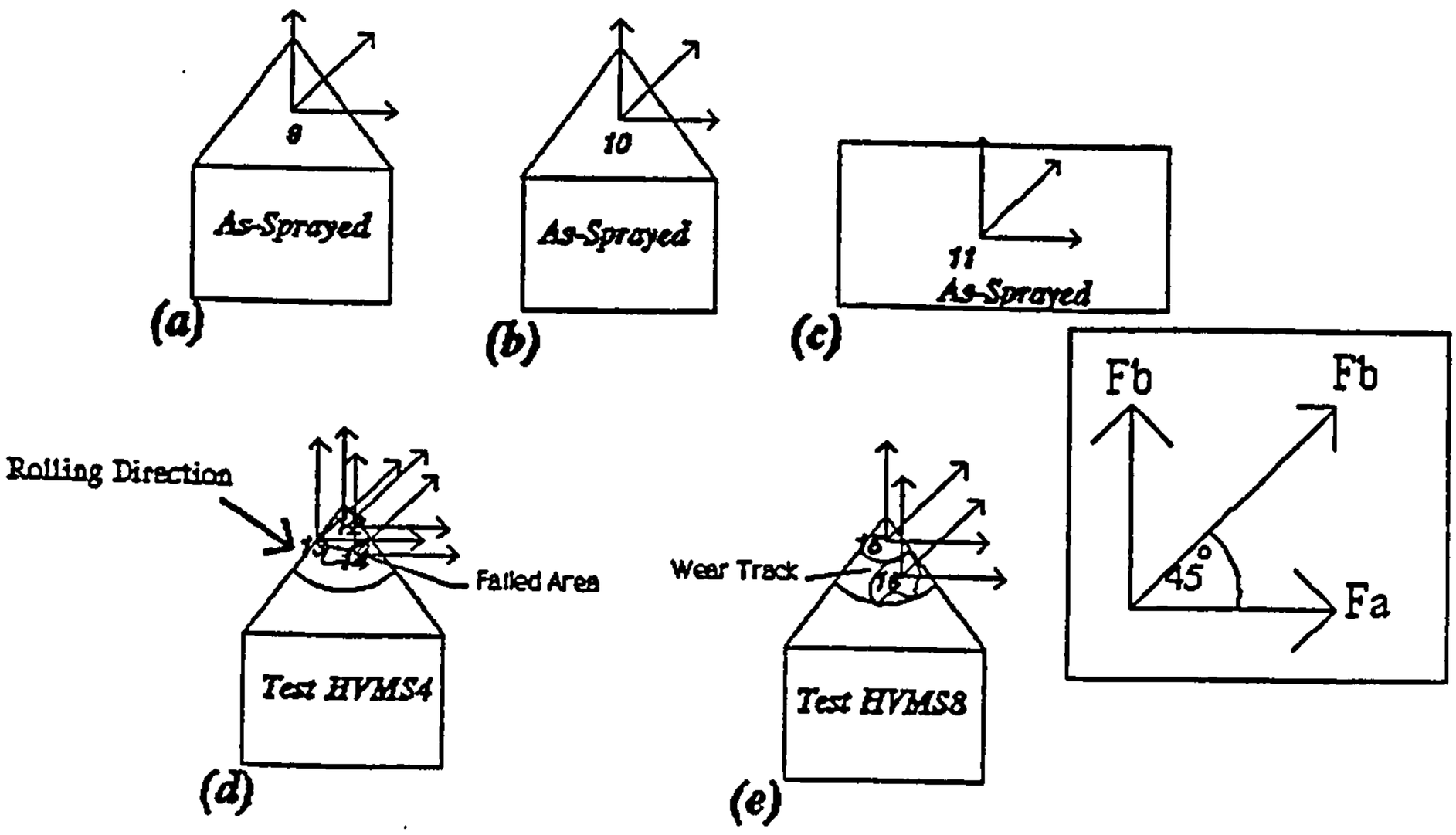

Figure 5.3.8, Residual stress measurement points on HVOF coated cones

Point No:	Test	Collimator Size (mm)	Time (min)	Residual Stress Values (MPa)		
				Fa (0 deg)	Fb (45 deg)	Fc (90 deg)
9	Sprayed	0.3	167	+75 ± 38	-72 ± 110	+232 ± 44
10	Sprayed	0.5	167	+12 ± 31	+62 ± 24	+127 ± 50
11	Sprayed	1	33	+148 ± 62	+37 ± 56	+148 ± 62
12	HVMS4	0.5	133	-216 ± 35	-244 ± 30	-246 ± 28
13	HVMS4	0.5	133	-436 ± 33	-308 ± 50	-369 ± 20
14	HVMS4	0.5	167	-43 ± 21	-52 ± 4	-453 ± 94
15	HVMS8	0.3	133	-237 ± 41	-385 ± 48	-288 ± 33
16	HVMS8	0.3	167	-123 ± 90	-101 ± 89	-151 ± 82

* Value not available

Table 5.4, Residual stress measurement results of HVOF coatings

5.4 High Velocity Oxy-Fuel Coated Balls on M-50 Steel Substrate

5.4.1 Introduction

In this section WC-Co coatings produced by the HVOF process are deposited on the surface of M-50 steel rolling element balls and studied for their fatigue performance in rolling contact. The main purpose of this study was to investigate the affects of a hard substrate material and the affects of maintaining the substrate hardness by keeping the substrate temperature low during the thermal spraying process on the RCF performance of WC-Co coatings.

5.4.2 Coated ball test elements

Thermally sprayed tungsten carbide cobalt (WC-12%Co) coatings produced by the HVOF process were deposited on the surface of the M-50 steel rolling element balls. The spray system was JP5000 having fuel (kerosene) supply pressure of 1.24 MPa and Oxygen supply pressure of 1.38 MPa (manufacturers data). The particle size of the coating powder was in the range of 53 ~ 10 μm (manufacturers data). The coating material was selected because of its high wear resistance, whereas the selection of the substrate material was based upon its ability to retain its hardness at moderate coating temperatures caused by the heat generated during the thermal spraying process. Extreme care was taken to avoid any softening of the substrate M-50 steel balls during the spraying process and the preheat temperature was kept very low to below 50°C (manufacturers data). This is consistent with the studies of sputtered Diamond Like Carbon (DLC) coatings by Sproul et. al. (1993). The substrate material was sand blasted prior to the coating process to improve the adhesive strength by creating increased bonding contact area and provide the mechanical interlock between the substrate material and the overlay coating.

The rolling elements were sprayed in a direction perpendicular to the contact area by rotating the balls during the HVOF process. Figure 5.4.1 shows the schematic of the spraying arrangement used to spray the samples perpendicular to the direction of rolling. The rotational speed of the rotating disk was kept low to allow sufficient time for heat dissipation by convection to the atmosphere thereby reducing the affect of the softening of the substrate material. Only half of the ball was coated as

required for the RCF tests. The average as-sprayed thickness of the rolling element balls were 150 μm. The rolling elements were ground and polished to give an average coating thickness of 110μm. The RMS surface roughness (R_q) of the coated rolling elements in the as-sprayed conditions, after grinding and after polishing was measured to be $6\pm1.5\mu m(R_q)$, $1.5\pm0.5\mu m(R_q)$ and $0.125\pm0.025\mu m(R_q)$.

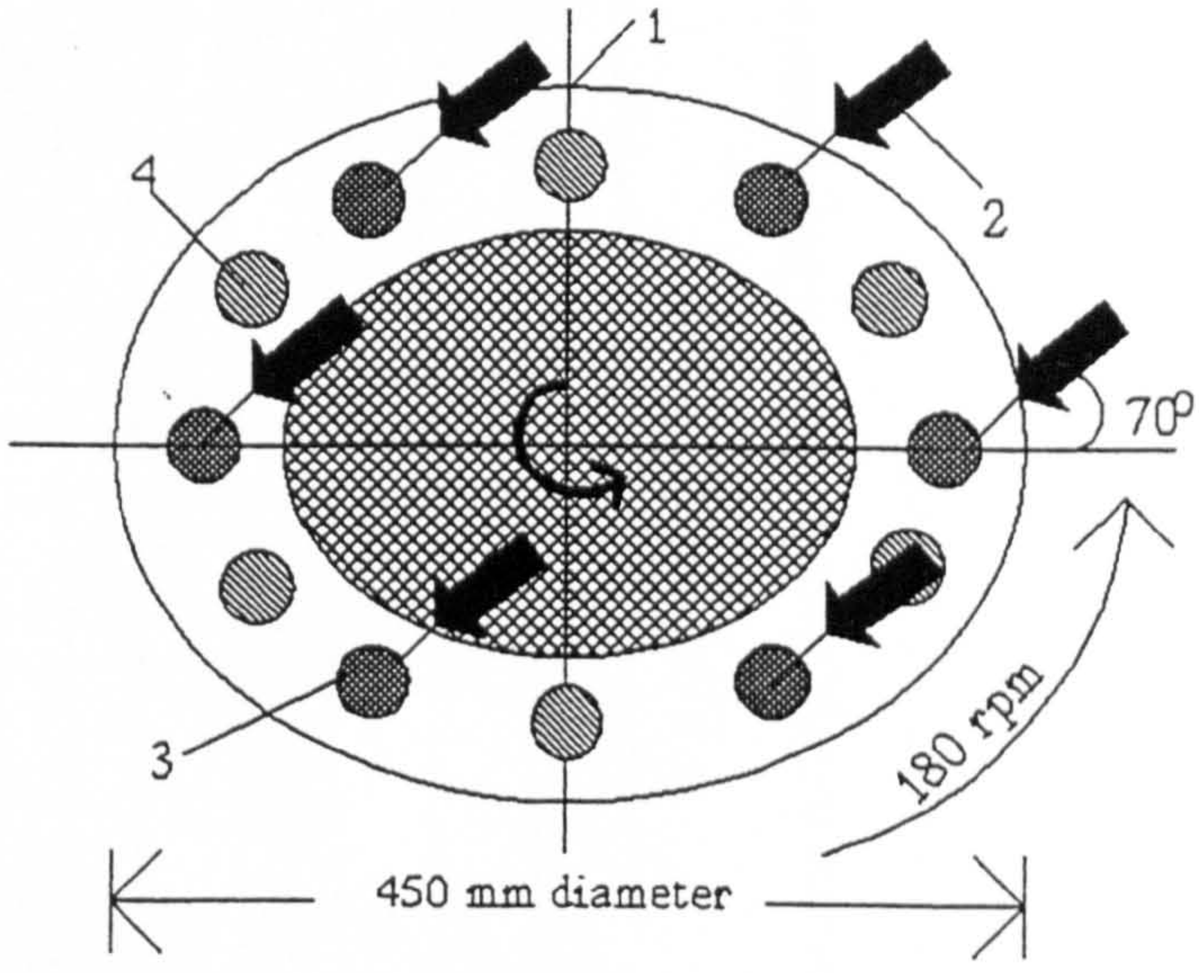

Figure 5.4.1, Schematic of the spraying arrangement
(1; Rotating plate, 2; Spraying direction, 3; Sample, 4; Sample holder)

5.4.3 Test conditions and experimental test results

The test lubricant used during this study was B.P. Hitec-174. Tests were conducted at an ambient temperature of approximately 23 °C and at a shaft speed of 4000 ± 5 rpm. The cup assembly was loaded at three different loads of 40 N, 160 N and 240 N respectively. The ratio (λ) of the approximate value of the Elasto-Hydrodynamic Lubrication (EHL) film thickness to the average surface roughness for the test lubricant under the above mentioned contact loading conditions was calculated to be $\lambda>4.0$, $\lambda>3.5$ and $\lambda>3.0$ respectively. The lower planetary balls were of bearing steel (SKF) and silicon nitride ceramic (NORTON). The experimental test procedures described in chapter 2 (article 2.3) were followed. Experimental measurement of the gross sliding in the four ball system by measuring the orbital speed of the planetary balls and, the frictional torque in the cup assembly using the techniques are described in article 2.5 and 2.6 respectively.

Test No	Contact load (N)	Lower balls	Contact stress* (GPa)	Contact width (mm) (a)	Depth of max: shear (0.5a) (μm)	Maximum lubricant temperature (°C)	Sliding (%)	Frictional Torque (N.m)	No: of stress cycles (10^6)	Time to Failure (minutes)
T1	240	steel	3.9	0.171	85	42	+1.9	0.06	3.654	406
T2	240	ceramic	4.4	0.161	80	24	+2.3	0.05	0.063	7
T3	160	steel	3.4	0.149	75	22	Ω	0.03	0.036	4
T4	160	ceramic	3.8	0.140	70	42	Ω	0.02	1.422	158
T5	40	steel	2.1	0.094	47	33	+3.6	0.05	52.38	5820**
T6	40	ceramic	2.4	0.088	44	30	+3.2	0.01	52.38	5820**

* UNCOATED CASE, ** Suspended test, Ω Value not available

Table 5.5, Rolling contact fatigue test results for HVOF coated rolling element balls on M-50 steel substrate

Table 5.5, shows the RCF test results for the HVOF coated rolling element balls under the various tribological conditions of testing. Results are presented in terms of the test configuration, Hertz contact stress, average frictional torque, gross sliding and the time to failure. The magnitude of contact stress values shown in table 5.5 represent the case of uncoated rolling elements, since the case of coating substrate combination cannot be readily applied in the Hertzian contact analysis. The RCF test results give an appreciation of the performance of the coated elements and are not intended to be used as a basis for the statistical fatigue life prediction.

5.4.4 Surface observations

Figure 5.4.2 shows the surface observations of the failed coated rolling element subjected to the test conditions described for the test. Figure 5.4.2(a) shows the overall view of the wear track and the failed coating area in BEI. The figure indicates that the coating failure was at the coating substrate interface as indicated by the atomic contrast image. The coating delamination at the interface was also confirmed by an electron probe microscopy analyzer (EPMA). Figure 5.4.2(b) shows the surface observation of the leading edge of the failed coating area. It can be seen that the failure starts from within the contact region and extends to greater lengths away from the wear track. Figure 5.4.2(c) shows the failed coating area at an inclined angle. Figure 5.4.2(d) shows the cliff edge of the failed area at higher magnification and many cracks can be seen on the surface of the rolling elements. The depth of failure was approximately 110μm. Figure 5.4.3 shows the surface observations of the failed coated rolling element subjected to the test conditions described for the test T3. Figure 5.4.3(a) shows the BEI of the overall view of the failed coating area. The coating failure can be observed to occur at the coating substrate interface which is consistent with the failure observed in the Figure 5.4.2(a). Figure 5.4.3(b) shows the surface observation of the leading edge of failed coating area and figure 5.4.3(c) shows the failed coating area at the trailing edge of the contact zone. Finally figure 5.4.3(d) shows the surface observation of the wear track and many cracks can be seen propagating from within the wear track and extending to greater lengths away from the contact zone.

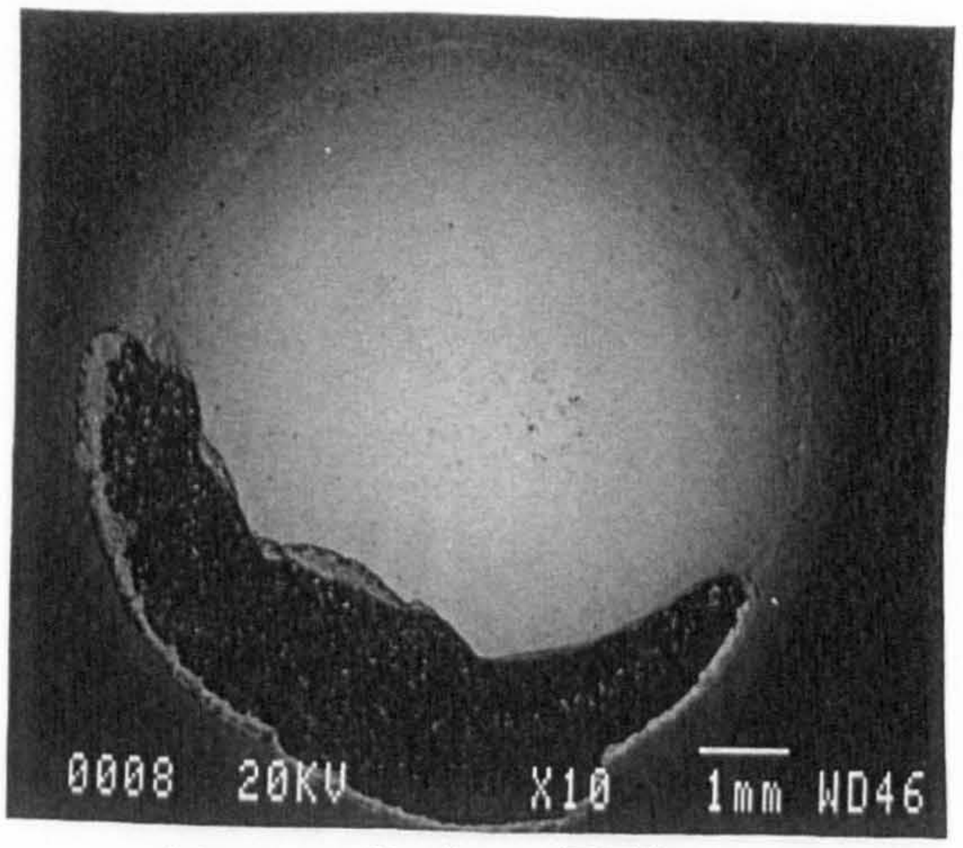

(a) overall view (BEI)

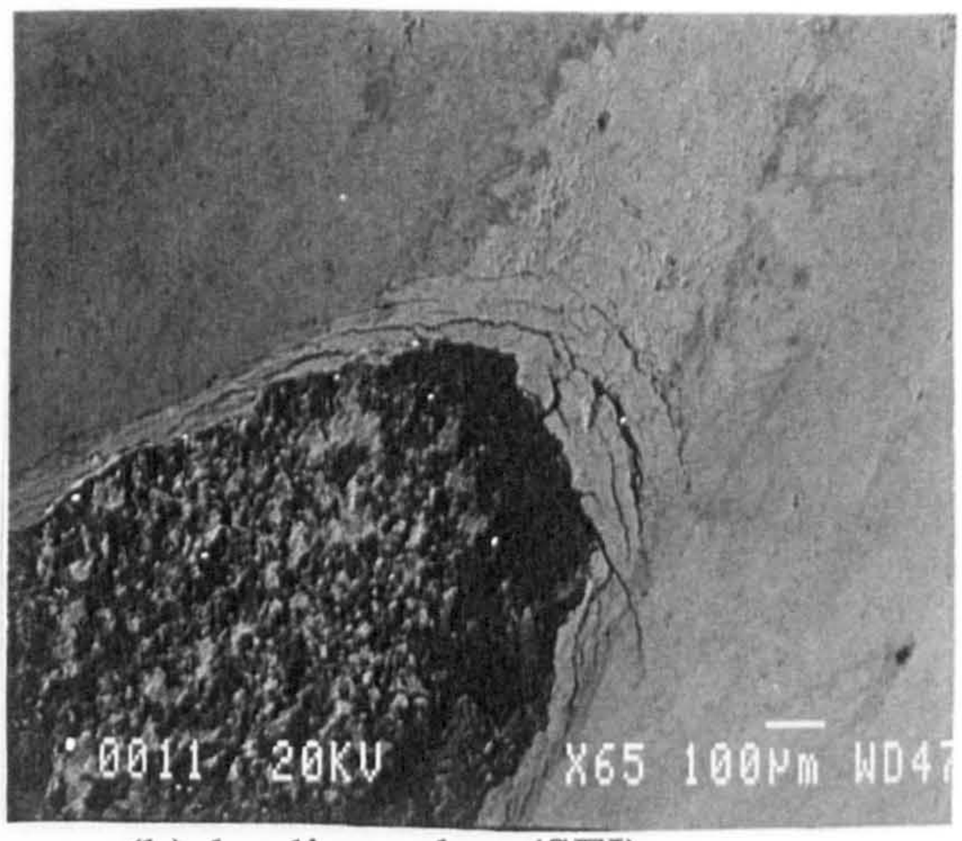

(b) leading edge (SEI)

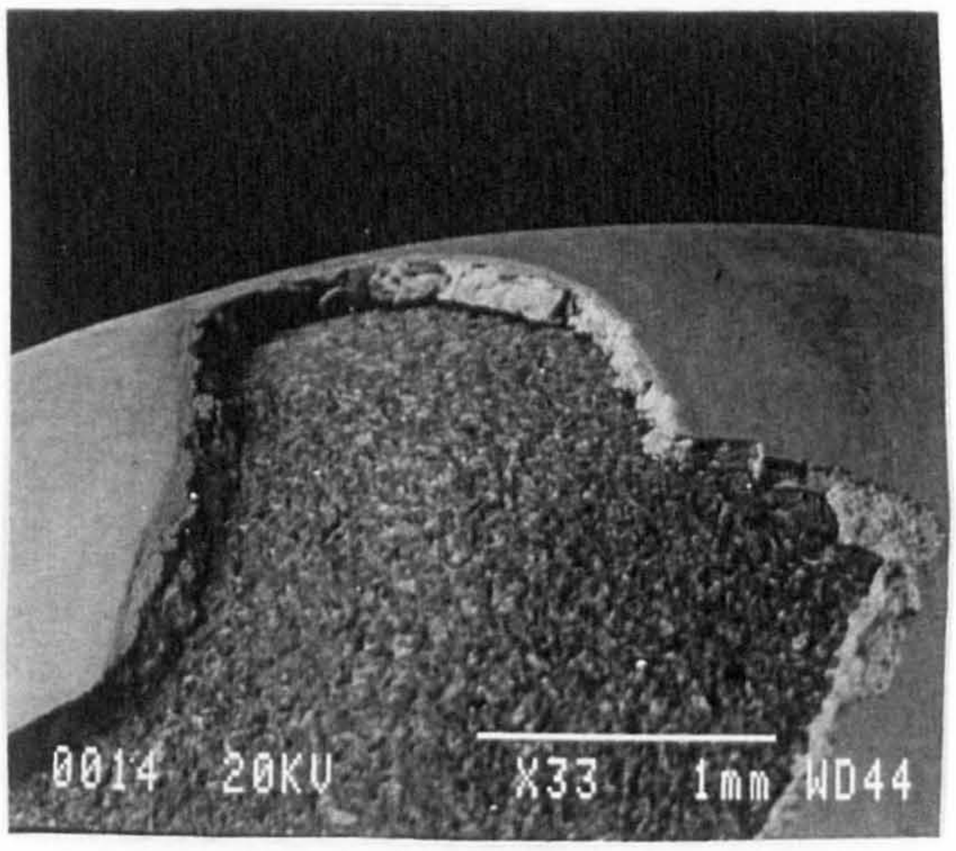

(c) inclined angle view (SEI)

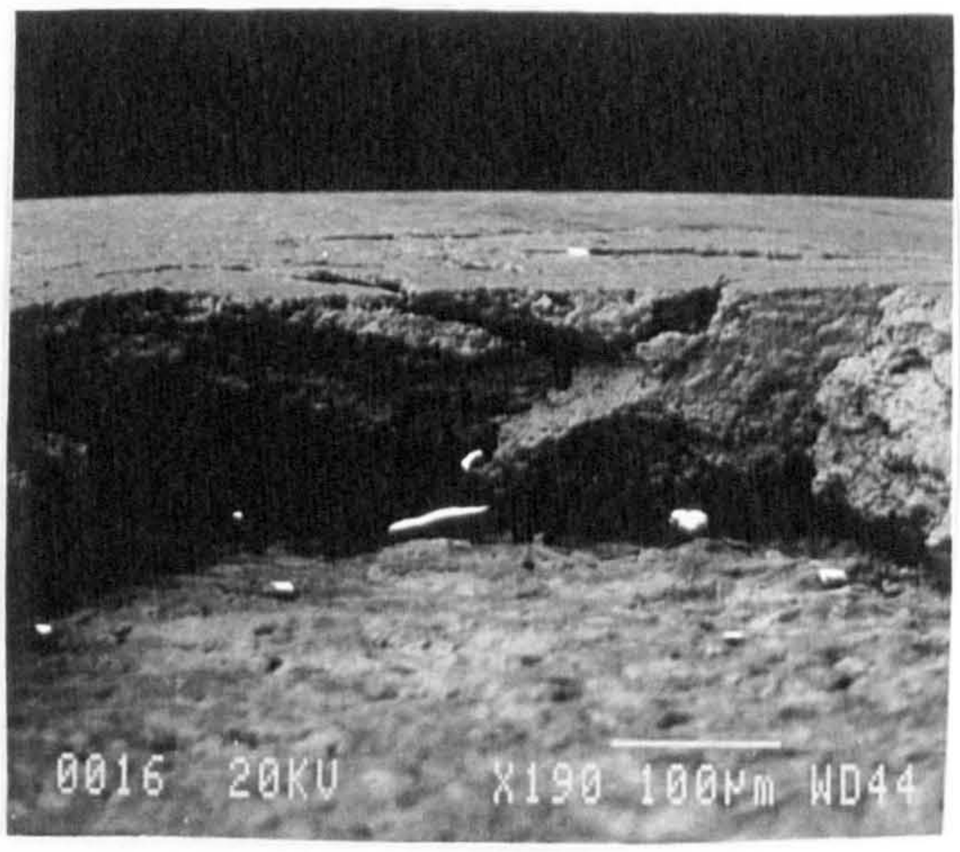

(d) cliff edge (SEI)

Figure 5.4.2, Surface observations of the rolling element ball (Test T2)

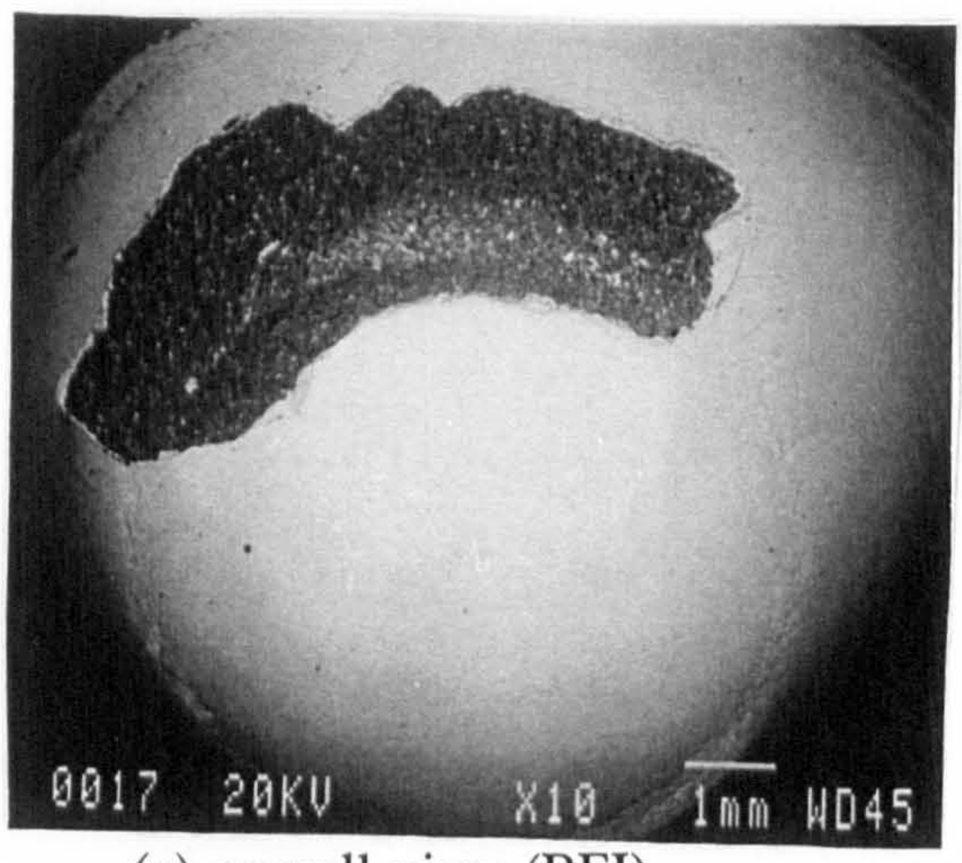

(a) overall view (BEI)

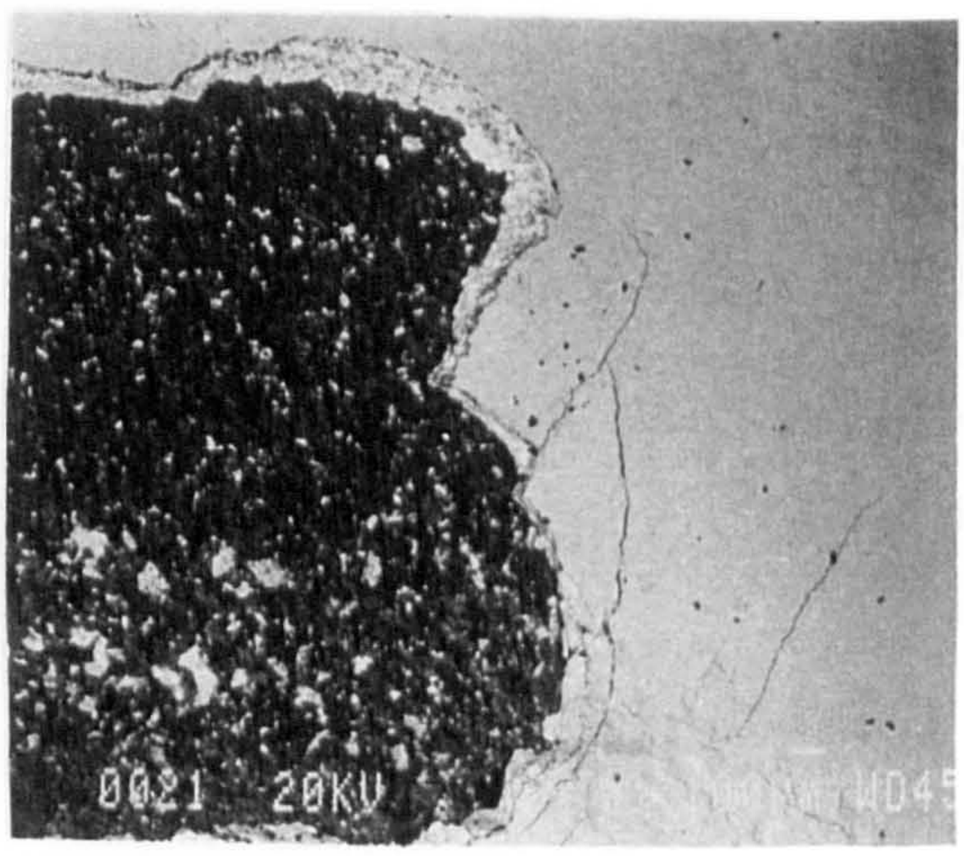

(b) leading edge (SEI)

Figure 5.4.3, Surface observations of the rolling element ball (Test T3)

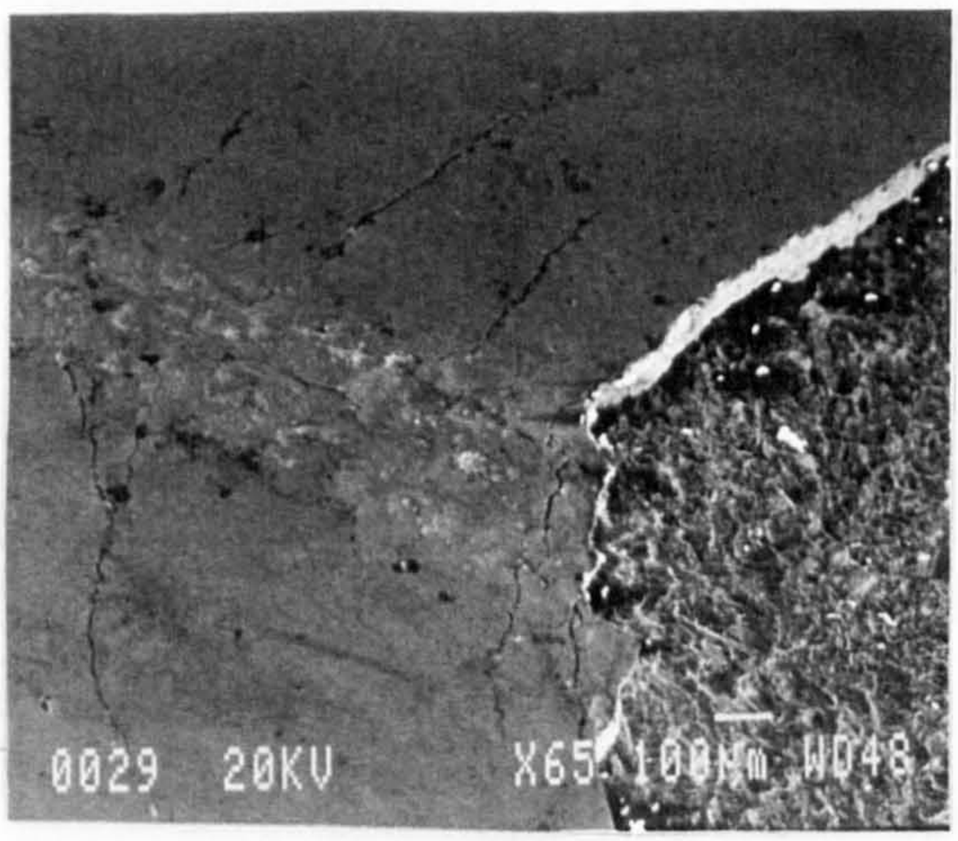

(c) trailing edge (SEI)

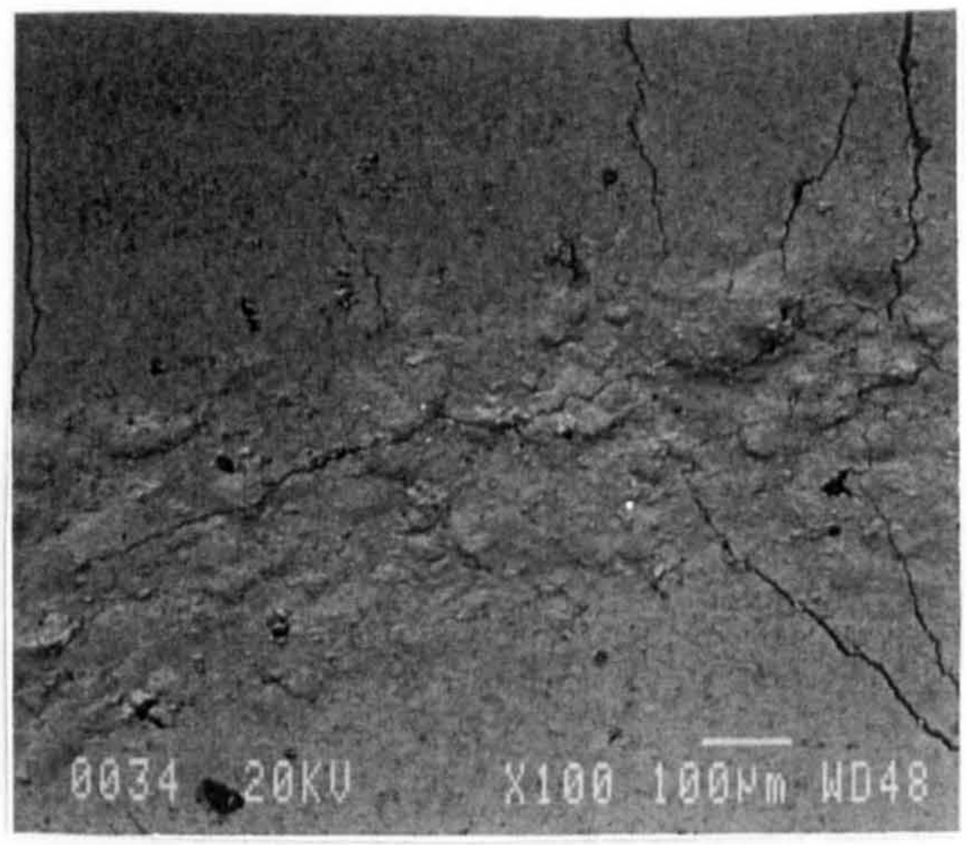

(d) wear track (SEI)

Figure 5.4.3, Surface observations of the rolling element ball (Test T3, continued)

Figure 5.4.4 shows the surface observations of the coated rolling element subjected to the test conditions described for the test T4. The RCF test in this case was suspended after 97 hours without any coating delamination. Figure 5.4.4(a) shows the overall view of the wear track in the BEI. Figure 5.4.4(b) shows the surface observation of the wear track at a higher magnification.

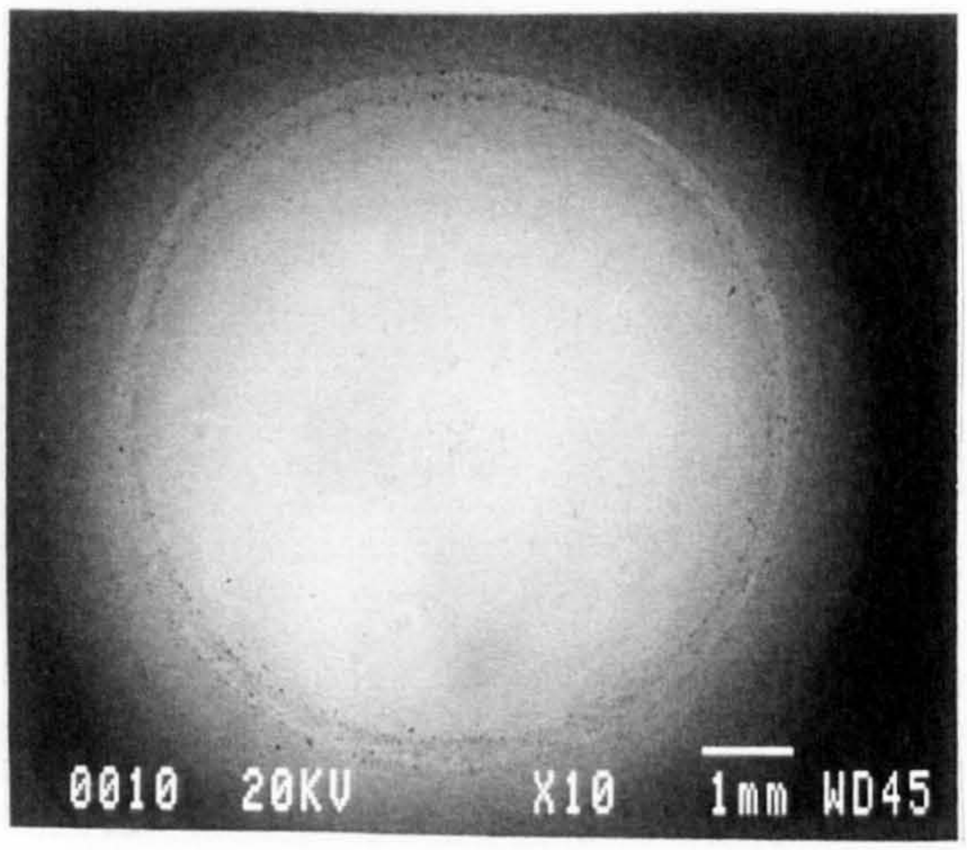

(a) overall view (BEI)

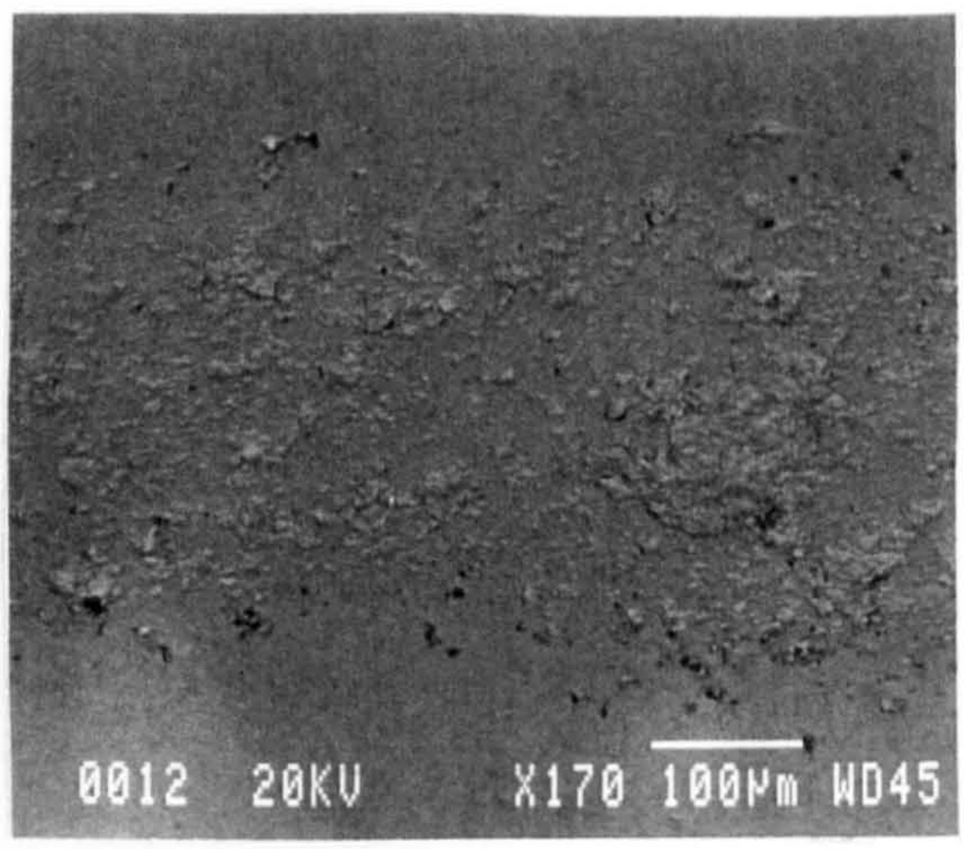

(b) wear track (BEI)

Figure 5.4.4, Surface observations of the rolling element ball (Test T4)

5.4.5 Debris analysis

The test lubricant used for the RCF tests was also analyzed for the delaminated wear debris particles. These particles were in the form of sheets of the coating material

having thickness similar to the thickness of the coating. Figure 5.4.5 shows the surface observations of a typical debris particle filtered from the test lubricant used for the test T2. Figure 5.4.5(a) shows the top surface of the debris particle whereas figure 5.4.5(b) shows the delaminated surface. The lower planetary balls were also analyzed for any debris particles adhered to their surface during the RCF test. However, no such behaviour was observed on the surface of the rolling elements.

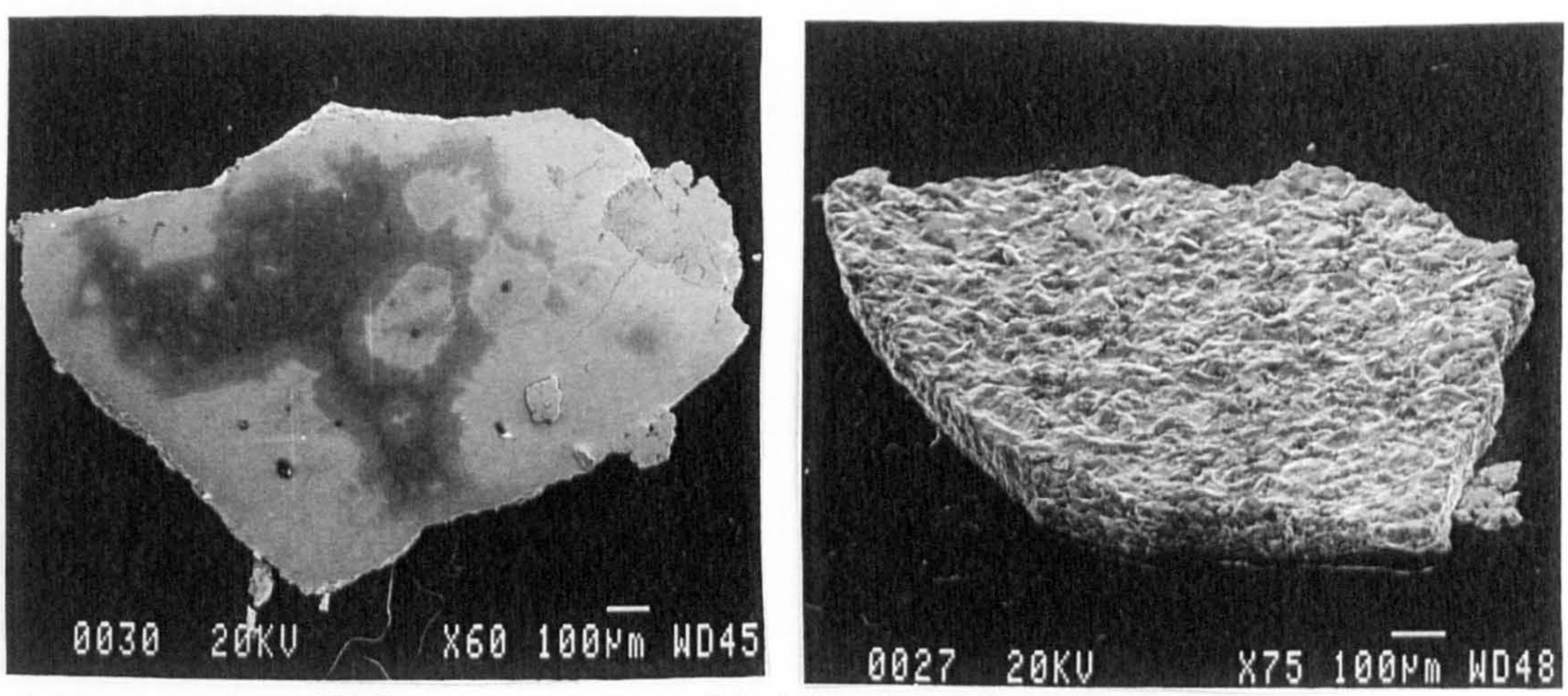

(a) top surface (SEI) (b) delaminated surface (SEI)

Figure 5.4.5, Surface observations of the debris (Test T2)

5.4.6 Coating microstructure

Figure 5.4.6 shows a typical microstructure of the coating cross section in SEM.

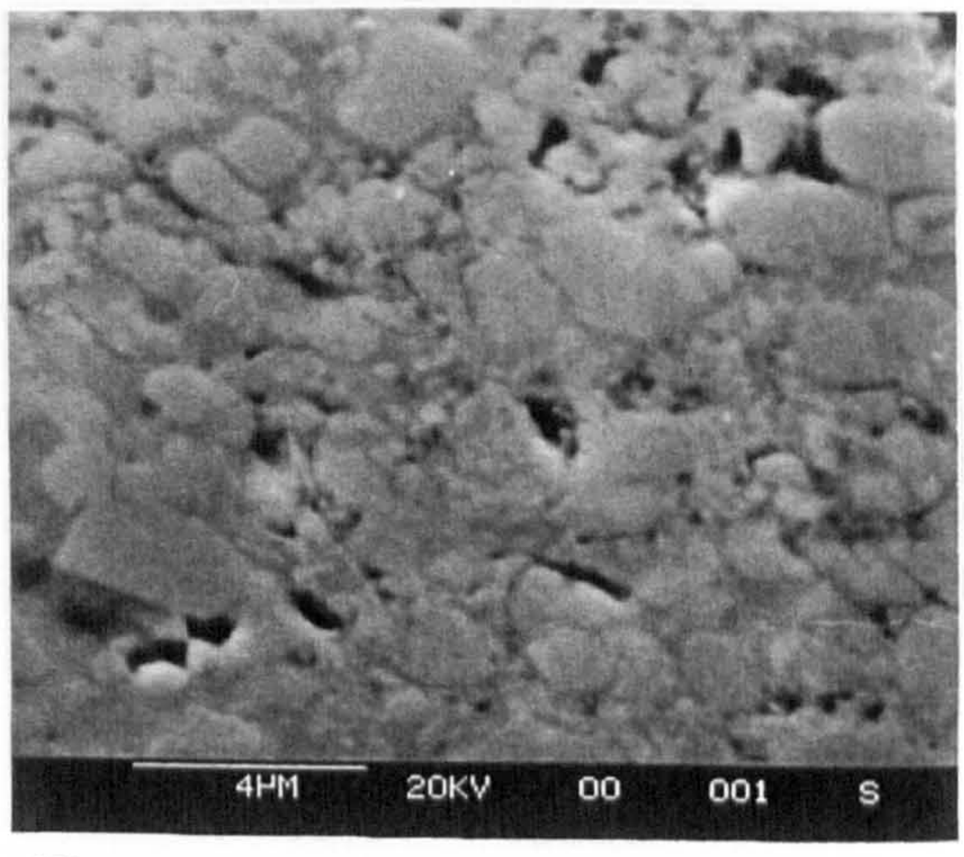

Figure 5.4.6, Coating microstructure

The size of retained WC particles vary from 1μm to 3μm. Numerous pores and

cracks are evident in the coating microstructure. The X-ray diffraction analysis of the microstructure confirmed that the amount of retained WC particles was high with small quantities of W_2C particles.This was verified by the atomic contrast in the BEI and using some X-Ray diffraction patterns.

5.4.7 Microhardness measurements

A Knoop and scratch hardness tester was used to measure the microhardness of thermally sprayed rolling element balls. The results indicate that the average microhardness of the coating material (HV_{300}) was 1390. The average microhardness of the substrate material (HV_{100}) was 803 at locations very near to the coating substrate interface on the coated side whereas on the uncoated side of the ball the average microhardness was measured to be 880. These values are averaged after neglecting the highest and the lowest values. It was appreciated that a slightly lower microhardness of the substrate material near the interface could be due to the softening of the balls by the heat generated during the thermal spraying process. However, these values are very close to the hardness of the lower steel rolling element ball, thereby indicating that the substrate material hardness was marginally affected by the spraying process.

The indentation fracture toughness (K_{1c}) and the critical strain energy release rate (G_c) of thermal spray coatings was also measured by using the following standard relations (Ostojic et. al. 1991) reproduced here for clarity:

$$K_{1c} = 0.025 \times E^{1/2} \times b \times P^{1/2} \times C^{-3/2} \quad \text{..... (5.4.1)}$$

$$G_c = 6.115 \times 10^{-4} \times b^2 \times P \times C^{-3} \quad \text{..... (5.4.2)}$$

where '2b' is the diagonal of the diamond indentation, 'C' is the crack length and P is the applied load. The value of the coatings Young's modulus (E) during the analysis was assumed to be 300 GPa. The indentation load was increased successively until the following crack length criteria was observed:

$$C > 2b \quad \ldots\ldots\ldots\ldots\ldots\ldots\ldots\ldots\ldots\ldots\ldots\ldots\ldots\ldots\ldots\ldots\ldots\ldots \quad (5.4.3)$$

Figure 5.4.7 shows a typical indentation at a load of 500p (4.9 N). The values of K_{1c} and G_c were calculated to be 1.8 $MNm^{-3/2}$ and 10.7 Jm^{-2}. It was interesting to note that these coatings have good homogeneity and cracks were only observed at the indentation loads greater than 300p (2.9 N).

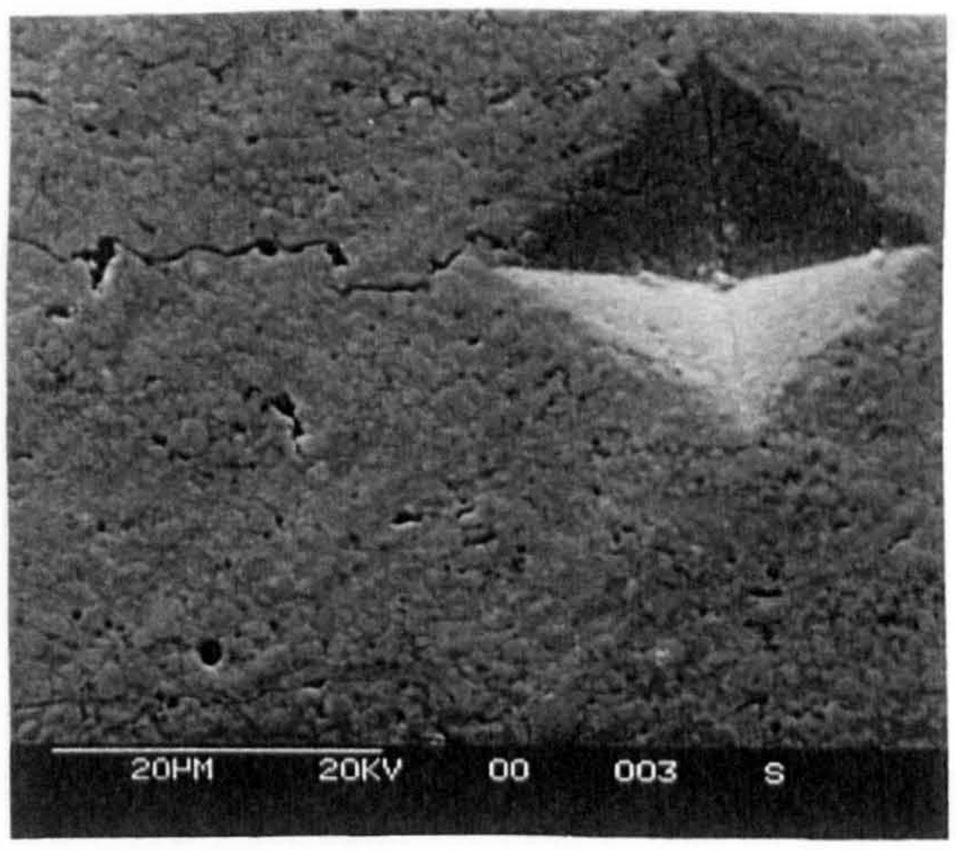

Figure 5.4.7, Microhardness indentation

5.4.8 Finite element modelling

An axisymmetric, frictionless, elastic finite element contact model described in chapter 3 (article 3.2) was developed to represent the case of a 110 μm thick coated upper ball contacting the lower steel ball of the modified four ball machine. The modulus ratio, which is defined as the ratio of the coatings Young's modulus to the substrate Young's modulus was varied to give four different coating types as indicated in chapter 3 (table 3.1). The thickness ratio (t/a) was kept constant to represent the case of a 110 μm thick coating subjected to a contact load of 400 N. Figure 5.4.8 shows the summary of the affect of these coating parameters on the different types of stresses. Figure 5.4.9 shows the maximum shear stress contours for the C2 coating type.

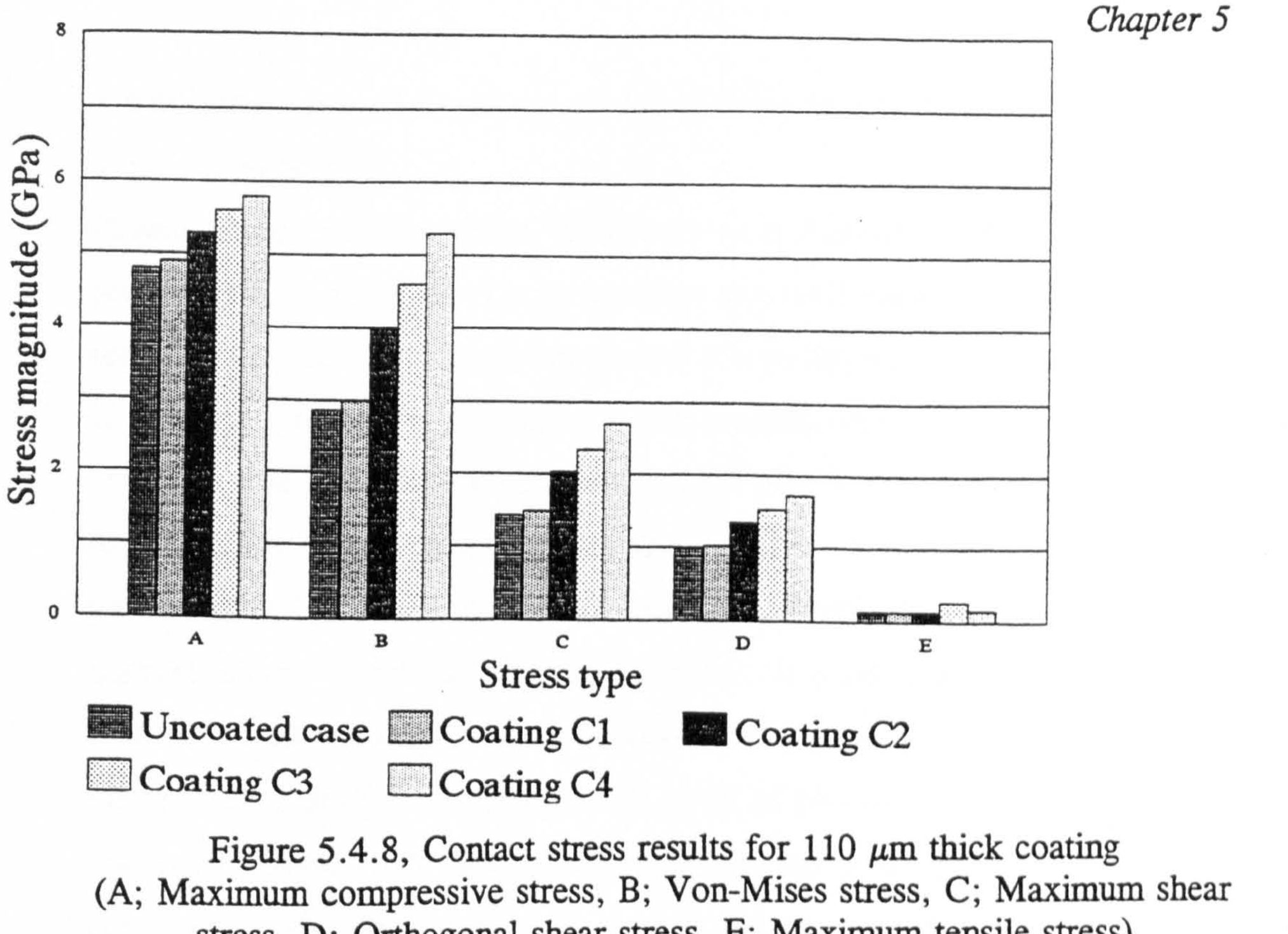

Figure 5.4.8, Contact stress results for 110 μm thick coating
(A; Maximum compressive stress, B; Von-Mises stress, C; Maximum shear stress, D; Orthogonal shear stress, E; Maximum tensile stress)

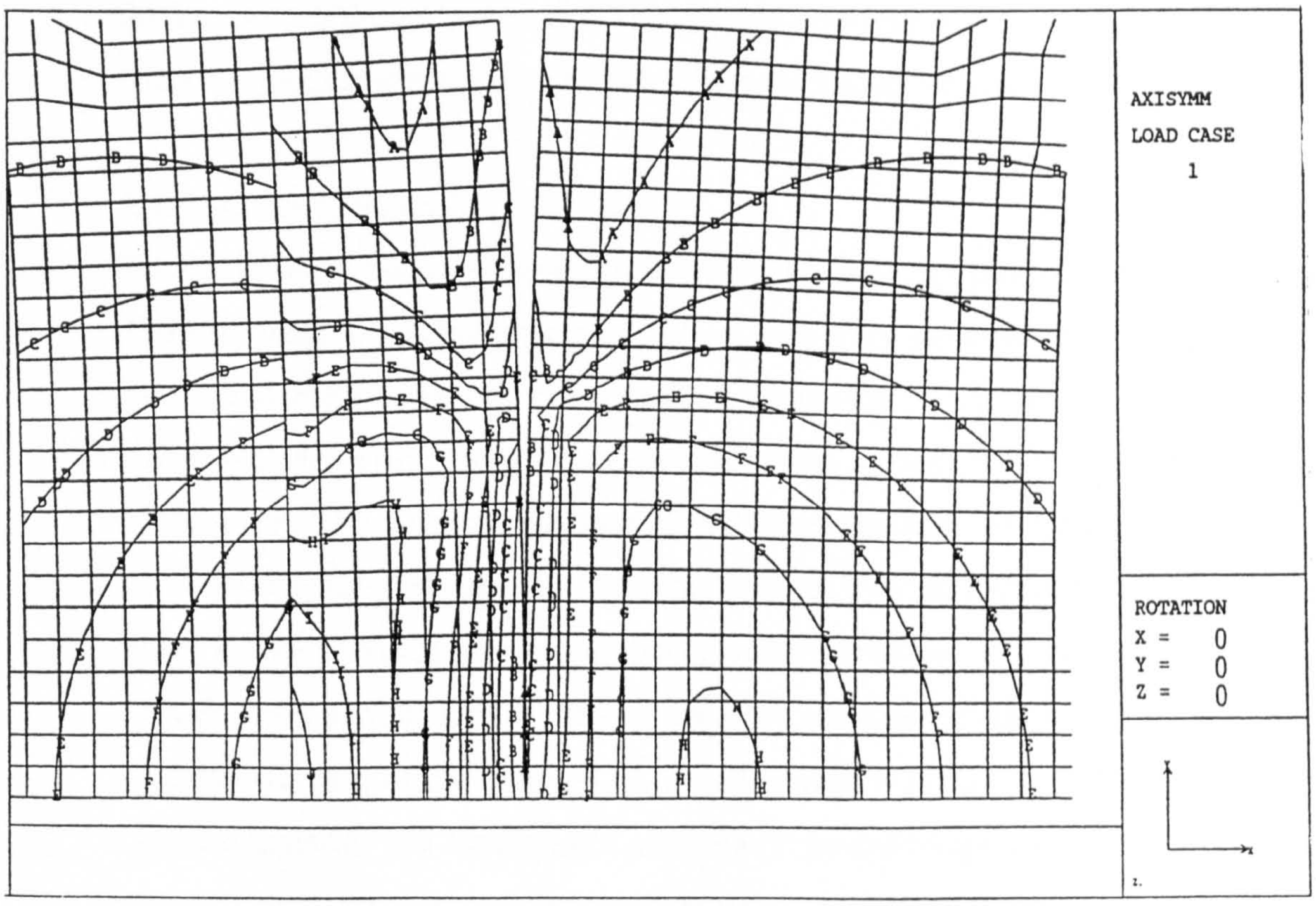

Figure 5.4.9, Maximum shear stress contours for C2 coating (GPa)
J=1.94, I=1.74, H=1.54, G=1.35, F=1.15, E=0.95, D=0.76, C=0.56, B=0.36, A=0.17

5.5 Plasma Sprayed Coatings on 440-C Steel Substrate Cones

5.5.1 Introduction

Plasma spray coatings utilize the energy in a thermally ionized gas to melt and propel powder particles. These coatings are well known for their high particle temperatures during the spraying process due to the plasma jet which can be useful in spraying materials having high melting temperatures, eg. ceramics, tungsten, etc. However, the particle speed in conventional plasma spraying ranges from 150 m/s to 400 m/s in comparison to approximately 900 m/s for D-Gun coatings. The low particle speed of the impacting lamella can result in a less dense and porous microstructure. Recent advancements in the air plasma spray coatings are geared towards a high velocity plasma spraying system. One of these advancements is the Gator-Gard system in which a particle speed of 1000 m/s has been achieved. These coatings (GG-WC-102) have shown improvements in combating sliding wear of the components like bushings, flap tracks, fan blade mid spans, etc. This study considers the rolling contact fatigue (RCF) performance of these coatings in various thicknesses subjected to various tribological conditions of contact configuration, contact stress, lubrication, and micro-slip in a rolling sliding contact.

5.5.2 Coated cone rolling elements

Plasma sprayed tungsten carbide (WC-15%Co) coatings produced by Gator-Gard (GG102) were deposited on the surface of a bearing steel (440-C) rolling element cones. The rolling element cones had a diameter of 15 mm and an apex angle of 109.4° and 90°. These rolling element cones were coated by spraying along the axis of the cone. The distance between the spraying gun and the rolling element cone was approximately 65 mm. The required coating thickness was obtained by several passes of the spraying gun perpendicular to the direction of spraying. The coating powder had a particle size of 10 ~ 25 μm. The substrate rolling element cones were machined from a bright finished 16 mm diameter bearing steel (440-C) rod. The substrate material was sand blasted and then preheated to approximately 100°C prior to the coating process for improved bonding at the interface by the mechanical interlock, increased surface area and reducing the quenching stresses of the impacting lamella.

The rolling element cones were sprayed to obtain an approximate coating thickness of 300 μm and 150 μm in the as-sprayed conditions. The cones were then ground and polished to give an average coating thickness of 230$\pm$10 μm and 60$\pm$10 μm for 109.4° apex angle cones and 150$\pm$10 μm and 90$\pm$10 μm for 90° apex angle cones. The average surface roughness of these rolling element cones in the as-sprayed, ground and polished conditions were 4$\pm$1.5 μm (R_q), 1$\pm$0.5 μm(R_q) and 0.1$\pm$0.05 μm(R_q) measured at a 0.8 mm cut-off length.

5.5.3 Test conditions and experimental test results

Rolling contact Fatigue (RCF) tests were conducted using the modified four ball machine at a spindle speed of 4000 $\pm$ 10 rpm and a contact load of 160 N on the contact surfaces. Experimental tests were conducted under immersed lubrication conditions using the high viscosity Hitec-174 lubricant and Exxon 2389 turbo lubricant. In addition to these lubricants, a test was also conducted in dry condition using air as a lubricant. The ratio (λ) of the fluid film thickness to the RMS surface roughness (R_q) for the given test conditions can be approximately as $\lambda \geq 3$ and $\lambda \geq 1$ for the Hitec-174 and Exxon-2389 lubricant respectively (see appendix E for details). The tests were conducted at an ambient temperature of 24$\pm$2°C. The lower planetary balls were of bearing steel (SKF) and silicon nitride ceramic (NORTON). The experimental test procedures described in chapter 2 (article 2.3) were followed. Experimental measurement of the gross sliding in the four ball system by measuring the orbital speed of the planetary balls and the frictional torque in the cup assembly during the RCF tests was done using the techniques described in article 2.5 and 2.6 respectively. Table 5.6 summarises the experimental test results in terms of contact stress, test configuration and test duration. The results of average frictional torque, and percentage sliding have also been included. The contact stress and contact area described represent the calculations based upon the assumption of uncoated contact configuration.

5.5.4 Surface observations

Figure 5.5.1 shows the surface observations of the 215 μm thick coated rolling element cone tested with steel lower balls subjected to the test GGIAX.

Test No	Average coating thickness (μm)	Lower balls	Contact stress* (GPa)	Contact width (mm) (b)	Depth of max: shear (0.65b) (μm)	Lubricant	Sliding (%)	Frictional Torque (N.m)	No: of stress cycles (10^6)	Time to Failure (minutes)
GG1AX	215	steel	2.74	0.132	85	Hitec-174	+2.3	0.0312	38.61	4290
GG2AX	215	ceramic	3.1	0.124	80	Hitec-174	+2.8	0.015	9.891	1099
GG3AX	260	steel	2.74	0.132	85	Exxon	+2.8	0.038	4.329	481
GG4AX	225	ceramic	3.1	0.124	80	Exxon	+2.8	0.003	0.891	99
GG5AX	260	steel	2.74	0.132	85	Dry	+0.3~-9.6	0.06~0.175	0.891	99
GG6AX	225	ceramic	3.1	0.124	80	Dye Penet	+3.2	0.04	1.125	125
GG1AY	60	steel	2.74	0.132	85	Exxon	+2.8	0.01	1.62	180
GG2AY	70	ceramic	3.1	0.124	80	Exxon	+0.3	0.03	0.441	49
GG3AY	60	ceramic	3.1	0.124	80	Hitec-174	+2.3	0.097	0.180	20
GG4AY	50	steel	2.74	0.132	85	Hitec-174	+0.3	0.05	4.662	518
GG1BX	140	ceramic	3.1	0.124	80	Hitec-174	-0.3	0.019	0.861	89
GG2BX	140	steel	2.74	0.132	85	Hitec-174	-3.25	0.04	4.354	450
GG3BX	140	ceramic	3.1	0.124	80	Exxon	-3.25	0.026	0.599	62
GG4BX	130	steel	2.74	0.132	85	Exxon	-0.3	0.01	1.190	123
GG1BY	90	ceramic	3.1	0.124	80	Exxon	-3.25	0.048	0.058	06
GG2BY	80	steel	2.74	0.132	85	Exxon	-3.25	0.036	0.870	90
GG3BY	90	ceramic	3.1	0.124	80	Hitec-174	-2.7	0.032	0.338	35
GG4BY	90	steel	2.74	0.132	85	Hitec-174	-2.7	0.033	0.870	90

* UNCOATED CASE

Table 5.6, Rolling contact fatigue test results for Plasma Sprayed coatings on 440-C steel substrate

Figure 5.5.1(a) shows the overall view of the failed area. The coating failure was from within the coating microstructure which was confirmed by the EPMA analysis. Figure 5.5.1(b) shows a portion of the wear track at a higher magnification. Numerous pits are visible on the surface of the wear track and the depth of these micropits was approximated as 5 μm based on the surface observations at a higher magnification taken at an inclined angle to the surface. The width of the wear track can be approximated as 700 μm and it can be appreciated that the width of the wear track is much greater than the contact dimensions of 132 μm (uncoated conditions) for the given test conditions indicating that the surface wear during the RCF test lead to the increased contact area. Although no delamination was observed in this case the micropits and the surface wear lead to the failure of the rolling element cone.

Figure 5.5.2 shows the surface observations of the 215 μm thick coated rolling element cone tested with ceramic lower balls subjected to the RCF test GG2AX. Figure 5.5.2(a) shows the overall view of the wear track. The rolling element failed from within the coating microstructure and it was confirmed by EPMA analysis and BEI image. Figure 5.5.2(b) shows a portion of the wear track at a higher magnification. The width of the wear track can be approximated as 450 μm. It can be appreciated that the width of the wear track in this case is smaller than what was seen in GG1AX which could be attributed to the contact with the lower ceramic balls (less contact width) and less duration of the test. A shallow pit of the approximate dimensions 300 μm $\times$ 300 μm can be seen in the middle of the wear track. It is possible that the failure is initiated by tiny shallow pits which combined with each other to form these bigger pits which eventually lead to the coating failure.

Figure 5.5.3 shows the surface observations for the test GG3AX. In this case the coating delaminated from within the coating microstructure at two locations. Figure 5.5.3(a) shows the overall view of the wear track in SEI whereas figure 5.5.3(b) shows the same image in BEI. Figure 5.5.3(c) shows one of the delaminated areas of the coating at higher magnification. The rolling direction was from the left to the

right of this figure and a crack can be seen at the leading edge of the delaminated coating. Figure 5.5.3(d) shows the delaminated area at an inclined angle and the depth of the delamination can be appreciated as 40 μm.

Figure 5.5.4(a) shows the overall view of the failed area for the test GG4AX in BEI. The coating delaminated catastrophically all the way around the wear track from within the coating microstructure. Figure 5.5.4(b) shows a portion of the wear track at a higher magnification and numerous cracks can be seen on the surface of the wear track.

Figure 5.5.5 shows the surface observations for the 140 μm thick rolling element subjected to the test GG1BX (ceramic lower balls). Figure 5.5.5(a) shows the overall view of the wear track in SEI whereas, the BEI image of the wear track is shown in figure 5.5.5(b). No delamination was observed in this case and the failure was similar to the surface observations of GG1AX and GG4AX except for the fact that the pits seem slightly deeper.

Figure 5.5.6 shows the surface observations of the 90 μm thick rolling element cone subjected to the test GG1BY and GG2BY. Figure 5.5.6(a) shows the overall view of the wear track in BEI for the test GG1BY. In this case the coating delaminated from within the coating microstructure at some locations whereas the coating delaminated at the coating substrate interface as seen on the left hand side of the figure. Figure 5.5.6(b) shows the interfacial delamination at a higher magnification. Figure 5.5.6(c) shows the same area at an inclined angle and the depth of delamination can be appreciated as 100 μm approximately. Figure 5.5.6(d) shows the inclined view at a higher magnification. Numerous cracks can be seen within the coating microstructure under the surface of the wear track. Figure 5.5.6(e) shows the overall view of the failed area of the coated rolling element cone GG2BY. The coating failed at the coating substrate as indicated by the dark regions of the BEI, whereas figure 5.5.6(f) shows the failed area at an inclined angle and the depth of failure can be approximated as 90 μm.

Figure 5.5.7 shows the surface observation of the rolling element cone tested under dry conditions (GG5AX). Figure 5.5.7(a) shows the surface of the wear track in BEI. The coating failed under severe surface wear. Figure 5.5.7(b) shows the surface of the wear track at a higher magnification. The depth of the wear track was approximated as 128 μm measured using the talysurf using a waviness filter at a cutoff of 0.8 mm.

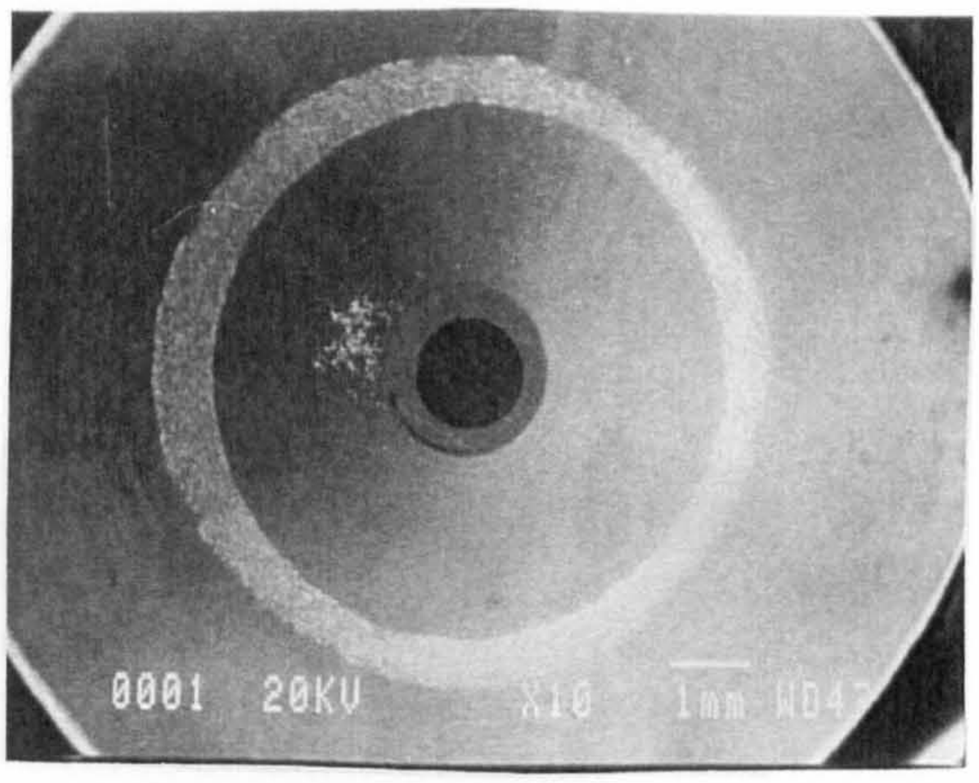

(a)overall view (SEI)

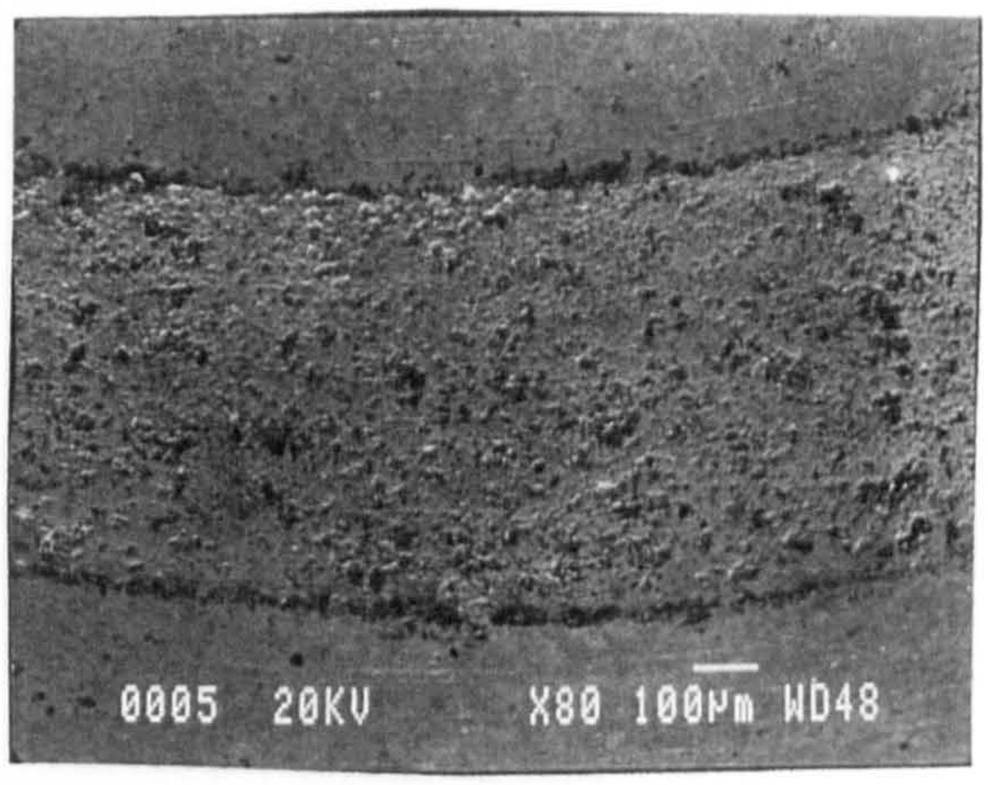

(b) wear track (SEI)

Figure 5.5.1, Surface observations of the rolling element cone GG1AX

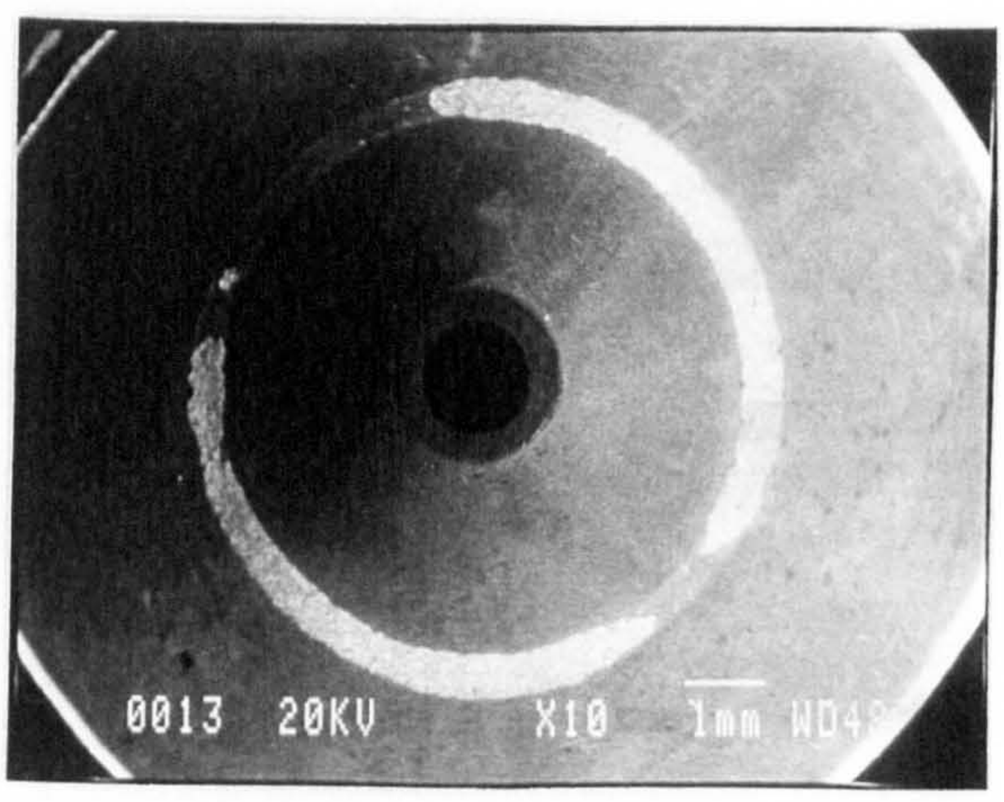

(a) overall view (SEI)

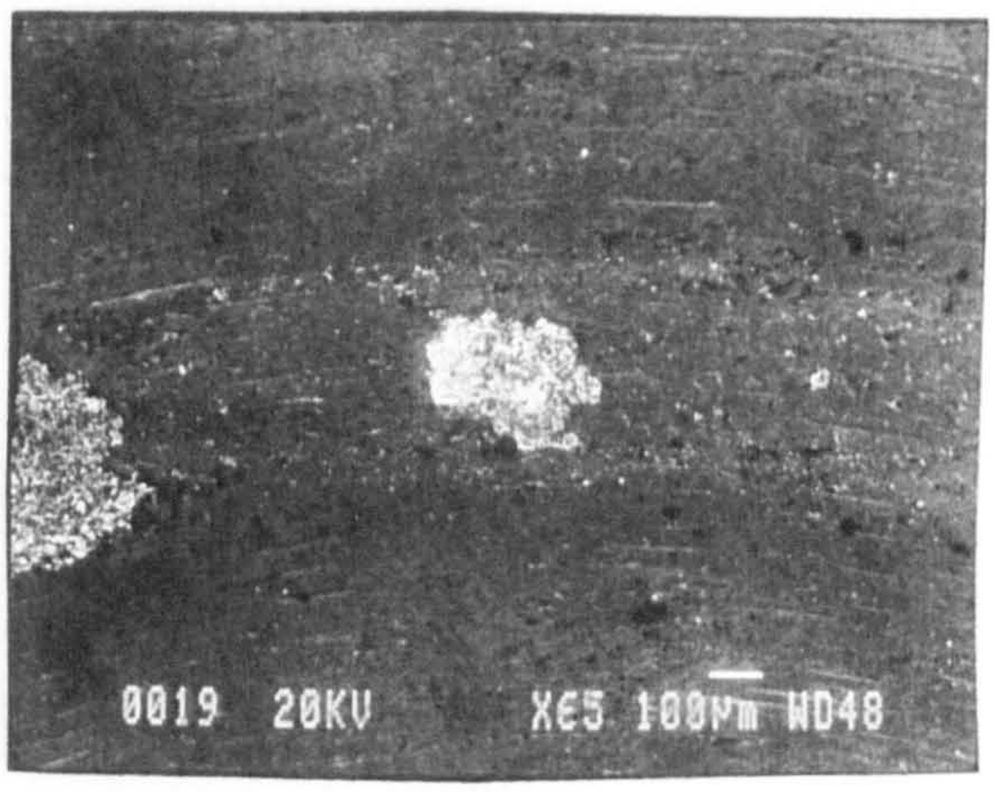

(b) wear track (SEI)

Figure 5.5.2, Surface observations of the rolling element cone GG2AX

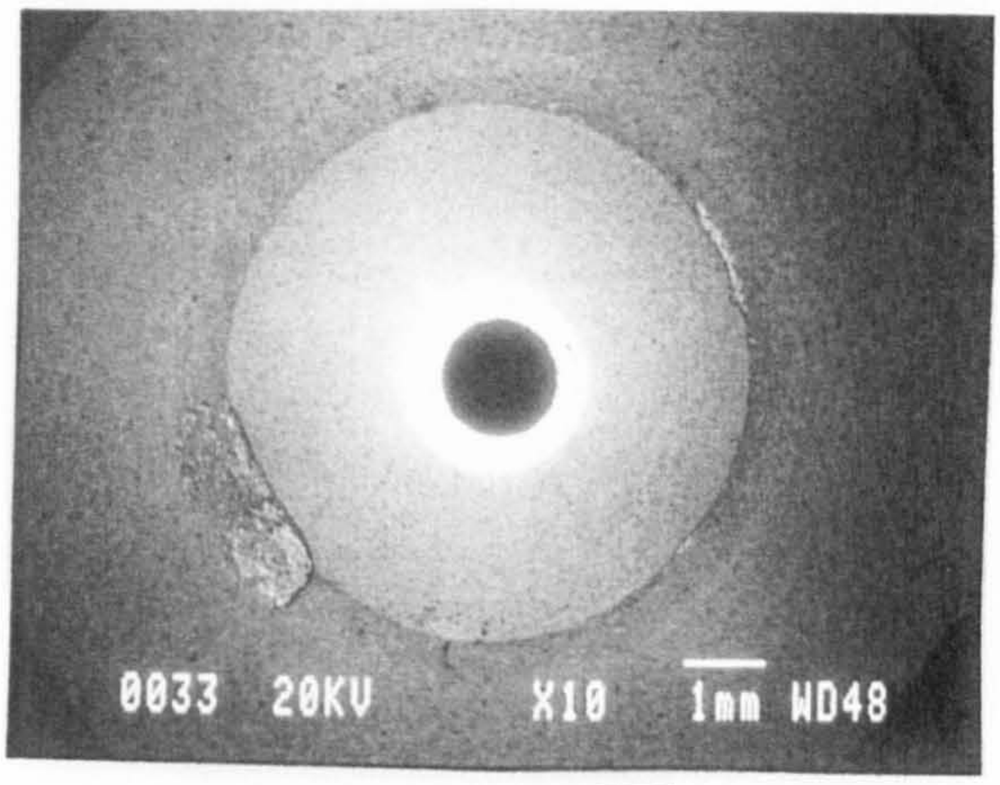

(a) overall view (SEI)

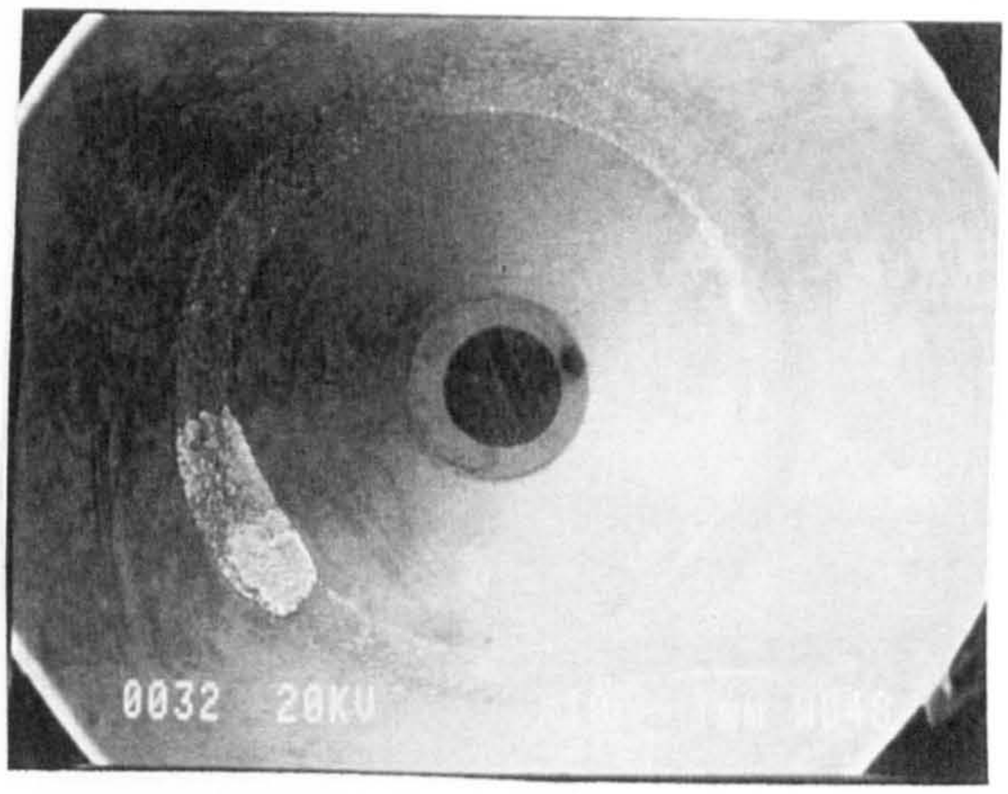

(b) overall view (BEI)

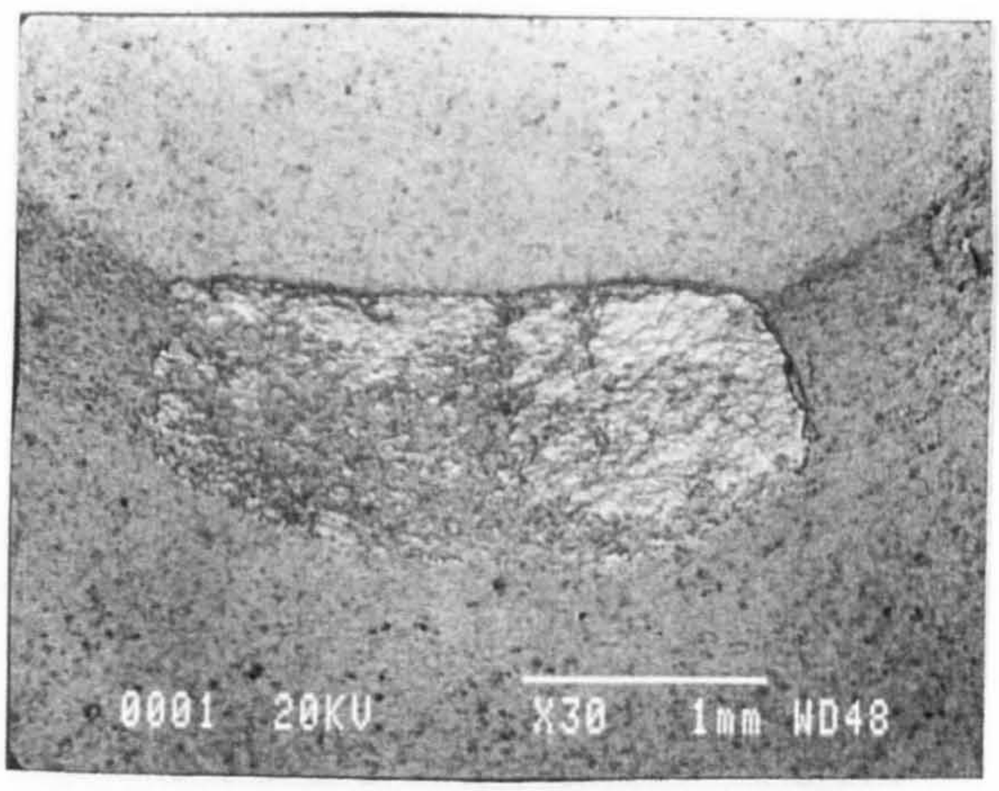

(c) coating delamination (BEI)

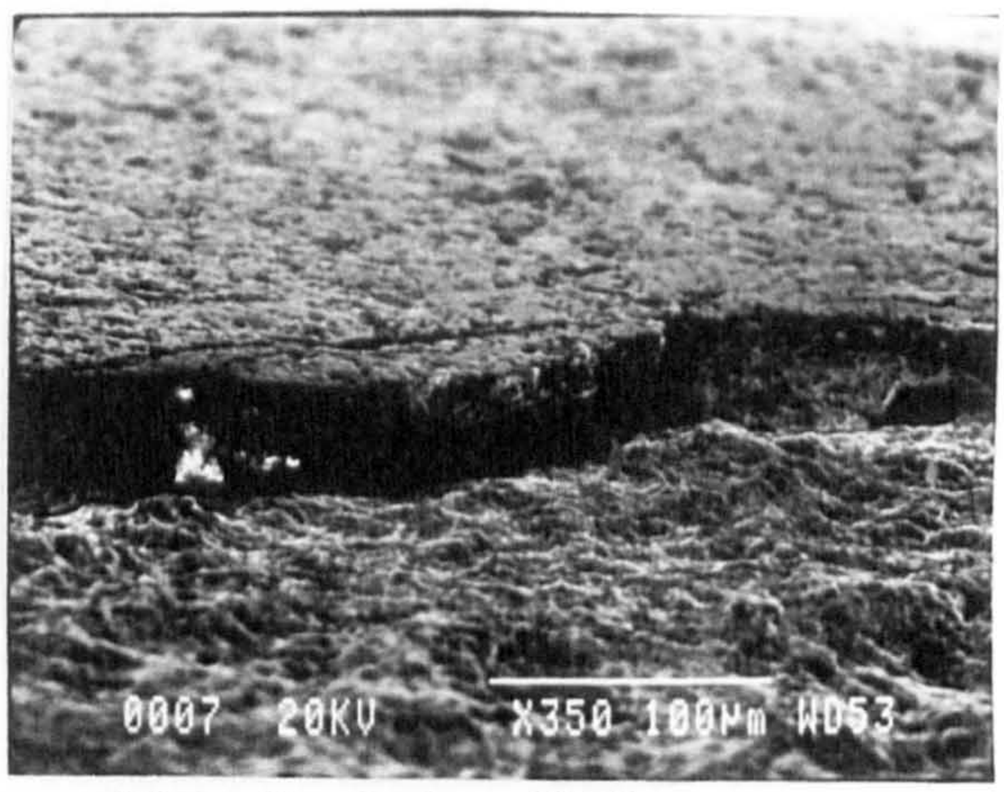

(d) inclined view (SEI)

Figure 5.5.3, Surface observations of the rolling element cone GG3AX

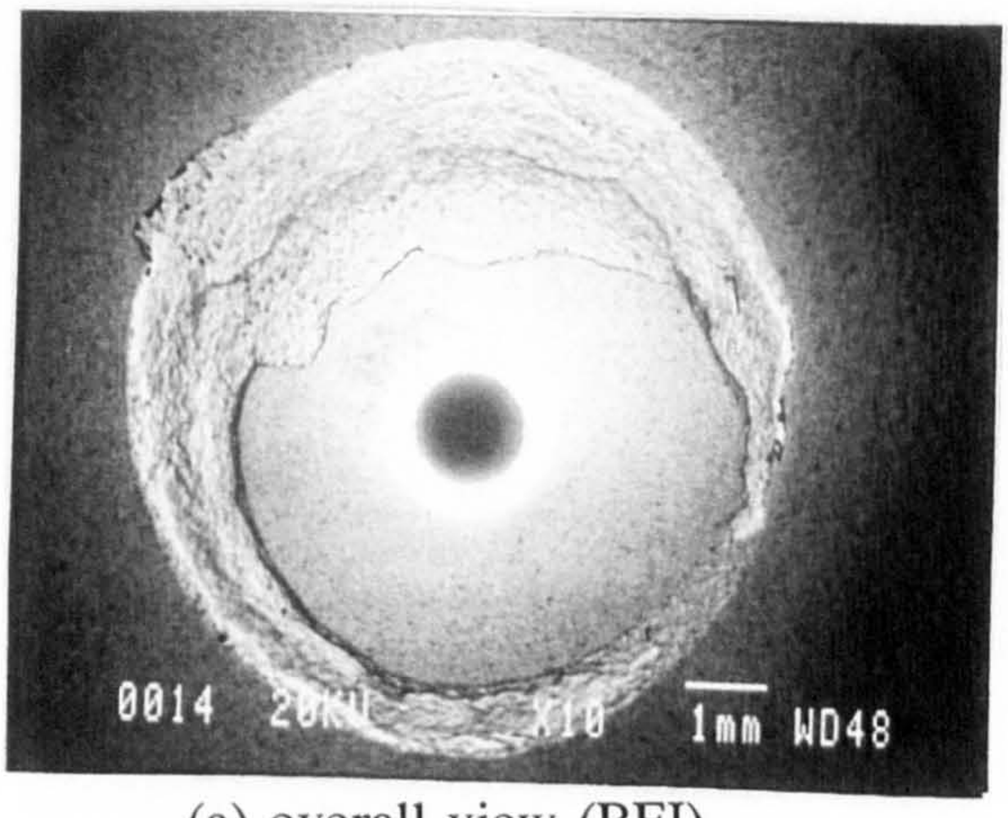

(a) overall view (BEI)

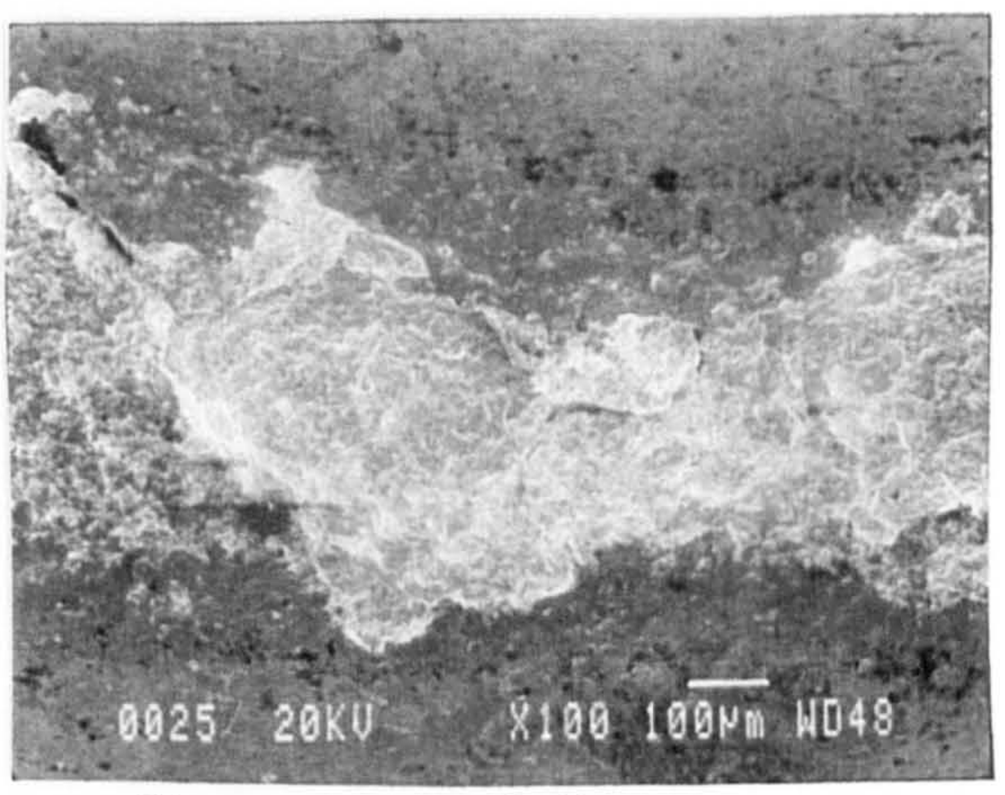

(b) wear track (SEI)

Figure 5.5.4, Surface observations of the rolling element cone GG4AX

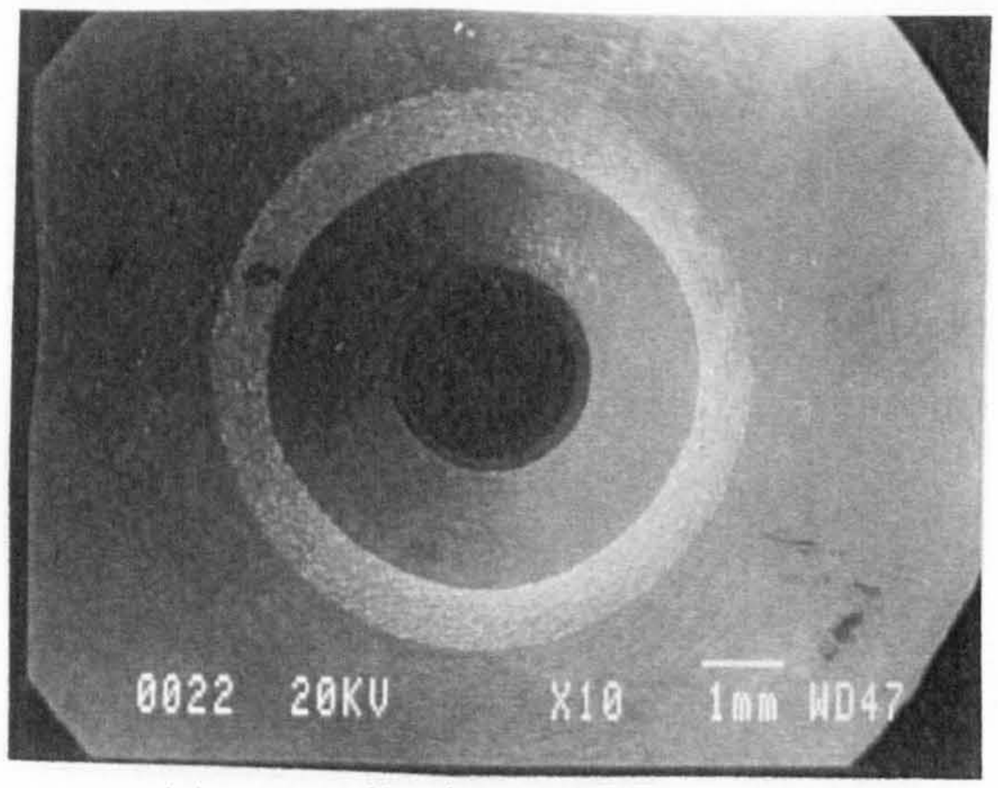

(a) overall view (SEI)

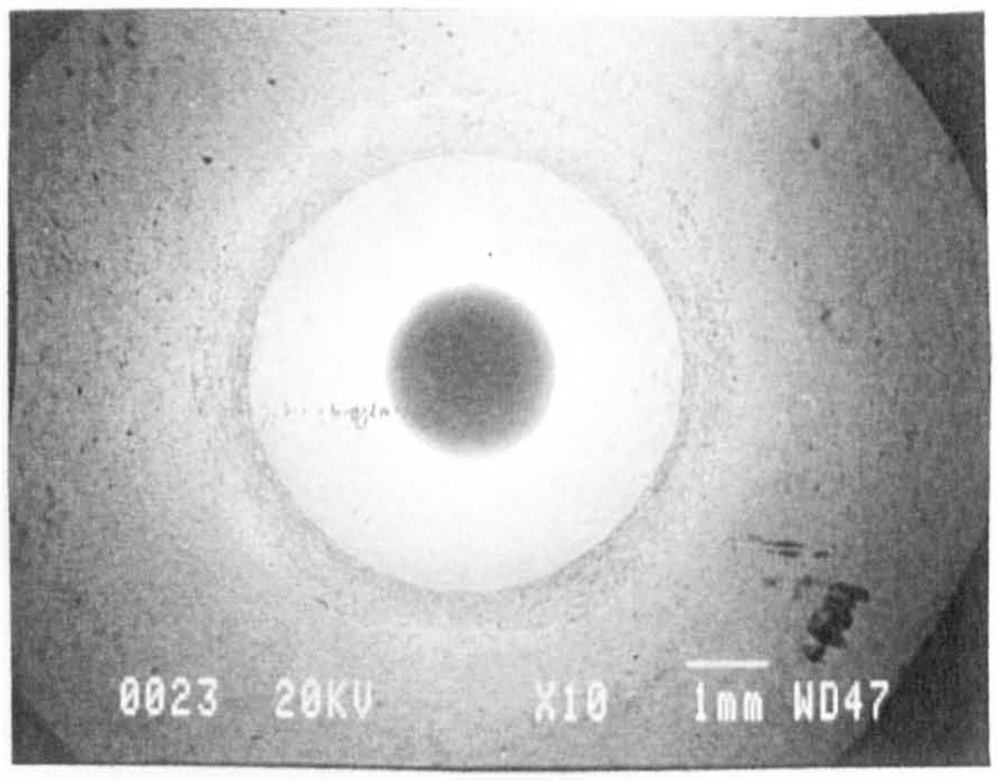

(b) overall view (BEI)

Figure 5.5.5, Surface observations of the rolling element cone GG1BX

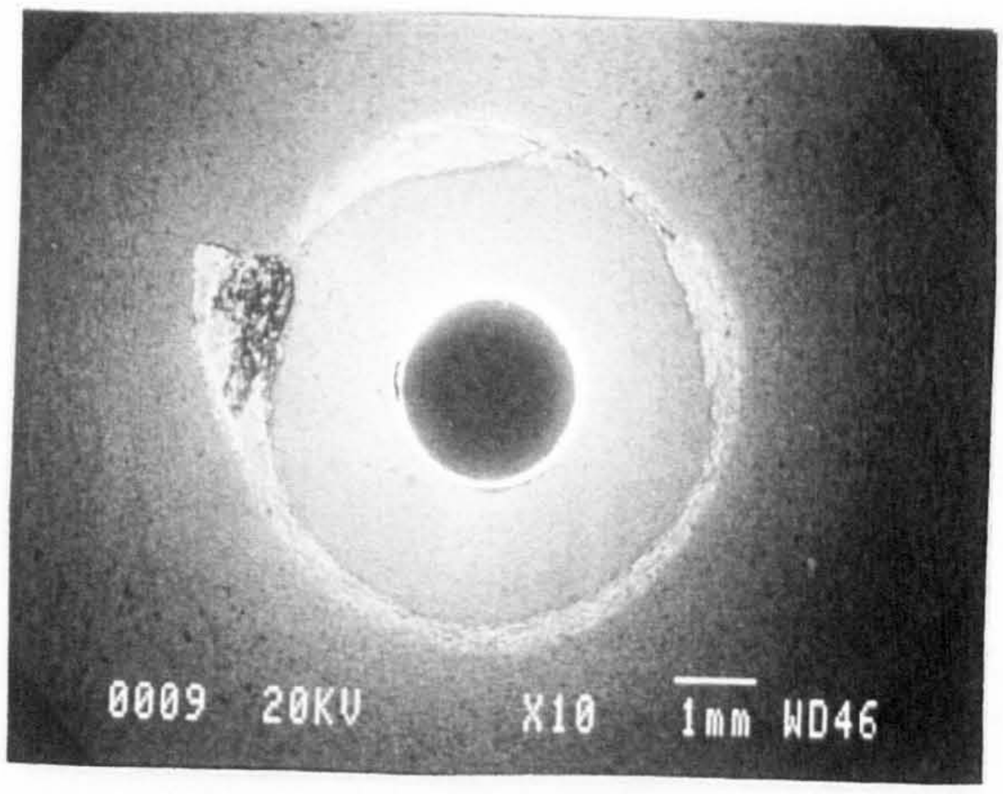

(a) overall view (BEI)

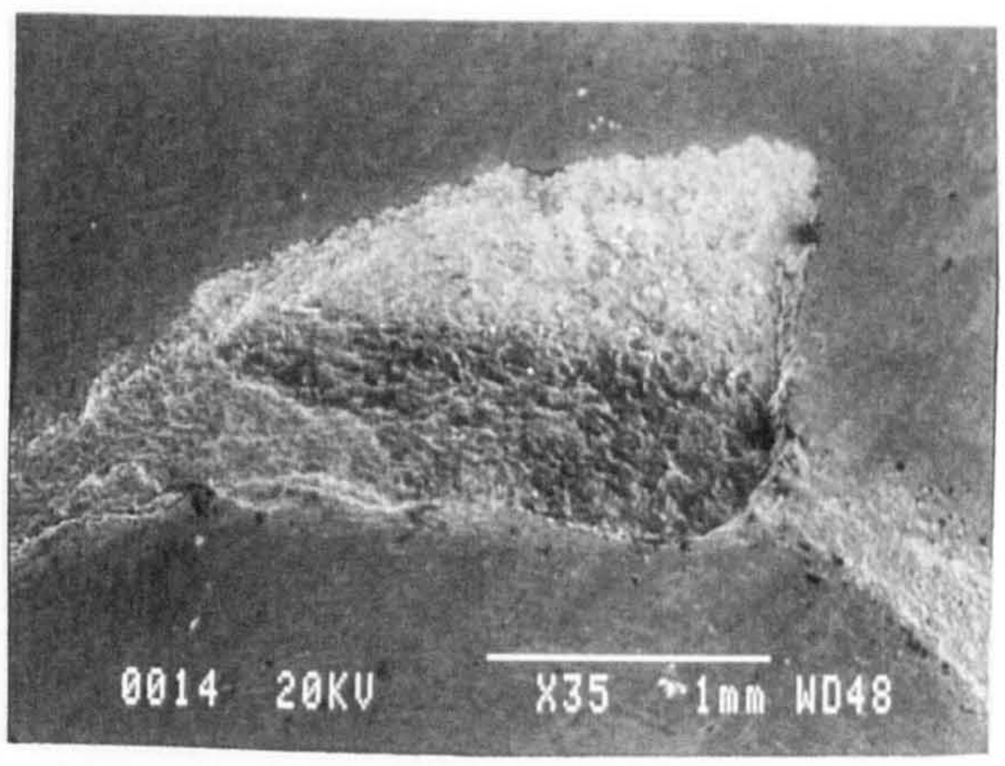

(b) coating delamination (SEI)

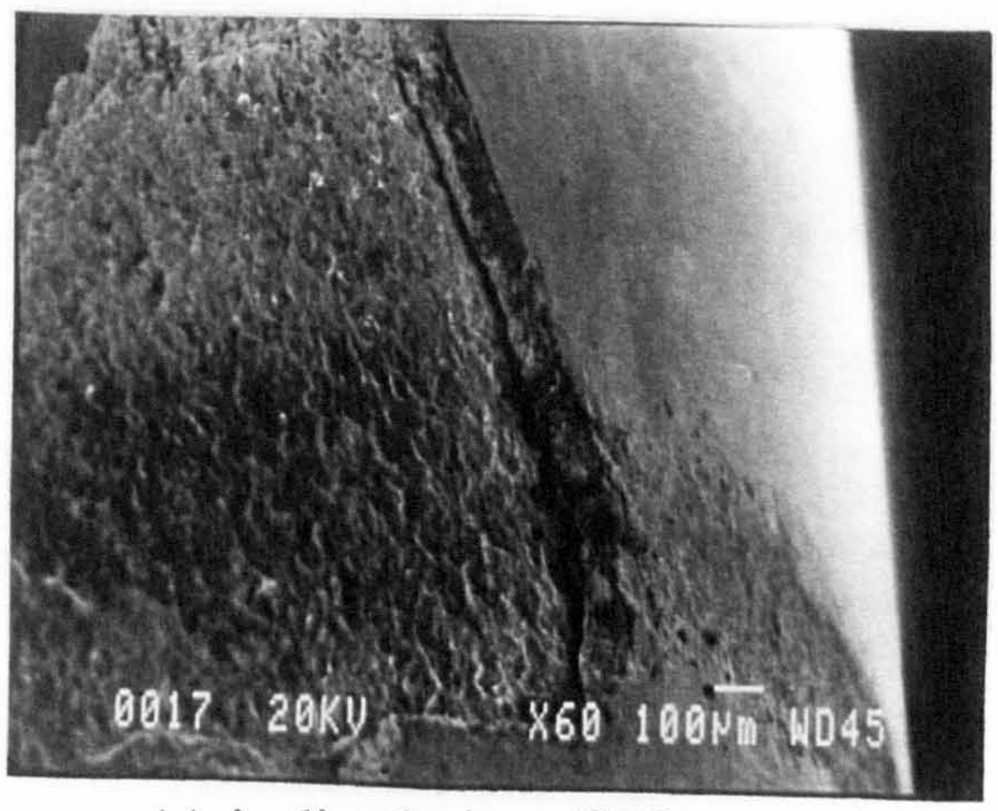

(c) inclined view (SEI)

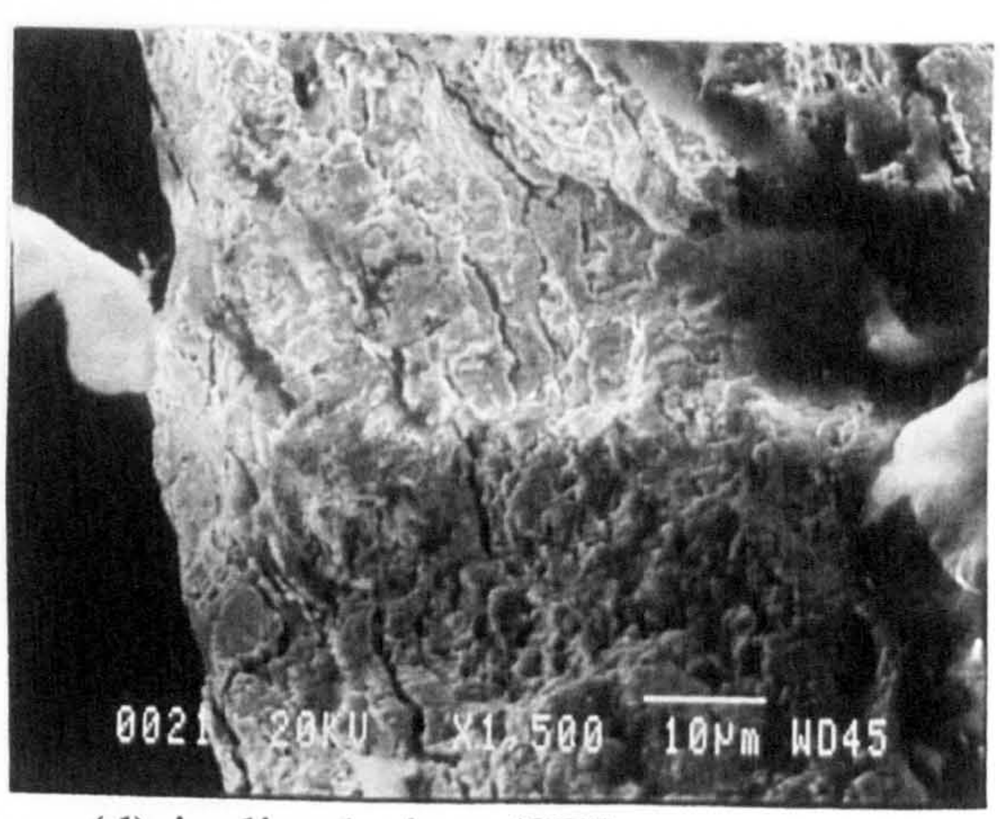

(d) inclined view (SEI)

Figure 5.5.6, Surface observations of the rolling elements GG1BY & GG2BY

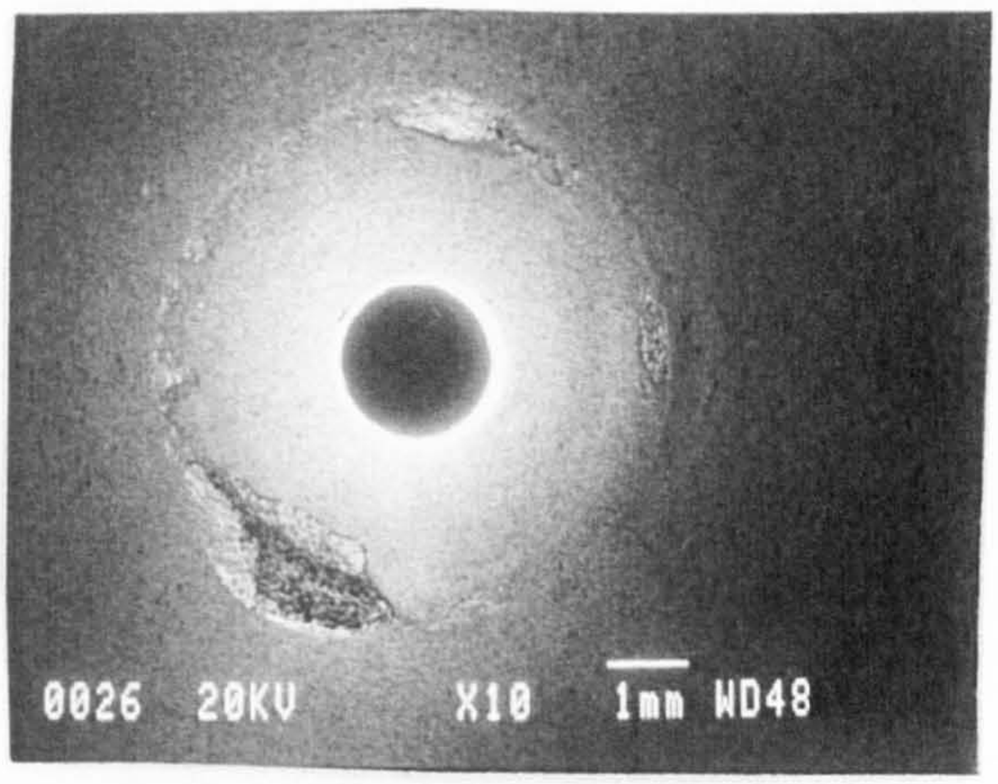

(e) overall view (BEI)

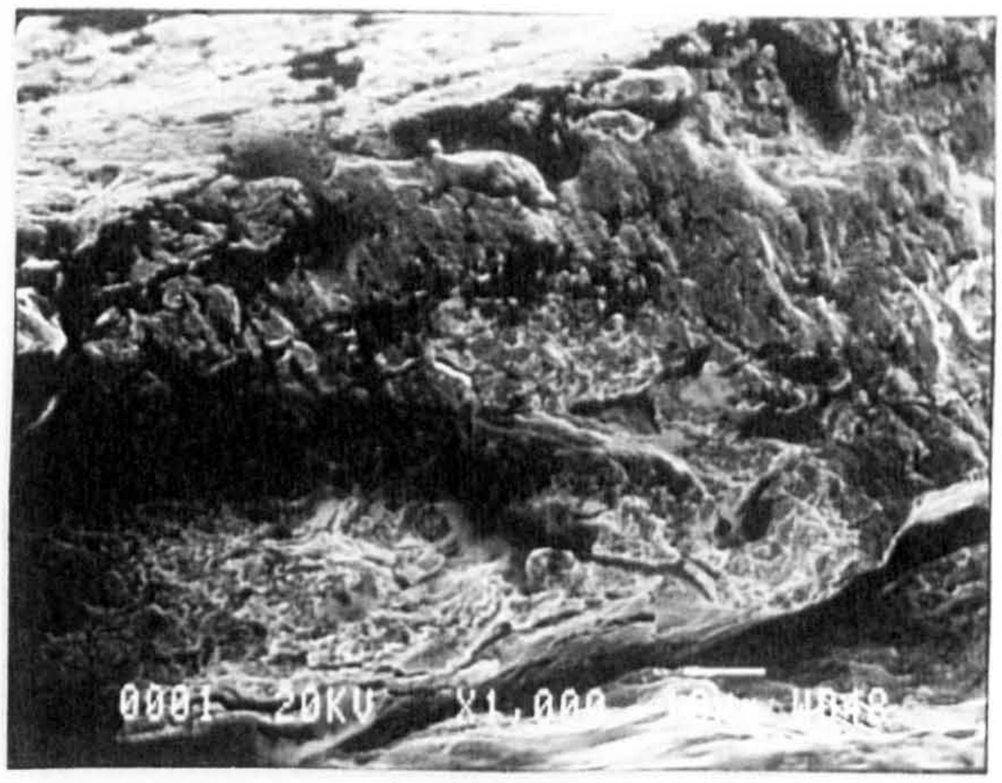

(f) inclined view (SEI)

Figure 5.5.6, Surface observations of GG1BY & GG2BY (continued)

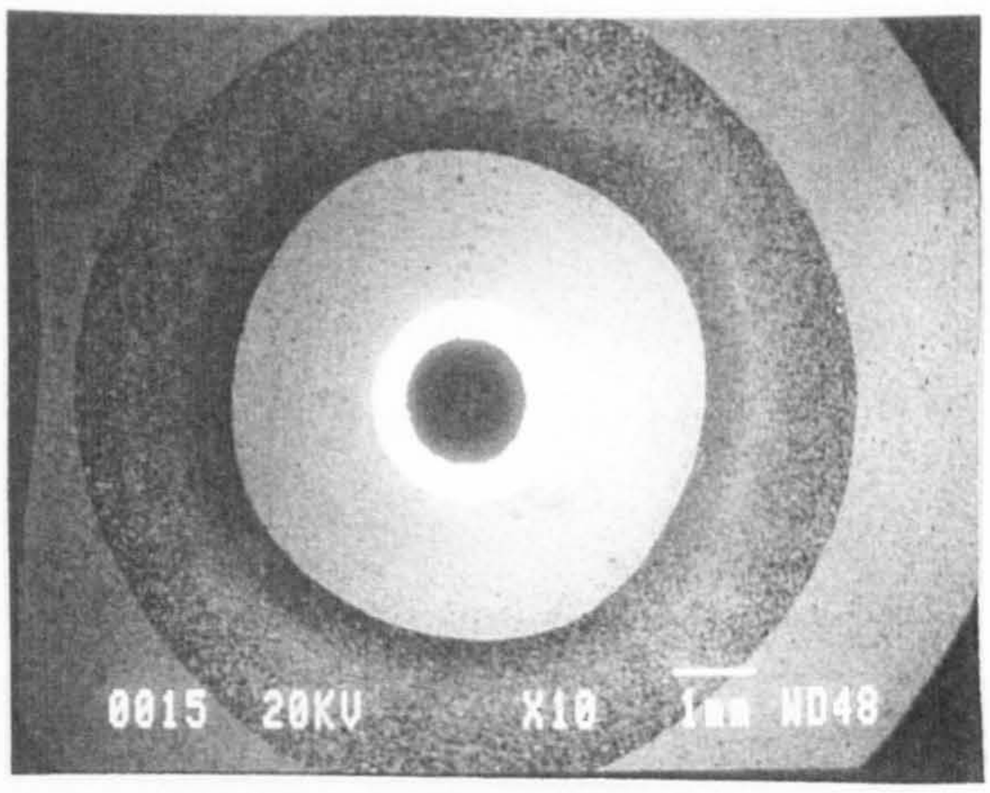

(a) overall view (BEI)

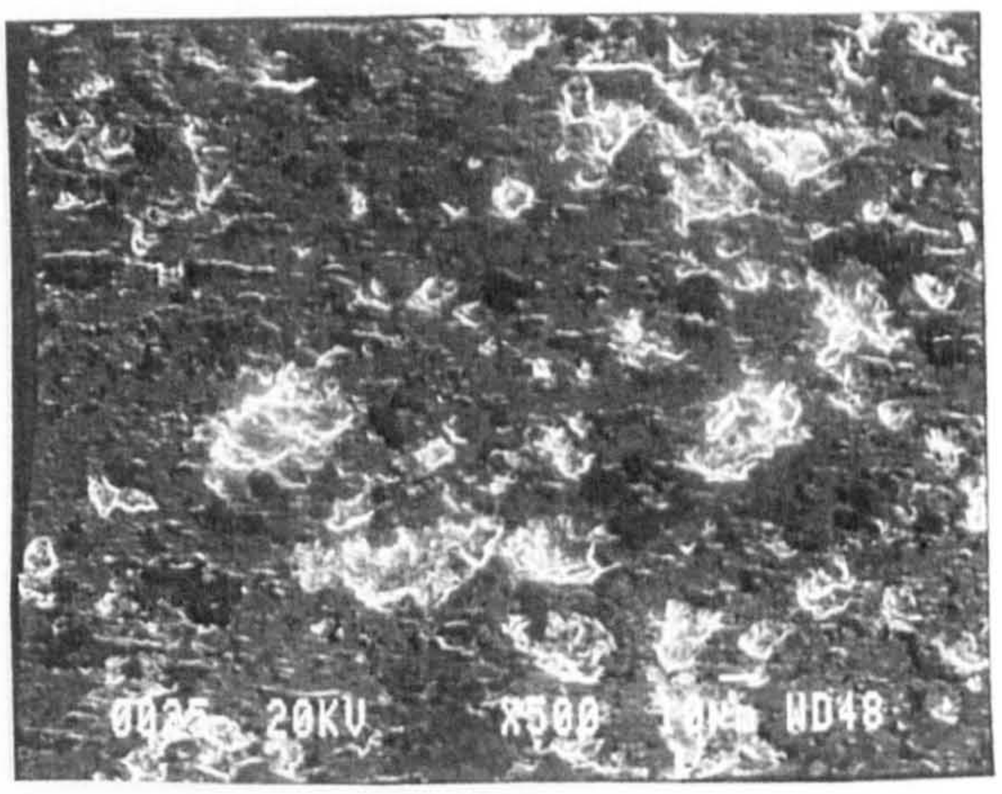

(b) wear track (SEI)

Figure 5.5.7, Surface observations of the rolling element cone GG5AX

5.5.5 Debris analysis

Figure 5.5.8(a) shows the debris collected from the lubricant (Hitec-174) used for the test GG1AX. EPMA analysis of the debris showed a mixture of W, Co and Fe which indicated that the debris were generated from the surface of the coated rolling element cone as well as from the lower planetary balls and cup. The size of these debris can be approximated as from 1 μm $\times$ 1 μm to 10 μm $\times$ 5 μm. Figure 5.5.8(b) shows the debris collected from the debris test (GG5AX). The size of debris can be appreciated as ranging from 1 μm $\times$ 1 μm to 20 μm $\times$ 5 μm. EPMA analyses of these debris show a combination of W, Co and Fe.

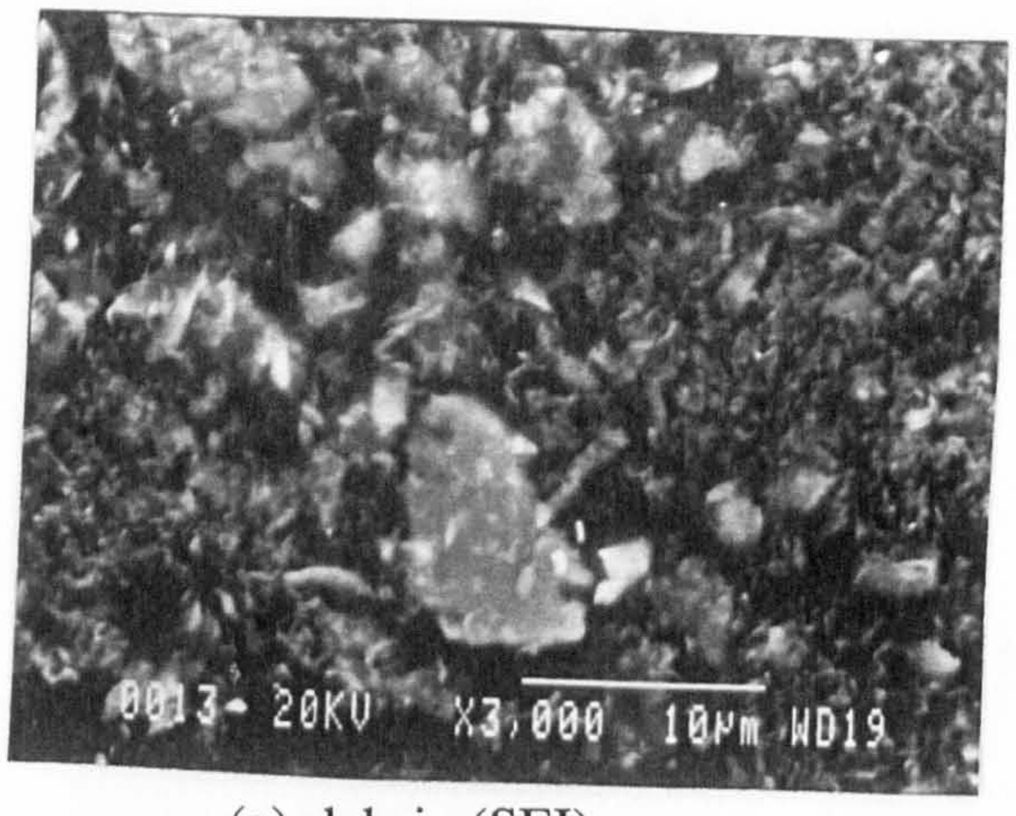

(a) debris (SEI)

(b) debris (SEI)

Figure 5.5.8, Surface observations of the debris (GG1AX and GG5AX)

Figure 5.5.9 shows the surface observations of the debris collected from the lubricant (Exxon 2389) used for the test GG4AX. Figure 5.5.9(a) the top surface of the WC-Co debris. Figure 5.5.9(b) shows the bottom surface of another debris collected from the lubricant an inclined angle. The thickness of debris can be approximated as 100 μm.

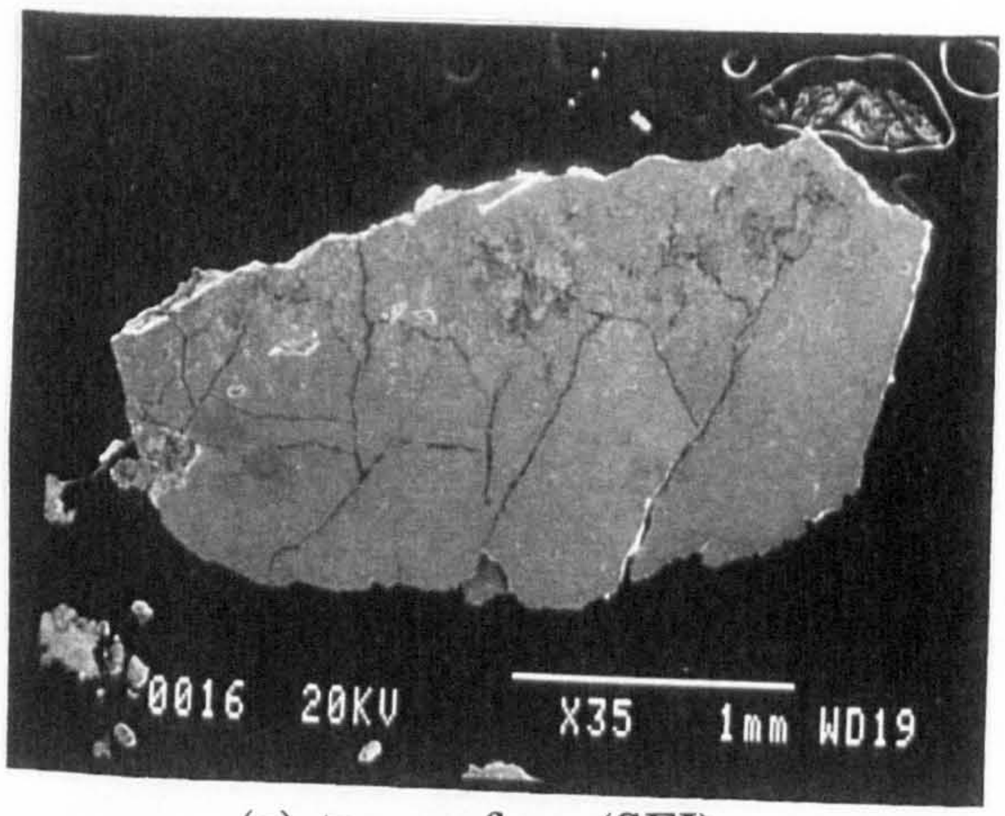

(a) top surface (SEI)

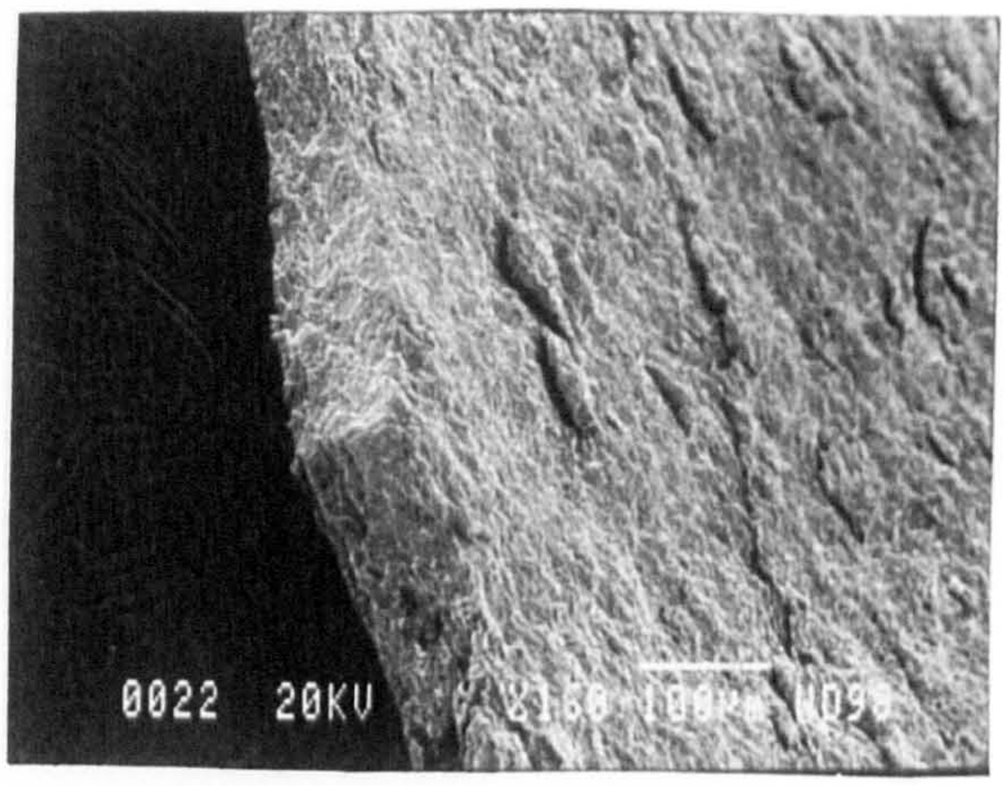

(b) inclined view (SEI)

Figure 5.5.9, Surface observations of the debris from the test GG4AX

5.5.6 Surface analysis of the lower planetary balls

The lower planetary balls after the RCF tests were ultrasonically cleaned in acetone and dried before examining their surface in SEM. Figure 5.5.10(a) shows the WC-

Co debris observed on the surface of the ball for the test GG1AX, in BEI. The size of the debris can be approximated as 1 μm $\times$ 0.5 μm. Similar sized debris were observed on the surface of other planetary balls. Figure 5.5.10(b) shows the surface observation of the wear track and many dents can be seen on the surface of the planetary ball at the location of the wear track.

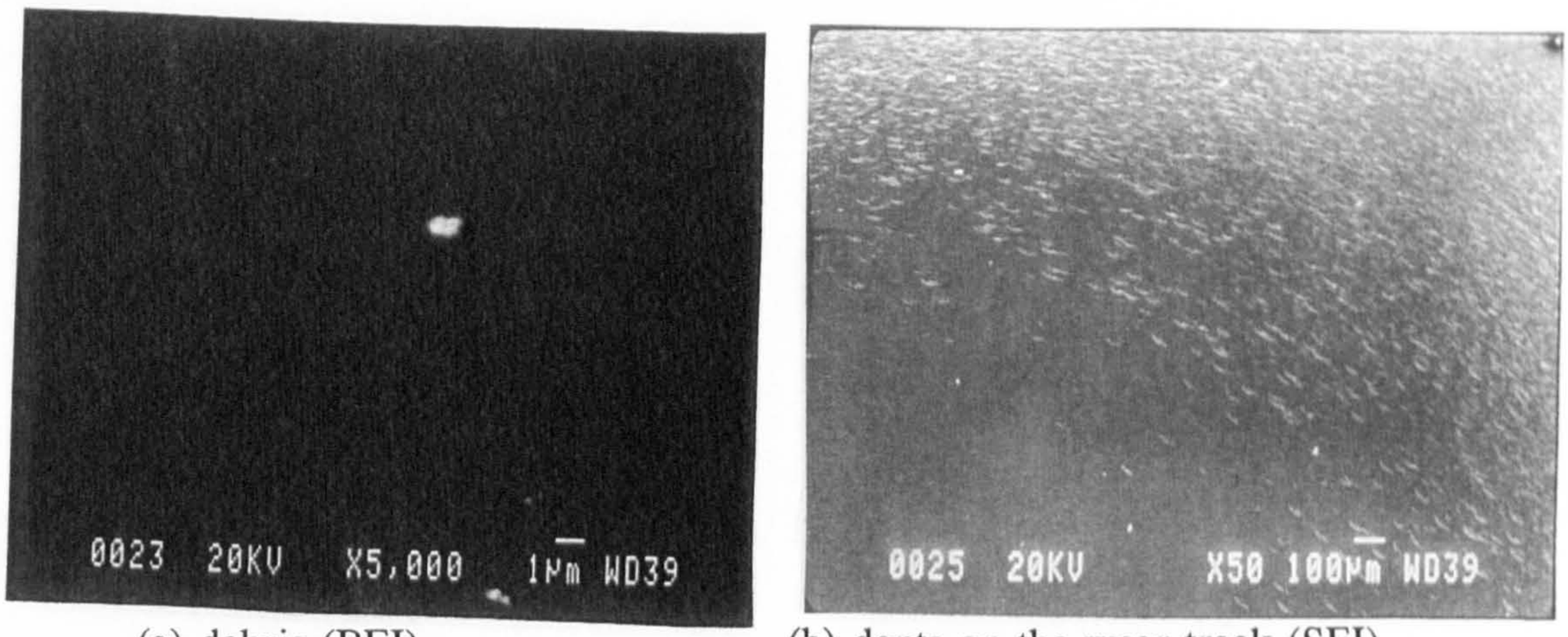

(a) debris (BEI) (b) dents on the wear track (SEI)

Figure 5.5.10, Surface observations of the planetary steel balls (test GG1AX)

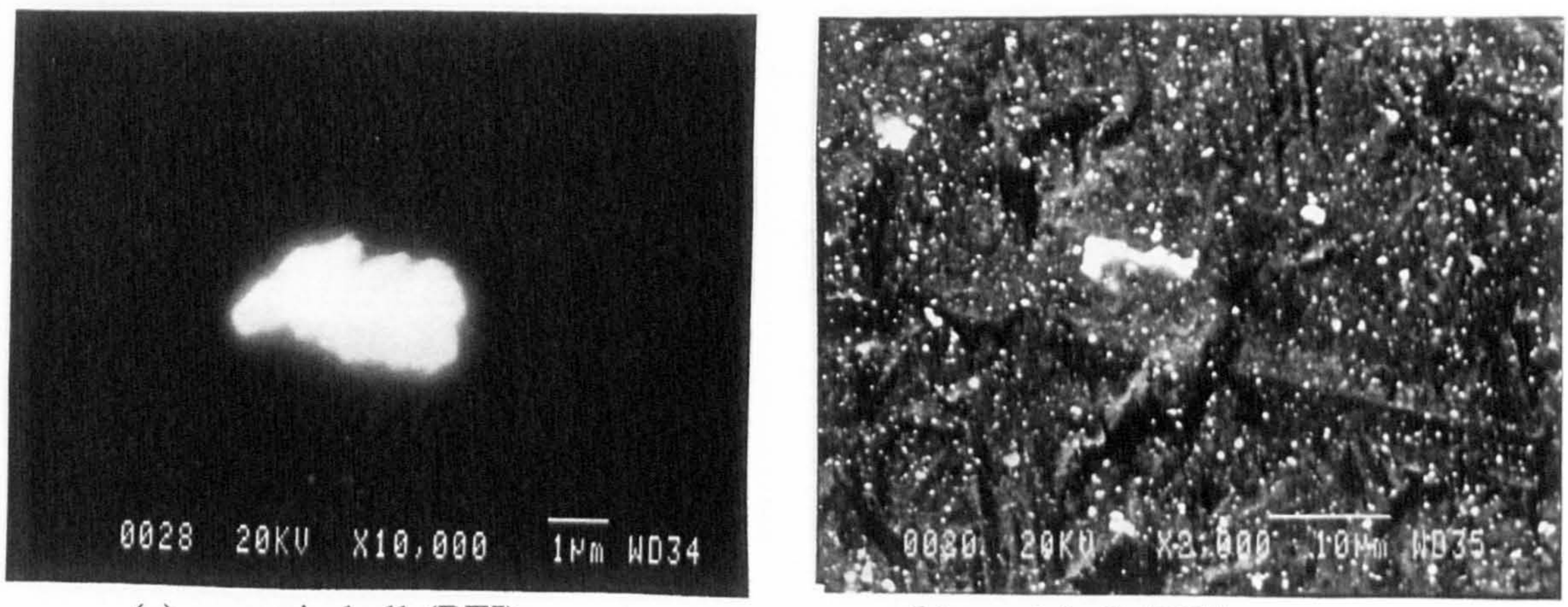

(a) ceramic ball (BEI) (b) steel ball (BEI)

Figure 5.5.11, Debris on the planetary balls

Figure 5.5.11(a) shows debris on the surface of the lower ceramic ball in BEI. The size of the debris can be appreciated as 5 μm $\times$ 3 μm and the EPMA analysis

shows W and Co. However, debris on the surface of the lower ceramic balls was very rare. Figure 5.5.11(b) shows the surface observation of the lower planetary balls used for the dry test (GG5AX) in BEI. The size of the debris can be appreciated as from 1 μm × 1 μm to 10 μm × 3 μm. These debris were confirmed to be W and Co by the EPMA analysis.

5.5.7 Coating microstructure

Figure 5.5.12 shows the coating microstructure revealed after polishing the coating cross section using conventional polishing techniques. Figure 5.5.12(a) shows the coating microstructure in SEI whereas figure 5.5.12(b) shows the microstructure in BEI. Figure 5.5.12(c) shows the coating microstructure at another location in which significant amount of porosity is visible. Figure 5.5.12(d) shows the BEI of the coating microstructure. It can be appreciated that the microstructure contains numerous pores and micro-cracks which can be seen within the WC particles. The atomic contrast images in the BEI indicate that there are secondary phase particles in the coating microstructure. The presence of secondary phase particles was further confirmed by the EPMA analysis taken at points A, B, C and D in figure 5.5.12(b). The darker WC particles seen as shown at point A indicate a strong peak of W and Co whereas, at location B which is a much brighter phase shows a strong W peak only. This indicates that some of W reacted with Co during the plasma spraying process. This behaviour of WC-Co coatings was also studied by (Harvey et. al. 1995) in which the formation of an amorphous W-Co-C phase was observed due to the melting of WC-Co particles. At location B, however, it appears that plain WC particles are present, which can be indicative either of retained WC in the coating microstructure or the presence of W_2C particles. The EPMA analysis at location C indicated a strong Co peak, whereas at location D there were weak peaks of W, Co, etc. with a high background noise in the signal which is typical of porosity in the coating microstructure. The size of angular WC or W_2C particles can be approximated as being in the range of 2 μm × 2 μm to 10 μm × 5 μm. Micro-cracks can also be seen in some of these angular particles. All these observations indicate that the coating microstructure is a combination of micro-pores, micro-cracks and secondary phase particles etc. No attempt was made to quantify the level

of porosity in the microstructure.

(a) coating microstructure (SEI)

(b) coating microstructure (BEI)

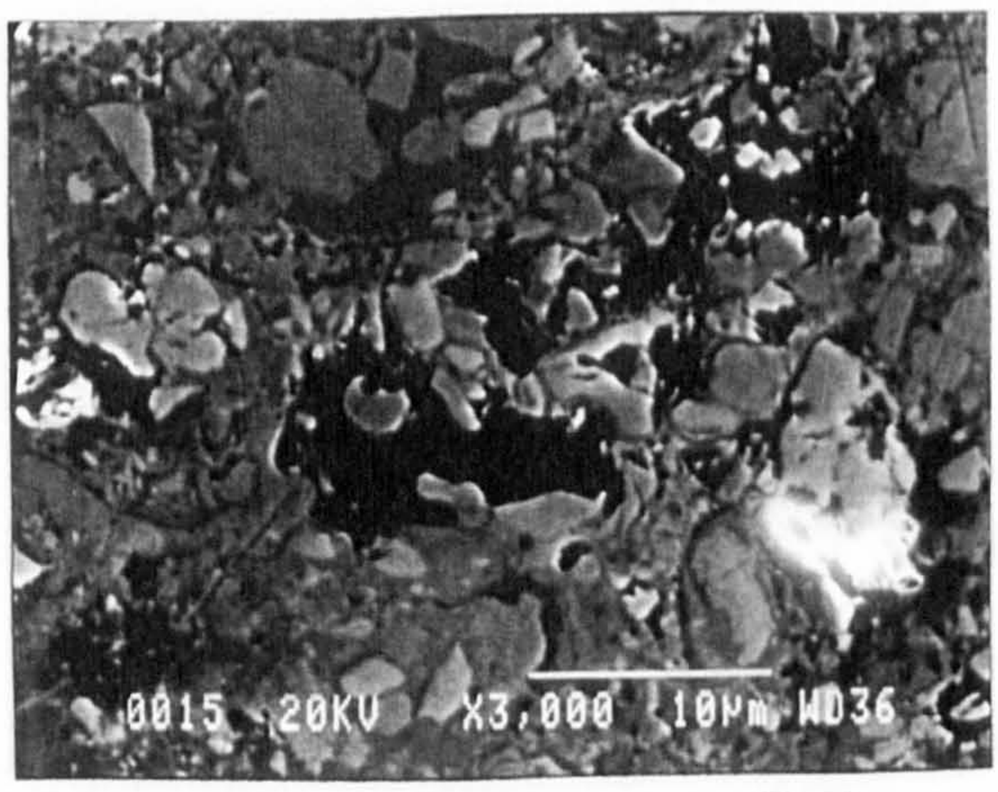

(c) coating microstructure (SEI)

(d) coating microstructure (BEI)

Figure 5.5.12, Coating microstructure

5.5.8 Subsurface observations

The surface observations of the failed rolling elements described in section 5.5.4 could be useful in understanding the types of tribological failures during the RCF tests. However, the understanding of mechanisms which could possibly lead to different types of tribological failures could not be explained without exploring the subsurface changes during the RCF tests. The studies of any microstructural changes such as plastic deformation, crack initiation and propagation, residual stress changes, etc. under the surface of the wear track can thus be helpful in understanding the failure mechanisms of the coated rolling elements. This section

deals with the subsurface investigations of the cracks which were carried out using the dye penetrant technique, the details of which can be appreciated from chapter 4 (section 4.3).

Figure 5.5.13 shows the subsurface observations of the rolling element cone used for the test GG3AX. The surface observations of this rolling element indicated that the rolling element delaminated from within the coating microstructure as was shown in figure 5.5.3. Figure 5.5.13(a) shows subsurface cracks observed under the ultraviolet light. Three different cracks are visible at two different depths under the surface of the wear track. A big crack can be seen at a deeper depth while two hairline cracks can be seen appearing on either end of the big crack at a shallower depth. Considering the magnification of the image and taking account of the apex angle, the coating thickness was approximated as 260 μm. Similarly the maximum depth of the big crack and the short shallow cracks on either ends for the contact was approximated as 90 μm and 40 μm respectively. The rolling direction was from the right to the left of the figure. Figure 5.5.13(b) shows the leading edge of the big crack at a higher magnification. Two independent cracks at two different depths can be seen. However, none of these cracks has reached the surface at this stage.

Figure 5.5.14 shows surface observations after some more grinding along the axis of the rolling element cone (GG3AX). Figure 5.5.14(a) shows the overall view of the subsurface cracks. It can be seen that the big crack shown in figure 5.5.13 has extended in length in both directions and joined with the short cracks at shallower depths. Also, another short and independent subsurface crack has appeared on the left of the big crack at a contact depth of approximately 90 μm. Figure 5.5.14(b) shows this crack at a higher magnification. It can be seen that the big crack has changed direction to combine with the crack at the shallower depth. However, none of the cracks have reached the surface at this stage.

Figure 5.5.15 shows the subsurface observations under the wear track as more grinding was done along the axis of the rolling element cone. The big crack has now extended on both ends to form a circumferential crack after joining with the

independent short crack shown in figure 5.5.15(a) on the left side (leading edge) and other cracks at a shallower depth of approximately 40 μm on the right (trailing edge). In addition to the crack propagation on both ends the circumferential crack has reached the surface approximately at its middle as shown at a higher magnification in figure 5.5.15(b). The rolling direction was from the right to the left of figure and the cracks seem to have progressed in the direction of rolling from subsurface to the surface of the wear track. This propagation of the crack to the surface also provided a path for the fluorescent dye to penetrate in the cracks.

As the progressive grinding/sectioning to observe the subsurface conditions continued along the axis of the cone, the circumferential crack extended to greater lengths as shown in figure 5.5.16. Figure 5.5.16(a) shows the overall view of the circumferential crack. Since it was confirmed by the above dye penetrant subsurface observations that the cracks were formed due to the rolling contact and not due the sectioning or grinding process the rolling element was observed under the SEM for detailed studies at higher magnification. Figure 5.5.16(b) shows the circumferential crack in SEI. It can be appreciated that the circumferential crack has now extended to a length of approximately 5 mm under the surface. The rolling direction was from right to the left of the figure. Figure 5.5.16(c) shows the leading edge of the circumferential crack at a higher magnification. The contact depth of this crack can be approximated as 90 μm which was the original depth of this crack as was shown in figure 5.5.13. Figure 5.5.16(d) shows the trailing edge of the circumferential crack at a higher magnification. The contact depth of this crack under the wear track can be approximated as 40 μm. The coating thickness can also be appreciated as 260 μm. These images indicate that the cracks propagated at two different depths of 90 μm and 40 μm under the contact surface.

In addition to the propagation of the circumferential crack in either directions more cracks appeared to the left of the circumferential crack under the surface of the wear track. Figure 5.5.17 shows the ultraviolet light and SEM images of those cracks. Figure 5.5.17(a) shows the overall view of the cracks appearing at a shallower depth. The delamination is also apparent at this stage indicating that we are well

within the wear track. The leading edge of the circumferential crack can also be seen at the right of the figure. Figure 5.5.17(b) shows the cracks at a higher magnification. The rolling direction was from the left to the right of the figure. A small crack has also appeared at this depth at the trailing edge of the long crack. Figure 5.5.17(c) shows the SEM observation of the cracks and delamination. This delamination was shown in figure 5.5.3(b) on the surface of the wear track. Figure 5.5.17(d) shows the subsurface cracks at a higher magnification. The contact depth of these subsurface cracks can be appreciated as 30 μm. At this stage the bigger delaminated part of the coating on the surface of the wear track was also apparent. This delamination was shown in figure 5.5.3(c).

As more grinding was done along the axis of the cone, the circumferential crack extended to greater lengths finally reaching the surface at its trailing edge. Figure 5.5.18(a) shows the SEM observation of the circumferential crack under the wear track in BEI. The length of the circumferential crack can now be approximated as 7 mm and it extends from the big delamination on the surface of the wear track as was shown in figure 5.5.3(c). In addition to the circumferential crack the short crack shown in figure 5.5.17 also extended to the surface as shown in figure 5.5.18(b). It can be appreciated that the two cracks shown in figure 5.5.18 have actually combined together to reach the surface.

The rolling element cone used for the test GG2BY was also studied for subsurface cracks in the similar manner as described above. This rolling element failed because of the coating delamination at the interface. Figure 5.5.19 shows the subsurface observations of the rolling element cone GG2BY. Subsurface Interfacial (coating/substrate interface) cracks were observed at the edge of the wear track. Figure 5.5.19(a) shows a view of these cracks under ultraviolet light whereas, figure 5.5.19(b) shows these cracks at another location at a higher magnification. Using basic trigonometric relations the contact depth of these interfacial cracks was approximated as 70 μm. As more grinding was carried out along the axis of the cone these subsurface cracks reached the surface exposing the delaminated area of the coating. Figure 5.5.20(a) shows these subsurface cracks under the delaminated

section of the coating at two different depths under the wear track. Similarly the coating delamination can also be observed at these two different depths under the surface of the wear track ie. (i) at the coating substrate interface as seen on the left of the figure and (ii) from within the coating microstructure at a contact depth which was approximated as 30 μm under the surface of the wear track. The rolling direction was from the right to the left of the figure. It can be appreciated that if these cracks were thought to initiate and propagate from the surface towards the interface of the coating, they must have propagated in the direction opposite to rolling. However, if the cracks initiated and propagated from subsurface to surface then the direction of propagation was in the direction of rolling at the leading edge of the contact and vice versa at the trailing edge of the contact. The surface observation of this delamination was shown in figure 5.5.6(e). As more grinding was done along the axis of the cone, cracks were observed under the surface of the wear track. Figure 5.5.20(b) shows the cracks observed under the surface of the wear track which were similar to the cracks shown in figure 5.5.20(a). Dye penetrant studies were also carried out on the rolling element GG4AY in which the failure mode was not delamination. The surface wear which lead to the failure of the rolling element can be appreciated from this figure at a contact depth ranging from $5 \sim 15$ μm.

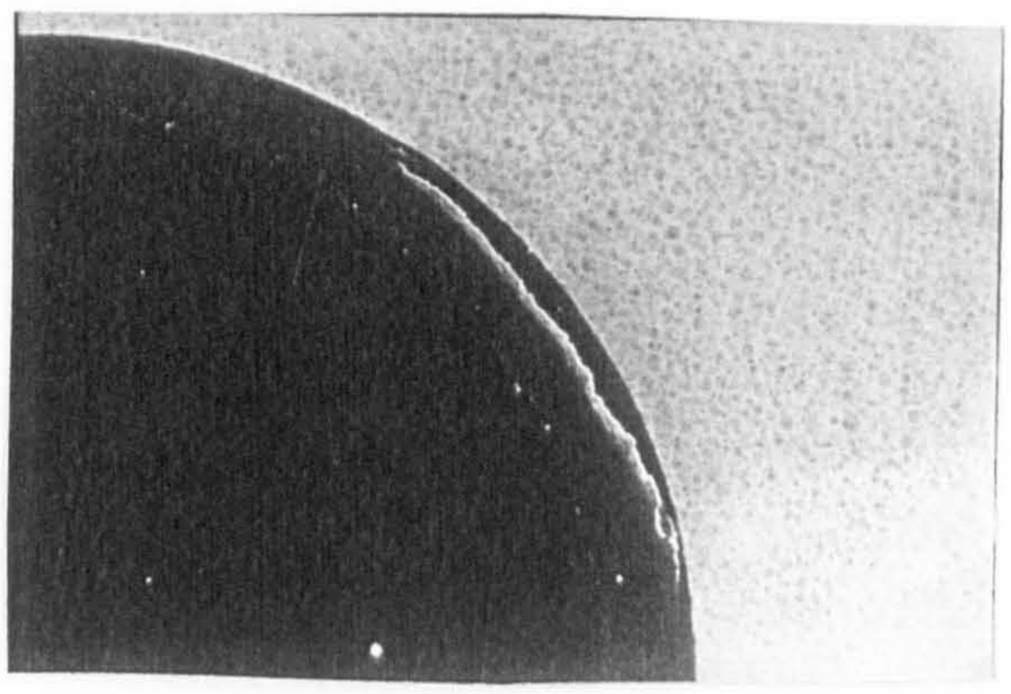

(a) Subsurface cracks

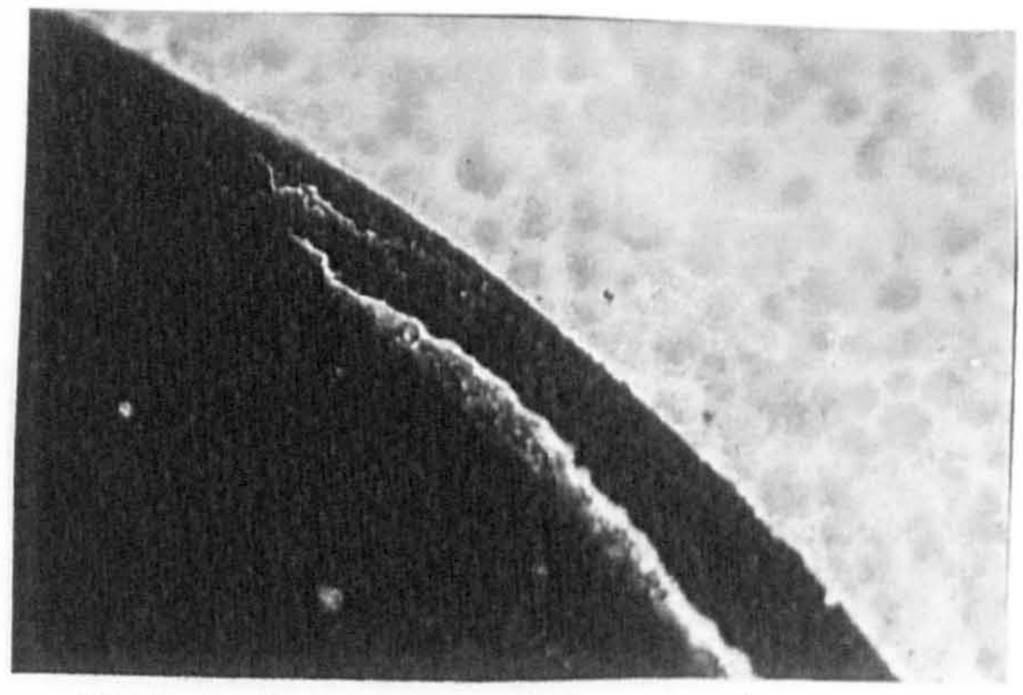

(b) Leading edge of the crack

Figure 5.5.13, Subsurface observations (GG3AX)

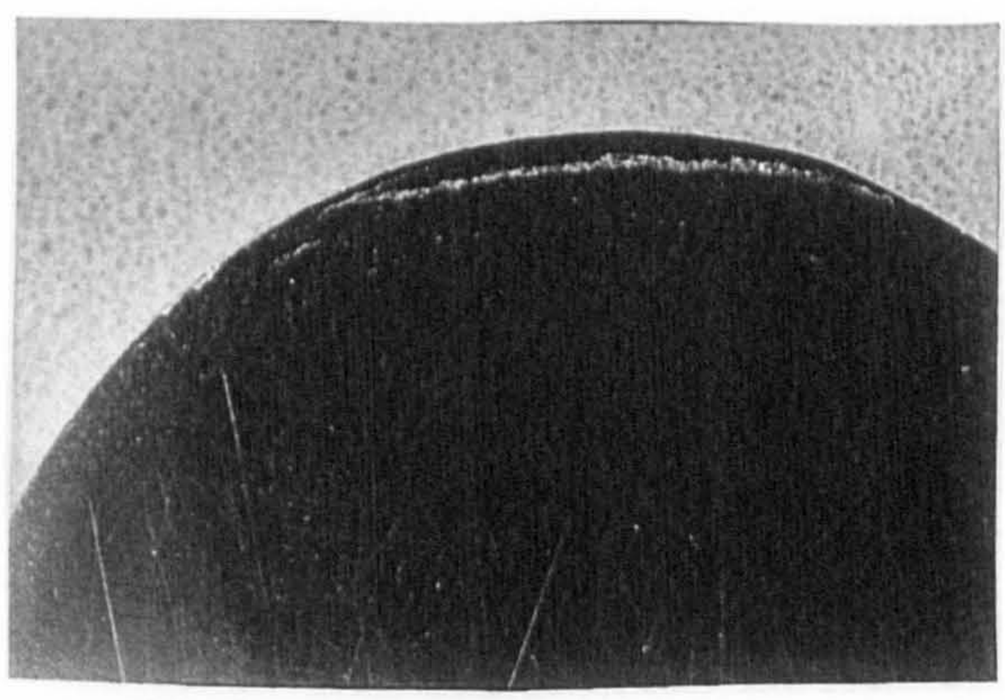

(a) Overall view

(b) Crack at higher magnification

Figure 5.5.14, Subsurface observations (GG3AX)

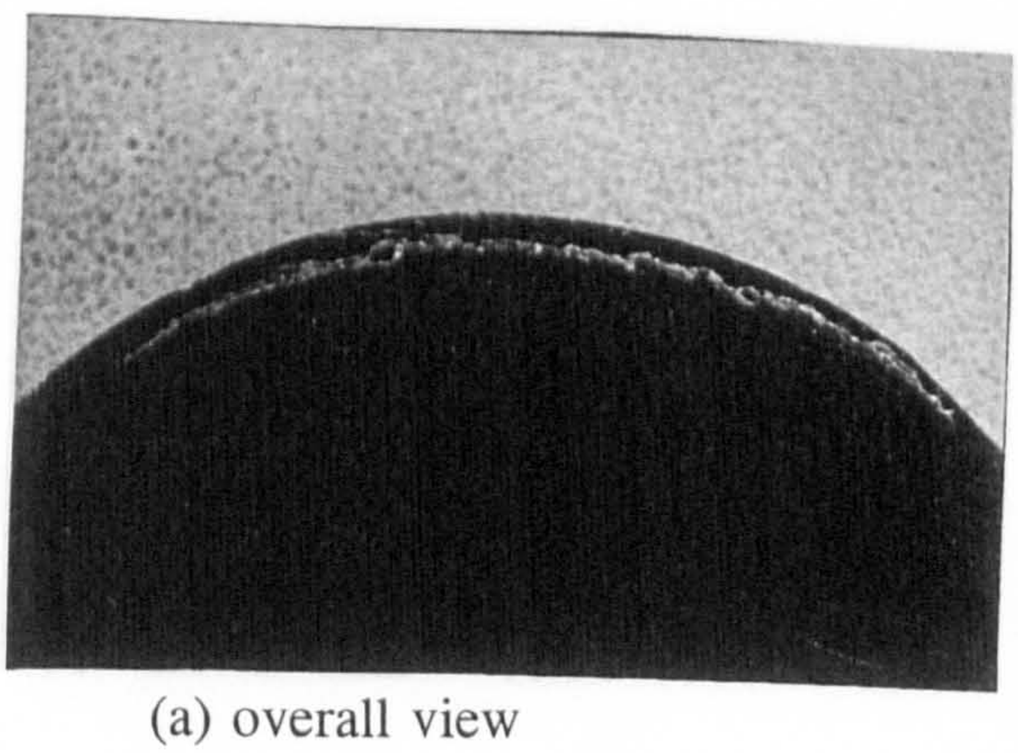

(a) overall view

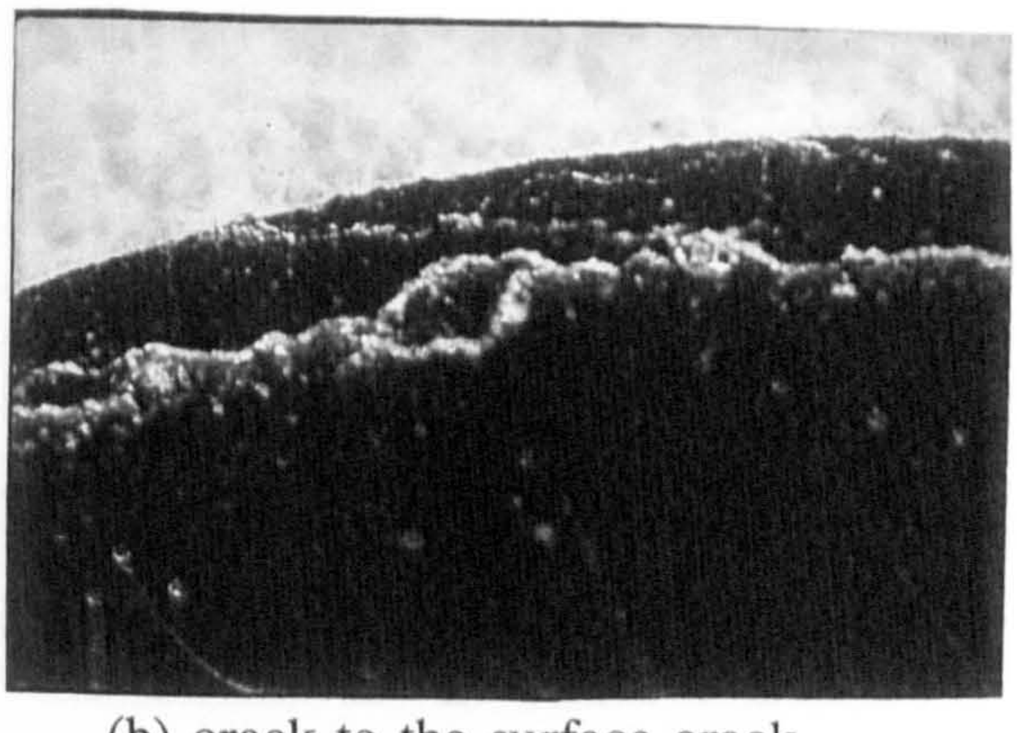

(b) crack to the surface crack

Figure 5.5.15, Subsurface observations (GG3AX)

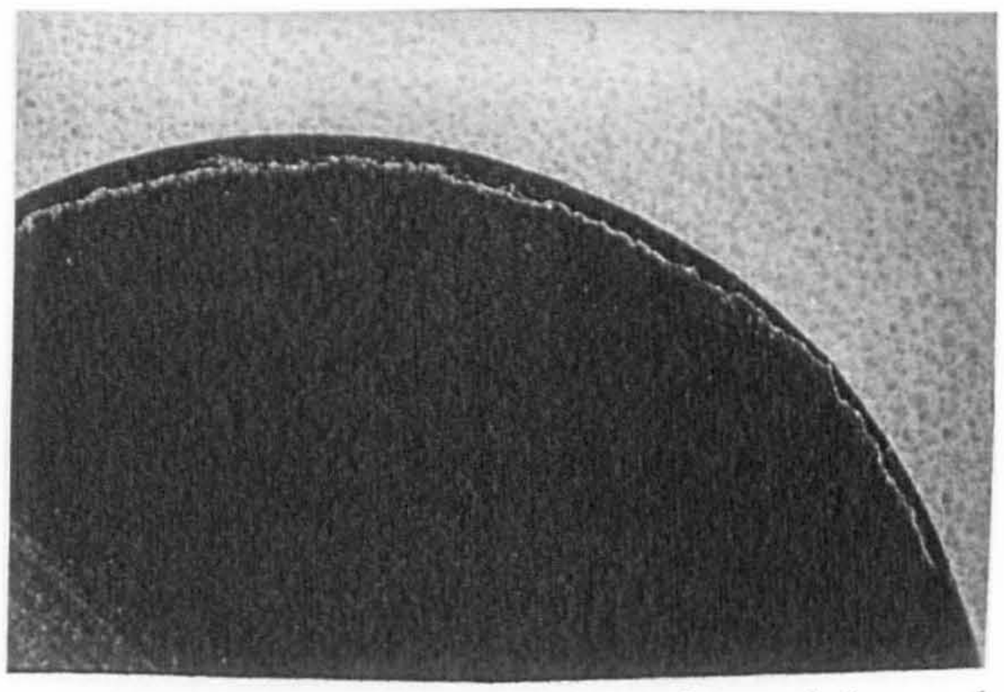

(a) Overall view of circumferential crack

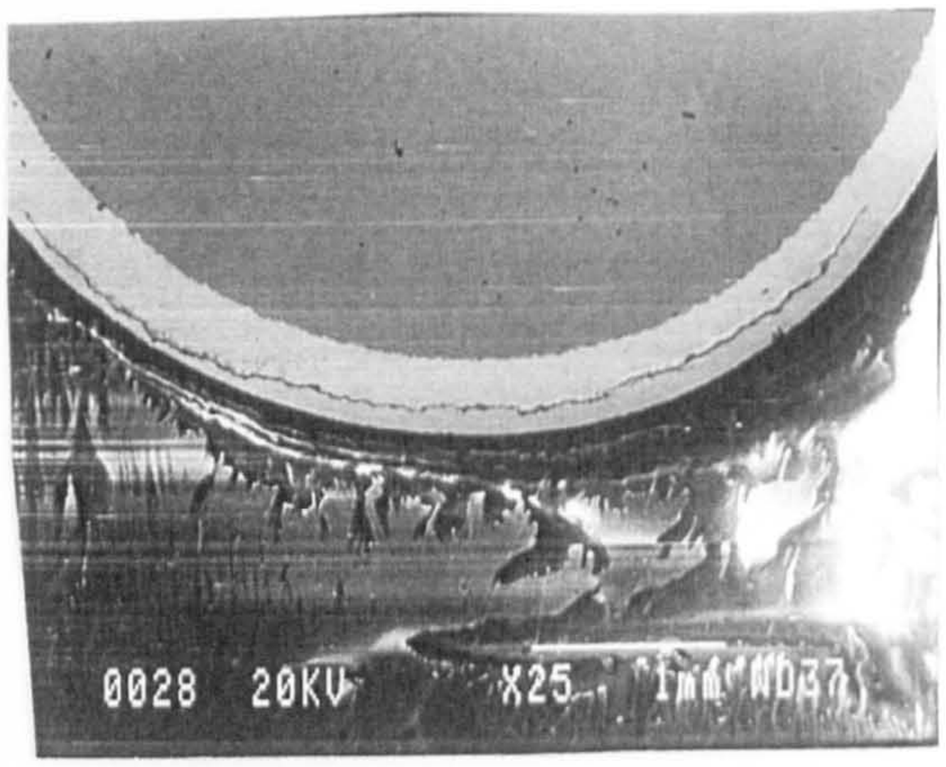

(b) circumferential crack (SEI)

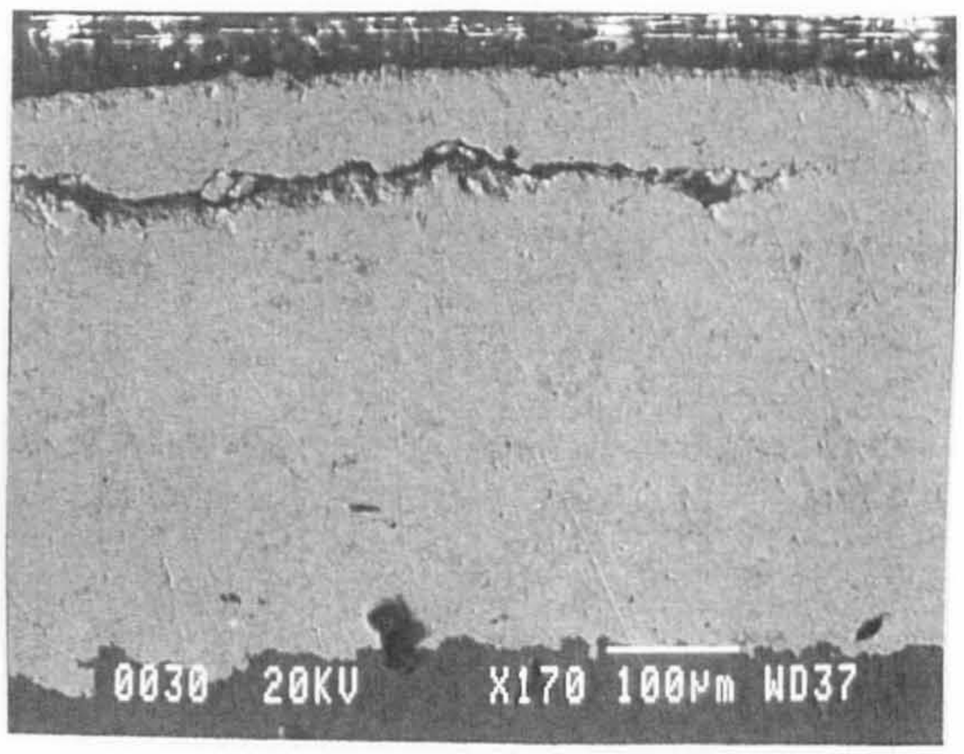

(c) Leading edge circumferential crack

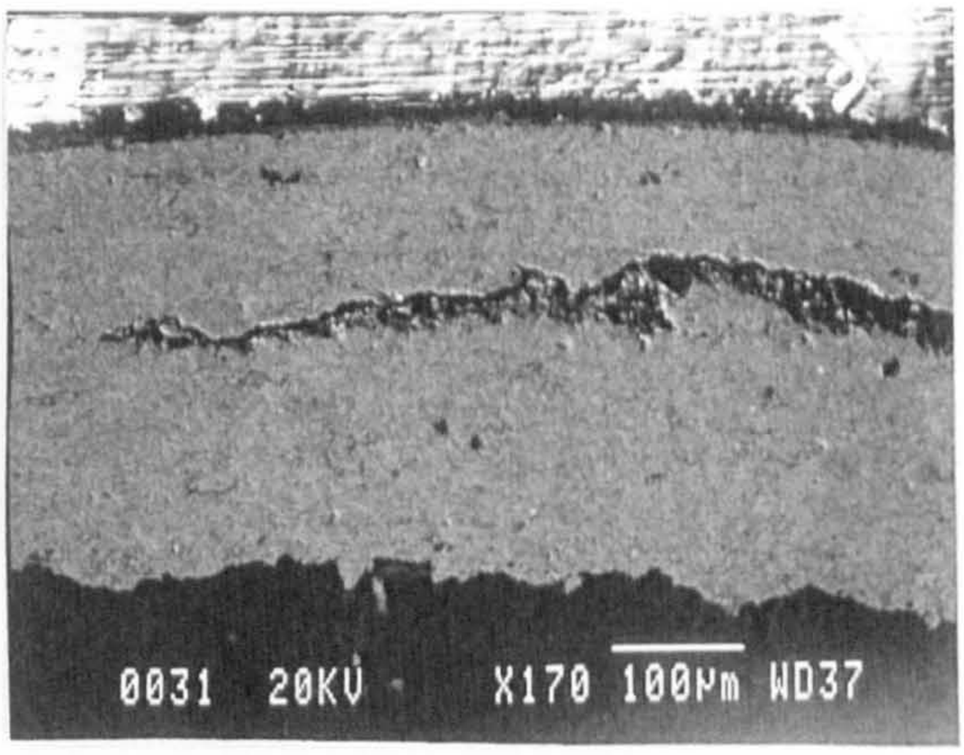

(d) Trailing edge circumferential crack

Figure 5.5.16, Subsurface observations (GG3AX)

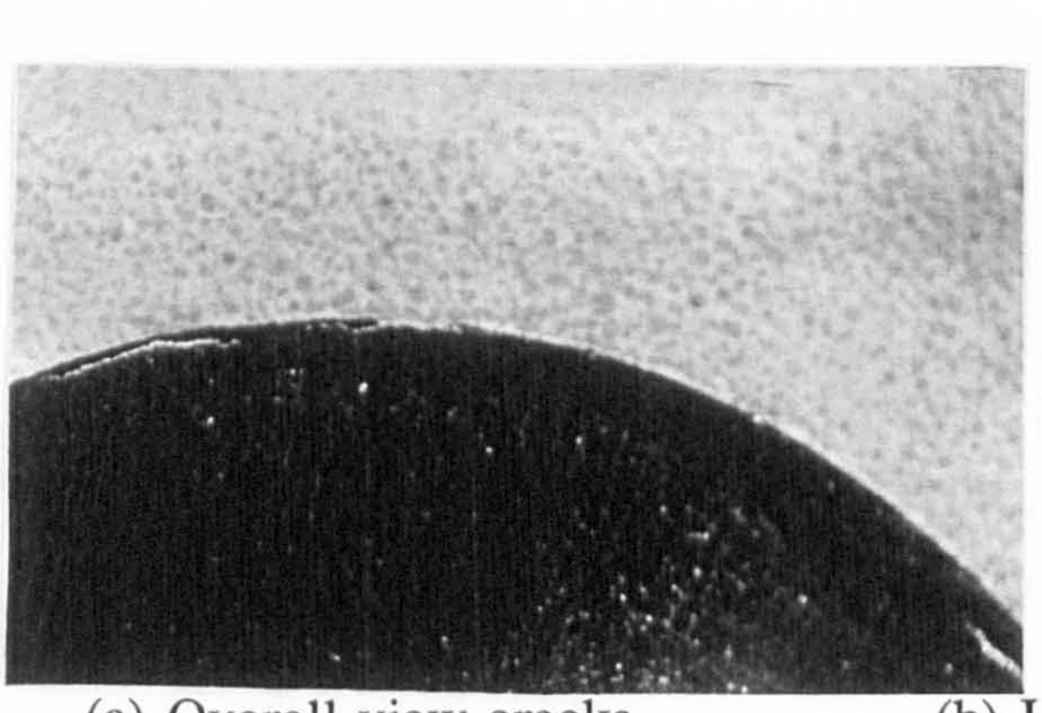

(a) Overall view cracks

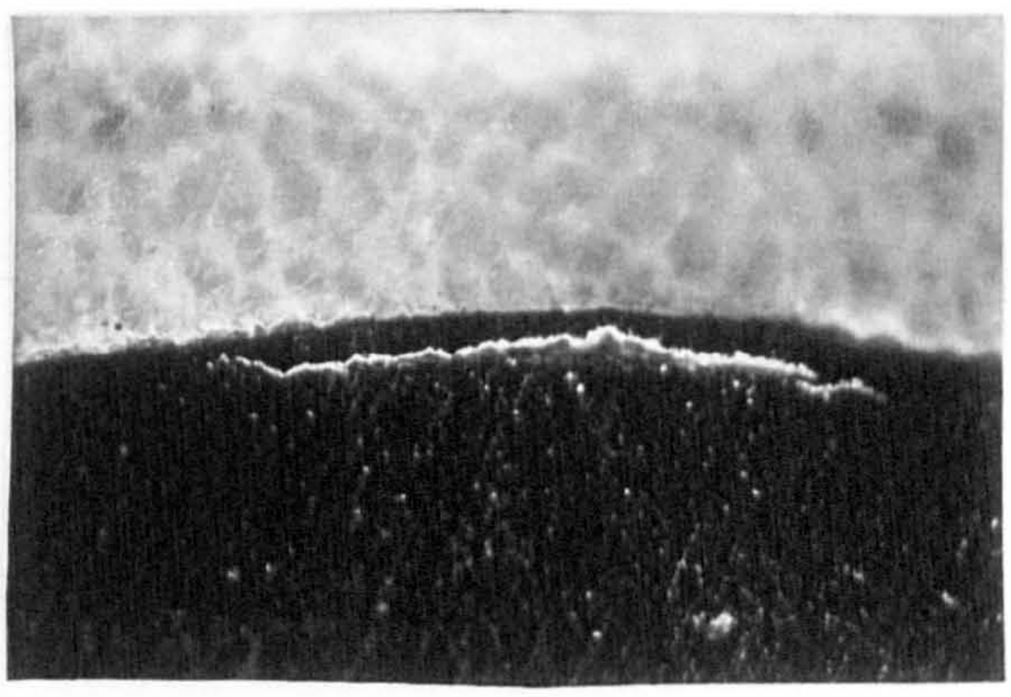

(b) Higher magnification of cracks

Figure 5.5.17, Subsurface observations (GG3AX)

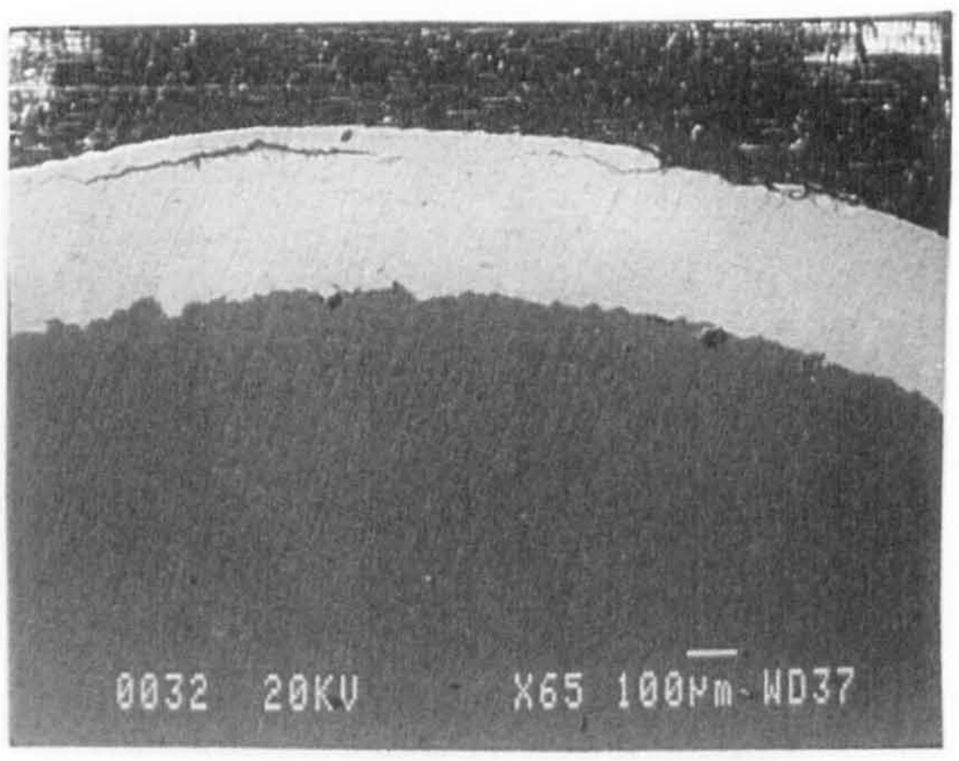

(c) Overall view cracks (SEI)

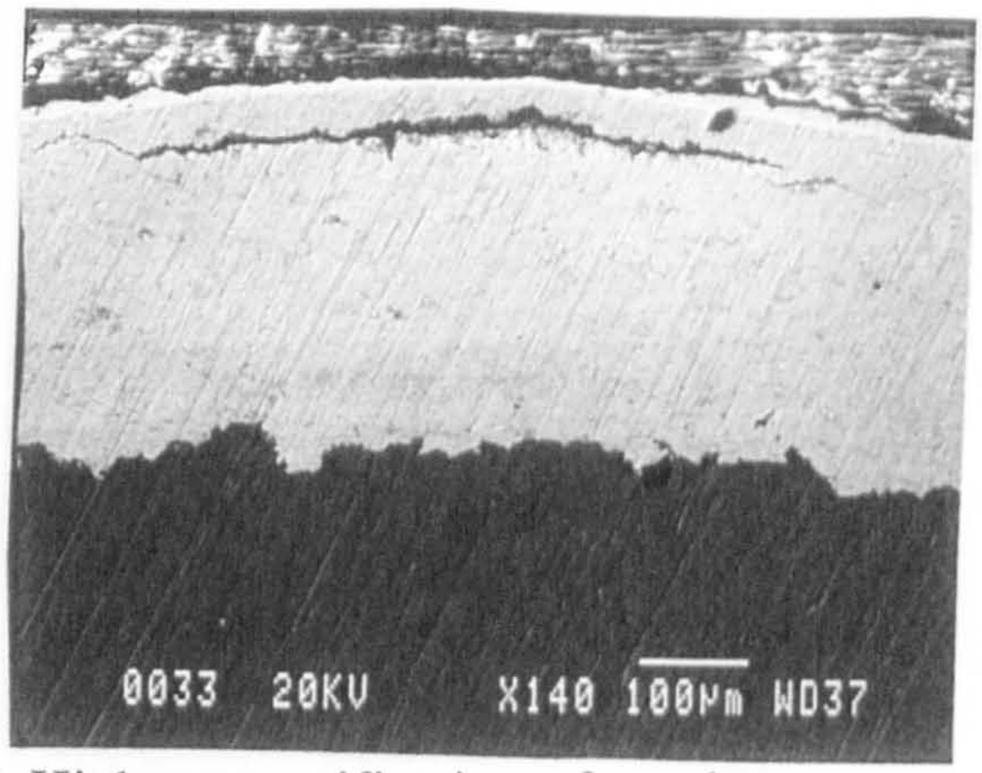

(d) Higher magnification of cracks

Figure 5.5.17, Subsurface observations (GG3AX, continued)

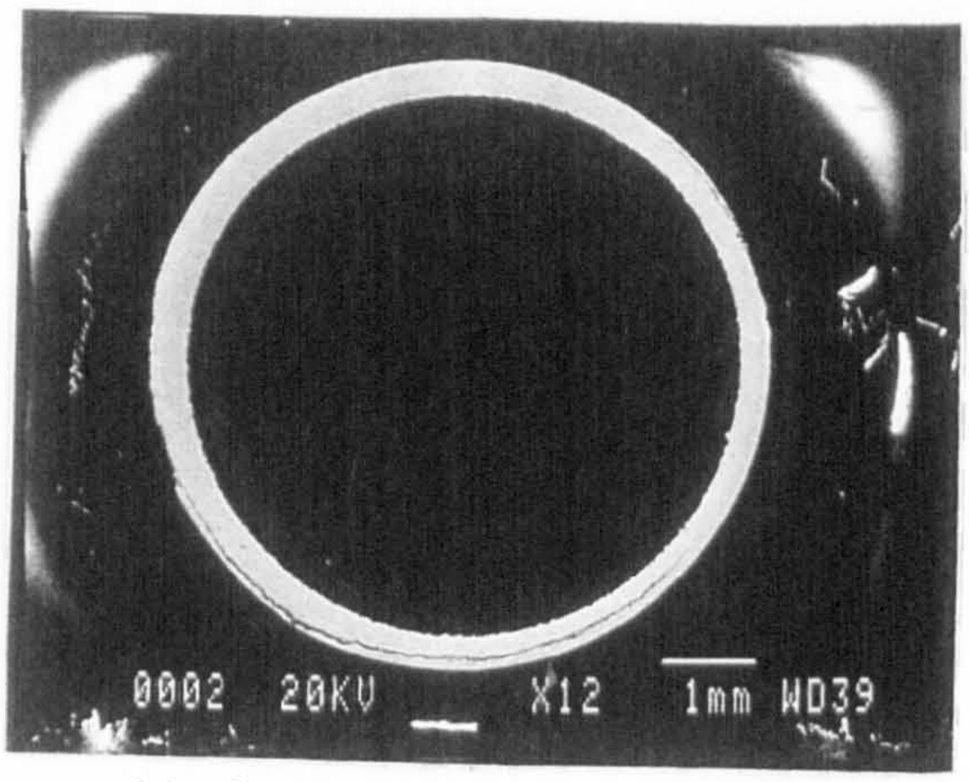

(a) circumferential crack (BEI)

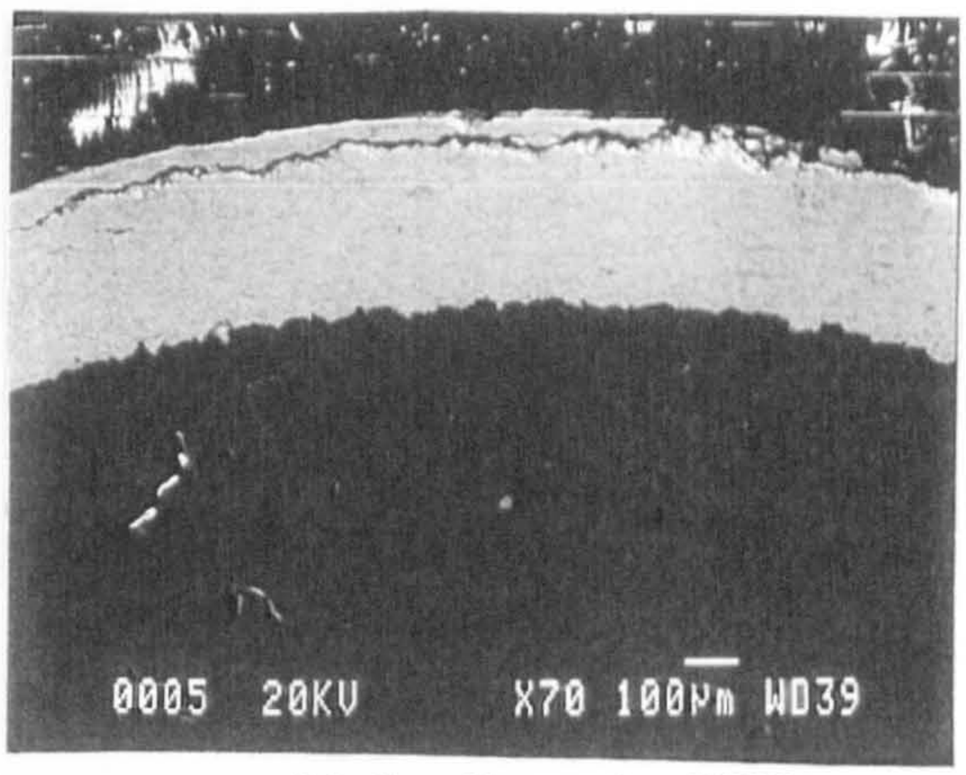

(b) Small cracks (SEI)

Figure 5.5.18, Subsurface observations (GG3AX)

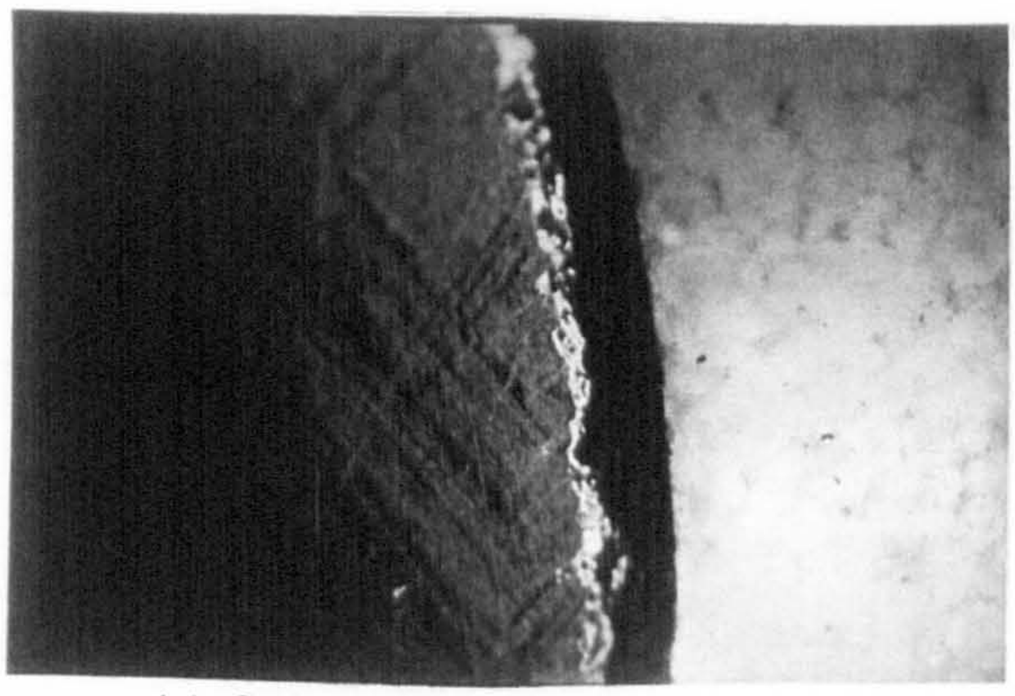

(a) Subsurface cracks

(b) Cracks at another location

Figure 5.5.19, Subsurface observations (GG2BY)

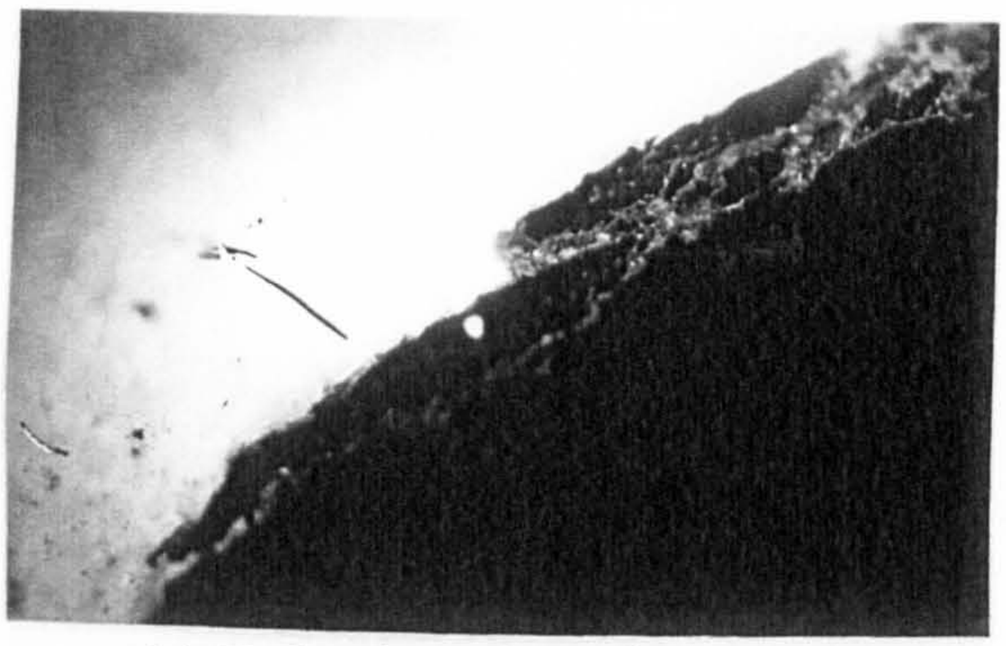

(a) Delaminated portion

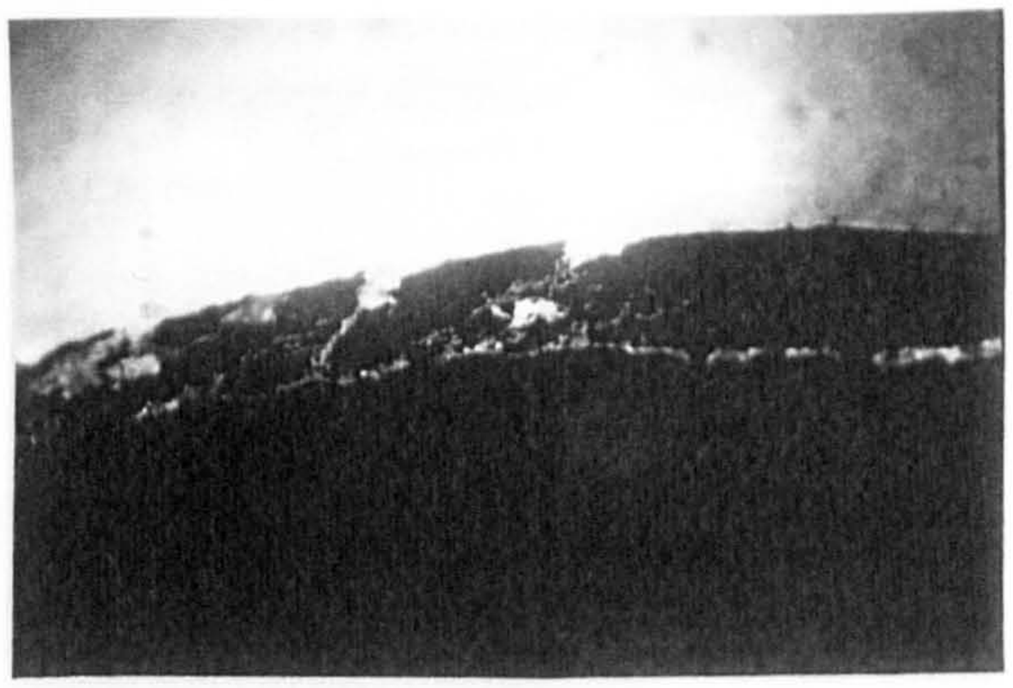

(b) Subsurface cracks

Figure 5.5.20, Subsurface observations (GG2BY)

5.5.9 Microhardness measurements

A Knoop and scratch hardness tester was used to measure the microhardness of plasma sprayed rolling element cones. The microhardness results indicated that the average microhardness of the coating material was 1158 (HV_{300}) and 1139 (HV_{200}). The average microhardness of the substrate material was measured as 700 (HV_{100}). These values were averaged for 12 readings after neglecting the highest and the lowest values.

Attempts were also made to study the indentation fracture toughness (K_{1c}) and the critical strain energy release rate (G_c) of thermal spray coatings. However, even after repeated attempts and extreme care to prepare the surface for microhardness indentations, it was not possible to obtain a reliable value of K_{1c} or G_c. It was mainly because the coating cracked at some locations at an indentation load of 100p and at other locations at load of a 300p or 500p. Moreover, the cracks did not satisfy the criteria ($C > 2b$).The cracks did not always originate from the notch of the diamond indentation but also from the sides of indentation. This indicates that the stress concentrations at the pores and micro-cracks within the coating microstructure were higher than the theoretically applied load which caused the cracks to originate and propagate during the indentation process. Figure 5.5.21 (a) shows a typical result in which the coating cracked at an indentation load of 300p. Moreover it was observed that the cracks at any indentation load did not necessarily

originate from the notch of the diagonal but seemed to be appearing from the sides at different orientations. Some of these observations are shown in figure 5.5.21(b).

(a) Indentation at 300p (SEI)

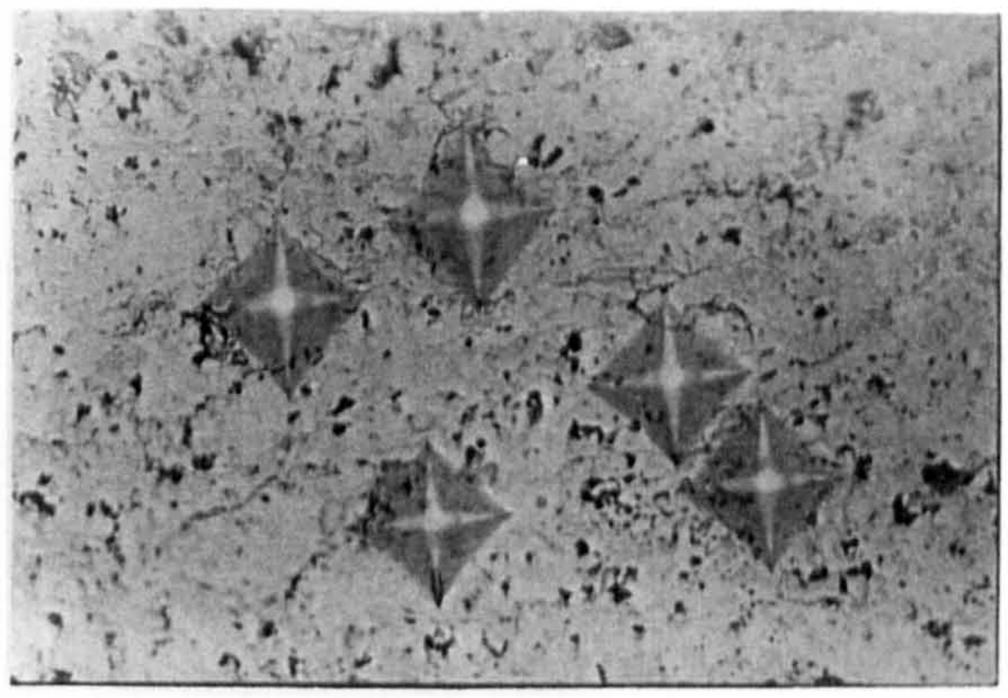

(b) Indentations at 500p

Figure 5.5.21, Microhardness indentations

5.6 High Velocity Oxy-Fuel Coated Cone on Bearing Steel Substrate

5.6.1 Introduction

This section of the thesis deals with the case of coated rolling elements which were thermally sprayed to produce WC-12%Co coatings using the High Velocity Oxy Fuel process on the surface of bearing steel (440-C) coated rolling element cones.

5.6.2 Coated cone test elements

Thermally sprayed tungsten carbide cobalt (WC-12%Co) coatings produced by the HVOF process were deposited on the surface of the 440-C steel rolling element cones. The spray system was JP5000 and the spraying direction was perpendicular to the apex of the cone by placing them on a rotating disc. The technique has already been described in the case of coated rolling element balls on M-50 steel substrate (figure 5.4.1). The substrate material was sand blasted and preheated to a temperature of approximately above 100°C (manufacturers data). The average as-sprayed coating thickness of the rolling element balls were 300μm, 200 μm and 100μm . The rolling elements were ground and polished to give an average coating thickness of 250$\pm$15μm, 150$\pm$15μm and 60$\pm$15μm respectively. The surface roughness (R_q) of the coated rolling elements after grinding and polishing was measured to be 1.5$\pm$0.5μm(R_q) and 0.065$\pm$0.015μm(R_q).

5.6.3 Test conditions and experimental test results

The RCF tests during this study were conducted under immersed lubrication conditions using B.P. Hitec-174 and Exxon-2389 as the test lubricant at an ambient temperature of approximately 23 °C and at a shaft speed of 4000 $\pm$ 5 rpm. The cup assembly was loaded at two different contact loads of 160 N and 400 N in conventional steel ball bearing (steel planetary balls) and hybrid ceramic bearing (ceramic lower balls) configurations. The ratio (λ) of the approximate value of the Elasto-Hydrodynamic Lubrication (EHL) film thickness to the average surface roughness for the test lubricants Hitec-174 and Exxon-2389 under the given test conditions were calculated to be approximately 8.4 and 1.6 respectively for the RCF tests at a contact load of 160 N and 7.8 and 1.4 respectively for the RCF tests at contact load of 400 N. These calculations were based on the case of steel planetary

balls the details of which can be seen from appendix E. The experimental test procedures described in Chapter 2 (article 2.3) were followed. Experimental measurement of the gross sliding in the four ball system by measuring the orbital speed of the planetary balls and the frictional torque in the cup assembly during the RCF tests was done using the techniques described in article 2.5 and 2.6 respectively.

Table 5.7 shows the RCF test results for the HVOF coated rolling element cones on bearing steel (440-C) substrate under the various tribological conditions of testing. Results are presented in terms of the test configuration, Hertz contact stress, average frictional torque, overall sliding and, the time to failure. The magnitude of Hertz stress shown in table 5.7 represents the case of uncoated rolling elements. The RCF test results give an appreciation of the performance of the coated elements and are not intended to be used as a basis for the statistical fatigue life prediction. Appendix D gives the details of the magnitude and location of the maximum shear stress and orthogonal shear stress under the contact surface.

5.6.4 Surface observations

Figure 5.6.1 shows the surface observations of the 250 μm thick coated rolling element cone tested with steel lower balls (test HVBS1). Figure 5.6.1(a) shows the overall view of the wear track in Backscattered Electron Image (BEI). This test was suspended after more then 100 hours of testing. Figure 5.6.1(b) shows a view of the wear track of this rolling element in BEI. Surface wear was appreciable on the surface of the wear track. Figure 5.6.2 shows the surface observations of the 250 μm thick coated rolling element subjected to the RCF test HVBS2. Figure 5.6.2(a) shows the BEI of the overall view of the failed coating area in Secondary Electron Image (SEI). Figure 5.6.2(b) shows the surface observation of the wear track in BEI. Surface wear and micropits were visible on the surface of the wear track which were similar but more prominent and larger than the one seen in the wear track of HVBS1 (figure 5.6.1(a)). Figure 5.6.3 shows the surface observations of the coated rolling element subjected to the test conditions described for the test HVBS3.

Test No	Coating thickness (μm)	Contact load (N)	Lower balls	Contact stress* (GPa)	Contact width (mm) (b)	Depth of max: shear (0.65b) (μm)	Maximum lubricant temperature (°C)	Sliding (%)	Frictional Torque (N.m)	No: of stress cycles (10^6)	Time to Failure (minutes)
HVBS1	225	160	steel	2.7	0.13	85	36	-0.3	0.022	68.58	7620**
HVBS2	225	160	ceramic	3.1	0.12	80	37	+0.5	0.021	30.78	3240
HVBS3	250	160	steel	2.7	0.13	85	29	+0.9	0.028	12.96	1440
HVBS4	250	400	steel	3.7	0.18	115	44	-0.3	0.015	13.545	1505
HVBS5	150	160	steel	2.7	0.13	85	36	-0.3	0.013	54.45	6050**
HVBS6	150	160	ceramic	3.1	0.12	80	40	+0.9	0.02	19.71	2190
HVBS7	150	160	steel	2.7	0.13	85	31	+0.9	0.035	14.58	1620
HVBS8	150	400	steel	3.7	0.18	115	45	+0.5	0.037	4.158	462
HVBS9	50	160	steel	2.7	0.13	85	37	+0.5	0.011	1.242	138
HVBS10	50	160	ceramic	3.1	0.12	80	40	+0.5	0.028	0.756	84
HVBS11	50	160	steel	2.7	0.13	85	29	+1.3	0.05	0.486	54
HVBS12	50	400	steel	3.7	0.18	115	30	+0.5	0.021	0.036	04

* UNCOATED CASE, ** Suspended test,

Table 5.7, Rolling contact fatigue test results for HVOF coated rolling element balls on bearing steel (440-C) substrate

Figure 5.6.3(a) shows the overall view of the wear track in the SEI. Figure 5.6.3(b) shows the surface observation of the failed areas within the wear track at a higher magnification. Pits and delamination can be seen on the surface of the wear track. Figure 5.6.3(c) shows the failed coating area on the right hand side in figure 5.6.3(c) at a higher magnification. Figure 5.6.3(d) shows an inclined angle view of the delaminated coating and the depth of delamination can be approximated as 40 μm. However, other delamination on the surface of this rolling element was observed to be approximately 110 μm deep. Figure 5.6.4 shows the surface observations of the 250 μm thick coated rolling element HVBS4. The test was conducted with the steel lower balls at a contact stress of approximately 3.7 GPa. Figure 5.6.4(a) shows the wear track whereas figure 5.6.4(b) shows the pits at a higher magnification in BEI.

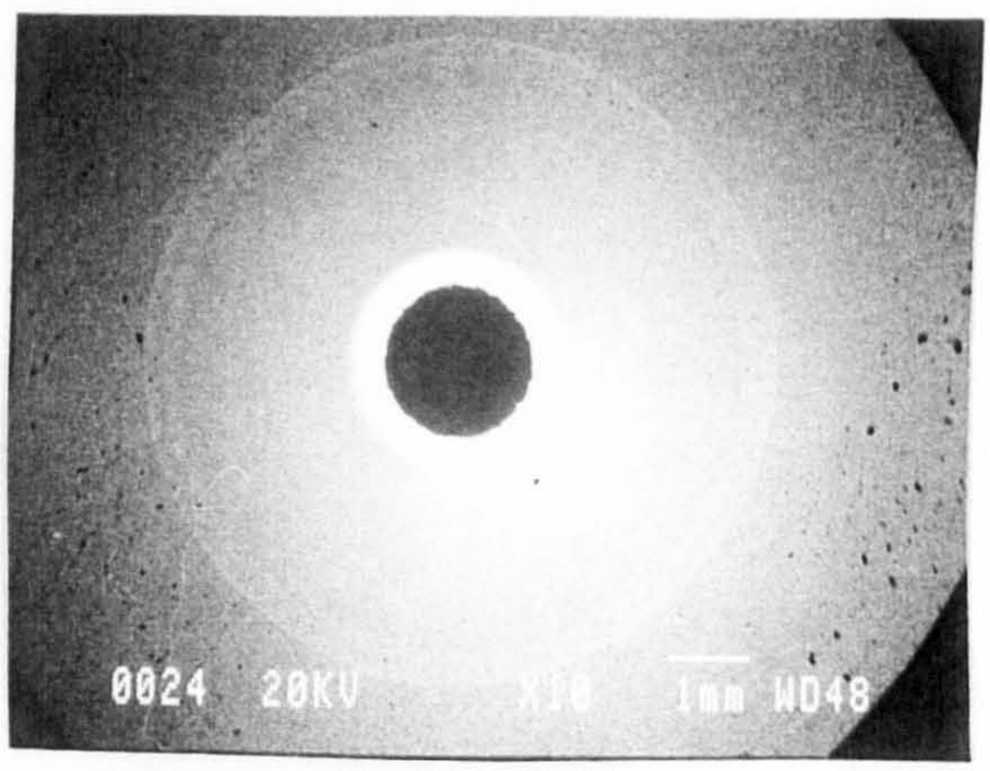

(a) overall view (BEI)

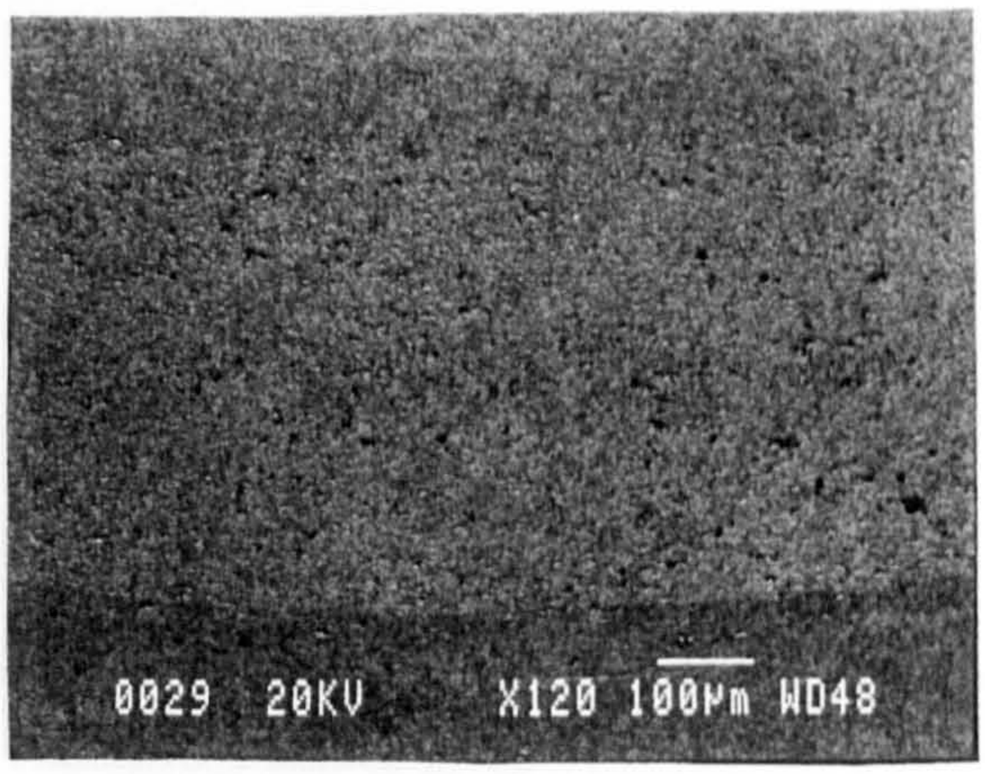

(b) wear track (BEI)

Figure 5.6.1, Surface observations of the rolling element cone (Test HVBS1)

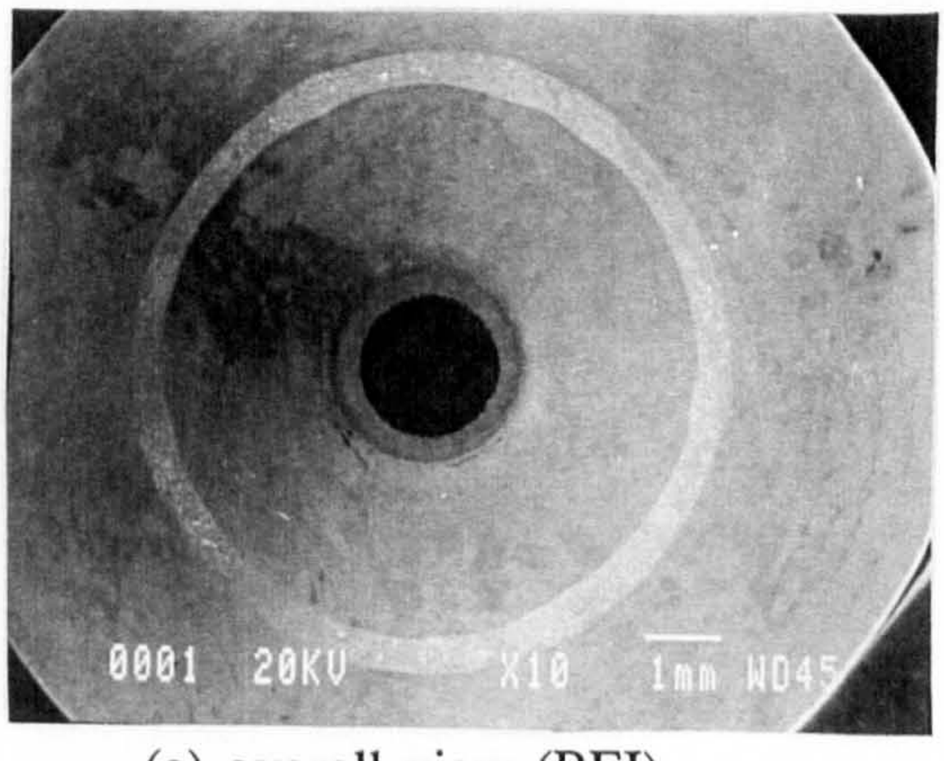

(a) overall view (BEI)

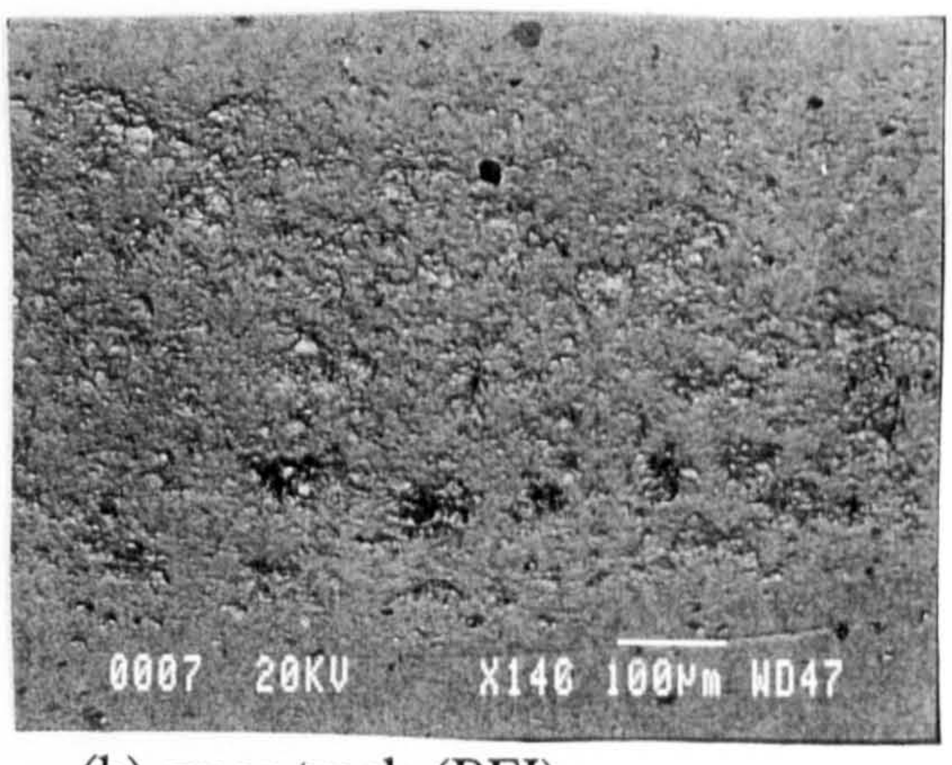

(b) wear track (BEI)

Figure 5.6.2, Surface observations of the rolling element cone (Test HVBS2)

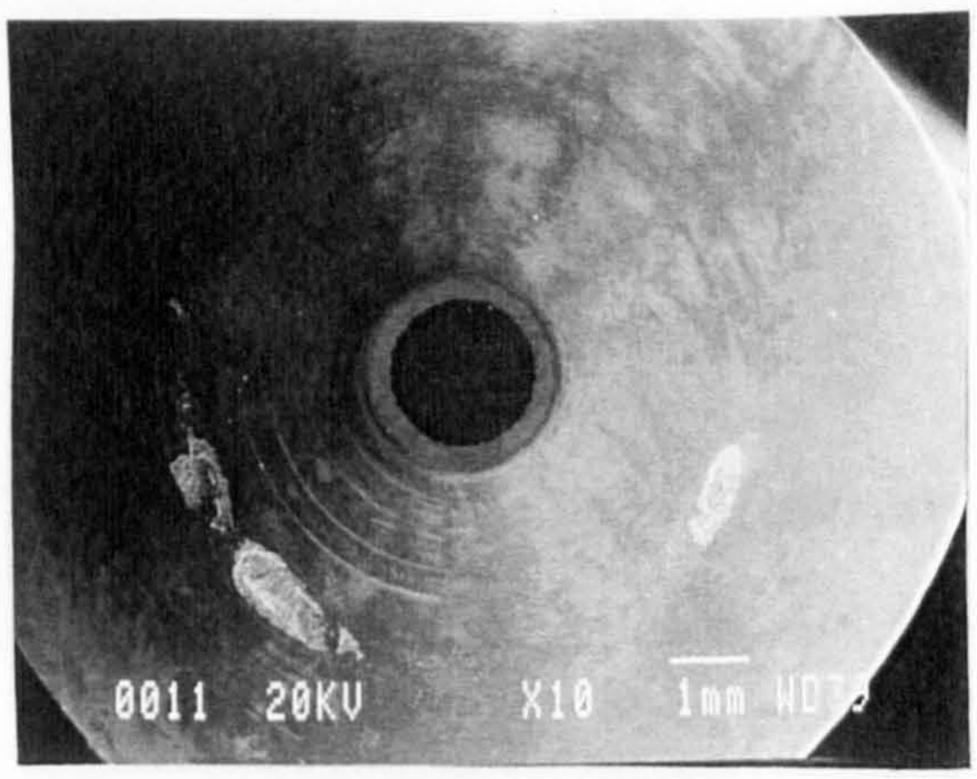

(a) overall view (SEI)

(b) failed area (SEI)

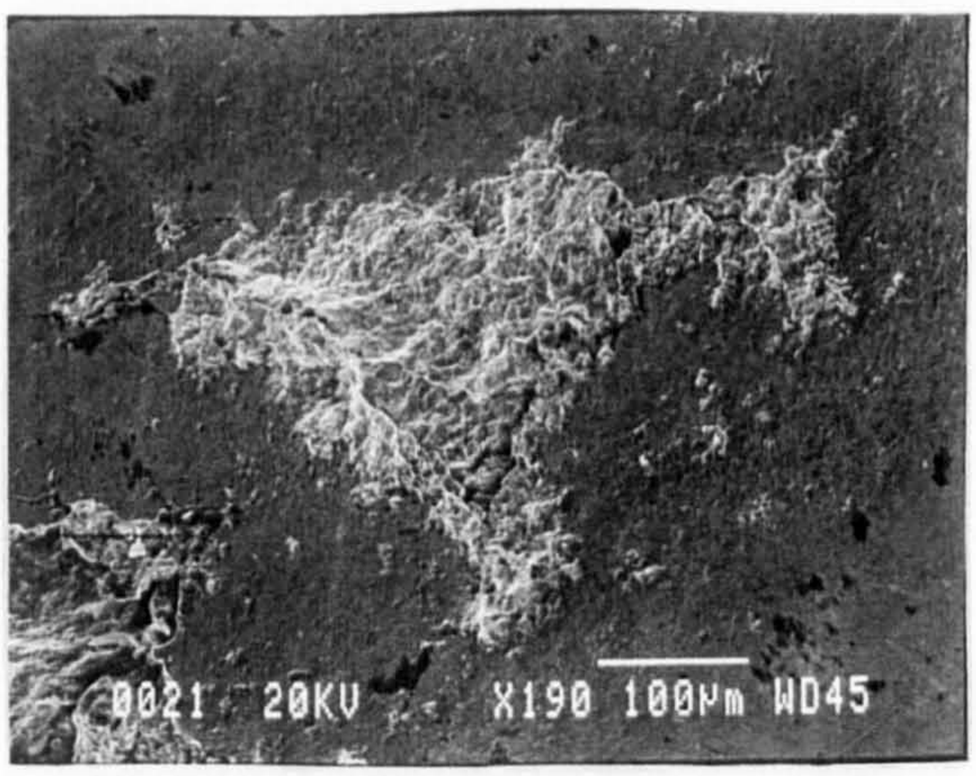

(c) higher magnification (SEI)

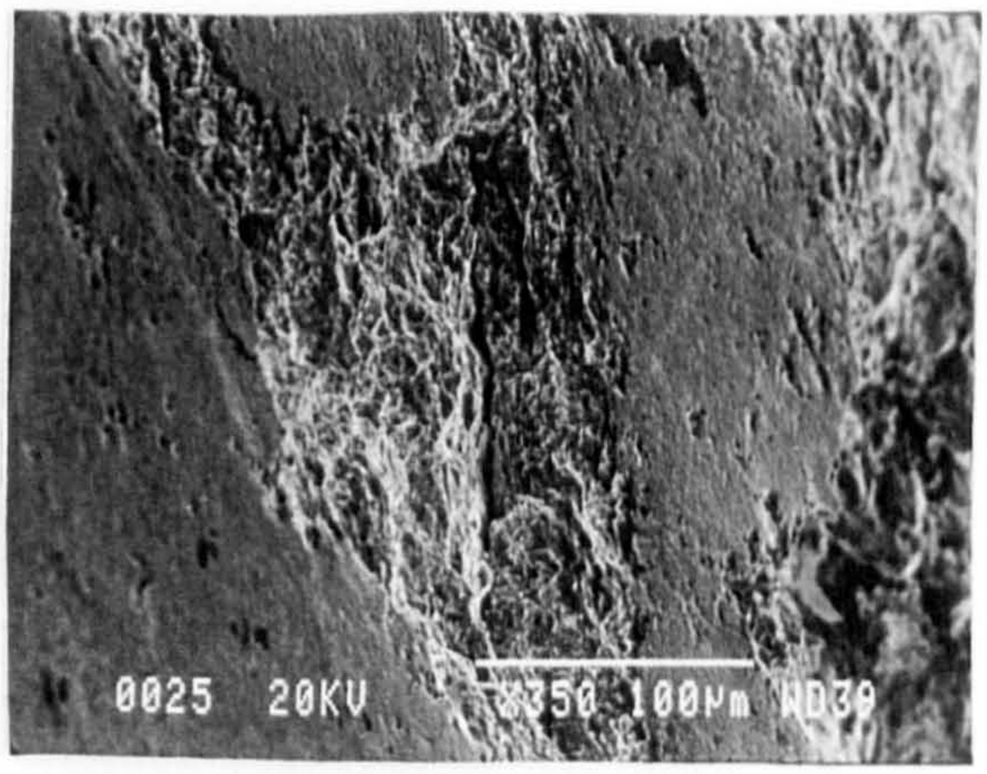

(d) inclined view (SEI)

Figure 5.6.3, Surface observations of the rolling element HVBS3

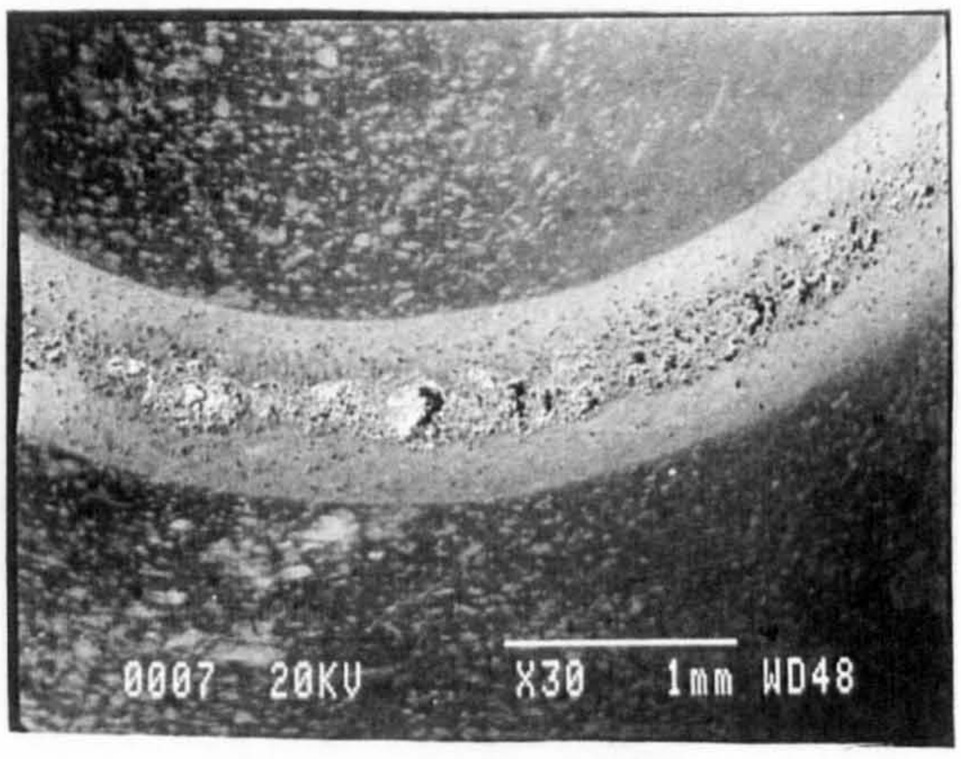

(a) wear track (SEI)

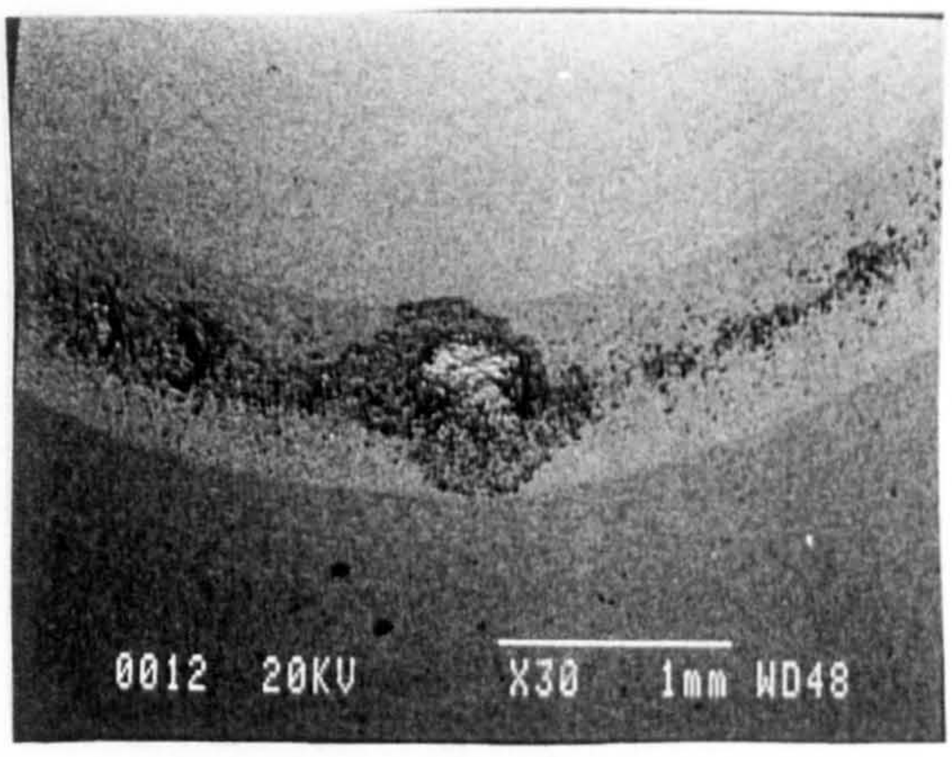

(b) higher magnification (BEI)

Figure 5.6.4, Surface observations of the rolling element HVBS4

The surface observations of the 150 μm thick coated rolling element cones were similar to the failures shown for the 250 μm thick rolling element cones described above. Figure 5.6.5 shows the surface observations of the 60 μm thick coated rolling element cones. Figure 5.6.5(a) shows the overall view of the failed coating of the rolling element HVBS11 in BEI. Figure 5.6.5(b) shows the failed coating area at a higher magnification. It was appreciated that in all of the cases of the 60 μm thick coated rolling element cones, the coatings failed by delaminating at the coating substrate interface. The test lubricant used for the RCF tests was also analyzed for the wear debris particles and those debris were similar to what were seen in the previous sections.

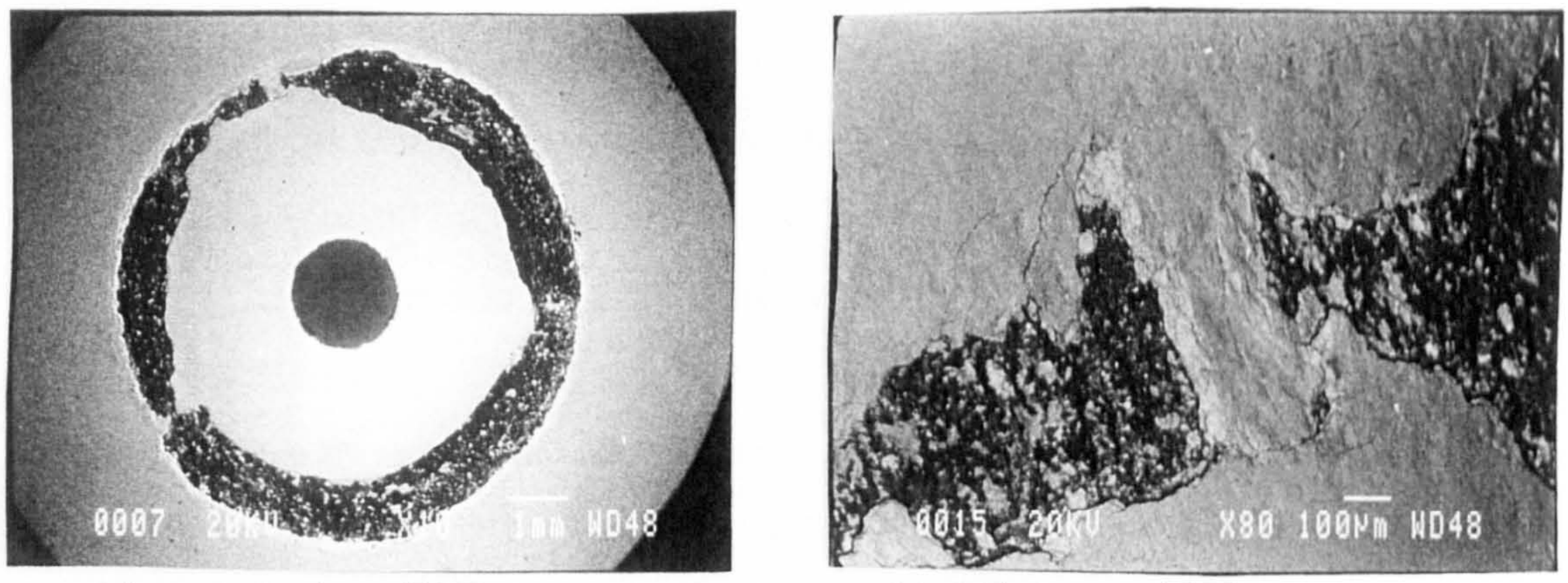

(a) overall view (BEI) (b) failed area (BEI)

Figure 5.6.5, Surface observations of the 60 μm thick coated rolling elements

5.6.6 Coating microstructure

Figure 5.6.6 shows a typical microstructure of the coating cross section in SEM. Numerous pores were evident in the coating microstructure. However, there did not seem to be microcracks appreciable at magnifications up to 6000×. The X-ray diffraction analysis of the microstructure confirmed that the amount of retained WC particles was high with small quantities of W_2C particles.This was verified by the atomic contrast in the BEI and using some X-Ray diffraction patterns. Figure 5.6.6(a) shows a typical image in SEI whereas, figure 5.6.6(b) shows the same image in BEI.

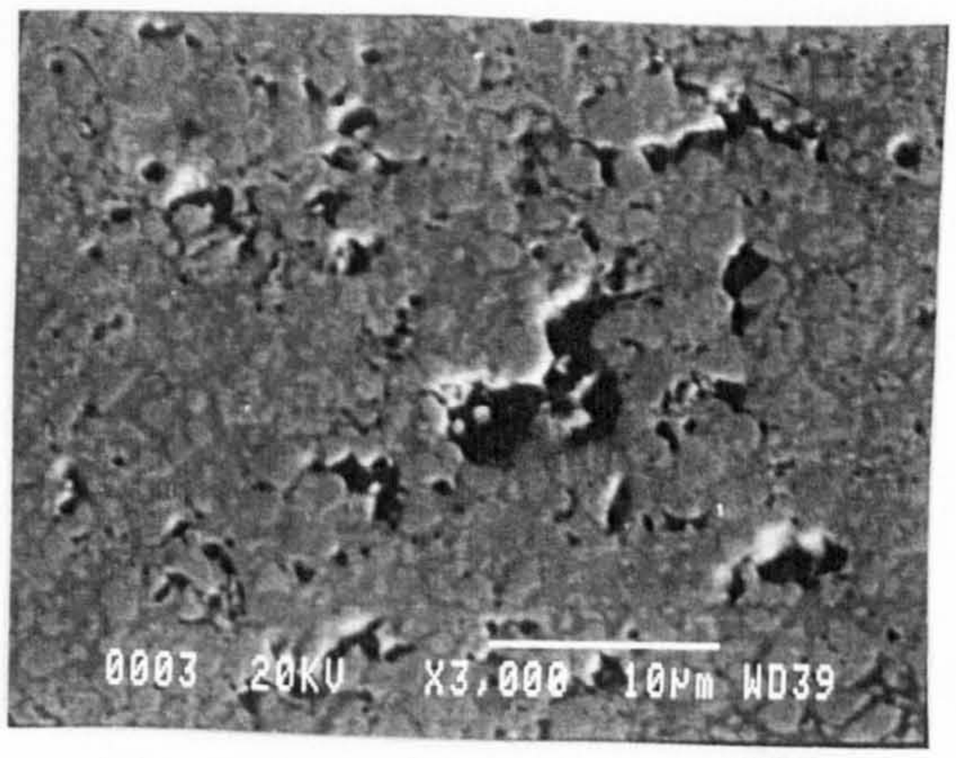

(a) coating microstructure (SEI)

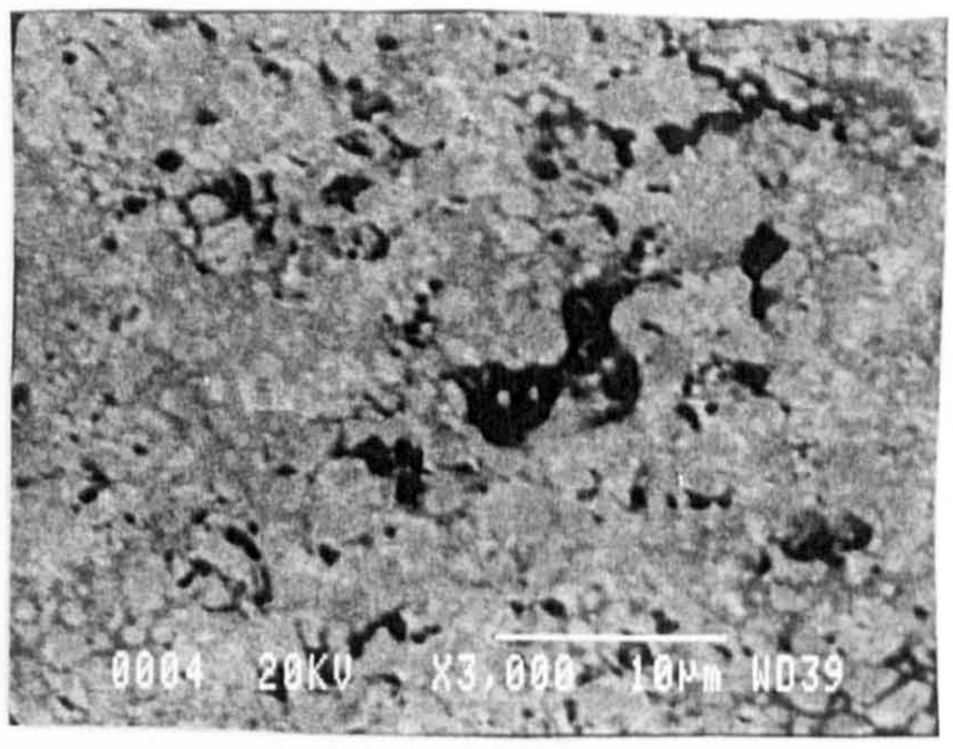

(b) coating microstructure (BEI)

Figure 5.6.6, Coating microstructure

5.6.7 Microhardness measurements

A Knoop and scratch hardness tester was used to measure the microhardness of thermally sprayed rolling element balls. The microhardness results indicated that the average microhardness of the coating material (HV_{300}) was 1296 and the average microhardness of the substrate material (HV_{100}) was 728. These values were averaged after neglecting the highest and the lowest values. Attempts were also made to calculate the indentation fracture toughness of thermal spray coatings using the indentation technique. The surprising result was that the coatings did not crack at indentation loads as high as 500p. Out of 10 indentations at a load of 500p and 15 indentations at an indentation load of 300p only one indentation cracked. Figure 5.6.7(a) shows an overall view of these indentations at the loads of 300p and 500p, whereas figure 5.6.7 shows a diamond indentation at an indentation load of 500p at a higher magnification. It was concluded that these coatings had an improved indentation fracture toughness in comparison to the coatings in the previous cases. However, it was not possible to evaluate the values of indentation fracture toughness K_{1c} and the critical strain energy release rate (G_c) as the cracked indentation did not fulfil the criteria 'C > 2b', where 'C' was the crack length and '2b' was the diagonal of the diamond indentation.

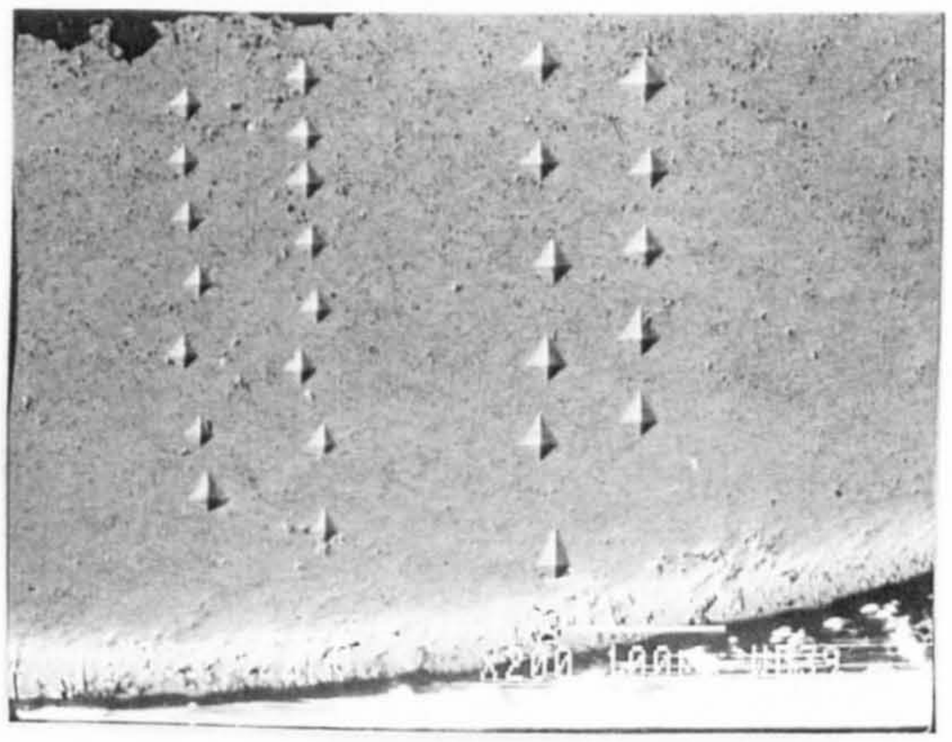

(a) microhardness indentations

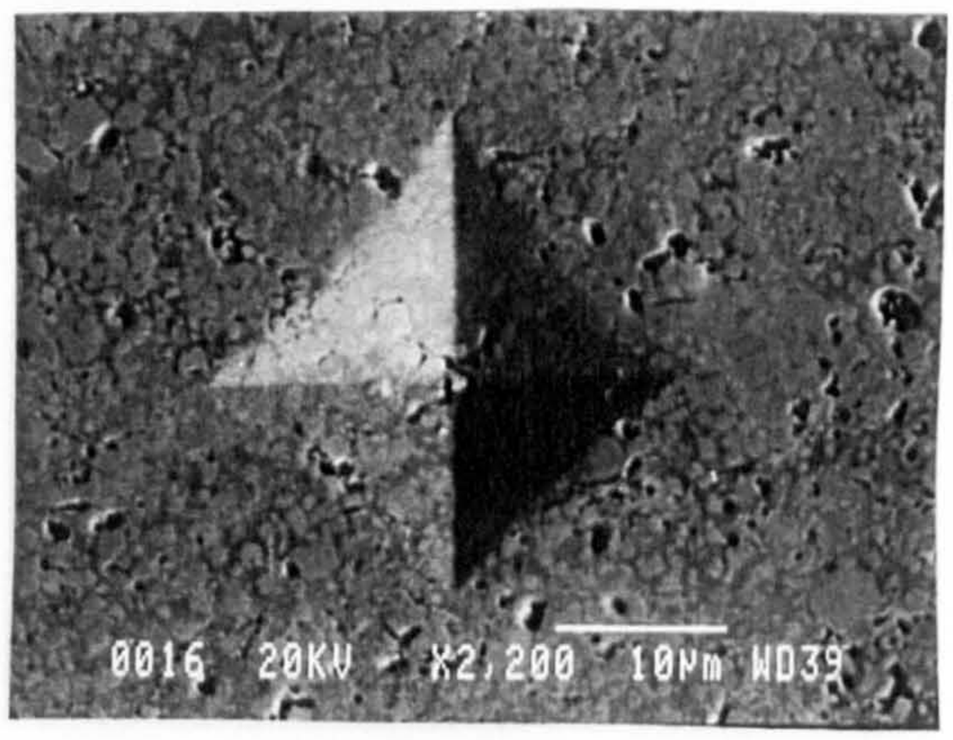

(b) indentation (500p)

Figure 5.6.7, Microhardness indentation

5.6.8 Subsurface observations

The subsurface observations of some of the failed coated rolling elements were carried out using the dye penetrant technique already described in chapter 4 of the thesis. Figure 5.6.8 shows the typical observations of the coated rolling element cone HVBS3. Figure 5.6.8(a) shows the appearance of subsurface cracks under the wear track and the appearance of delaminated coating on the surface of the wear track. The contact depth of these cracks was approximated as 110 μm and the coating thickness as 270 μm. Figure 5.6.8(b) shows these subsurface cracks at a higher magnification. These cracks were parallel to the surface of the rolling element. As more grinding was carried out the length of the crack increased and a minute crack also appeared to the right of the long crack as shown in figure 5.6.8(c). As grinding/sectioning continued the length of the crack extended and the tiny crack which was seen on the right of long crack, joined with the long crack. Figure 5.6.8(d) shows the extended length of the subsurface crack which joined the delaminated part of the coating. Some other subsurface cracks were also seen extending from the delaminated coating as seen on the right hand side. Figure 5.6.8(e) shows the cracks joining the delaminated coating at a higher magnification. The delaminated coating from within the coating microstructure and the small and large subsurface cracks appeared as the grinding/sectioning continued. At this stage the sectioned coated rolling element cone was observed under the Scanning Electron Microscope (SEM). Figure 5.6.8 (f) shows the overall view of the sectioned rolling

element in SEI. Figure 5.6.8(g) shows the delaminated coating at a higher magnification. Numerous cracks can also be seen from this figure.

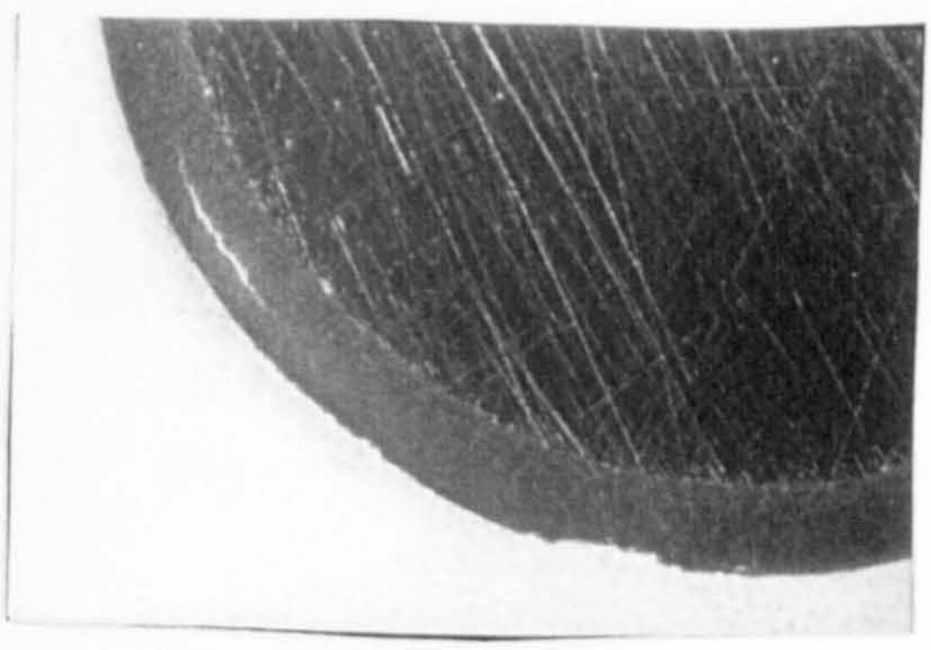

(a) subsurface cracks

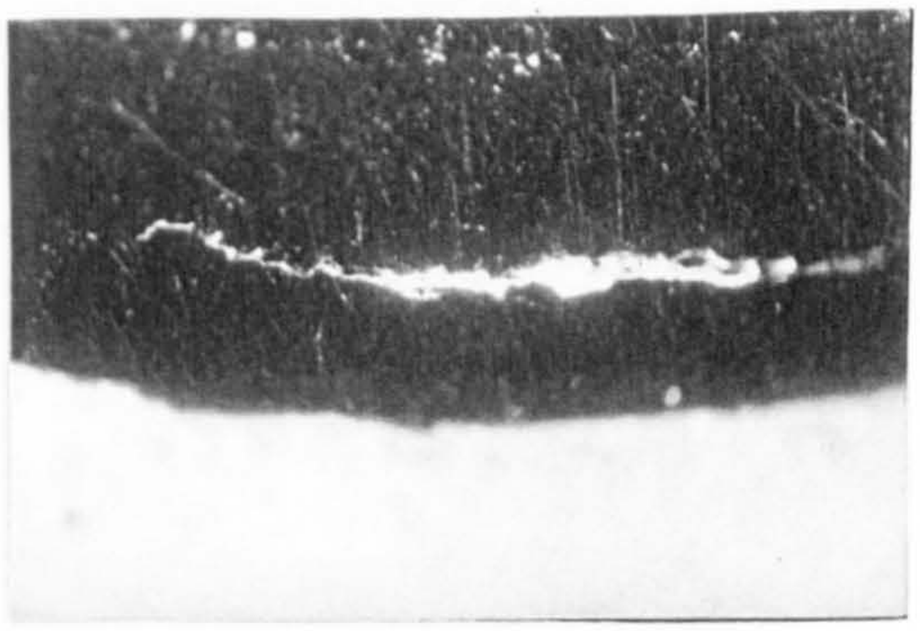

(b) higher magnification

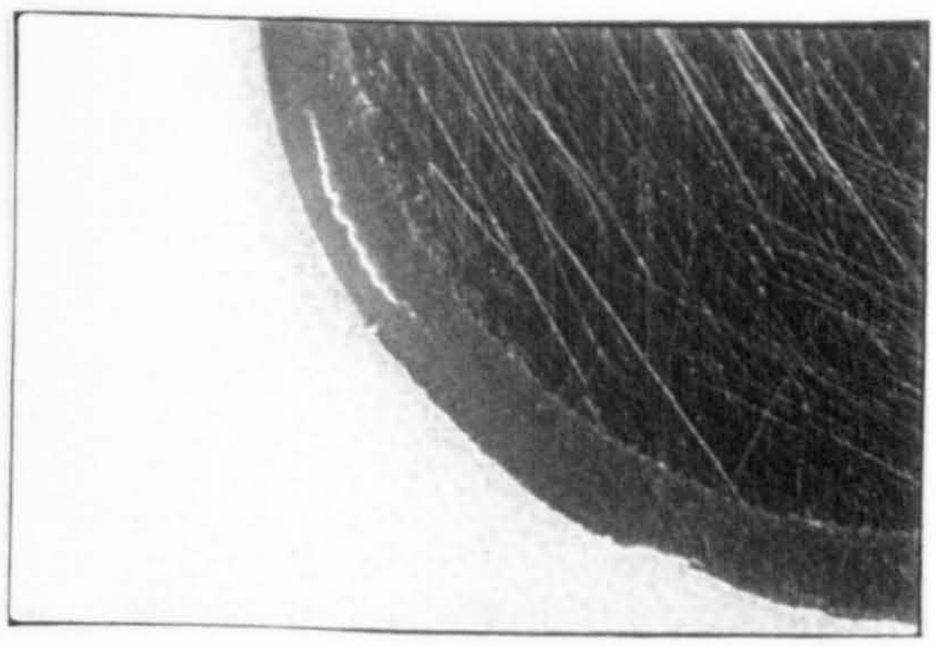

(c) subsurface cracks

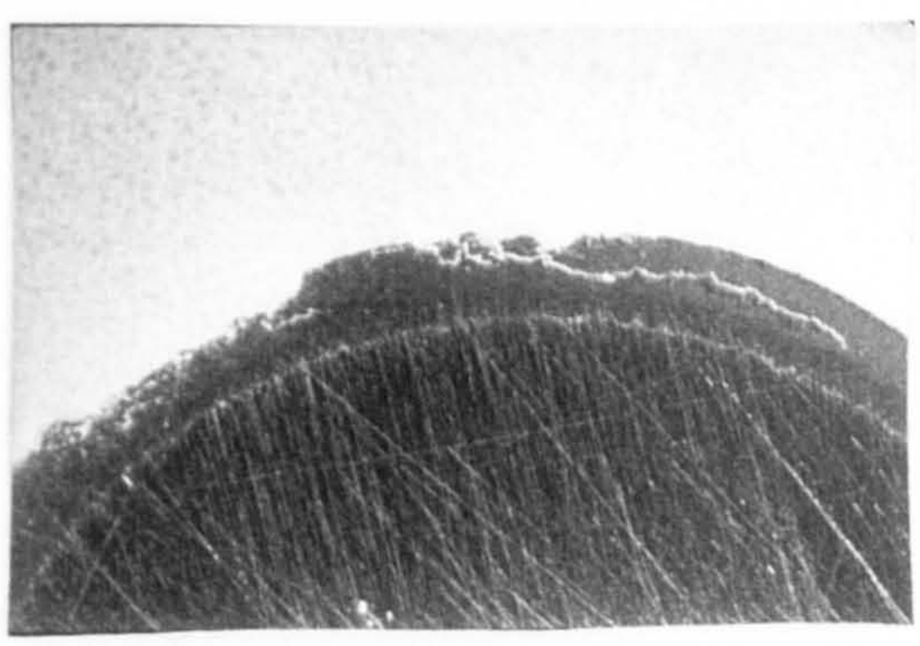

(d) long crack

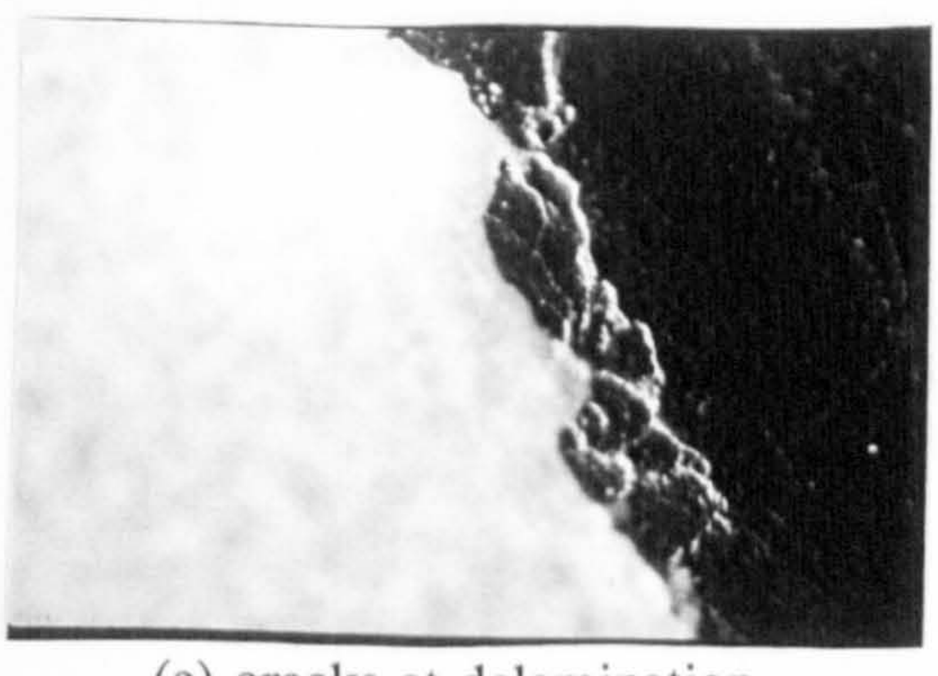

(e) cracks at delamination

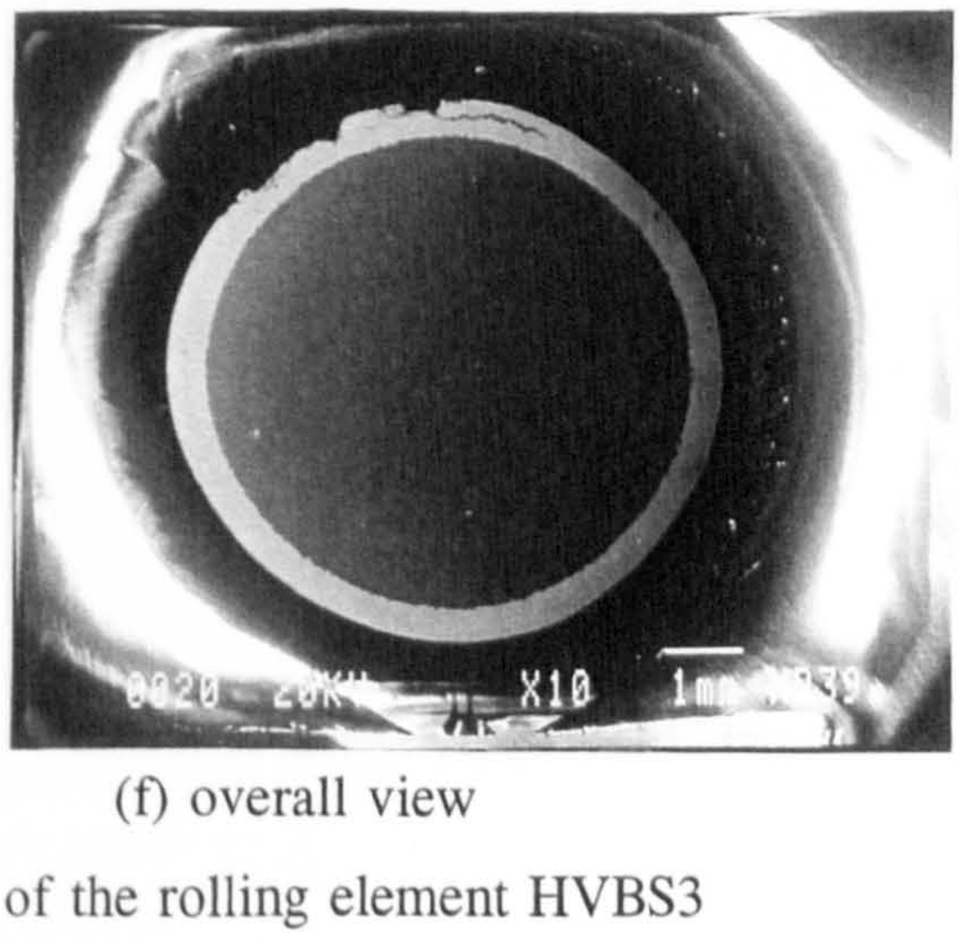

(f) overall view

Figure 5.6.8, Subsurface observations of the rolling element HVBS3

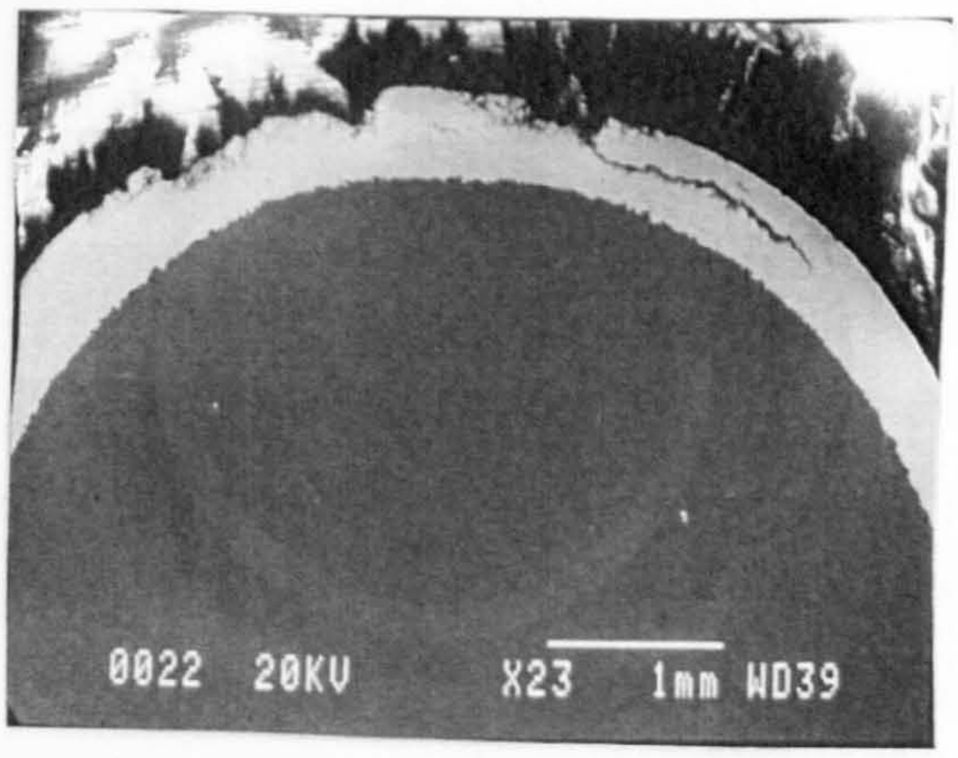

(g) higher magnification (SEI)

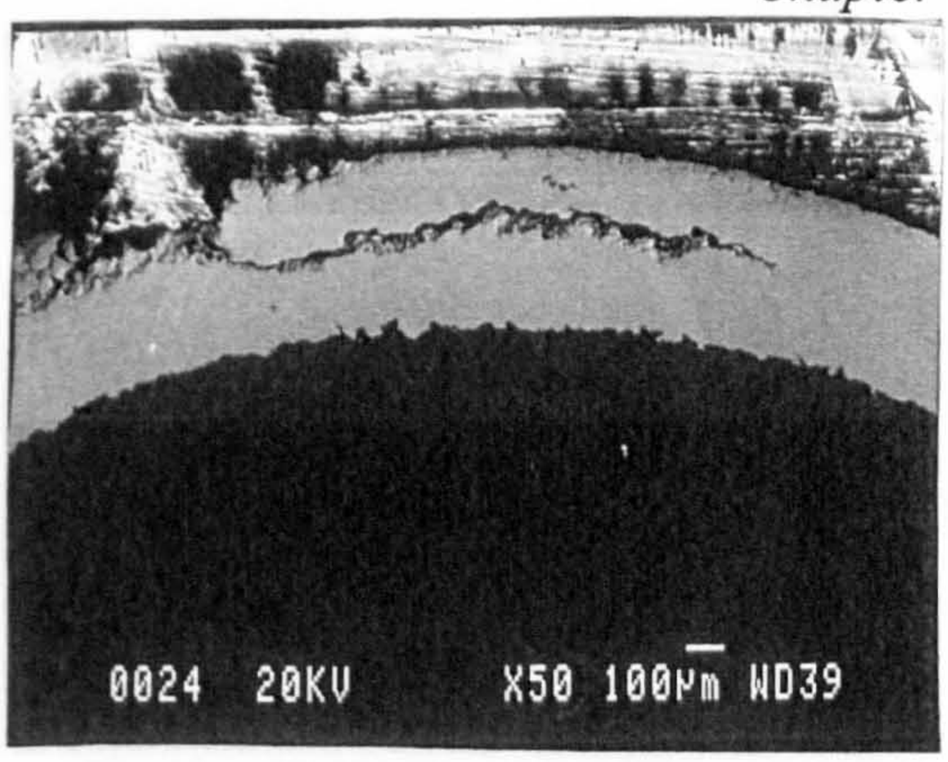

(h) subsurface crack (SEI)

Figure 5.6.8, Subsurface observations of the rolling element HVBS3 (continued)

Figure 5.6.8(h) shows the large subsurface crack parallel to the surface of the coated rolling element at a higher magnification at a contact depth of approximately 110 μm. A subsurface investigation of cracks was also carried out on coated rolling elements HVBS2 and HVBS8. However, none of those investigations revealed any subsurface cracking.

Chapter 6
DISCUSSION

6.1 Discussion

The main objectives for this experimental study were to investigate the performance of thermal sprayed coatings during the RCF tests subjected to various tribological conditions for different coating thicknesses on a variety of substrate steels, and to classify the types of tribological failures and possible failure mechanisms leading to these failures on the basis of surface and subsurface investigations. These features can then be used to understand the main causes which could have lead to these coating failures. It should be appreciated that in this study we were only concerned with the RCF performance of these coated rolling elements and also the types of coating failures to provide a better understanding of the tribological behaviour of these coatings whereas the coating process parameters, coating powder etc used to spray the coatings were of conventional industrial practice which will not be discussed.

6.2 Detonation Gun Coated Balls on Bearing Steel Substrate

The study of ceramic coatings by Tobe et. al, (1990) and preliminary studies by Ahmed et. al. (1997) indicated that the failure mechanism of ceramic coatings was different from WC-Co coatings. In the case of ceramic coatings the adhesive strength seems to be lower than the cohesive strength of the bulk coating and it represented a mismatch between substrate and coating materials. Similarly, the previous studies indicated that the performance of WC-Co coatings was comparatively better, though of the same order of magnitude as the ceramic coatings. The purpose of this study was to investigate further the performance and failure modes of the WC-Co coatings produced by the D-Gun process on conventional bearing steel substrate. It can be appreciated from the RCF test results shown in table 5.1, that although these coated rolling element balls showed slightly improved lifetimes in comparison to the previous studies (Ahmed et. al. 1997), these lifetimes were still of the same order of magnitude and therefore not suitable for the high stress applications. The slight improvement in the lifetimes can be attributed to the tribological changes caused by the differences in the contact geometry of a

coated ball or a coated cone in the four ball system (ie. contact area, microslip, sliding) and due to the better surface finish of the coated rolling element balls indicating the affect of lubrication regime. Similarly, the residual stresses and X-ray diffraction studies indicated a poor microstructure of those coatings (appendix F). Although, these tribological factors showed some affect on the RCF performance of these coated rolling element balls, almost no affect of these changes was observed on the failure modes of these coatings. It can be appreciated from the surface observations (section 5.2.4) that regardless of the changes in the load, lubricant and, the contact configuration the failure mode of the WC-15%Co coated rolling element balls remained as delamination at a depth of approximately 40 μm. The existence of edge cracks on the failed surfaces indicated that the coating failure can to be related to the tensile stress at the edge of the contact area either as a source of crack initiation or the occurrence of subsurface cracks at the surface due to the tensile stress. The FEM results (figure 3.10 and 3.11) revealed that although the maximum shear stress and the sharp stress gradients exist at the interface, the orthogonal shear stress was located at the depth of failure. A stress concentration in the coating due to applied load and coating defects followed by the rolling motion of the ball causes abrupt changes in stress at this depth. This affect of the rate of change of orthogonal shear stress on the RCF performance was also observed in the high speed tests in the previous studies, where these coatings failed instantly at the shaft speed of 7500 rpm. Although the magnitude of orthogonal shear stress at the depth of failure was less than the maximum shear stresses occurring at the interface, the stress range was maximum at the depth of failure. Due to non-homogeneity and the presence of porosity, secondary phase particles in the coating microstructure, the coating could not cope with these abrupt changes in the shear stress and this caused the coating to delaminate. This is consistent with the cryogenic fracture study of plasma spray WC coatings by George et. al, (1995) which revealed that these coatings not only have significant porosity but also secondary phase particles and lack of fusion. The porosity and secondary phase particles were also evident from the coating microstructure (figure 5.2.5). The delamination failure of these coatings can be thought to be as a result of three affects, i.e. lack of cohesion between the lamellae, porosity and secondary phase particles. The fact that the coating did not fail at the

coating substrate interface represents that there was sufficient adhesive bonding between the coating and the substrate to combat the coating failure at the coating substrate interface under the given test conditions. The mechanical interlock due to sand blasting of substrate prior to coating process and the preheat temperature improved the coating adhesion which prevented the coating failure at the interface.

The substrate micro-hardness test results indicated that the substrate microhardness was comparatively low. This was mainly because the substrate rolling element balls were tempered before the spraying process to assist the sand blasting, and also the preheat temperature was high. Microhardness tests on standard rolling element bearing balls indicate an average hardness of 850 Hv_{100}. This value was 41% higher than the substrate hardness value of 600 Hv. The micro-hardness measurements showed a variation in the Vicker's hardness throughout the coating section. It was in accordance with the analysis presented by Lin et. al, (1993). The FEM studies (chapter 3) indicated that the changes in coating thickness will have very little affect on the magnitude of the contact stresses. Thus the improvement in material properties of the coating like porosity, homogeneity, Young's modulus and fracture toughness can be helpful in improving the performance for a given coating thickness. Another observation from FEM analysis was that the change in coating thickness influences the location of dominant stresses and future studies were made to investigate this affect as discussed in following section (section 6.3, 6.5, 6.6).

6.2.1 Residual stress studies in D-Gun coated rolling element balls

Analyses of the first two residual stress measurement points on the surface of the pre-test rolling elements indicated the affect of the substrate geometry on the magnitude of the stress values. The area of the coated ball section at point 2 (figure 5.2.4) was greater than at point 1, and considering that the coating thickness was constant, higher stresses were generated at point 2 due to the substrate volume affects. A comparison of stress measurement results of the post-test rolling elements in the middle of the wear track, ie. measurement points 3, 4 and 7 (figure 5.2.4) which related to the RCF tests DG4, DG3, and DG2 respectively, indicated that the magnitude of the compressive residual stress attenuated during the RCF test. This

also indicated that the nature of stress fields generated during the RCF tests was tensile in nature on the surface of the rolling elements. The magnitude of this stress change in the direction of rolling ranged from 300 to 400 MPa, calculated from the difference in stress values before and after the RCF test. It is appreciated that the depth of residual stress measurement was very near to the surface and stress changes were caused by plastic flow and change in the contact area (Kapoor et. al. 1991). The surface changes were due to shakedown affects, microslip and asperity contact etc during the rolling contact. It should be appreciated that under steady state conditions plastic deformation due to shakedown can be present in a narrow layer near the surface (Johnson 1985) which can lead to residual stress generation. However, due to the lamella and brittle microstructure of thermal spray coatings microcracks appeared on the surface of the wear track (figures 5.2.1(c) and (d)) during the rolling contact which attenuated the residual stress on the surface of the rolling elements. The tensile stress at the edge of the contact area during the RCF tests is postulated as a possible cause of this microcracking. Once microcracks appeared on the surface and the contact stress removed as a consequence of the cyclic loading the stored energy (residual stress) was released due to the formation of new surfaces. Although, the possibility of plastic deformation can also accelerate the mechanism of residual stress attenuation, it is not clear at present if any plastic deformation was present in addition to the microcracking as, discussed later. This affect (microcracking) was more prominent on the failed coating areas (figure 5.2.1(d)) where the coating microstructure fractured leading to loose debris particles. The fact that the depth of residual stress measurements was limited to a few microns, due to the low penetration depth of X-rays in the coating material, indicates that the these measurements were limited to the near surface and the cyclic strain in this near surface layer relaxed the stresses during the rolling contact. However, the studies relating to the plastic deformation of the coating microstructure within the wear track requires Transmission Electron Microscopy (TEM) analysis. This analysis was not carried out during this work. The subsurface residual stress fields can thus be different from surface stress values as indicated in the studies by Muro et. al. (1973). Hence, the affect of the residual stress changes caused by the shakedown phenomenon in thermally sprayed surfaces is not clear at

present. However, the analytical approaches to measure the shakedown affects in coated elements (Wong et. al. 1996), indicated that it was possible to calculate the shakedown affects for coated elements (in sliding contact) and the shakedown can improve the performance if the coating thickness was greater than a critical value (depending upon the elastic and the plastic properties), unfortunately thermal spray coatings are neither homogenous nor isotropic which makes the shakedown analysis complicated in rolling contact. An experimental approach by measuring the surface and subsurface residual stress fields can thus provide an understanding of the residual stress fields in thermal spray coatings due to rolling contact. The magnitude of the residual stress generation during the RCF tests depends upon the test duration and the magnitude of the Hertz contact stress during the test. However, it was difficult to appreciate which of the two factors had more significant affect on the residual stress. The residual stress measurements also indicated that the measurements perpendicular to the direction of rolling show less change in surface stress values after the rolling contact.

There are two main reasons postulated for this difference in the magnitude of stress generation in the two directions, ie. along the rolling direction and a direction perpendicular to it. Firstly, the rolling motion causes a maximum variation in the stress value at the leading and trailing edge of the contact along the direction of rolling, ie. the stress range is maximum along the direction of rolling. Secondly, the Hertz contact stress (compressive) value was maximum in the middle of wear track and minimum at the edge of the contact area (tensile) which affects the residual stress generation. It is appreciated that the polishing of samples before RCF tests could have caused some changes in the residual stress values. Hence the calculations for the residual stress generation due to RCF testing are performed on the basis of the difference in the stress values for the polished samples and the values after RCF tests. This was done to ensure that the stresses are representative of the RCF testing only.

6.3 High Velocity Oxy-Fuel Coated Cones on Mild Steel Substrate

The RCF test results shown in table 5.3 indicated that the coatings performed better

with the high viscosity lubricant (Hitec-174). Moreover, 20 μm thick coatings showed an improved RCF life with respect to the 50 μm & 150 μm thick coatings at low contact stress (1.7 GPa). The contact stress reduced during the test due to conformity of contact resulting from surface wear. The value of contact stress based on the width of wear track (approximately 320 μm, figure 5.3.4(a)) at the end of RCF test can be approximated as 0.7 GPa. The trend was however not consistent for the test lubricant Exxon-2389. The tests with the ceramic lower balls (test lubricant ($BF+H_2O$)) showed reduced RCF life in comparison with the tests conducted with steel lower balls. It could be a result of higher stresses due to higher modulus of elasticity of the ceramic balls. This increase was from 1.7 GPa to 1.9 GPa for the tests HVMS13 and HVMS14 (table 5.3). The surface observations of the failed coated rolling elements indicate that two possible wear mechanisms were operational in the failure of these coatings ie. delamination of the coating underneath the wear track and the surface wear due to the asperity contact. Delamination was however not seen in the case of 20 μm thick coated rolling elements. Although, some surface wear was present in all the cases this mechanism (surface wear) was mainly responsible for the failure of 20μm thick coated rolling elements.

The delamination behaviour (figure 5.3.1, 5.3.3) was seen in all the cases for 50 μm and 150 μm thick coated rolling elements with all the three test lubricants. The depth of failure in these coatings was approximated as 40 μm (figure 5.3.3) or 80 μm (figure 5.3.1) . Most of these failures were parallel to the surface of the wear track. This was further verified by the shape and thickness of debris collected from the test lubricants (figure 5.3.6). This was mainly due to the crack propagation in the coating microstructure parallel to the surface which may have been caused due to the orthogonal shear stress reversal underneath the wear track for 40 μm deep coating failures and maximum shear stress for 80 μm deep coating failures. Although the depth of failures varied slightly from the calculated depths of orthogonal shear stress reversal and maximum shear stress as indicated in table 5.3 and appendix D, these differences may have been caused by the assumption of uncoated case in theoretical calculations. However, a good agreement exist between the depth of failure and indicated depth of stresses. The specific nature of thermal

spraying results in layers of the coating material parallel to the surface. This microstructure contain pores and microcracks not only within the individual layers but also between the layers. The applied contact load causes stress concentration in these pores and cracks. This results in a crack propagation parallel to the surface at the depth of orthogonal shear stress reversal and maximum shear stress depending upon the coating thickness and tribological conditions during the test. These cracks emerge on the surface at the edge of the wear track due to tensile stress at the edge of the contact area. This results in a delamination of the coating parallel to the surface of the wear track. However, there was no definite trend between the depth of delamination at the location of maximum shear stress or orthogonal shear stress and the coating thickness and the tribological conditions during the test eg. 150 μm thick coatings failed at a depth of 40 μm (debris from HVMS3) and 90 μm depth (debris from HVMS4).

The reason that 20 μm coatings did not fail in delamination within the coating microstructure can be explained on the basis that the depth of the shear stress reversal shifts in to the substrate material. Hence the substrate material was critical to the RCF performance of coated rolling elements by not only supporting the coating microstructure but also to resist the fatigue when maximum shear stress and orthogonal shear stress are present in the substrate material. This can be seen in figure 5.3.4(d), in which cracks and plastic deformation are visible in the substrate material. It is important to appreciate that although in the case of 20 μm thick coatings under the given RCF test conditions the maximum shear stress and the orthogonal shear stress were present in the substrate material these coatings can still suffer from the stress concentration at the interface, due to the difference in the modulus of elasticity of the coating and the substrate material. Since the coating delamination at the interface under the given test conditions was not observed for the 20 μm thick coatings it was appreciated that the mechanical interlock at the coating substrate interface and the compressive residual stresses due to the difference in coefficient of thermal expansion of the coating and substrate material resisted this failure mechanism. This affect of coating thickness on the coating failures due to the shift of the location of shear stresses from within the coating

microstructure to the coating substrate interface and finally in to the substrate material has been summarized in figure 6.3.1.

As indicated above the surface wear of the coating was the main mechanism leading to the failure of 20μm thick coated rolling elements, this mechanism was thought to be due to the asperity contact during the RCF test. The asperity contact can cause loose wear debris due to the weak interlamellar strength of the coating as was seen by the generation of the cracks during the hardness measurements and the peeling behaviour of the coating (figures 5.3.8). It is possible that mixed and boundary lubrication conditions during the tests conducted with lubricants Exxon-2389 and (BF+H_2O), resulted in adhesion and ploughing of asperities. This is also evident from the presence of WC debris on the surface of the planetary balls. However, there is also a possibility that these debris were not a result of adhesion but debris produced during the RCF test by other wear mechanisms or delamination were embedded on the surface of the planetary balls due to the higher hardness of the coating debris, by rolling between the cup and the plenary balls.

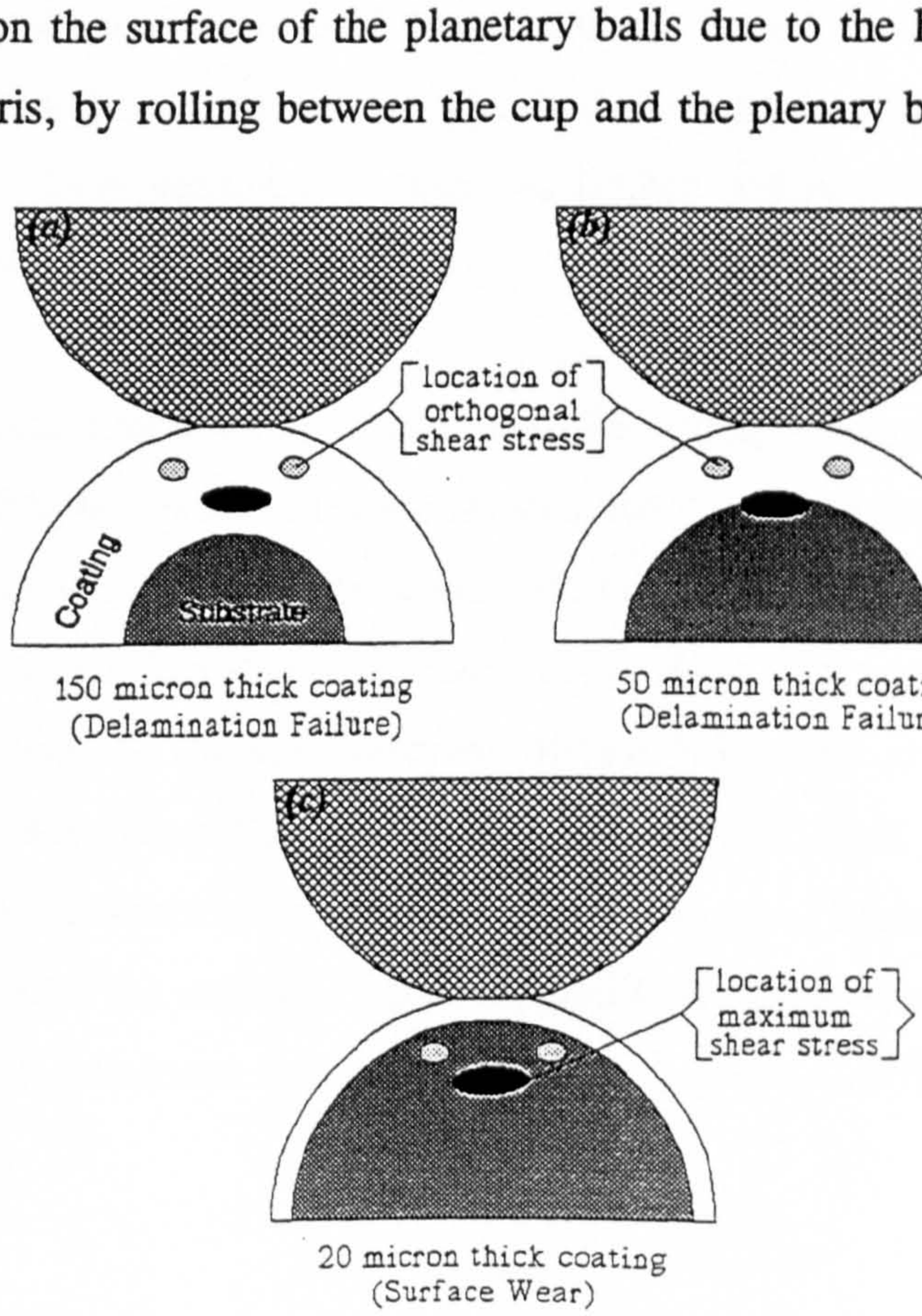

Figure 6.3.1, Affect of coating thickness on failure mechanisms.

The talysurf analysis of the wear track (figure 5.3.4(b)) indicated that the plastic deformation was present at the edge of the wear track. This can be due to the ductile nature and low hardness of the substrate material which did not support the coating during the RCF tests. This behaviour was more prominent when the coatings were tested at higher stresses of 2.75 GPa, where large plastic deformations were observed at the edge of the wear track as indicated in the figure 5.3.2(b)(c)). This behaviour is explained in figure 6.3.2 which represents the plastic deformation of the substrate material leading to the bulk material failure of the rolling element. Figure 6.3.2(a) shows the mild deformation of the coating due to lack of support from the substrate and deformation of the coating material at low contact loads of 40 N in the case of 150μm thick coatings. Sectioned examination of these rolling elements (HNMS1) indicated that there was hardly any deformation of the substrate and yet deformation was seen at the edge of contact area (figure 5.3.4(b)) by the talysurf measurements. This behaviour was also confirmed by some three dimensional measurements of the wear track. Thus it is not clear that which of the two postulated mechanisms, i.e. plastic deformation of the coating material or lack of support from substrate, caused this limited deformation at the edge of contact area at low contact load.

As the contact load was increased and the coating thickness reduced the substrate material was subjected to higher stresses and the mechanism of plastic deformation was accelerated leading to bulk material failure of the rolling element as shown in figure 6.3.2(b). This shows the detrimental affect of a thin coating (20~50 μm) at higher stresses on the soft substrate. Hence, thin coatings could only be useful at lower stresses where the advantage of the shift of shear stresses in the substrate material is maximized and contact stresses are low enough to avoid any plastic deformation in the substrate material. Similarly, the lubricant film should be fully developed to minimize the surface wear of the coated rolling elements.

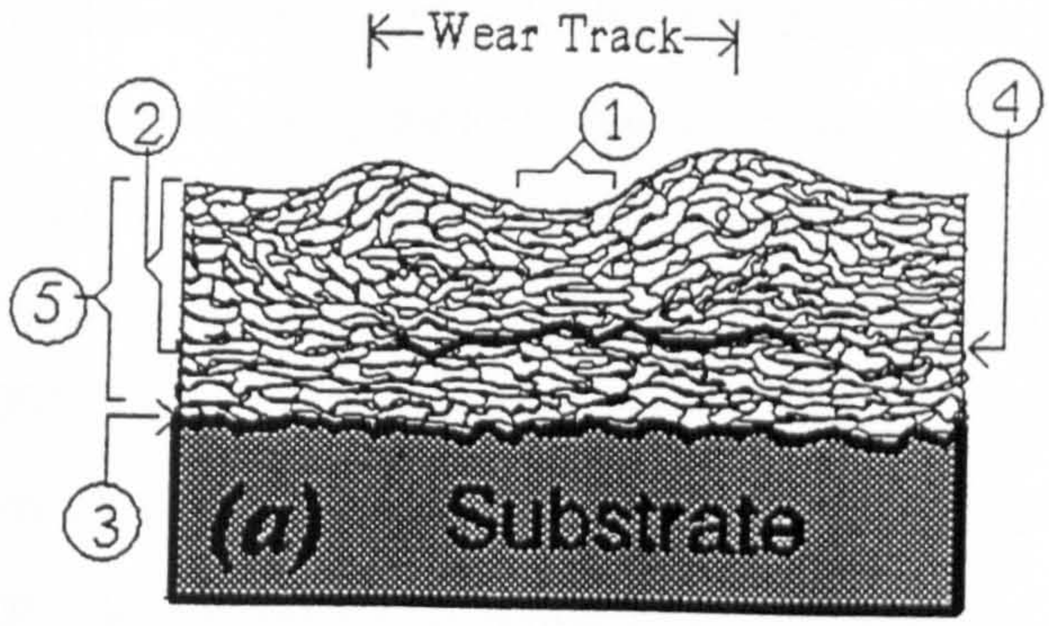

150 micron thick coating at 40 N contact load

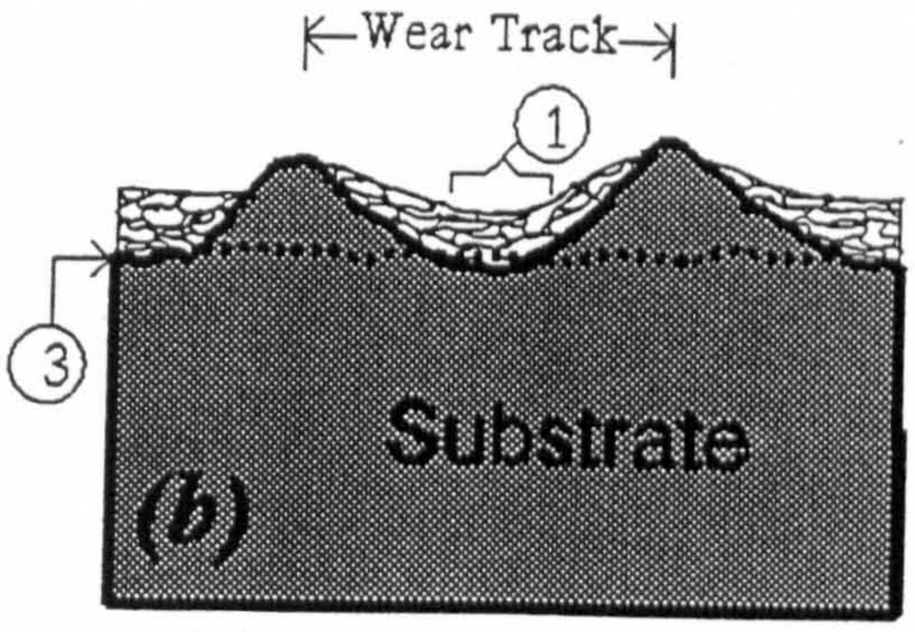

50 micron thick coating at 160 N contact load

Figure 6.3.2, Bulk material failure due to plastic deformation.
(1; max: compressive stress, 2; depth of failure, 3; coating substrate interface, 4; crack, 5; coating thickness)

In general, it was seen that the substrate hardness to support the coating, coating thickness to alter the depth of orthogonal shear stress reversal and the lamella coating microstructure are important to the RCF performance of the coatings. The surface wear at the wear track indicated that the surface roughness and lubrication film was critical to the performance of these coatings which can alter the asperity contact behaviour. Studies were also made to investigate any oxidation affect of the test lubricant ($BF+H_2O$), but no such evidence was found on the surface of the wear track. This can be due to the high corrosive resistance of WC-Co coatings under the given test conditions.

6.3.1 Residual stress studies in HVOF coatings

The residual stress studies of these HVOF Coatings showed variations in the stress

value caused by the coating thickness and surface geometry. A comparison of stress measurement results of as-sprayed samples, ie. measurement points 9, 10, and 11 (figure 5.3.8), indicates that the stress values were dependent upon the geometry of the sample and the coating thickness. This was in accordance with the work reported by Brandt (1995). Stress measurement results indicate that for the coating on a flat substrate the stress values did not change in the axial and the longitudinal directions. It can be appreciated from the residual stress values for flat plate at measurement point 11, which are exactly the same at 0^0 and 90^0 directions. However, for conical shaped specimens these values change in the three directions of measurement for the two coating thicknesses. This was mainly because the rate of heat transfer varies along the axis of the cone i.e. from the apex to the base of the cone. It is important to appreciate that the Coefficient of Thermal Expansion (CTE) of the steel substrate is approximately twice that of WC-Co coating. This should result in a net compressive stress in the coating. However the as-sprayed samples show residual stress of tensile nature. This was mainly a result of the following two factors:

a) Firstly, the depth of measurement by X-ray diffraction technique for most of the coatings is limited to a few microns (Gill. 1993), which represents the coating deposited in the final pass of thermal spraying process. The quenching stresses will thus be significant at this depth, moreover there will be no shotpeening affect on the final layer of coating.

b) Secondly, the affect of residual stress caused by the difference in CTE of the coating and the substrate is more significant near the interface. The intensity of stress due to this affect will reduce with the increase in distance from the interface. This can also be the reason for slightly higher tensile residual stress values for 200 μm thick coatings in comparison to 100 μm thick coating. This behaviour is evident by the analysis done by Greving et. al. (1994b), Gudge et. al. (1990), Knight et. al. (1993) and Provot et. al. (1993), in which the residual stress values change from tension to compression within the coating thickness.

An analyses of residual stress measurements in the middle of fractured coatings at

the measurement points 14 and 16, shows very low compressive stress values at the depth of failure with the exception of measurement point 6. This indicates that the crack propagation relaxed the compressive residual stresses generated by thermal spraying process. Several other factors eg. brittle or ductile fracture, subsurface plastic strain, interlamella cracking due to the applied stress leading to micro and macro stress relaxation (Lin et. al. 1995) etc can also have an affect. The SEM analyses of the failed specimens reveal that these coatings do not fail near the interface, which could be due to the high compressive residual stresses (Clark et al. 1985) near the interface and the mechanical interlock caused by the sandblasting of substrate. It is interesting to note that several cracks can be seen within the coating microstructure above the depth of failure (Figure 5(a) and 5(b)) but coatings do not delaminate at these depths, which represent that under the given tribological conditions the failure was subsurface crack propagation at different depths.

In general, residual stress measurement results presented in table 5.4 and previously in table 5.2 showed variation in the stress values, not only in the as-sprayed samples of different geometries, but also after the RCF tests. The residual stress measurements for the D-Gun and HVOF coated elements after the RCF test attenuated the affect of residual stresses induced by the spraying process due to the cracking within the coating microstructure and the coating failure was associated with this attenuation of the residual stress.

6.4 High Velocity Oxy-Fuel Coated Balls on M-50 Steel Substrate

The main purpose of this study was to investigate the affect of retaining the substrate hardness of the coated rolling element balls by coating (M-50) bearing steel balls at low preheat temperature. The RCF test results shown in table 5.5 indicate that the coated rolling elements performed poorly at the Hertz contact stress levels greater than 2.4 GPa. It is possible that at higher stress levels the maximum shear stress induced in the coated rolling elements and the stress concentrations caused by the stress gradients at the interface were greater than the adhesive strength of the coating which led to the coating delamination at the coating substrate interface. The maximum shear stress contours shown in figures 5.4.8 indicated that

maximum shear stress with sharp interfacial stress variations was located at the coating substrate interface. Similarly, the maximum orthogonal shear stress was located within the coating microstructure at a depth of approximately 50μm under the given test conditions. The surface observations of the delaminated coatings indicated that the coating failure was at the coating substrate interface regardless of the changes in the tribological conditions. Thus it is possible that the embryo of the crack in these coatings originated at the coating substrate interface due to the maximum shear stress at this location and the mismatch of the coating substrate properties. The cracks then travelled through the interface to certain lengths until they finally reached the surface. The microhardness and fracture toughness measurements indicated that these coatings had an improved fracture toughness which resisted the through thickness coating delamination indicating an improved cohesive strength of the coating.

It is important to appreciate that the rolling elements were sprayed in such a way as to minimize the temperature rise in the substrate material. Although this has the advantage of retaining the hardness of the substrate material after spraying to support the coating microstructure, there were two drawbacks of reducing this preheat temperature:

(a) The compressive residual stress due to the difference of the coefficient of thermal expansion (CTE) of the coating and the substrate material was not high enough to improve the coating adhesion at lower substrate temperatures in the case of WC-Co coatings on steel substrate. The compressive residual stress can resist mode-I (tensile) cracking and hence improve adhesion. However, extremely high values can deteriorate the performance by microcracking at the interface.

(b) The impacting lamellae on the cold substrate will quench and solidify instantly thereby introducing high quenching stresses in the lamellas at the interface and reducing the time for the mechanical and any possible chemical bonding between the lamella and the substrate material.

Thus it is important to optimize the preheat temperature without excessive loss of the substrate material hardness. The microhardness measurements indicated that the substrate M-50 steel retained its hardness after the spraying process. Although, this had the advantage of supporting the coating microstructure at higher stresses, high hardness of the substrate material can affect the sandblasting prior to the coating process which can in turn affect the wettability and mechanical interlock at the coating substrate interface. Hence, the substrate hardness should be selected so as to support the coating and also to provide a maximum adhesive strength to the coated rolling element. The affect of the modulus ratio on the magnitude of the stress fields (figure 5.4.7) indicates that there was not a significant variation on the magnitude of stresses for most of the coatings considered. Thus the change in coating material for these rolling elements will not significantly affect the stress contours; however it can affect the residual stress behaviour owing to the difference in the CTE of the coating and the substrate material. As the surface observations did not indicate cohesive failure of the coating, these coatings had good cohesive strength, and it was appreciated that the micropores in the coating microstructure did not significantly affect the coating failure.

A solution to the interfacial delamination behaviour as seen for these coated rolling elements could be to functionally grade the coating substrate interface to avoid sharp stress variations at this location. A typical example is shown in figure 6.4.1 where a 30 μm thick layer (E=300 GPa, ν=0.25) was added below a 80 μm thick C2 type coating. This results in the same overall thickness as considered in the previous case but the sharp interfaces at the interface are reduced. However experimental research is required to validate the hypothesis. In general, the case of HVOF coated M-50 steel rolling element balls represented the extreme case of retaining the substrate hardness to support the coating microstructure. The experimental test results showed that this can deteriorate the performance of these coatings by poor adhesive strength due to the lack of mechanical interlock and wettability at the interface and also the role of residual stresses cannot be overlooked.

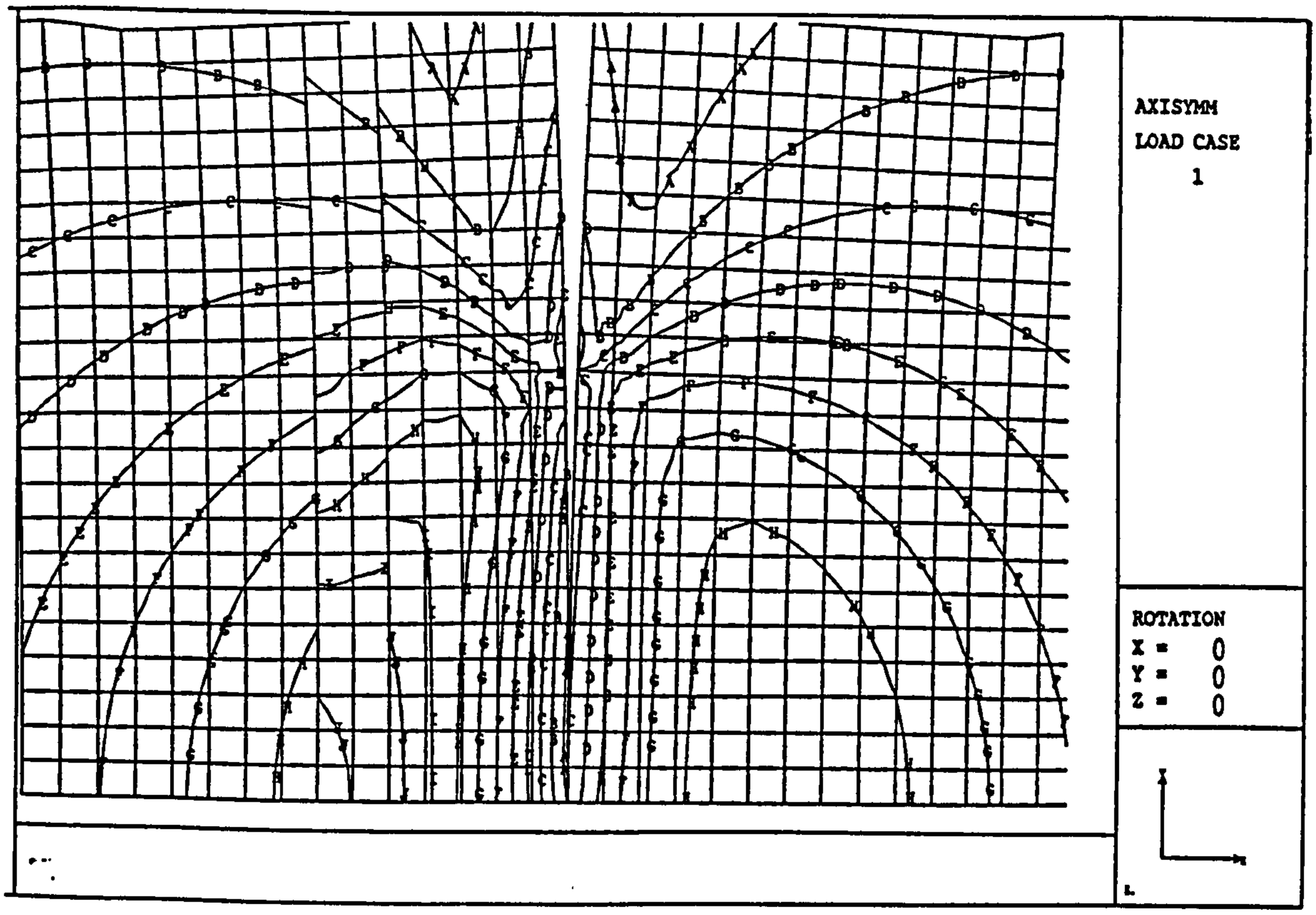

Figure 6.4.1, Maximum shear stress contours for graded coating (A=0.17, B=0.34, C=0.52, D=0.69, E=0.87, F=1.04, G=1.22, H=1.39, I=1.57, J=1.74)

The ratio (λ) of the approximate value of the EHL film thickness to the average surface roughness under the given test conditions indicates that full film exists avoiding asperity contact between the rolling elements. However, the surface observations of the wear track of the rolling elements (figures 7d, 8a, 8b) indicate an appreciable amount of surface wear on these rolling elements. The reasons for this difference will be postulated later in the discussion of plasma sprayed coatings.

6.5 Plasma Sprayed Coatings on 440-C Steel Substrate Cones

Table 5.6 not only summarises the RCF performance of the coated rolling element cones but also defines the tribological conditions (parameters) varied during the RCF tests. It will be helpful to clearly explain these tribological parameters before appreciating their influence on the RCF performance of these rolling elements. It can be seen from table 5.6 that four tribological parameters were varied in the testing programme. These parameters were as follows:

a) The contact configuration i.e. steel lower balls or ceramic lower balls to vary the contact area, contact stress etc.

b) The test lubricant to vary λ value from 1 to 3. All other changes due to variation in the test lubricant have been neglected.

c) Coating thickness in the range of 60 μm to 220 μm.

d) Gross sliding during the RCF tests caused by the differences in the apex angle of the rolling element cones.

The affect of these individual tribological parameters on the RCF performance of the coated rolling element cones can be appreciated from the experimental test results. The affect of contact configuration on the RCF performance can be seen by comparing the RCF tests conducted in conventional steel ball bearing and hybrid ceramic bearing configurations. As summarized in table 5.6 it can be seen that in all the cases of RCF tests, the coated rolling elements performed better with steel lower balls than the ceramic lower balls. This reduction in RCF life was approximately 25% to 50% when ceramic lower balls were used.

The test lubricant was another perimeter varied during the testing programme. As indicated above, we were only interested in the affect of test lubricant on the lambda value by varying the lubrication film thickness. As explained in section 5.5.3 this ratio (λ) was approximately 1 and 3 for the Exxon-2389 and Hitec-174 lubricant respectively. Considering the RCF test results it can be appreciated that in all the cases except the tests GG3AY and GG4BY. The coated rolling elements performed better with Hitec-174 lubricant than Exxon-2389. This was not only the trend for the RCF tests with lower steel balls but also for the lower ceramic balls. In most of the cases the RCF performance was reduced by approximately 65% to 90% when Exxon 2389 was used as the test lubricant. The reason for difference in the behaviour for the rolling element GG3AY might be due to high frictional torque during that specific RCF test.

Another parameter controlled during the testing programme was the coating thickness. Two different coating thicknesses were used in each set of cones i.e. the

set of cones having 109.4° apex angle and 90° apex angle. These coatings can be broadly classified as thick coatings i.e. (230 ± 10 μm and 150 ± 10 μm) and thinner coatings i.e. (90 ± 10 μm and 60 ± 10 μm). This brand classification is based on the approximate depth of maximum shear stress under the given test conditions i.e. the coating was thick if maximum shear stress was located within the coating microstructure and was regarded thinner if it was located at or below the coating substrate interface so that the affect of stresses at the coating substrate interface became important. This broad classification will be used in the further discussion of this thesis for clarity reasons. It can be appreciated from table 5.6 that thicker coatings performed better in all the cases of RCF tests in comparison to their thinner counterpart. Moreover, the reduction in RCF lifetimes when thinner coatings were used ranged from 50% to 90% with the exception of the test GG4BY in which case the reduction was less than 50%.

The last parameter controlled during the RCF tests was the extent of gross sliding (and also microslip) occurring during the RCF tests. Before discussing any affect of this gross sliding it will be important to clarify the sign convention used to represent gross sliding in table 5.6. When the lower planetary balls were orbiting slower than their theoretical speed (calculated under frictionless and pure rolling conditions) a positive sign was used indicating that the coated rolling element was on the faster side of the rolling sliding contact. Similarly if due to the contact geometry in the four ball assembly the lower planetary balls were orbiting faster than their theoretically calculated speed, a negative sign was used to indicate the sliding direction thereby meaning that the coated rolling element was on the slower side of the rolling sliding contact. However, it should be appreciated that only the orbital velocity of the planetary balls was considered during this analysis and any change in orbital velocity will conversely affect the spin velocity of the lower planetary balls i.e. when the planetary balls are orbiting slower than the theoretical velocity there will be a higher spin component and vice versa to satisfy the dynamic equilibrium of the components in the cup assembly. If this analogy was followed it can be appreciated that, when the coated rolling element was on the slower side of the rolling sliding contact (all the cases of 90° apex cones) , the RCF performance

(eg. comparison of GG2AX and GG2BX, etc., table 5.6) was significantly reduced. This reduction in performance ranged from 40% to 90% when the coated rolling element was on the slower side in the rolling/sliding contact with the exception of GG3AY which should be due to high frictional torque during that specific test as indicated earlier.

Although the RCF results were not intended to be used for statistical fatigue life prediction but in general the affect of these tribological parameters varied the RCF performance from 50% to 90% in all the cases except the case of contact configuration in which case the affect was in the range of 25% to 50%. We have so far analyzed the affects of each of the four tribological parameters on the RCF performance of plasma sprayed rolling element cones. Although, an understanding of the extent of influence of these individual parameters on the lifetimes have been established, we have not discussed the ways these factors could have influenced the RCF lifetimes.

It can be appreciated that when the contact configuration was changed from conventional steel ball bearing (lower steel balls) to hybrid ceramic bearing (ceramic lower balls) not only the contact area was reduced but the Hertzian contact stress also increased. Under the given test conditions the contact load had to be increased by 50% (from 160 N to 240 N) to increase the contact stress from 2.7 GPa to 3.1 GPa for steel lower balls and vice versa. Similarly the contact load has to be decreased by 25% (from 160 N to 120 N) to achieve the same contact area as was seen for ceramic lower balls. Both of these factors indicate severe tribological conditions leading to higher contact stresses when ceramic lower balls were used. This explains the reasons for the poor RCF performance (reduction of 25% to 50%) of the coated rolling elements when used in hybrid ceramic bearing configurations. Apart from the changes in the contact width and Hertzian contact stresses other factors such as the hardness and wear resistance, etc. of the planetary balls also becomes important when the lubrication conditions were in the mixed regime because it can change the asperity contact behaviour during the RCF tests in a rolling sliding contact. This factor can be understood from the surface observations

of the of the lower planetary balls (section 5.5.6). The surface observations of the lower planetary balls indicated that except in one case (figure 5.5.11(a)) it was almost impossible to detect any debris on the surface of the lower ceramic balls. However, debris were seen in abundance on the surface of the lower steel balls. This behaviour was consistent with the observations of the HVOF coatings in the previous sections of the thesis. Similarly, dents were seen on the surface of lower steel balls but not on the surface of lower ceramic balls. The abrasion between the coated rolling element cone and lower balls with or without the presence of any wear debris damaged the lower steel balls resulting in dents but not the lower ceramic balls. Both of these observations (debris and dents) indicate that the asperity behaviour also changed when ceramic lower balls were used. Although, it was not possible to confidently say if asperity adhesion was a phenomenon leading to the failure of rolling elements but if any such mechanism took place (adhesion of asperities) it must have been more pronounced with lower steel balls as more debris were seen on its surface. However, there is also a possibility that these debris were rolled between the cup and planetary balls and eventually embedded on the surface of planetary balls. Moreover, no ceramic debris were seen in the test lubricants indicating that lower ceramic balls had much high wear resistance than coated rolling elements. This could mean harsh tribological conditions when ceramic lower balls were used due to its higher wear resistance and hardness in comparison to steel lower balls leading to quick failure. Several researchers (Chao et. al. 1996), (Sayles, 1995), (Goddard et. al. 1995) have analytically and experimentally studied the behaviour of wear debris within the contact area of the bodies in rolling contact and indicated that the size, shape of debris along with other tribological conditions can affect this behaviour. In general, the mechanism of asperity contact in rolling sliding contact is very complex depending upon the hardness, surface roughness, material, size and shape of debris, speed and lubricant behaviour and any more discussion on this is beyond the scope of this work. However, a point has been made that it is not only the contact area and contact stresses which can be affected by changing the planetary balls from steel to ceramic and visa versa but also the asperity contact in the rolling sliding contact operating in mixed lubrication conditions. When the test conditions were such that the lubricant film was fully developed ($\lambda \geq 3$), this factor

can be ignored and only the contact area and stresses should be considered.

This can also be used to explain the better performance of the rolling elements when Hitec-174 was used as the test lubricant in comparison to Exxon 2389. When Exxon 2389 was used as the test lubricant asperities must have come in contact thereby accelerating the surface wear and increasing the frictional forces leading to quick failure of the rolling elements. Although, the difference seen in the frictional torque measurements when the test lubricant was changed was neither significant nor consistent but it could be mainly due to the fact that the frictional torque measurements were representative of the frictional torque in the four ball assembly and not just the coated rolling element cones and the lower balls indicating that the component of frictional torque due to the contact between the drive rolling element and the lower balls was small in comparison to other components of the frictional torque under the given test conditions. Frictional torque measurements should therefore only be used for comparative studies and not for estimating the coefficient of friction. Moreover, the values presented in the table 5.6 indicate the steady state values. These values were comparable when the RCF tests were done with uncoated steel upper balls (chapter 2). However, it is also possible that some asperity contact was present with both the test lubricants as surface wear was observed in both the cases of lubrication, the reasons for which will be discussed later when dealing with the type of surface failures of the coated rolling elements. This could mean that the component of rolling friction caused by the asperity contact was present with both the lubricants and hence no appreciable difference was observed in the values of frictional torque when the test lubricant was changed. It should also be appreciated that the frictional torque of 0.06 Nm at the start of dry test in which asperity contact must have contributed substantially in the overall frictional torque was of the same order of magnitude as was generally observed with the lubricated tests (0.03 Nm). However, as the dry test continued the generation and presence of debris in the contact area significantly increased the frictional torque to 0.175 Nm.

Another observation made from the RCF test results was that the thicker coatings performed better than thinner coatings under the given tribological conditions. It can

be appreciated from table 5.6 that the depth of maximum shear stress ranges up to a depth of 90 micron under the surface of the wear track and its magnitude varies from 1 to 1.2 GPa under the given test conditions. This indicates that when thicker coatings were used the affect of the applied load at the coating substrate interface became less important as the majority of the stresses lie within the coating microstructure. The better performance of thicker coatings indicates that the shear resistance of the coating microstructure was better than the shear resistance at the coating substrate interface. These observations indicate that the crack initiation and propagation due to shear stresses at the interface must be higher at the coating substrate interface than from within the coating microstructure thereby reducing the RCF life of thinner coatings. It could be mainly because the coating substrate interface represents a mismatch of the properties of the coating and substrate material leading to stress concentrations. Even if the stresses are considered within the elastic range the strain experienced by the coating and substrate will vary depending upon their modulus of elasticity and poison's ratio. This difference in strain acts as a stress gradient at the interface leading to coating failure at the interface. This can be confirmed by the finite element studies (chapter 3) in which thinner coatings indicated a sharp stress gradient which leads to stress concentrations at the interface. It should be appreciated that the only mechanisms by which the coating and substrate are bonded together is the mechanical interlock and compressive residual stresses due to the mismatch in the thermal expansions of the coating and substrate material.

Studies on the residual stress measurements of WC-Co coatings produced by a variety of different techniques explained in the previous sections indicated that the compressive residual stress in the rolling elements can be several hundreds of Megapascals but not of the order of magnitude of GPa. The applied shear stress of approximately 1.2 GPa can thus prove extremely high at the coating substrate interface. Hence the advantage of compressive residual stress to resist the coating failure diminishes as the applied stresses increases. Similarly the quenching stresses will be higher at the coating substrate interface at low preheat temperatures due to quick cooling of the lamella leading to additional stress concentrations. It does not

imply that the quenching stresses, micro-pores, micro-cracks and secondary phase particles which are generally present within the coating microstructure do not lead to stress concentrations within the microstructure but it takes longer for the cracks to initiate and propagate from within the coating microstructure than at the coating substrate interface thereby providing a possible explanation for the better performance of thicker coatings. However, the reason for poor performance of thinner coatings when the coating failure was not due to delamination but due to the surface wear is not clear at this stage and can only be thought of an affect of residual stress variations with the changes in coating thickness.

6.5.1 The affect of sliding direction

The direction of sliding also had a pronounced affect on the RCF performance of the coated rolling element cones. This is consistent with the work done by Sado et. al. (1981) and Tyfor et. al. (1994) for uncoated rolling elements and Yoshida et. al. (1995) and, Nakajima et. al. (1997) for the coated rolling elements. A comparison of the RCF test results during this study and previous studies by other researchers indicated that the direction of sliding significantly affected the performance in a rolling sliding contact. Regardless of the test machines eg. two roller type, three roller type or four ball machine and the affect can be observed for a homogenous materials as steels as well as for the coated rolling elements. All of these experimental studies suggest that the fatigue cracks propagate in the driven rolling element (negative sliding) and crack propagation was resisted on the driving rolling element. This is thought to be a function of the direction of load movement to the direction of traction as shown in figure 6.5.1(a). Previous studies have indicated that when the direction of traction was opposite to the direction of load movement which happened in the driving part of the rolling sliding contact crack propagation was resisted and visa versa. Studies by Hills et. al. (1985) have however shown some understanding of the stress state in the driving and driven components in which the Von-Mises yield contours shift towards the surface to a greater area in the driven part increasing the probability of crack propagation in the driven part as shown in figure 6.5.1(b). However, his studies on the basis of the maximum tensile stress indicated the opposite to the experimental observations. The actual case of sliding

in the four ball system is however much more complex due to the presence of a spin component and no analytical studies were done to study the influence of this component during this experimental work.

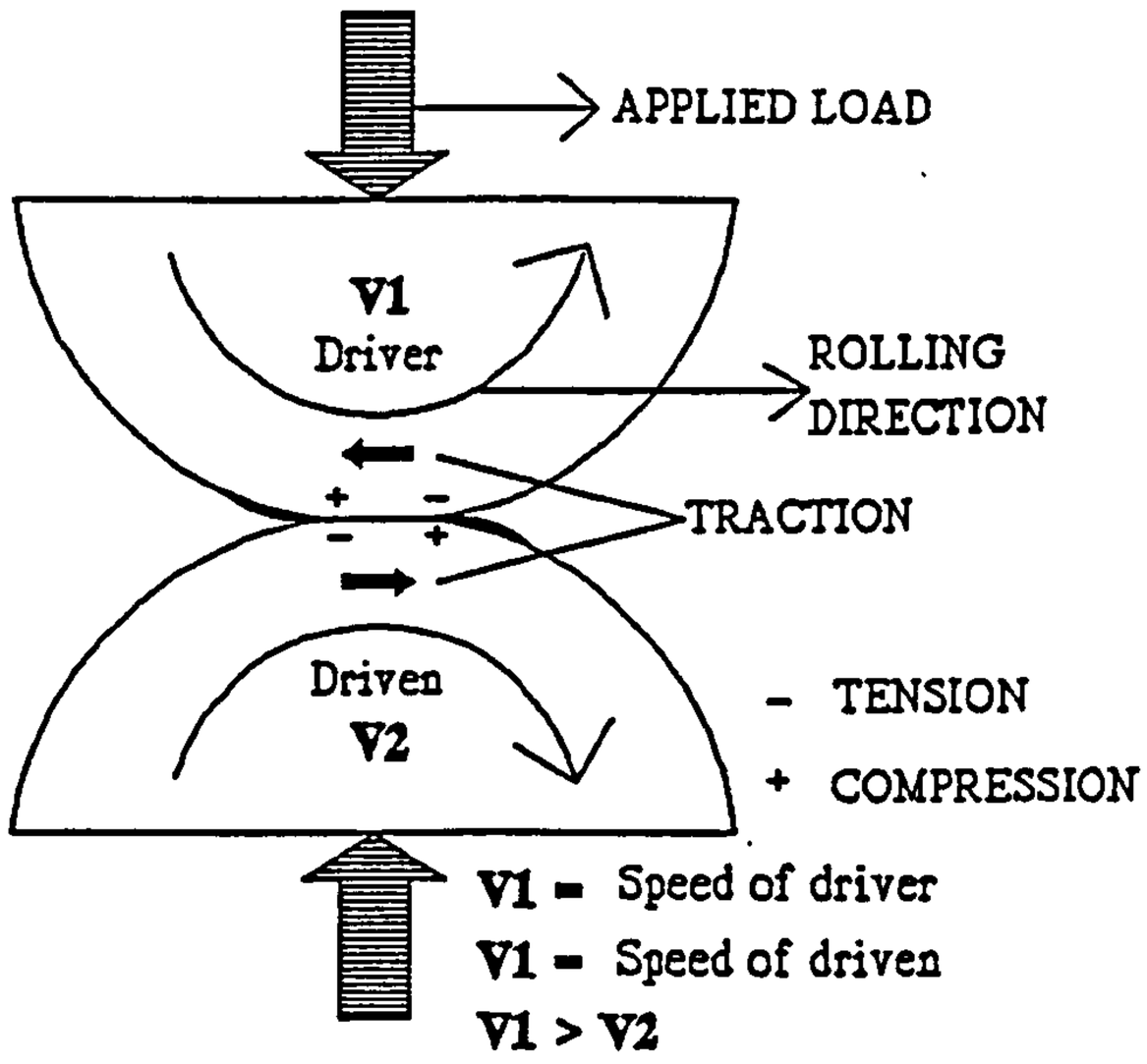

(a) traction directions in rolling sliding contact

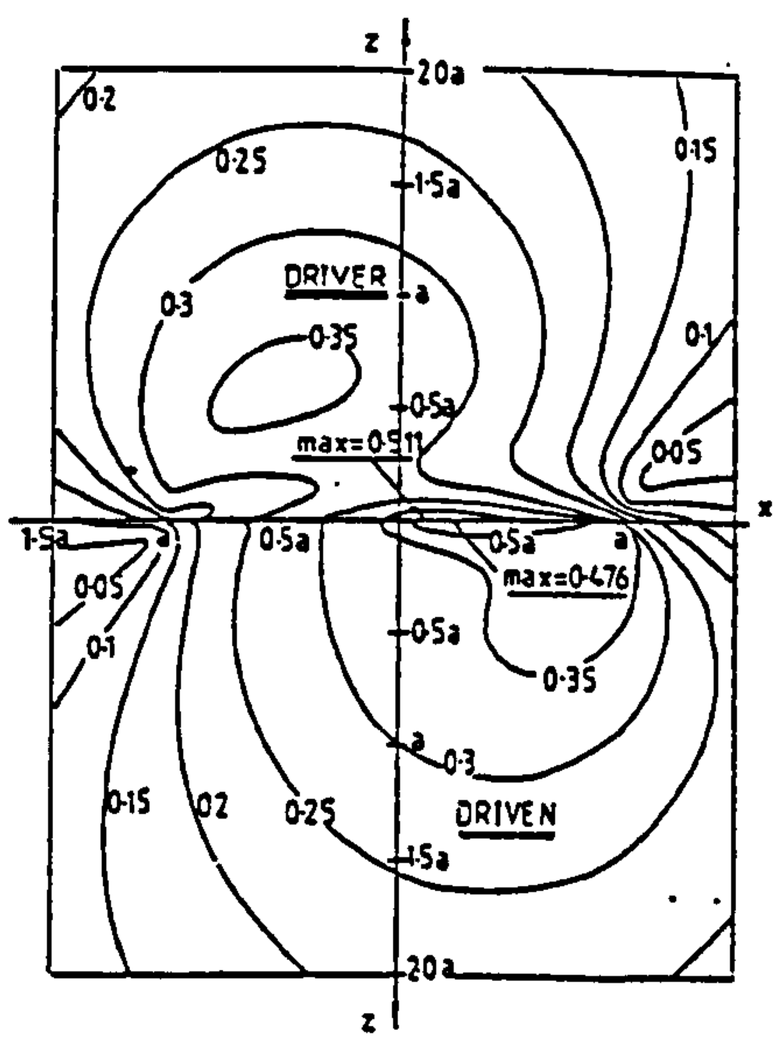

(b) Von-Mises yield contours for in driver and driven components (Hills, 1985)

Figure 6.5.1, Rolling sliding contact

6.6 High Velocity Oxy-Fuel Coated Cones on Bearing Steel (440-C) Substrate

The RCF test results shown in table 5.7 indicate an improved performance of the coated rolling elements specially for the coating thicknesses greater than 150 μm and

the contact stresses values up to 2.7 GPa with a high viscosity lubricant (test HVBS1 and HVBS5). These tests were suspended after more than 100 hours of testing (60 million stress cycles) without significant damage on the surface of the wear track (figure 5.6.1). When similar tests were conducted with the ceramic lower balls (test HVBS2 and HVBS6), similar behaviour was observed but the damage at the wear track (figure 5.6.2) was significant to terminate the test due to the vibrations in the cup assembly. These observations indicate an improved performance of the coating under the given test conditions which can be attributed to the improved microstructure of the coating in comparison to the previous cases considered in the thesis. A similar trend was observed during the microhardness measurements (figure 5.6.7). However, when similar tests were conducted under mixed lubrication conditions (lubricant Exxon-2389), or at higher contact stresses (test HVBS4 and HVBS8), the rolling elements failed either in fatigue pit type failure as shown in figure 5.6.4 or in a delamination type failure as shown in figure 5.6.3, without any definite trend between the tribological conditions and the type of failure. The small fatigue type pits shown in figure 5.6.4(a) indicated an advanced stage of the surface wear type failure and were much like the observations made with plasma sprayed coatings (figure 5.5.2). The delamination type failure was similar to the observations made in the previous sections of the thesis (figure 5.2.2) with the depth of failure relating to the approximate depth of shear stress reversal. However, the subsurface observations of this coated rolling element cone (figure 5.6.8) revealed that although the delamination took place at the depth of orthogonal shear stress subsurface circumferential cracks were present at the depth of maximum shear stress. This behaviour was consistent with the studies on the plasma sprayed coatings (section 5.5.8).

The RCF test results indicated a poor performance of the 50 μm thick coated rolling element cones (test HVBS9~12), and in all cases the rolling elements failed by delaminating at the coating substrate interface (figure 5.6.5). This behaviour was consistent with the previous studies of HVOF coatings on mild steel substrate and is attributed to the exposure of the coating substrate interface to shear stresses. Hence in general, thicker coatings (coating thickness $>$ 150 μm) should be

preferred for high stress applications at higher stresses in rolling contact specially under fully developed lubrication conditions for the improved RCF performance.

6.7 Types of Coating Failures

One of the objectives of the of this study was to classify the types of tribological failures observed on the surface of coated rolling element cones. Surface observations presented in section 5.5.4 for plasma sprayed coatings and in the other sections for the D-Gun and HVOF coatings indicated that the coating failures observed on the surface of coated rolling element cones can be classified in to three main categories ie. surface wear, subsurface delamination and the bulk material failure. The bulk material failure, when the substrate deform plastically under the applied load has already been described in the previous section as shown in figure 6.3.2. The discussion in this section will therefore be made on the first two types of coating failures. The rolling elements failed in either one of these types of failures or a combination of these depending upon the tribological conditions prevailing during the RCF tests. These types of failures will now be discussed.

6.7.1 Surface wear

Surface wear was a failure mechanism seen with both the lubricants in all the cases of the RCF tests. However, in some cases this type of failure was observed along with the delamination type of failure and in some cases this was the only mechanism of coating failure. Figures 5.5.1, 5.5.2, and 5.5.7, represent some of the cases in which surface wear was mainly responsible for the failure of rolling elements for the plasma sprayed coatings. Similar observations (figure 5.2.1(c), 5.2.2(d), 5.3.4 5.4.4, and 5.6.2) were made in the case of D-Gun and HVOF coatings. In this type of failure a shallow wear track was formed, the depth of which varied depending upon the contact configuration and the time to failure. As a result of this surface wear the contact became conforming and the width of wear track increased. Small wear debris of the type shown in figure 5.5.8 were produced during this type of failure. Small pits of the type shown in figure 5.5.1(b) were initially produced on the surface of the wear track. As the test continued these small and shallow pits joined together to form bigger pits which lead to the failure of coated rolling

element. A typical example of this behaviour can be seen from figure 5.5.2 in which these smaller and larger pits can be seen in the middle of the wear track. This type of failure was mainly due to the asperity contact, and due to the action of loose wear debris in the presence of gross sliding and microslip during the RCF tests. When the lubrication conditions were in the mixed region surface asperities come into contact. The presence of gross sliding and microslip within the contact region provided a tangential force at the junction of asperities. This tangential force produced small debris due to conventional wear mechanisms like ploughing and possibly adhesion. Although both of these mechanisms were possible it is not clear either one or both of these mechanisms operate to produce small debris. This phenomenon of the generation of initial wear debris was also confirmed by manually stopping the RCF test after a short period of time and analyzing the test lubricants which indicated the presence of tiny wear debris of the coating material long before the rolling element failed. Once small debris were produced the wear mechanism accelerated due to additional mechanism of three body abrasion which eventually lead to the failure of coating. Similar mechanism of asperity contact leading to surface wear of the coated rolling element cone but at an accelerated rate was observed during the surface observations of the dry test (GG5AX). The process was accelerated due to the absence of lubricant film within the contact region. The surface of the wear track of the failed rolling element cone (figure 5.5.7(b)) had similar pits as were seen with lubricated contacts (figure 5.5.1(b), 5.5.2(b), 5.5.5(b)) and similar debris were seen on the surface of the lower planetary balls (figure 5.5.11(b)) as were seen with the lubricated contacts (figure 5.5.10(a)). Also the size of debris collected after the RCF tests from the cup assembly was of the same order of magnitude for the dry test (figure 5.5.11(b)) as was seen for the lubricated tests (figure 5.5.10). These observations indicate that the lubricant film affected the duration of the RCF test but the mechanism of surface wear was present in both cases of lubricant and the dry test.

It can be appreciated that when the RCF tests were conducted with Hitec-174 as the test lubricant the lubricant film should be fully developed completely separating the two surfaces thereby avoiding any asperity contact. Thus surface wear should not

be observed with this lubricant. However, the surface observations indicated that this type of failure i.e. surface wear was also present with this lubricant. This difference can be mainly due to the following reasons:

a) At the start of RCF tests the EHL film is not fully developed providing a possibility of asperity contact within the contact region. Also, the affect of running in period cannot be overlooked.

b) During the RCF tests theoretical film calculations indicate a value of λ in the range of $3 \sim 4$ which indicate the beginning of fully developed film. As these calculations are based upon the average RMS value of surface roughness some asperities will always be higher than the average asperities which can provide an asperity contact leading to the generation of initial wear debris. Moreover, two dimensional surface roughness parameters are used in the calculations of λ value and approximate values of pressure viscosity coefficient were used which may not represent the actual behaviour. Once initial wear debris were generated the mechanism was accelerated by the process of three body abrasion.

In general, the mechanism of surface wear initiated from the generation of small debris due to asperity contact which accelerated the process of surface wear due to three body abrasion for the RCF tests conducted in immersed lubrication conditions. However, for the test conducted with splash feed lubrication system this affect can be overlooked. Also, The lubricant film thickness affected the rate of the process and the process of surface wear was accelerated as the λ value was reduced.

6.7.2 Coating delamination

Coating delamination was another type of failure seen on the surface of the rolling element cones. This type of failure was seen for the tests conducted with both the lubricants. Moreover, when the coated rolling element failed in delamination type failure the RCF performance was reduced. Figure 5.5.3, and 5.5.6 show typical examples of this type of failure for the plasma sprayed coatings. Similar observations were made for the D-Gun and HVOF coated rolling elements as shown

in the previous sections of the thesis (figures 5.2.1, 5.2.2, 5.3.1, 5.3.3, 5.4.2, 5.4.3, and 5.6.3). In this type of failure larger chunks of coatings delaminated parallel to the surface of the wear track resulting in sheet like debris as shown in figure 5.5.13. In the case of thinner coatings (coating thickness $< 100\ \mu m$) this type of failure generally took place at the coating substrate interface at an approximate depth of maximum shear stress except for the case of D-Gun coatings under the given test conditions where the rolling elements showed high adhesive strength. However in thicker coatings (coating thickness $> 150\ \mu m$) the delamination took place from within the coating microstructure. The surface observations of the plasma and HVOF sprayed coatings indicated that the depth of these failures can either be approximated as 40 micron or 90 μm under the given test conditions, which can be related to the depths of orthogonal shear stress or maximum shear stress respectively. However, even when the coatings delaminated at the depth of orthogonal shear stress subsurface cracks were observed at the depth of maximum shear stress as was observed in the subsurface observations of the wear track. The mechanism of this type of coating failure can be explained on the results of subsurface investigations of the rolling elements as discussed below.

6.7.3 Mechanism of coating delamination

Consider the subsurface observations of the coated rolling element plasma sprayed cone GG3AX. In this case the approximate coating thickness was 260 micron which can be classified as thick coating under the given test conditions. Figure 5.5.13, 5.5.14 and 5.5.15 indicate that the subsurface cracks were initiated at the depth of maximum shear stress and orthogonal shear stress. The origin of these cracks can be thought due to the stress concentrations owing to the micropores, microcracks, secondary phase particles as were seen in the surface observations of the coating microstructure (figure 5.5.12) for the plasma sprayed coatings and in figure 5.2.3 for the D-Gun coatings. This is consistent with the work described by Littmann (1966) in which subsurface inclusions and oxides were thought to be the cause of subsurface fatigue due to crack initiation and propagation at he depths of maximum shear stress and orthogonal shear stress, and later studies using vacuum furnaces for preparing better quality bearing steel showed much improved life due to reduced

inclusion levels but it also revealed that with some steels there was not significant improvement which suggested that other complex mechanisms are also operational and responsible for rolling contact fatigue. The stress concentrations due to the defects in the coating microstructure also resulted in poor behaviour of the coating during the microhardness indentations (figure 5.5.21 and 5.3.8) in which the coating cracked readily at low indentation loads (100p). As the indentation load was applied the defects in coating microstructure lead to stress concentrations resulting in the cracking of the coating microstructure at low indentation loads. When similar tests were done on the lower steel and ceramic planetary balls no cracking was observed which indicates the poor fracture toughness of these coatings. Also the affect of quenching stresses cannot be overlooked. The fact that these cracks propagated at specific depths of shear stresses also indicated a strong possibility that the coatings had a poor shear strength. The crack initiation was also seen at depths other than the depth of shear stresses as was shown in figure (5.2.1(b), 5.2.2(d), and 5.5.6(d)). This indicated that microcracks appear at different depths under the wear track but they propagate generally at the depth of shear stresses. The cracks at specific depths of shear stress also indicate that the crack propagation was in shear mode (mode II). However, the possibility of initial cracking in mode I or a combination of mode I and II cannot be excluded. The investigation of crack initiation mode for a brittle, lamella and anisotropic coating microstructure is complex and beyond the scope of this experimental work. The coating microstructure generally behaves in a complex way and it is even difficult to quantify the exact values of stress intensity factor shear strength, etc., and there is a significant scatter in published literature on the mechanical properties of thermal spray coatings tested using different techniques. However, it can be confirmed on the basis of surface and subsurface observations of the failed coated rolling elements and the shape and size of debris that whatever was the mode of initiation, the cracks propagated at the depth of maximum shear stress and orthogonal shear stress due to the stress concentrations owing to the defects in the coating microstructure under the applied load.

Once these cracks were initiated they propagated at their specific depths to certain length(s). Although, these cracks were three dimensional in nature and seem to

propagate in the directions of rolling and opposite to rolling (figure 5.5.14(a), 5.5.15(a)) it was not possible to verify the specific direction of crack propagation. The shape of the delamination debris (figures 5.3.5 and, 5.3.9) also support this hypothesis since these cracks reached the surface in both directions. These crack can propagate in mode I or II or a combination of both. As discussed above, no studies were done to study this affect. It was observed that the behaviour of propagation of the cracks at two different depths was different. The cracks at the depth of maximum shear stress continue to develop either by the propagation of single crack or by the combination of small cracks at the same depth (figure 5.5.15(b)). However when the location of these cracks became such that they occur in the vicinity of a crack at orthogonal shear stress than these cracks (at maximum shear stress) approach the crack at the depth of orthogonal shear stress by changing its direction of propagation towards the surface and combine with the crack at the depth of orthogonal shear stress (figure 5.5.14(b)). In general these cracks did not directly reach the surface. After the combination of the two cracks which initiated at two different depths the combined crack generally propagated at the depth of orthogonal shear stress. The cracks at the depth of orthogonal shear stress propagate in the same manner as the cracks at maximum shear stress, ie. parallel to the surface but these cracks propagate much faster (towards the surface) and reached the surface much quicker after a certain crack length thereby delaminating the coating at the depth of orthogonal shear stress. If the coating delaminated due to a single crack at orthogonal shear stress the depth of delamination was uniform however, if the delamination occurred at or near the junction of the cracks at two different depths the depth of delamination varied accordingly depending upon the behaviour of cracks under the surface as shown in figure 5.5.20(a). Similar phenomenon was observed during the subsurface observations of the HVOF coatings as shown in figure 5.6.8.

Consider the subsurface observations of the rolling element cone GG2BY. In this case the coating thickness was approximately 80 micron and the coating can thus be regarded as a thin coating. The subsurface observations of the rolling element GG3AX indicated that the cracks were developed at the depths of orthogonal shear

stress and maximum shear stress which in the case of GG2BY lies near the coating substrate interface. The initiation and propagation of these cracks can be attributed to the same factors as described above with the addition of the affects of mismatch of coating and substrate properties at the interface. This affect of mismatch of the mechanical properties (Young's modulus, Poison's ratio etc.) and the possibility of the presence of inclusions, contamination layers at the interface provided an acceleration in the crack initiation and propagation at the interface. Therefore, in the case of thinner coatings the cracks at the depth of maximum shear stress (interface) initiate and propagate much quicker than the cracks at the orthogonal shear stress (figure 5.5.19). These cracks reach the surface either independently leading to coating delamination at the interface or after joining with cracks at orthogonal shear stress thereby delaminating the coating from within the coating microstructure. Figure 5.5.20(a) shows a view in which both types of delamination are visible. However, in most of the cases of thinner coatings, the mechanism of interfacial cracking and interfacial delamination was common. The poor performance of thinner coatings can thus be understood by the accelerated crack propagation at the coating substrate interface.

The subsurface observations of the rolling element cone GG4AY indicated no subsurface cracks and no delamination was seen on the surface of the rolling element cone. This shows that the coatings which did not delaminate actually resisted the subsurface crack initiation.

Observing the subsurface crack behaviour of these coatings the mechanism of delamination can be summarized as follows:

1) Cracks are initiated at different depths (figure 5.2.1(b), 5.2.2(d), and 5.5.6(d)) under the wear track but they propagate at the depths of maximum shear stress and orthogonal shear stress. For thicker coatings these cracks lie within the coating microstructure and for thinner coatings within the coating microstructure as well as at the coating substrate interface. These cracks are thought to be initiated due to stress concentrations due to the presence of

pores, microcracks and secondary phase particles within the microstructure and an additional factor of mismatch of properties at the interface for thinner coatings. The cracks under investigation were the ones observed under the ultraviolet light and porosity was not considered as a crack.

2) For thicker coatings (coating thickness $>$ 150 μm) these cracks propagate slowly at their respective depths within the coating microstructure however, for thinner coatings (coating thickness $<$ 100 μm) the cracks at the coating substrate interface propagate faster than the cracks at the depth of orthogonal shear stress. This observation was based on the evaluation of the performance (time to failure) of failed rolling elements and the lengths of cracks observed at the two depths during subsurface observations.

3) For thicker coatings the cracks at maximum shear stress extend to greater lengths until they meet a crack at the depth of orthogonal shear stress by changing its direction. For thinner coatings the cracks at interface had the greater tendency of reaching the surface independently and in some cases they combine with the cracks at the depth of orthogonal shear stress and eventually reach the surface.

4) For thicker coatings the cracks from the depth of orthogonal shear stress reach the surface much more quickly than the cracks at the depth of shear stress thereby leading to coating delamination at the depth of orthogonal shear stress. In the case of thinner coatings the affect is generally the opposite and interfacial delamination takes place.

A schematic of this delamination process has been shown in figure **6.7.1** in which both thick and thin coatings have been considered. The above discussion and schematic presentation explains the mechanism of delamination during the RCF tests for thick and thin coatings on the basis of location and orientation of subsurface cracks based on the surface and subsurface observations of the failed coated rolling elements and indicate that coating delamination was a subsurface failure mechanism.

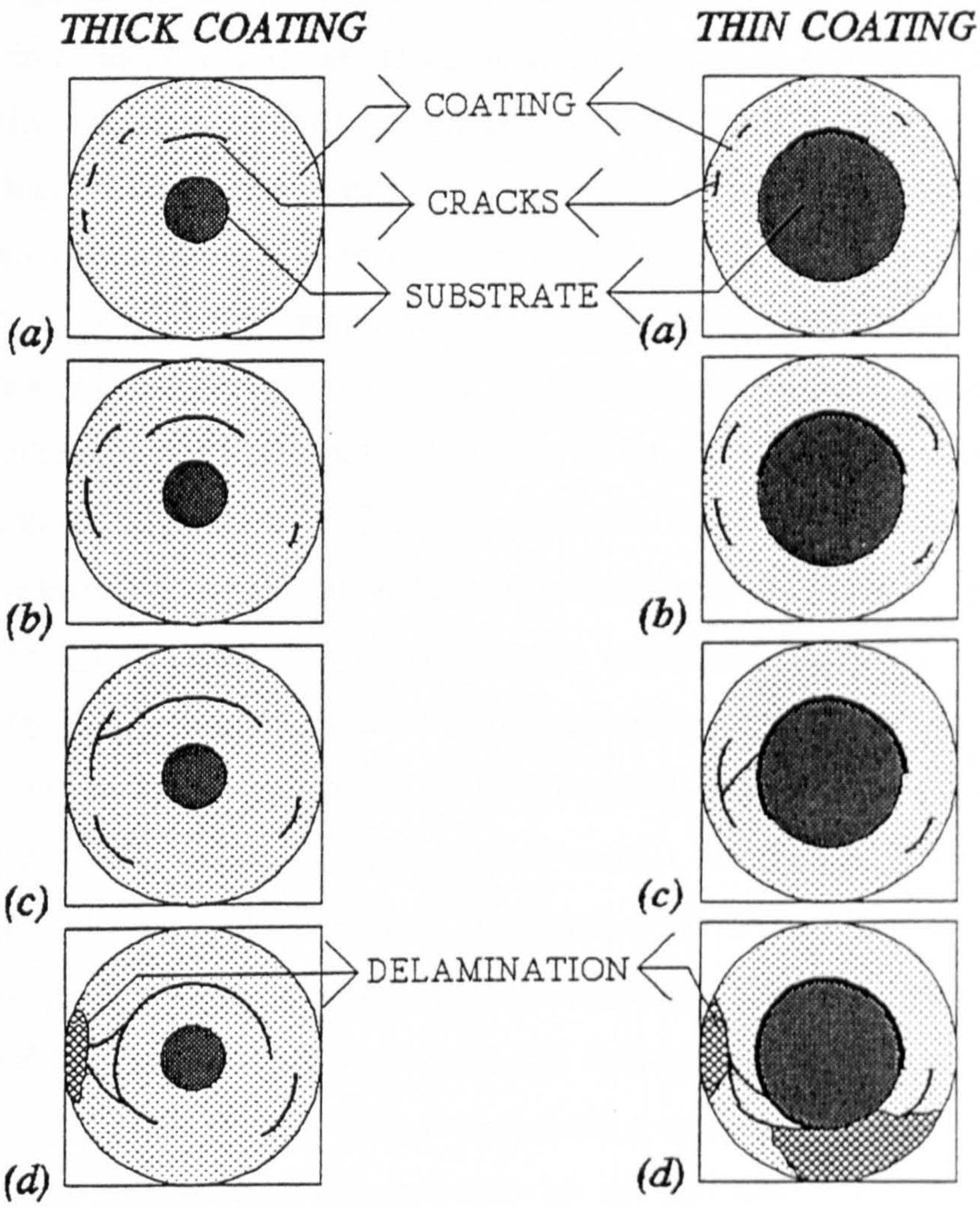

Figure 6.7.1, Schematic of coating delamination process

(a; initiation of cracks at the depths of maximum shear and orthogonal shear stress, b; propagation of cracks parallel to surface, c; combination of cracks, d; coating delamination)

Surface initiated fatigue crack propagation due to lubricant entrapment has been an area of debate since the pressurising mechanism suggested by Way (1935). He suggested that the oil penetration of very small surface cracks with a certain initial direction is the reason for the growth of fatigue cracks until the particle was separated from the body of the rolling element. Although the subsurface observations strongly suggested the coating delamination was a subsurface mechanism it is important to explore the possibilities if lubricant entrapment could

have significantly contributed to the coating delamination. The complexity of the problem is mainly due to the affects of surface roughness and topography, lubricant viscosity, residual stresses, magnitude and direction of traction and asperity behaviour which all should be considered along this mechanism. Many researchers have tried to study the affects of some of the above factors but the complexity caused by the above mentioned tribological factors have made it difficult to confidently conclude this theory, yet the experimental evidence suggest that cracks only propagate in the presence of lubricant and if traction is present in the preferred direction of load movement (Bower, 1988) and Tyfor (1994). After Way's theory later researchers suggested additional mechanisms to support this theory by considering a mode II crack propagation due to reduced coefficient of friction at the crack tip due to the presence of lubricant causing the surfaces to slide. Others suggested the mechanism of lubricant entrapment leading to hydrostatic pressure build-up causing the crack tip to open in mode I and then in mode II due to the leakage of the entrapped lubricant. In general, there is substantial awareness of the possibility of lubricant related crack propagation. The actual mechanism(s) of lubricant initiated crack propagation leading to fatigue failure is however beyond the scope of this work. However, the experimental investigation conducted in this thesis suggest that delamination occurred with all the test lubricants and in some cases within a few seconds with Hitec-174 lubricant (appendix F, section F1.3), which indicate that there was not sufficient time for the high viscosity lubricant to entrap and propagate the cracks. Similarly the test with dye penetrant (table 5.6) was conducted as a measure accelerated lubricated entrapment mechanism because of the ability of this lubricant to entrap and penetrate in the cracks. The surface and subsurface observations of this rolling element however did not result in any delamination or subsurface cracking thereby indicating that lubricant entrapment mechanism was not significant in coating delamination.

The above mentioned mechanism of coating delamination (section 6.7.3) concluded that the mechanism of crack initiation and propagation was subsurface due to stress concentrations. It can however be established that even if lubricant entrapment was operational during the RCF tests it is not likely to be a mechanism leading to

coating delamination on the basis of following observations:

a) The delaminated coating and subsurface cracks extended beyond the width of the wear track as seen in figure 5.5.8(c), 5.5.4(a) and 5.5.9(c) which can not explain the mechanism of hydrostatic pressure build-up as the stresses must be tensile at the edge of the wear track.

b) Cracks occurred subsurface and only at specific depths and travelled circumferentially parallel to the surface.

c) Delamination occurred with both lubricants and considering the extremely high viscosity of Hitec-174 it does not seem likely for this lubricant to penetrate the cracks.

d) The cracks propagated and reached the surface in the direction of rolling and opposite to the direction of rolling (figure 5.5.21(b) and 5.5.27).

e) The cracks were long and it will require a high load and extremely low viscosity oil to cause pressure build-up at the crack lengths of 5 mm as seen in the subsurface observations.

f) Tests conducted with dye penetrant as the test lubricant did not delaminate.

g) Studies have shown that cracks can only occur at the edge of the wear track (Hadfield et. al. 1995) which can not explain the lubricant entrapment mechanism.

h) The delaminated debris were of constant thickness with straight edges whereas if the crack was from surface to subsurface it should be inclined.

i) Coating delamination was observed for the RCF tests which lasted less than a minute, therefore not allowing significant time for lubricant entrapment.

The mechanism(s) of lubricant initiated crack propagation may or may not be present but the above observations indicate that the likelihood of such mechanism(s) significantly affecting the coating delamination were rare. Similar behaviour was observed by Nieminen et. al. (1995), when they reported that subsurface cracking of the coated rolling elements during the dry tests, thereby excluding any possibility of lubricant entrapment mechanism to aid the delamination crack propagation in thermally sprayed rolling elements under the given test conditions.

In general the coated rolling element cones failed either due to surface wear, subsurface delamination or bulk material failure (figure 6.3.2) due to the reasons as discussed above and these failures can be summarised as shown in figure 6.7.2.

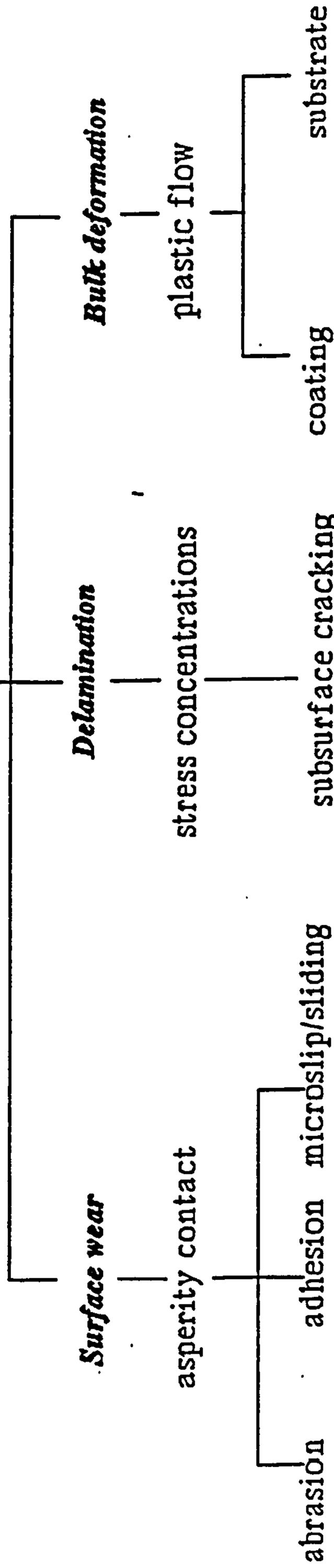

Figure 6.7.2, Types of coating failures

Chapter 7
CONCLUSIONS and FUTURE WORK

Experimental investigation of the RCF performance and failure modes of WC-Co coatings produced by a variety of thermal spray techniques and tested under various tribological conditions indicated that HVOF coatings performed better than D-Gun or air plasma sprayed coatings. These studies have shown that under certain specific test conditions these coatings can last more than 60 million stress cycles without appreciable damage to the coating. The surface and subsurface investigation revealed that the failure of these coatings can be classified in three categories amongst which one was catastrophic delamination.

The RCF studies indicated that the coating process, coating thickness, substrate material, lubricant, contact stress and the kinematics in the four ball machine affect the performance and failure modes of these thermal spray coatings. Similarly, the residual stress studies have shown dependence of coating failure on the residual stress behaviour.

7.1 Conclusions

(1) WC-Co coatings studied in this thesis indicated that thicker coatings performed better than thinner coatings under all tribological conditions on bearing steel substrate.

(2) WC-Co coatings produced on mild steel substrate indicated an improved performance for a coating thickness of 20 μm in comparison to the coatings greater than this thickness at low contact stresses up to 1.7 GPa in high viscosity lubricant. All other conditions suggest improved performance as the coating thickness increases.

(3) Residual stress studies have shown that these coatings not only have residual stress ranging up to hundreds of MPa, but also the residual stress attenuates during the RCF tests and the coating failure results in very high attenuation

of these stresses.

(4) The coating failures can be categorized into three classes as surface wear, subsurface delamination and bulk material failure. Surface wear was operational under all the test conditions considered in this work, whereas bulk material failure was only seen on mild steel substrate coatings. There was no definite trend between the delamination type failure and the tribological conditions.

(5) The delamination type failure was due to the propagation of cracks at the depth of orthogonal shear stress and maximum shear stress due to the defects in the coating microstructure.

(6) The performance of these coatings was dependent upon the direction of sliding during the RCF tests.

(7) The RCF performance was significantly reduced by changing the contact configuration from conventional steel ball bearing to hybrid ceramic bearing under all test conditions.

(8) Low preheat temperatures lead to very low adhesive strength of the coatings and premature coating failures at the coating substrate interface.

7.2 Recommended Further Work

The studies presented in this thesis on the WC-Co coatings and previously on Al_2O_3 coatings have shown that the RCF performance was material dependent which was mainly due to the differences in coating microstructure and the role of residual stresses due to the differences in the coefficient of thermal expansions of the coating and substrate material. Similar studies can be made on WC-Co-Cr coatings. Post treatment of these coatings by Hot Isostatic Pressing (HIP) and laser treatments etc. can also be looked at for improved performance of these coatings. The coating process parameters used in this study were of conventional industrial practice and

investigations can be made to study the affect of the parameters controlled during the coating process and the RCF performance of these coatings.

The crack initiation and propagation in this thesis was based upon the surface and subsurface investigations. Fracture mechanics and finite element modelling approaches should be also made by taking account of the defects in the coating material. One such study can be to model the porosity and cracks in the microstructure and than study the affect of applied loads on the initiation and propagation of these cracks.

The affect of sliding direction should also be looked at from mathematical view point for a better understanding of the RCF process.

The residual stress investigations in this thesis were limited to near surface investigations and more powerful techniques can be used for obtaining the residual stress profile at different depths.

Appendix A
THE MODIFIED FOUR BALL MACHINE

The modified four ball machine shown, in pictorial view as figure A-1, represents the family of tribological machines which are extensively used to investigate the rolling contact fatigue performance of engineering materials under the various tribological conditions of loading, temperature, speed and cup configuration. The Institute of Petroleum (Tourret et. al. 1977) gathered various papers which give an indication of the RCF test results ball dynamics and kinematics of the modified four ball machine. Other commonly used machines used for the RCF testing of materials are the five ball machine, the ball on rod machine, the ball on disc, etc. The I.P-300 give a standard procedure for performing the rolling contact fatigue tests for fluids using the modified four ball machine. During this research programme the RCF tests were conducted in accordance with the IP-300 procedures for high speed tests at room temperatures. The test machine was qualified by conducting initial tests according to the standard requirements and the machine was found to comply with the requirements. The coated test samples during the testing programme were designed in the geometry of a ball or cone. Although the modified four ball machine has not previously been reported as the test method to investigate the RCF performance of thermal spray coatings, significant data are available when the modified four ball machine was used to investigate the rolling contact fatigue performance of coatings produced by gaseous state processes, like reactive sputtering (Sproul et. al. 1993).

Figure A-2 shows a schematic of the modified four ball machine. The machine consists of an upper rolling element which drives the three lower plenary balls. The modified four ball machine differs from a conventional four ball machine in that the lower planetary balls are free to rotate. The machine represents the configuration of the deep groove rolling element ball bearing in which the upper balls act as the inner race and the three planetary balls as the rolling elements. The plenary balls

are free to rotate in the cup which represents the outer race of a rolling element ball bearing. Figure A-3 gives the arrangement and dimensions of the four ball assembly. A K-type thermocouple embedded in the base of the cup holder was used to measure the temperature of the oil bulk during the test. A heater placed underneath the cup assembly can be used to perform the tests at elevated temperatures. The dead weight applied at the end of the lever arm is used to produce the required Hertz stress between the upper rolling element and the plenary balls via a piston at the base of the cup assembly. The lever arm can be set to have an arm ratio of 10:1 or 20:1 and is balanced by a counterweight at the other end of the lever arm.

The driving rolling element is fixed to the spindle through a spring steel collet and the spindle speeds may be varied up to 20,000 rpm. The spindle is driven by a shunt type electric motor via a high or low speed drive belt. The motor speed is controlled by a motor speed controller, which protects the motor from excessive current. Test times and spindle revolutions are recorded by a timer and tachometer. A vibration sensor connected to the body of the machine measures the vibration amplitude. The machine can be set to stop at either a required revolution number or a preset vibration amplitude.

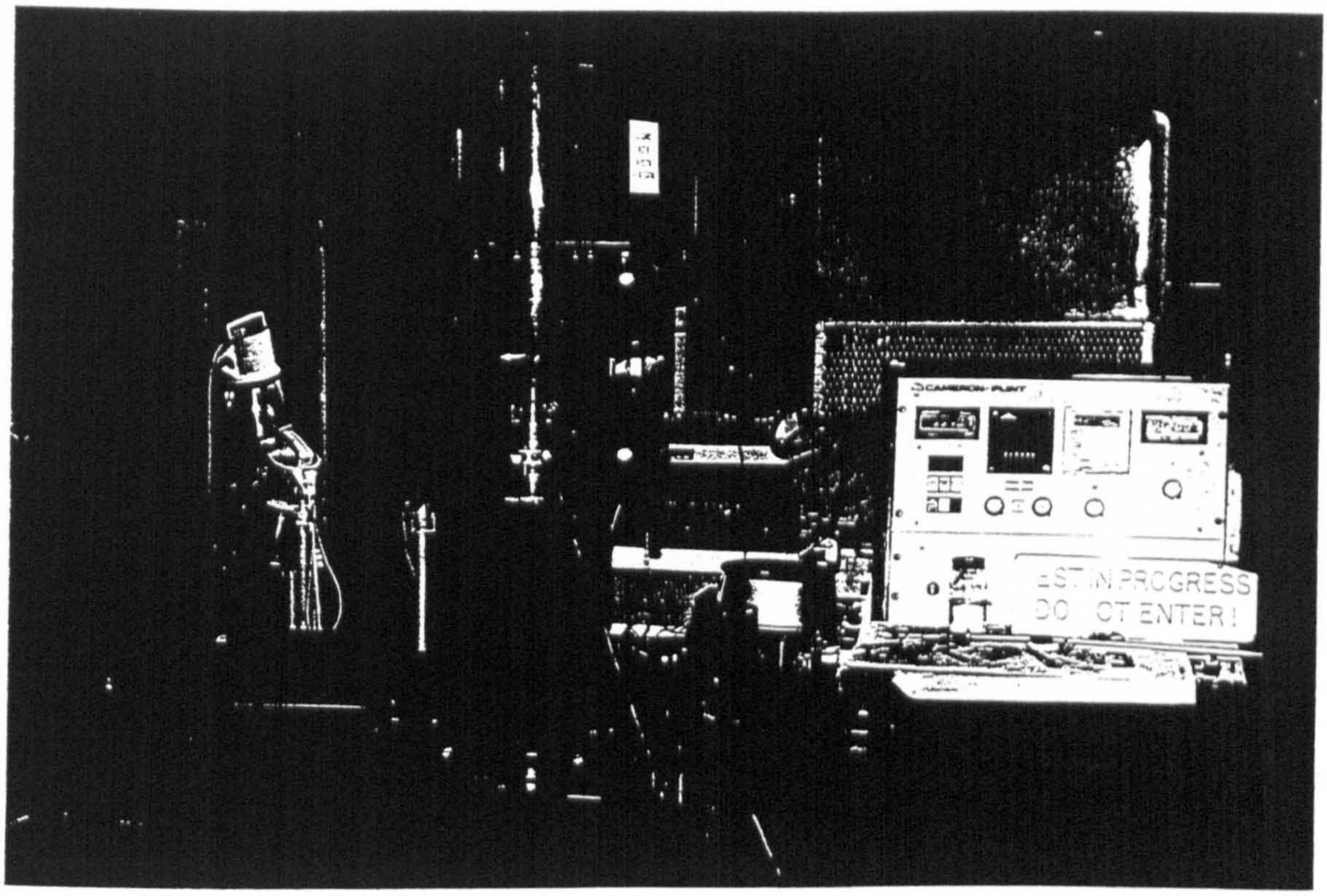

Figure A-1. Four ball machine (pictorial view).

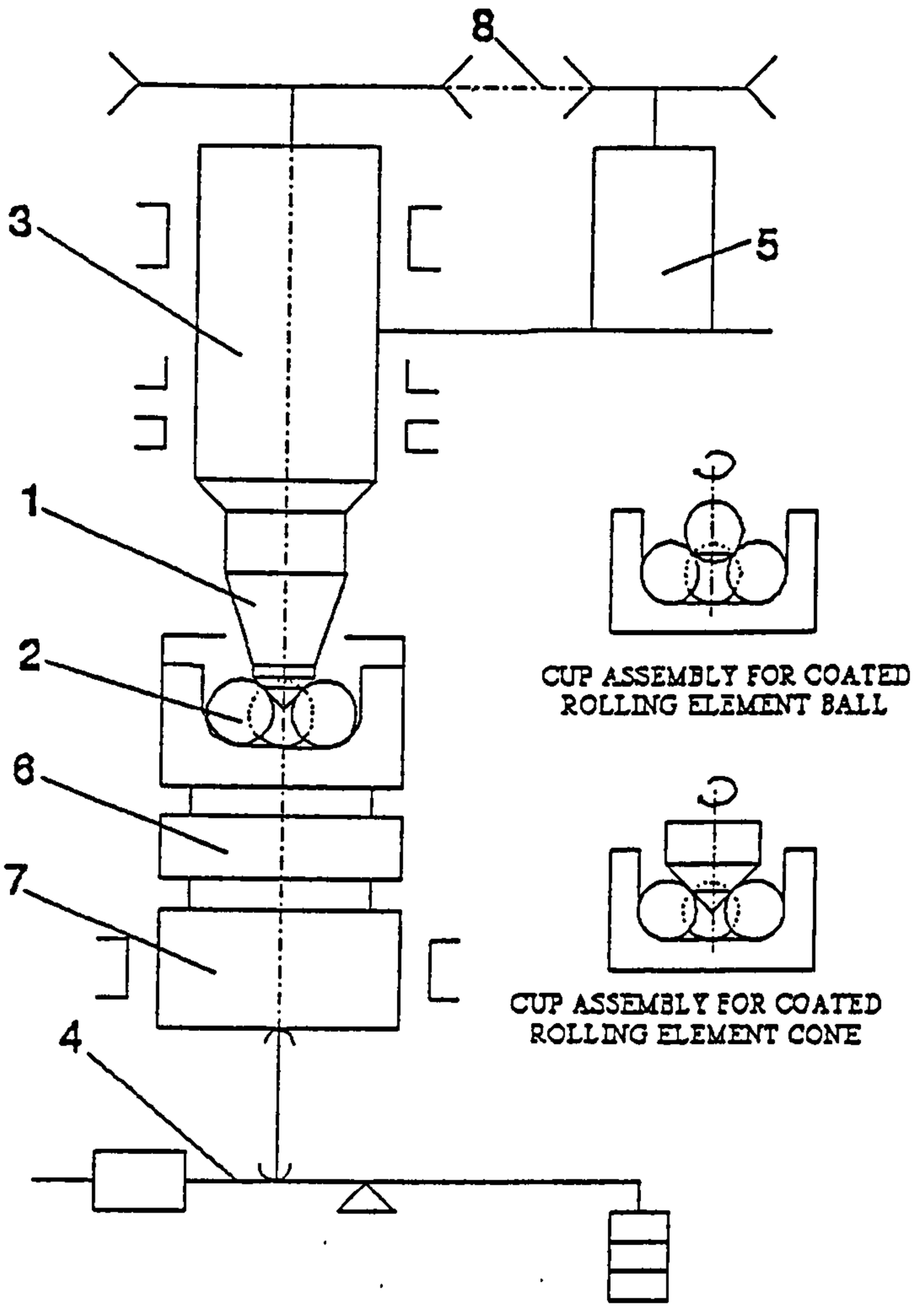

Figure A-2, Schematic of the modified four ball machine.
(1; collet and driving rolling element, 2; lower balls, 3; spindle, 4; loading lever, 5; driving motor, 6; heated plate, 7; loading piston, 8; belt drive)

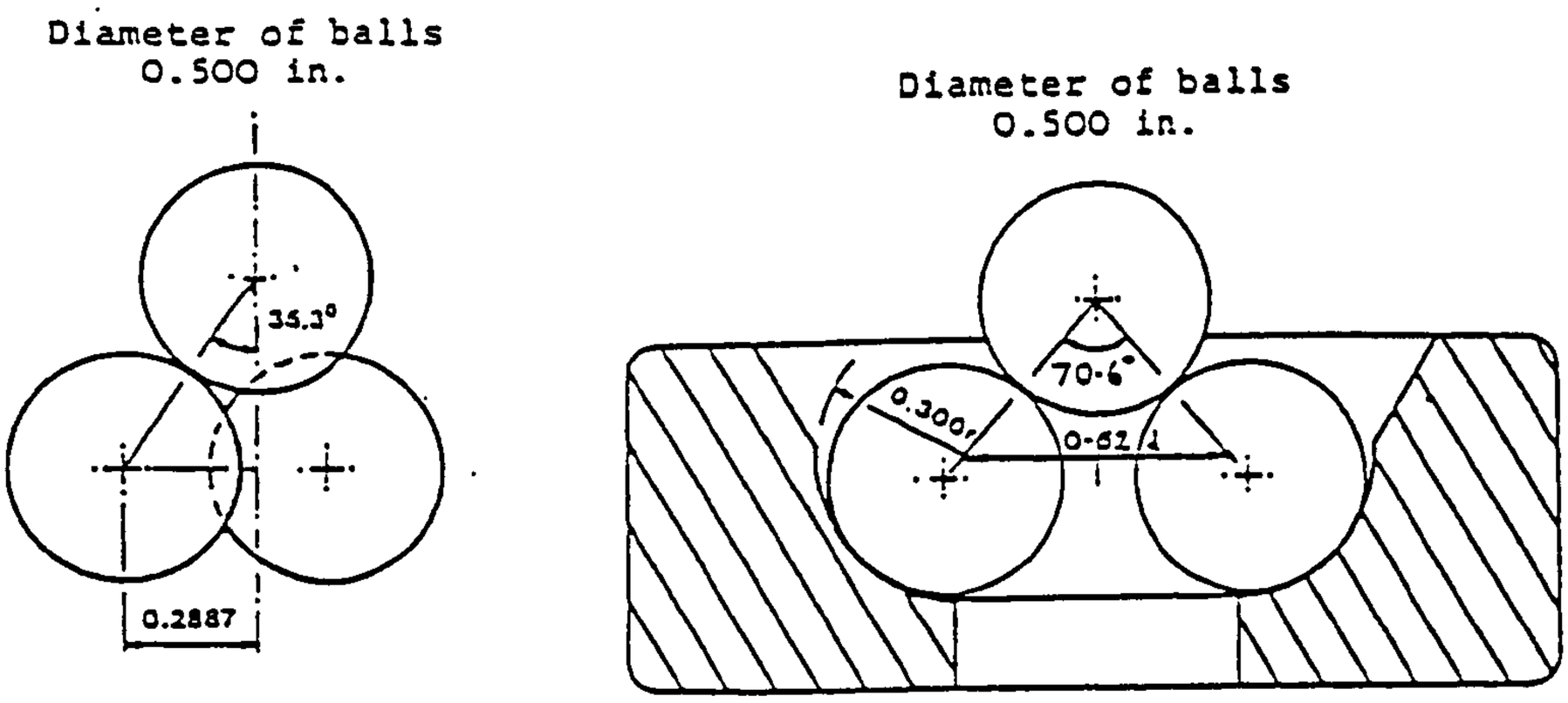

Figure A-3, Dimensions of the cup assembly.
[Ref: Modified four ball machine manual]

Appendix B
THERMAL SPRAY COATINGS

B1.1 Introduction

Thermal spraying can be regarded as a universal coating technique because of the almost unlimited number of coating and substrate materials (Eschnaver, 1991). In the thermal spraying process the coating material in the form of a powder, or a wire, etc. is melted and accelerated which impacts to form a deposit on the substrate material. Thermal spray coatings are regarded as overlay coatings (ie. they do not alter the composition of the substrate material) and the coating processes are generally classified on the method of heat generation which is required to melt the spraying material. However, classifications can also be made on the basis of velocity, temperature or material, etc. of the impacting coating particle. Figure B-1 describes a basic classification of the thermal spray coating processes, defined on the basis of the method of heat generation. Among these coating processes flame spraying was one of the first thermal spraying techniques which became available to the industry. This technique was used because of its high deposition rate and the oil retention properties due to the inherent porosity in the coating microstructure which made them suitable for tribological applications like piston rings etc. However, the later advancements in thermal spraying techniques, eg. Detonation Gun, High Velocity Fuel Spraying, Plasma Spraying, etc. were geared to improve the application range of thermal spray coatings due to improved microstructure. These improvements were caused not only by the higher velocity of the impacting particles for a dense coating microstructure but also by increased temperature which is specially useful for spraying ceramic materials. Kudinov et. al. (1989) gave a general classification of the impact velocities and temperatures of WC-Co particles for different thermal spraying systems as indicated in figure B-2.

In the present study, three coating techniques, i.e. Detonation gun (SDG 2040), High velocity Oxy Fuel (Plasma Technick) and Plasma spraying (Gator Guard) were

used to investigate the RCF performance of thermal spray coatings. A description of these coating techniques is given below, however the process parameters are not included (because of patented designs and confidentiality requirements), and these parameters were of conventional industrial practice used by the coating supplier.

B1.2 Detonation Gun Coatings

The Detonation gun (figure B-3) is a combustion spraying process which uses the energy released by a controlled series of detonations of fuel gas to heat and accelerate the coating powder to high velocities. During this process, a gas mixture of measured volumes of oxygen and acetylene (45% by volume) are fed into the combustion chamber at the breach of a gun barrel and ignited by an electric spark, which heats and accelerates the particulate. Temperatures of 4500 K and velocities of 750 m/s can be obtained by the D-Gun process (Pawloski, 1995). After detonation the D-Gun is purged with nitrogen and the process is repeated from 1 to 15 cycles per second. An advancement in the D-Gun coatings is the super D-Gun in which particle velocities of 900 m/s (Pawloski, 1995) can be achieved. Figure B-4 shows the schematic of the super D-Gun process. This process is commonly used in the industry to produce tungsten carbide and aluminium oxide coatings, although fourteen coating compositions are catalogued by Union Carbide. The D-Gun coatings produced during this study were produced by a super D-Gun (SDG 2040) which is also a patent of union carbide.

B1.3 High Velocity Oxy-Fuel Coatings

The High Velocity Oxy-Fuel (HVOF) process is one of the latest modifications in thermal spraying technique. During this process the coating powder is melted inside the combustion and gas injector chambers prior to being sprayed on to the substrate. The spraying gun used for the HVOF technique consists of an internal combustion chamber in which a gaseous or liquid fuel, eg. acetylene, kerosene or propane etc. and oxygen are injected at high pressure and high flow rates. The products are then ignited continuously and the resulting flame being allowed to expand supersonically and exit in to the atmosphere through a long nozzle. A typical feature of the process

is the presence of shock diamonds as seen in the flame of spraying. Two developments in the process are High Velocity Air Fuel and the High Velocity Impact Fusion (HVIF) processes.

During this study the continuous detonation gun of plasma technick was used to deposit the WC-12%Co (HVOF) coatings. Powder particle size of 5 to 40 μm was used. Figure B-5 shows a schematic of the typical HVOF coating process.

B1.4 Atmospheric Plasma Spray Coatings

The Plasma spray process utilizes the energy contained in a thermally ionized gas to melt and propel powder particles. The plasma spray consists of an anode (eg. copper) and a cathode (eg. tungsten). An inert gas (eg. argon or nitrogen) is caused to flow around the cathode and through the anode which is shaped in the form of a converging nozzle as shown in figure B-6. The high frequency electric discharge is used to initiate an arc between the electrodes which is carried by the ionized gas plasma. Most of the conventional plasma spray torches use subsonic gas flow conditions but the incorporation of converging/diverging nozzle geometry in the anode can enable supersonic gas flow rates. The plasma spraying technique is further classified as Air Plasma Spraying (APS), Argon Shroud Plasma Spraying (ASPS) and Vacuum Plasma Spraying (VPS).

An advancement in the plasma spraying technique is the Gator Guard coating process. This technique uses a high temperature and high velocity (typical particle velocity 1200 m/s) to deposit metal or ceramic particles on the substrate materials. Figure B-7 gives a comparison of the conventional plasma and Gator Guard coating systems. The WC-12%Co plasma spray coatings used during this study were deposited by Gator Guard (GG 102) systems. The powder particle size was 5 to 25 μm and the spraying distance was 65 mm.

B1.5 Coating Formation

Thermal spray coatings have a lamellar structure and are formed by the buildup of

individual coating particles which splat on to the surface of the substrate or an already solidified lamella. These particles can be fully or partially melted or solid at the time of impact. Figure B-8 (Wilms, 1978) shows a schematic of the typical coating microstructure. This figure shows that these coatings are not homogenous as many pores, cavities, microcracks etc. can be present in a typical coating microstructure. The resulting microstructure of the coating depends upon the conditions of the impacting particle and their behaviour at the time of impact. The flow and solidification of a molten particle upon impact is very complex, since freezing occurs in a few micro seconds. Thus the wetting and flow properties of the liquid droplets upon impact are the most important factors which govern the coating microstructure. In general, the temperature, speed, size, material of the impacting particle, coating atmosphere as well as the material, temperature and surface conditions of the underlying substrate or coating are the major factors which govern the microstructure of the coating deposit. These factors are not only dependent upon the coating material and the coating process, but also upon the parameters controlled during the coating process.

Depending upon the behaviour of the impacting lamella, the conditions of the particle at the time of impact and the heat dissipation during thermal spraying, the coating microstructure can suffer from various degrees of porosity, microcracks, secondary phase particles, inclusions, etc. The impacting particles can be subjected to shadowing affects, and thus the real area of contact can be very low. Moreover, since the particles can acquire different sizes and shapes after the impact, the coating microstructure suffers from numerous defects. Some of these defects are shown in figure B-9. Although, the degree of these defects can vary for different coating processes. The latest advancements in thermal spray coatings are thus synergized to make the microstructure of these coatings as homogenous as possible. It is worth mentioning that even if the coating is free from all the possible defects, the behaviour will still be anisotropic due to the typical directional arrangement of lamellae, however the degree of anisotropy can vary.

B1.6 Coating microstructure

Lin et. al. (1995) described the coating microstructure as a three dimensional structure of discs which are interrelated to form a material of composite nature which is anisotropic and heterogenous in behaviour. Kudinov et. al. (1989) have described the coating microstructure as a combination of three structural elements, i.e. coating substrate interface, layer-layer interface and particle-particle interface, whereas each hardened and solidified particle has its own complex structure. Similarly, the levels at which the coating microstructure can be studied were discussed by Yankee et. al. (1993). It is appreciated that these individual particles behave as the building blocks for the coating microstructure and a thorough understanding of particle behaviour at the time of impact is of extreme importance before any understanding of the coating microstructure can be developed. It is for this reason that this has been a topic of extensive experimental and analytical research during the last decade. Kudinov et. al. (1989) performed a comprehensive study on the interaction of Al_2O_3 particles with the substrate and the adjoining particles. Their investigations revealed that the deposited material can be an aggregation of eight different states of particles as shown in figure B-10. They summarised thirty different cases in which a particle can behave at the time of impact. Figure B-11 describes the sectioned view of these particles. They explained the formation of microcracks, spheroid voids, microvoids and small pores on the basis of the particle behaviour shown in the above figures (B-10 & B-11). However, it should be appreciated that the flattening and solidification of thermal sprayed particles involve very rapid changes in dynamic and thermal state of molten particles that depend upon many factors some of which are unknown or not well known.

The experimental and analytical studies revealed that the coating microstructure is very sensitive to the splat behaviour which not only relies on the temperature, viscosity, velocity and wettability, etc. of the impinging particle but also on the thermal conductivity, temperature and surface roughness of the underlying substrate or lamella. Even if the process parameters are kept constant the splat behaviour changes at the interface and through the coating thickness because of the changes

in temperature, eg. heating due to coating process, cooling due to the rastering of the spraying gun, surface roughness affects and the variations in the impinging particle size, temperature, velocity depending upon its location in the stream of impinging particles. All these parameters make the theoretical models complex and experimental investigations limited to the specific spraying processes and process parameters. Hence, future research can be geared to develop a fundamental understanding of the coating microstructure depending upon the modelling of splat behaviour at the time of impact. It should be appreciated that the importance of understanding of the coating microstructure is vital for high stress applications like, components in rolling/sliding contact, where the stress concentration near the voids, microcracks and unmelted and secondary phase particles can significantly affect the crack initiation and propagation and thus alter the failure mechanism. Thus, it is not only the extent of porosity which should be investigated but also the shape, size and location of porosity within the coating microstructure should be studied. This can also enable a better understanding of the mechanical properties of these coatings i.e. the variation in properties can be linked to the coating microstructure.

B2.1 Coating Properties

The mechanical properties of thermal spray coatings largely depend upon the interlamellar bonding and the bonding at the coating substrate interface. This is mainly because of the variations of the microstructure with coating thickness, compatibility of the coating material with the substrate, variations in the residual stress pattern and coating anisotropy. It is for these reason that only averaged values of the mechanical properties are available and every coating manufacturer provides his own data on these properties depending upon the coating process and process parameters used. Another way to obtain these properties can be laboratory tests which can be made to evaluate the coating properties for a batch of coatings under investigations. Even in that case the measured values can vary due to the differences in measuring techniques as indicated below and the difficulties involved with the quality control of thermal spray coatings. Hence, in most of the case the values available can be thought of as approximate. In applications like rolling contact the

properties like Young's modulus and Poisson's ratio, hardness, residual stress and fracture toughness are of paramount importance. The following section describes some of these properties:

B2.1.1 Young's modulus

Young's modulus is an important property which defines the stress/strain behaviour of a material. Many techniques have been shown to measure the magnitude of Young's modulus in thermal sprayed materials. Some of these techniques are mechanical, eg. a tensile test to predict the value of E from stress strain relation ship, a three point bending test to calculate the magnitude of E from the deflection of a coated beam or detached coating, similarly deflection of a coating ring and measurements of the coating indentation area can also be used as shown by Nakahira et. al. (1992). Other techniques like nano indentations, and ultrasonic method of measurement can also be used which depends upon the reflection of the transmitted wave the detail of which can be seen from Kawase et. al. (1990) and Richard et. al. (1992). The Young's modulus of thermal spray coatings largely depend upon the coating microstructure which in turn depends upon coating type, process and process parameters, etc. Moreover, the anisotropy of thermal spray coatings makes it extremely difficult to get accurate values of E, by various measurement techniques defined above.

Nakahira et. al. (1992) have described the coating anisotropy to be approximately 2, where anisotropy is defined as the ratio of the Young's modulus parallel to the coating plane to the Young's modulus perpendicular to the coating plane. Significant data are available on the values of Young's modulus of thermal spray coatings produced by different techniques as indicated by Powlaski (1994). However, the discussion in this appendix is limited to the coating materials and coating processes used for the production of sprayed rolling elements ie. WC-Co and Al_2O_3 coatings. Kawase et. al. (1990) have shown that the measured value of Young's modulus varies significantly depending upon the measurement technique. They reported that for sintered Al_2O_3 coatings the magnitude of E was approximately 110 GPa by the

mechanical method, 310 by the X-ray method and 60 GPa by the ultrasonic method. They indicated that the values by X-ray method are higher because strain is measured as an average of the crystalline phases. However, it should be appreciated that the values by the X-ray method should only be used when calculating the residual stress by the X-ray method. Brent (1995) measured the Young's modulus of WC-12%Co and WC-6%Co coatings produced by HVOF process. In his study, using a three point bending test method he measured the magnitude of Young's modulus as 240 GPa and 260 GPa respectively for the two coatings. Morishita (1992) measured the Young's modulus of WC-12%Co coatings using the stress strain curve. He measured a value of 32 GPa and 44 GPa for the coatings produced by the J-Gun and Plasma coatings respectively. Kuroda (1991) have shown that the Young's modulus of coatings measured by three point bending test can be one third of the Young's modulus of the bulk material. From this approximation the E value for WC-12%Co coatings can be calculated as 220 GPa. However it should be appreciated that the value of Young's modulus of the sprayed material can be as low as 10% of the bulk material as indicated by Gudge (1990) or less than 50% of the bulk material as indicated by Kingswell et. al. (1990). Brandt (1995) have indicated that the magnitude of Young's modulus can be 40% of the value of sintered hard metals. Similarly, Pawlowski (1994) indicated that the Young's modulus of WC-Co coatings is more dependant on the coating technique than the binder content i.e. cobalt. It can be appreciated that the magnitude of measured Young's modulus not only depends upon the coating process and the process parameters but also upon the method and direction of measurement. In most of the cases the three point bending test method is used to evaluate the magnitude of Young's modulus. When these measurements are made on the detached coatings the mechanical interlock and residual stress at the interface are neglected. When these measurements are made on the composite beam principle they will be indicative of the specific coating material, process and thickness on the specific substrate material. Extreme care is required in quoting these values as in most of cases only an approximate value is available which is typical of the coating process.

B2.1.2 Microhardness

Hardness may be defined as the resistance of a material to plastic deformation, eg. indentation, abrasion, scratching and machining, etc. The term hardness here means the resistance to the plastic deformation from indentation. The SI unit of hardness is N/m^2 and can be represented as the ratio of the applied load to the area of indentation ie:

Hardness = (Load applied to the indentor, Kgf)/(Contact area of indentation, mm^2)

Various hardness indentation tests differ from each other in shape, size of the indentor and the time of indentation, eg. Brinell hardness tests use steel ball as the indentor, Vickers hardness uses a pyramid shaped diamond as the indentor while the Rockwell tests can be conducted using a diamond cone or hard steel ball as the indentor. For thermal spray coatings, Vickers microhardness tests offer some practical advantages like small indentation size and precise location of indentation which can be helpful in predicting the microhardness variations through the coating microstructure. The use of Vickers microhardness at different indentation loads is thus fairly common in thermal spraying industry. Vickers microhardness test use a diamond indentor of pyramid shape having an angle (θ) of 136^0 between the opposite faces of the indentor. The load (P) is applied for 15 seconds and the area of indentation is calculated as:

$$d^2/(2\ \sin\theta/2) = d^2/1.854 \text{ (for the given value of } \theta = 136^0)$$

If the applied load P is in grams and the width of the indentation diagonal d is in μm, the vickers hardness (VHN) can be calculated as:

$$\mathbf{VHN} = 1.854\ (P * 10^{-3})/(d^2 * 10^{-6}) = \mathbf{1854\ P/d^2}$$

ASTM E384 gives a test method for the measurements. The applied load in Vickers hardness covers a range of 1 to 1000 grams in the microhardness range and 1 to 120

Kg in the macrohardness range. Vickers microhardness of most of the engineering materials is given at specific loads because measurements performed at different loads can result in different values due to elastic recovery and strain hardening affects etc. The relationship between the applied load P and the diagonal of indentation was given by Meyer as follows:

$$P = ad^n$$

where a is the resistance to first penetration for the material and n is a material constant. The value of n is 2.0 for materials which do not work-harden and 2.5 for materials which work-harden easily.

It is a well established fact that the microhardness of a thermally sprayed material not only depends upon the coating process but also upon the parameters during the thermal spraying process. Due to the inherent anisotropy of thermal spray coatings the microhardness varies in the transverse and longitudinal direction (Powlaski, 1994). Similarly, the load of indentation, position of measurement and the microstructural changes due to post treatment (eg. HIP treatment) or service loading (eg. Temperature variations in thermal barrier coatings) all affect the microhardness of thermal spray coatings. All these factors provide a great scatter in the values of measured microhardness.

Wira et. al. (1995) indicated that the microhardness of tungsten carbide coatings varies significantly throughout the coating microstructure. They revealed that this variation was due to the presence of lamellae of different chemical composition produced during the spraying process. Lin et. al. (1993) observed that the microhardness of thermal spray coatings varies not only in the as-sprayed samples but also during the service conditions. They indicated that the microhardness of thermal barrier coatings may vary according to the operating temperature and can thus affect the lifetime of coatings.

Harvey et. al. (1995) in their study indicated the affect of fuel gas during HVOF spraying process on the average microhardness of WC-Co coatings. They indicated that the average microhardness of WC-Co coatings vary from 997 HV_{300} to 1074 HV_{300} depending upon the gas composition. Similarly Mutasim et. al. (1990) indicated that the average microstructure of WC-Co coatings produced by high velocity vacuum plasma spraying can vary from 1385 HV_{300} to 1210 HV_{300} depending upon the spraying distance whereas, for the high velocity air plasma spraying the values vary from 1050 HV_{300} to 900 HV_{300} depending upon the spraying distance. These studies indicate the affect of coating process and process parameters on the microhardness of WC-Co coatings.

In general it is seen that the variation in microhardness with the coating process and process parameters is well understood but the scatter in the measured values need mathematical interpretation of the results. One technique was used by Lin et. al. (1993) when he adjusted the microhardness results by neglecting the two lowest and highest values. However, their later studies (Lin et. al. 1995) indicated that the Guassian and Weibull distribution can be used for better interpretation of microhardness results.

B2.1.3 Fracture toughness

Measurements on the fracture toughness of the thermal spray coatings can be helpful in predicting the failure when these coatings are subjected to high stress applications. The principle of fracture toughness in most case is the strain energy release rate, G (J/m^2) for a given crack length and known applied load to a material of known dimensions and can approximated as:

$$G = (P^2 / 2B) \times (dC/da)$$

where P is the force required to extend a crack(N), a is the crack length(m), B is crack thickness(m) and C is compliance(m/N). This strain energy release rate can be related to fracture toughness K_x (where x is the fracture toughness in mode I, II

or III), by using the relation:

$$K_x = (EG)^{0.5}/(1-v^2)$$

where E is the Young's modulus and v is the Poisson's ratio of the coating material. When G exceeds a critical value G_c, crack propagation occurs and failure of the coating system occurs. Lin et. al. (1994) have used this theory to access the tolerance of thermal spray coatings to cracks by measuring their fracture toughness. Thus mechanical adhesion of thermal spray coatings to the substrate can be measured in terms of adhesion strength or fracture toughness. They discussed the test methods like double cantilever beam (DCB), double torsion test, three or four point bending test, microhardness assessment etc. in the light of fracture toughness. They indicated that all these tests suffer from their own disadvantages, eg. DCB method requires elaborate and expensive test equipment and special specimen preparation, tensile adhesion test suffer from epoxy preparation and alignment problems. However, the indentation technique has been successfully used to measure the fracture toughness of wide range of bulk materials and is a single test that can be used to access the fracture toughness of sprayed coatings. Unfortunately, cracking mechanisms are different for the indentation in the cross section and in-plane orientations. When the indentation is performed in the cross section, the coating tend to crack along the lamella interface as well as from the four corners of the indentor. Moreover, the indentation fracture toughness measurements were observed to be greater than those from DCB tests. Because of the variations in the crack pattern they suggested an analysis on the weibull modulus because the highly anisotropic coatings because randomly placed indentations do not produce consistent fracture toughness values.

Richard et. al. (1992) and Dal Maschio et. al. (1992) have shown that microhardness indentations can be used to measure the fracture toughness of the coatings at the interface. Beshish et. al. (1993) have used the microhardness indentations to measure the fracture toughness of ceramic coatings produced by

plasma spraying. They used the following relation to calculate the fracture toughness in mode I:

$$K_{Ic} = 0.016\ (E/H)^{0.5}(P/C^{3/2})$$

where P is the indentor load (kgf), E is the Young's modulus (GPa), H is the hardness (GPa) and C is the crack length as shown in figure B-12. The load P was based on the criteria $c > 2a$. They indicated that the ideal case will be to evaluate the microhardness by lower load and then carry out indentation at a higher load for fracture toughness, but this requires very accurate equipment. The variations in crack length and hardness were averaged to provide a single value of fracture toughness for the sprayed ceramics. It should be appreciated that although the indentation method of measurement is a simple and quick method to approximate the magnitude of fracture toughness of sprayed coatings the variations in the crack length can be significantly high for coatings at random locations. This is mainly due to the presence of microcracks and voids in the coating microstructure and in certain cases the cracks propagate from the edges of the indentation diagonal as well as from within the indentation. This cause inaccuracies in the measured values. Hence, the crack behaviour within the coating microstructure have so far only been dealt on the basis of the Weibull modulus. Thus it is reasonable to use approximate values of fracture toughness for a specific coating type as exact values will vary significantly. Tuker (1974) have shown that the fracture toughness of WC-Co coatings varies with the cobalt content in the coating and the coating method. The magnitude of fracture toughness can be 5-10% of the fracture toughness of the bulk material, eg. a value of 380 MPa is seen for WC-12%Co coating produced by APS.

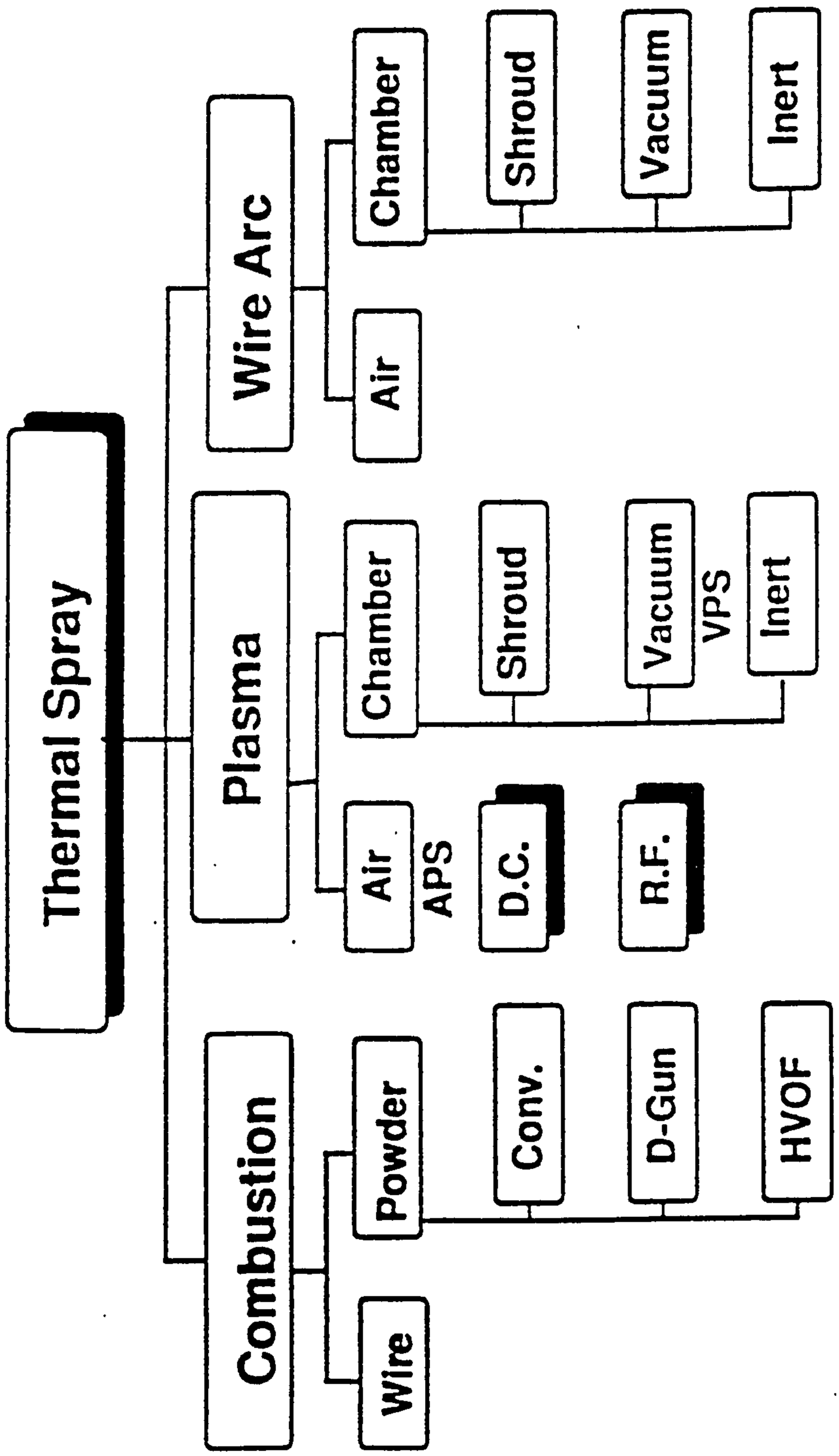

Figure B-1, Thermal spraying methods.
[Ref: Basics of thermal spraying, 1990]

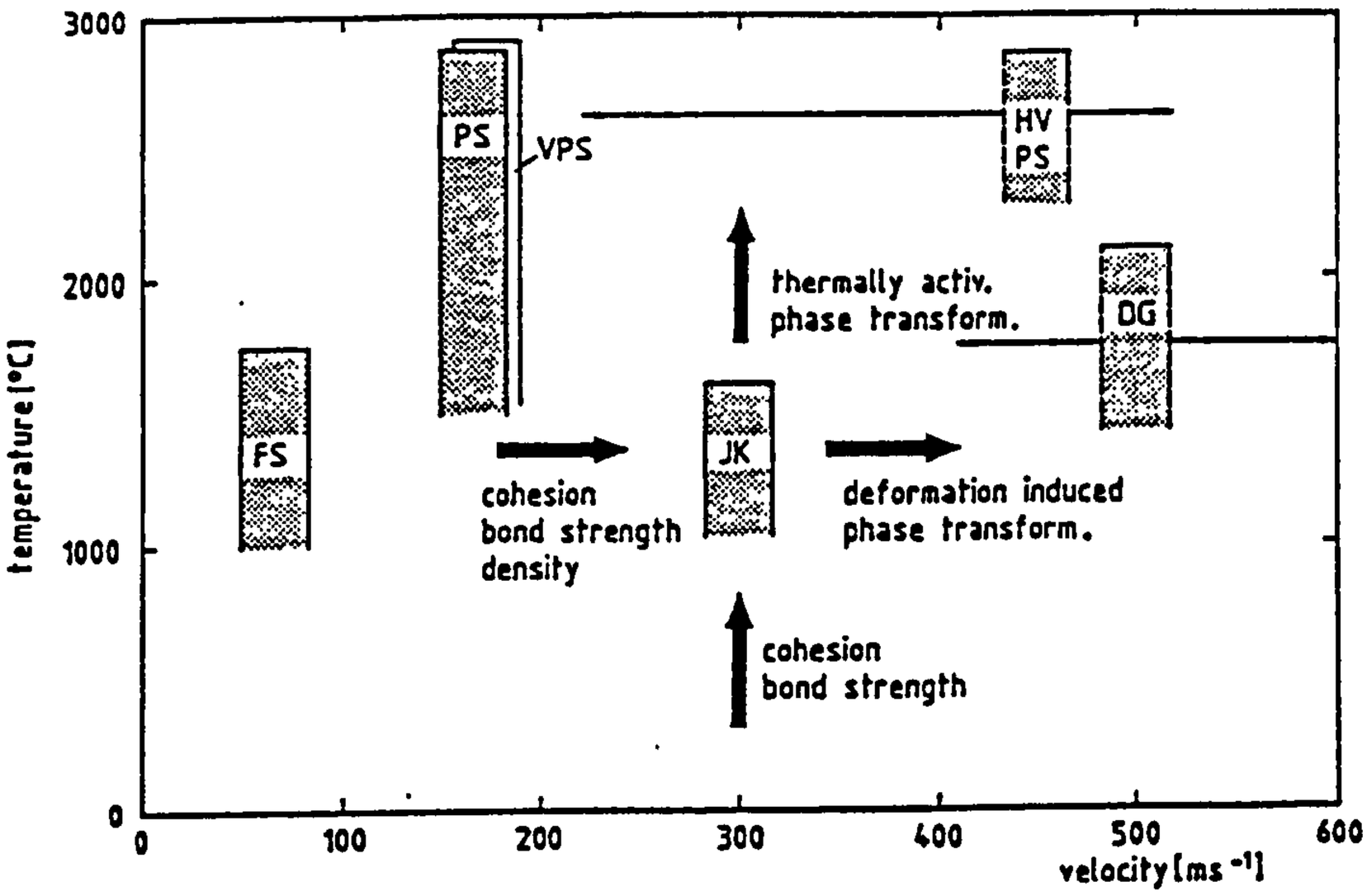

Figure B-2, Temperature and impact velocity of WC-Co particles in various spraying processes.
(FS, flame spray; PS, plasma spray; JK, jet kote; HV, high velocity; DG, detonation gun)
[Ref: Kudinov et. al. 1989]

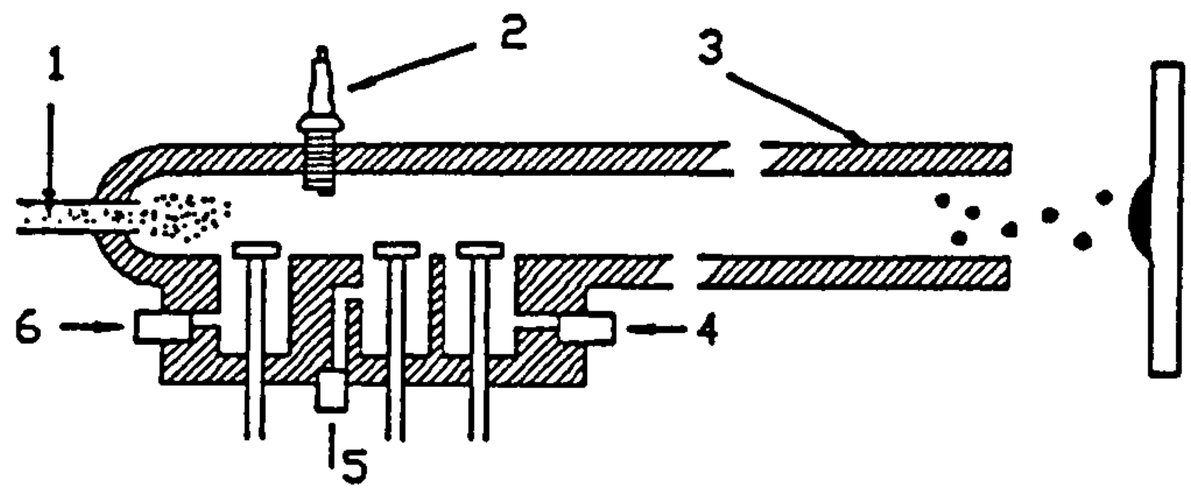

Figure B-3, Schematic of D-Gun™.
(1;powder injection 2;spark plug 3;gun barrel 4;oxygen input 5;nitrogen input)
[Ref: Powlowski, 1995]

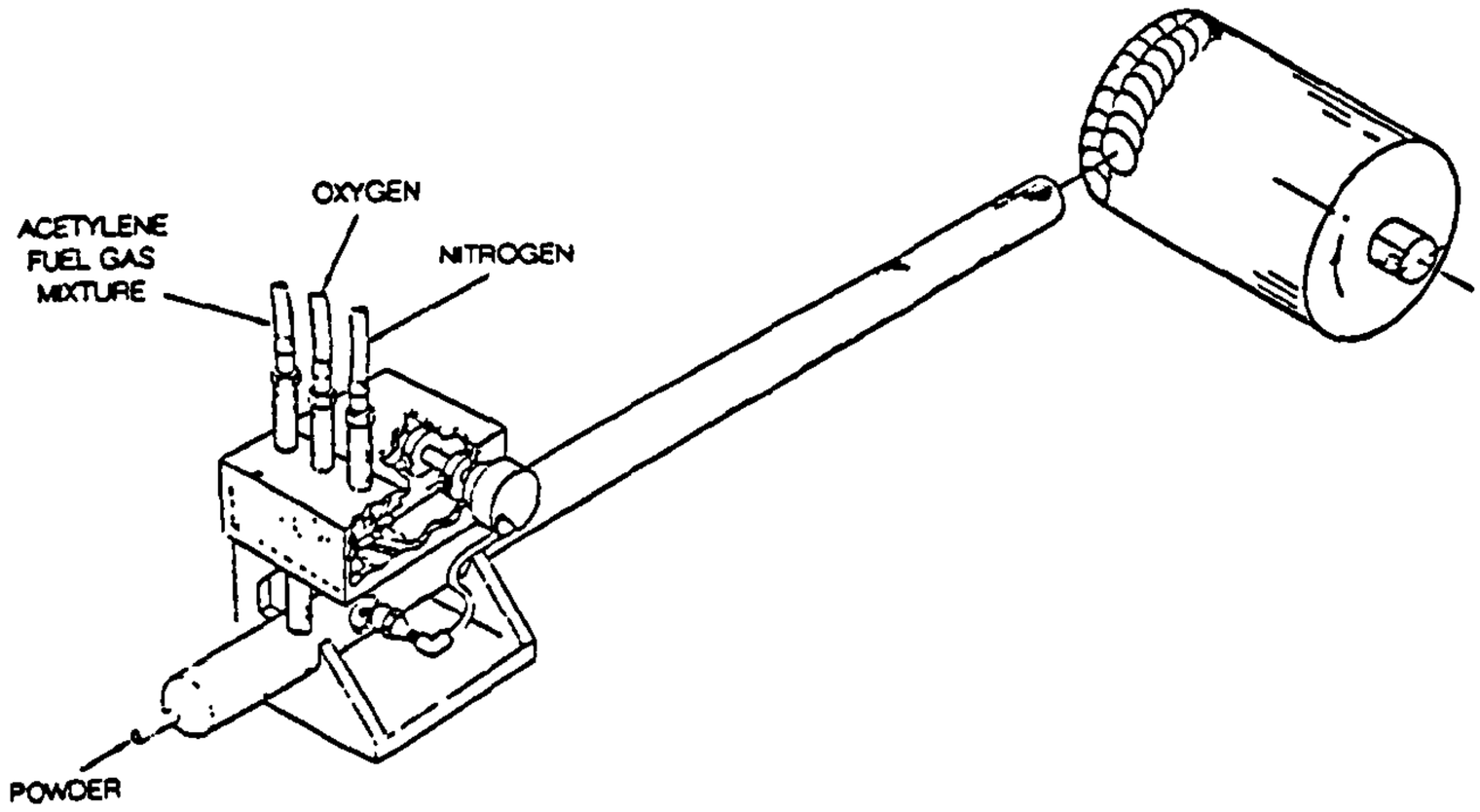

Figure B-4, Schematic of super D-Gun™.
[Ref: Powlaski 1994]

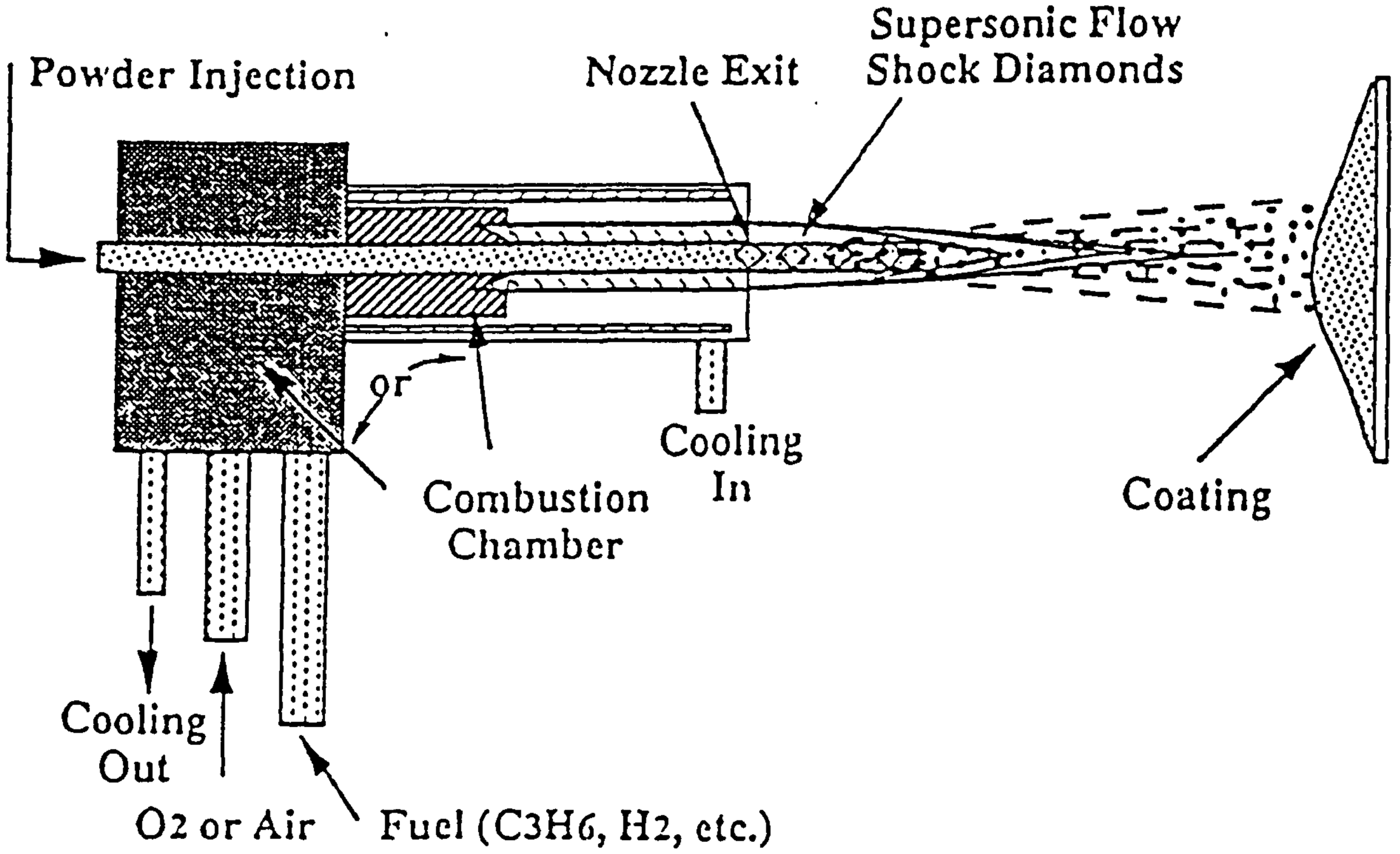

Figure B-5, Schematic of a typical HVOF Gun.
[Ref: Irving 1993]

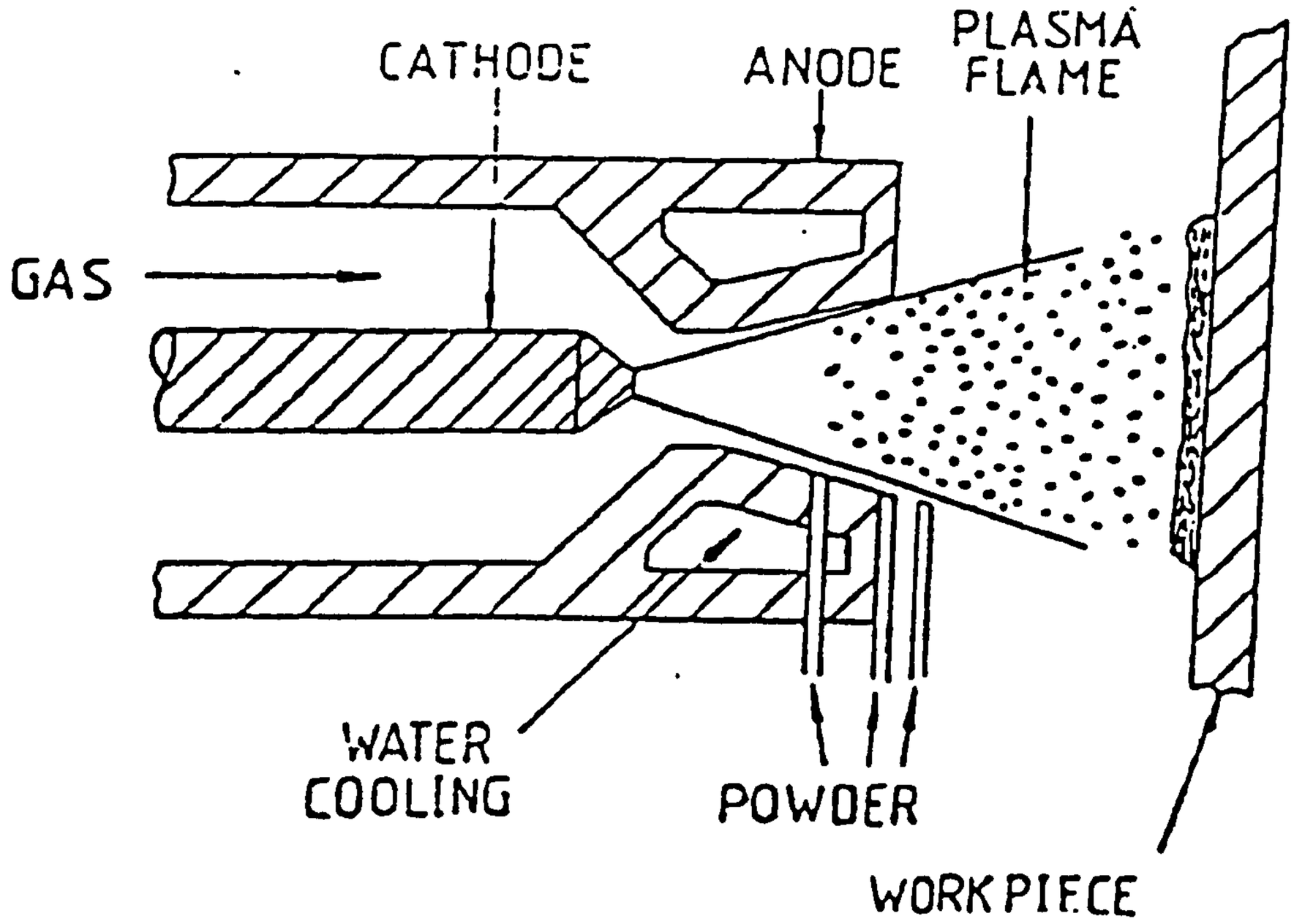

Figure B-6, Schematic of plasma torch.
[Ref: Gill 1986]

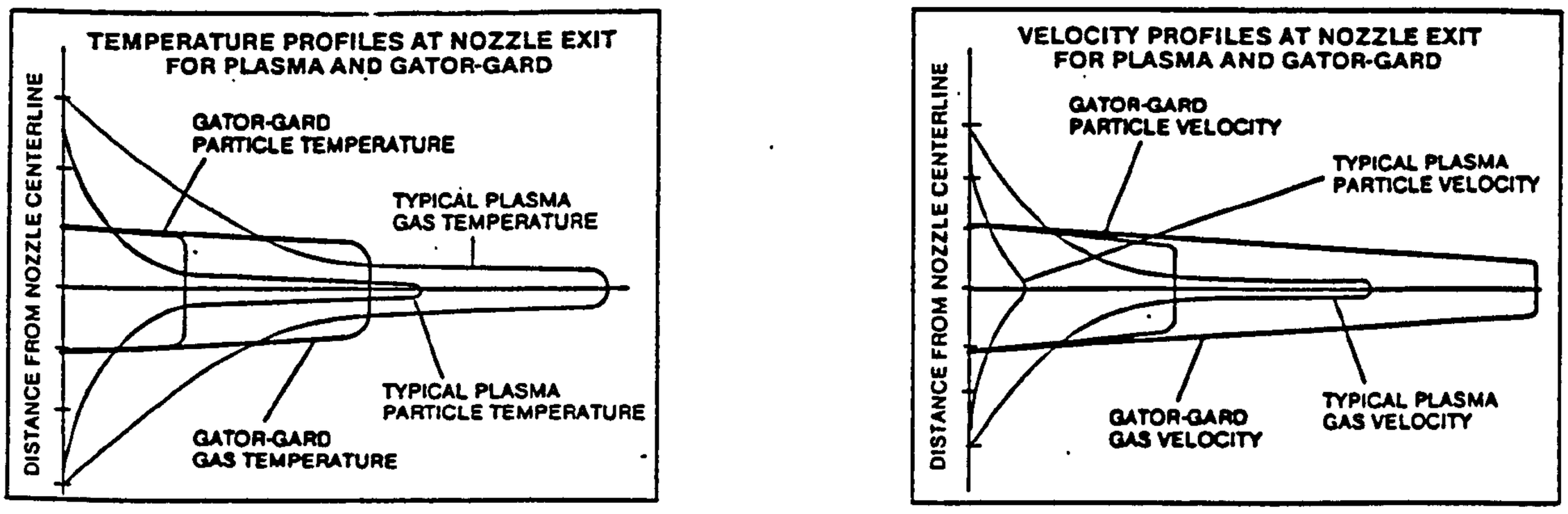

Figure B-7, Comparison of Gator Gard and conventional plasma spraying systems.
[Ref: Gator Gard technical data sheet]

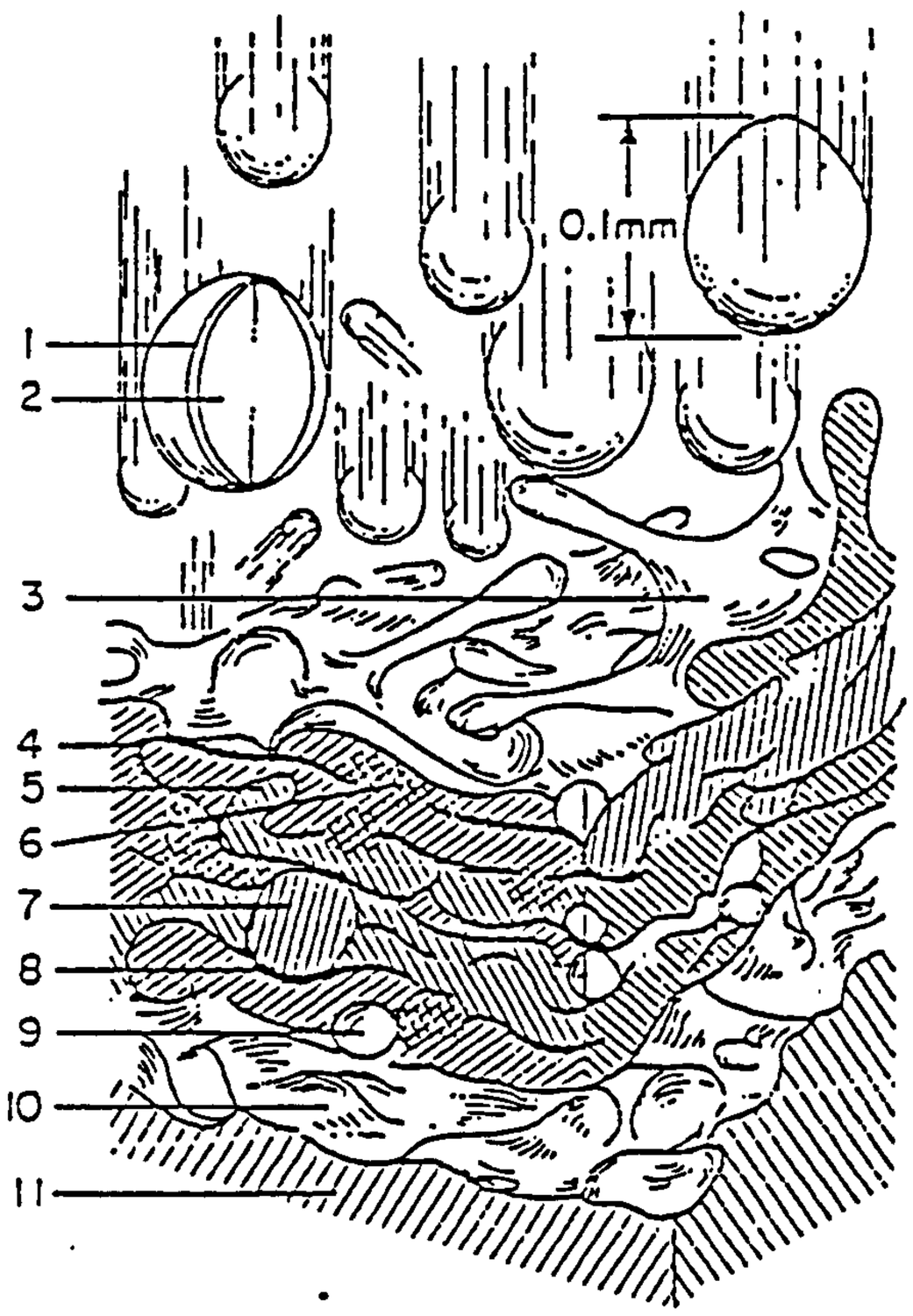

Figure B-8, Typical coating microstructure.
(1;partially sectioned oxide layer formed on a metal droplet in flight 2;metal particles- centre still in liquid state 3;impinging metal droplet-partially splashing away 4;burst open oxide sheet situated between two metal layers 5;interconnection-keying of two splashed out particles 6;partial alloying of two simultaneously impinging particles 7;encapsulated pre-solidified spherical particle 8;microcavity due to uneven flow of splatted particles 9;micropore caused by entrapped gases 10;bond layer-grit blasted surface 11;substrate material)
[Ref: Wilms et. al. 1978]

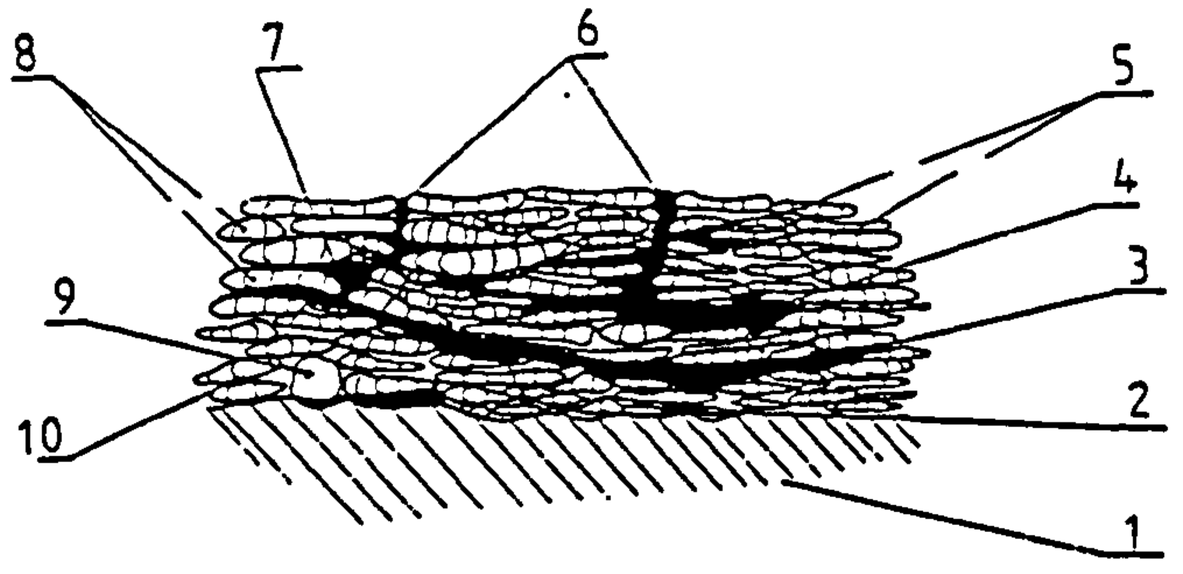

Figure B-9, Coating defects

(1;substrate 2;poor contact to the substrate 3;crack resulting from the relaxation of one torch pass stresses 4;crack due to relaxation of residual stress in the vertical direction 5;columns of solidification in the lamellae 6;open porosity 7;void due to partially melted particle 8;lamella of well melted particle 9;unmelted particle 10;void due to poor interlamella contact)
[Ref: Powlaski 1994]

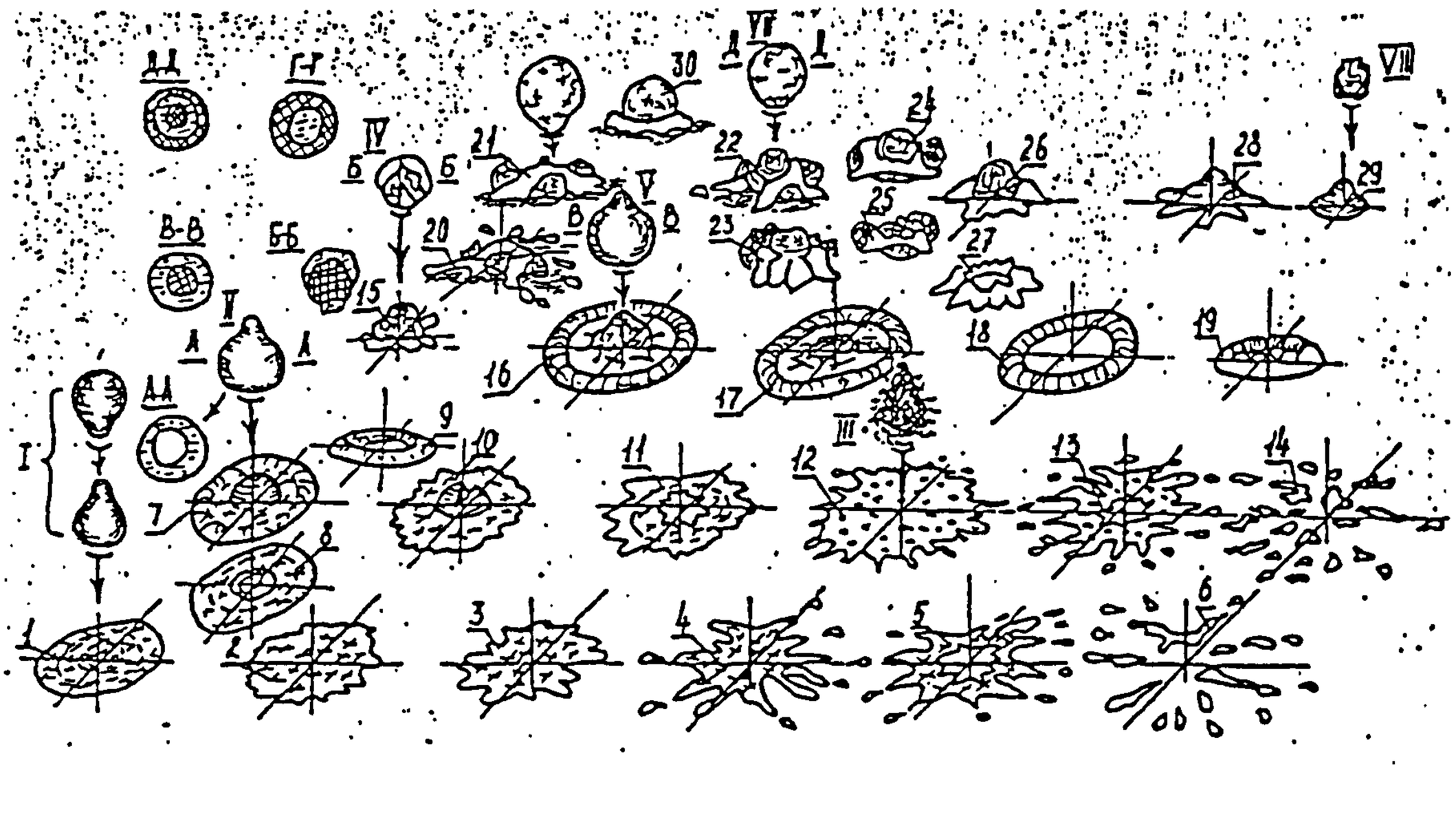

Figure B-10, Schematic of interaction of disperse phase particle with substrate.

(I;completely melted-1,2,3,4,5,6, II;completely melted with gas filled cavity, section A-A:7,8,9,10,11, III;overheated evaporating-12,13,14, IV;fused at surface projections-15, V;with molten shell and solid nucleus, section B-B:16,17,18,19, VI;with rehardened shell and molten nucleus-20,21,30 VII;with rehardened shell, melted interlayer & solid nucleus, section D-D:22,23,24,25,26,27,30, VIII;solid highly accelerated particles-28,29)
[Ref: Kudinov 1989]

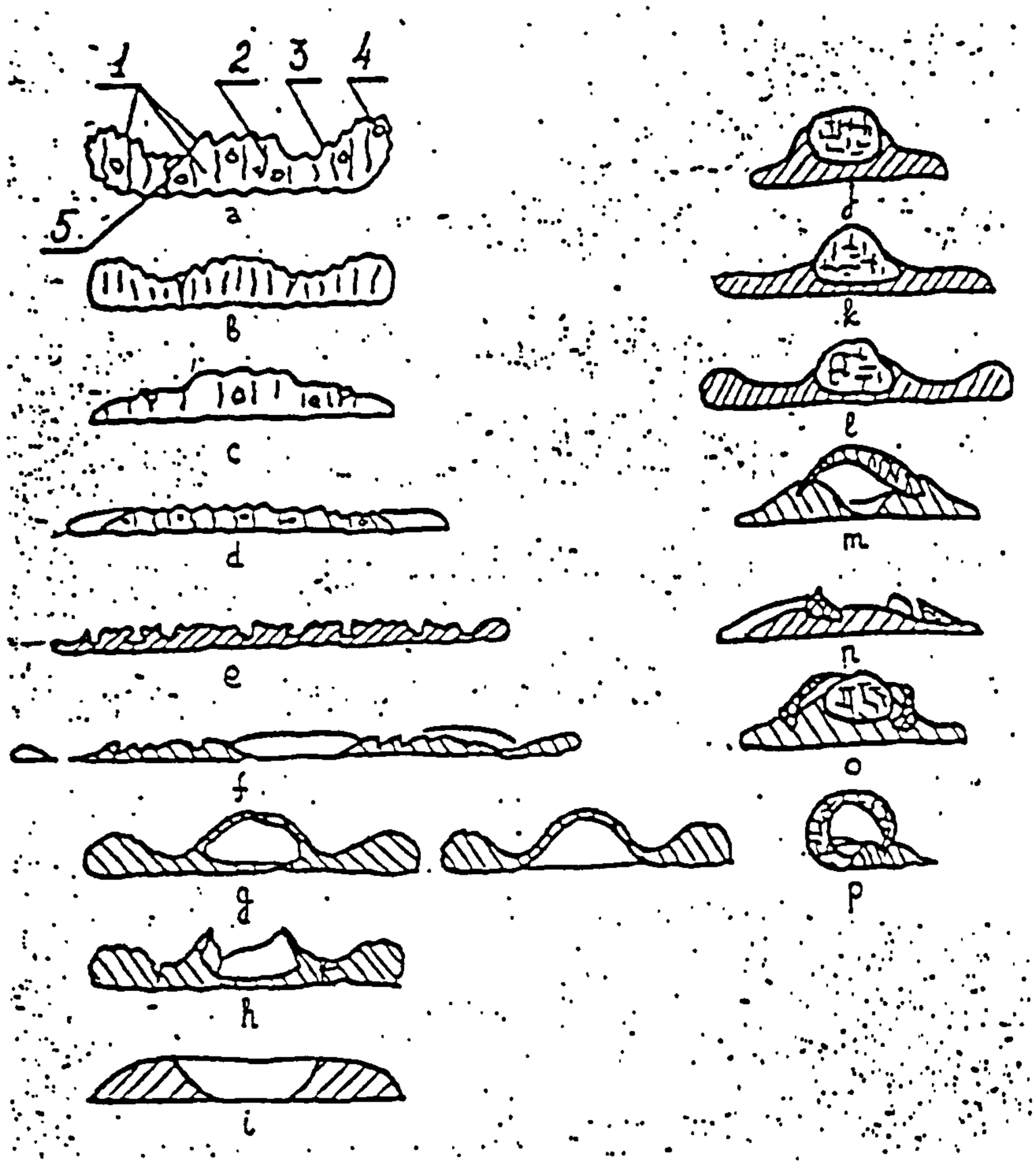

Figure B-11, Structures of particles of different type as shown in B-10.

(a,b,c,d-disk 1,2,3 in figure B-10; e,f-stellate particles 3,4,5,6,12,13,14 in figure B-10; g,h-sombrero 7,8,10 in figure B-10; i-rings 9,19 in figure B-10; j,k,l,msombrero with solid nucleus 15,16 in figure B-10; n,o-lump like particles 22,23,24,25,20,21 in figure B-10; p-balloons spheres 30 in figure B-10)
[Ref: Kudinov 1989]

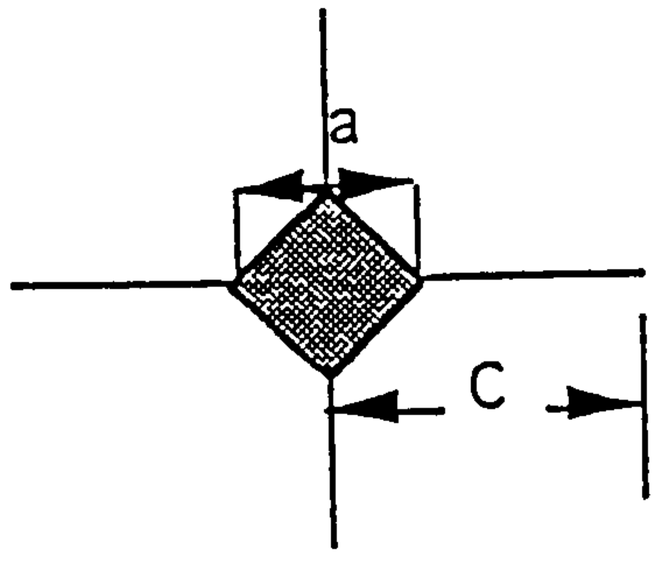

Figure B-12, Schematic of vickers indentation setup.
(c;crack length, a;hardness impression diagonal)
[Ref: Beshish 1993]

Appendix C

FINITE ELEMENT ANALYSIS (DATA FILE)

Inorder to evaluate the contact stresses in the post processor of the FE code, a DATA file was essential to indicate the shape, material and loading etc. of the model and to define the type of analysis required. This was performed by a number of different modules which comprise the DATA file as shown below. The actual entries used in these modules been omitted for simplicity, only the name and purpose of each module is defined. The details of these modules can be appreciated from the PAFEC Data Preparation User Manual:

CONTROL MODULE

This module defined the problem as an axisymmetric stress analysis.

NODES MODULE

This module was used to define the nodes and assigned the node numbers, axis number and the cartesian coordinates to these nodes.

ELEMENTS MODULE

This module defined the elements and used to assign the element number, element type and the topology of nodes in the elements. Every element had a property entry which is related to the properties defined in the material module.

LOADS MODULE

This module was used to define the structural loading and defined the node for the applied point load, along with the magnitude and direction of the applied load.

GAPS MODULE

This module assigned the gap nodes during the iterations for equilibrium of

the structure. This module defined the frictionless gap nodes (N1, N2), the direction of the gaps to be opened and the offset between the gap nodes.

RESTRAINTS MODULE

This module was used to restrain the degree of freedom of the constrained nodes. The node number, axis number, plane and direction of the nodes to be restrained were defined in this module.

STRAIN ENERGY DENSITY

This module was used to define that the strain energy density of the elements should also be calculated.

PLATES AND SHELL MODULE

This module was used to define the relation between the element property (Elements module) and the related material (Materials module).

MATERIAL MODULE

This module defined the physical properties of the material for the required stress analysis. Only Young's modulus poisson's ratio are defined for the stress analysis. The module entries were overwritten to define the coating material properties.

Appendix D
CONTACT ANALYSIS

D1.1 Introduction

The study of mechanics of the contacting bodies have been an area of research ever since Heinrich Hertz presented his theory in 1881 (published in 1882). Hertz on the basis of his experiments by considering the pattern of interference fringes concluded that the distribution of contact pressure would produce elastic displacements in the contacting bodies which were compatible with the proposed elliptical area of contact (Johnson. K. L, 1985). Although Hertz theory was based on the frictionless and perfectly elastic contacts, several later advancements in the understanding of the subject of contact mechanisms have enabled the analysis of the effect of friction and inelastic behaviour on the stress distribution and deformation of contacting bodies (Johnson. K. L. 1985). Similarly, numerical approaches like finite element modelling have also been successfully applied to evaluate the deformation and stress distribution within the contacting bodies.

D1.2 Contact Force

The contact load between the upper drive rolling element and the driven planetary ball can be evaluated by trigonometrically resolving the applied load transferred from the lever arm to the cup assembly. If 'M' was the mass in kg which was applied at the end of the lever arm having an arm ratio of 'R' and θ was the angle of contact between the drive and driven rolling element in the cup assembly of Type II configuration then the contact force can be simplified as:

$$\text{Contact force} = (M \times R \times 9.81 / 3\ \text{Cos}\theta) \quad \ldots\ldots\ldots\ldots\ldots \text{(D1)}$$

In the current studies 'R' was set 20:1 and the angle θ was 35.3° for the upper drive rolling element ball and cone with an apex angle of 109.4°. Whereas, the angle θ was calculated as 45° for the upper drive rolling element cone having an

apex angle of 90°. Inserting the values for the case of upper drive ball at a lever arm load of 2 kg, the contact force can be calculated as 160.2 N.

D1.3 Contact Stresses

Contact stresses define an important tribological parameter during the RCF Tests. In the present study a simplified version of the contact mechanics approach to evaluate the contact stresses by assuming a frictionless and perfectly elastic contact have been used. Similarly, the effects of the lubricant film and surface roughness effects have been neglected. The analysis is only applied to the non-conforming contact between the drive rolling element and the driven planetary balls since there, the stresses will be extremely high in comparison to those occurring elsewhere in the cup assembly of the four ball system. The stresses are evaluated on the basis of the uncoated case of the drive rolling element. A number of simplified versions of the theory are available in the published literature, the analysis in this work was based on the equations given by Timoshenko et. al,(1982) and Engineering Science Data Unit (ESDU 84017, 1984). A general case is considered which gives the contact pressure as follows:

$$Po = (3 \times \text{contact force} / 2\pi \times a \times b) \quad \ldots\ldots\ldots\ldots\ldots\ldots \quad (D2)$$

where 'a' and 'b' are the magnitude of the contact ellipse which are calculated on the basis of contact geometry and elastic constants. The values of Young's modulus, Poisson's ratio for steel and ceramic planetary balls are used as 207 GPa, 0.3 and 310 GPa, 0.27 respectively. Inserting the values of elastic constants, dimensions of the contact geometry and applied load the stress can be calculated as summarized in tables D1, D2, D3, D4, D5 and D6 respectively.

Lever Arm Load (Kg)	Contact Force (N)	Contact Radius (mm)	Peak Compressive Stress (GPa)	Maximum Shear Stress (GPa)	Depth of Max: Shear (mm)	Orthogonal Shear Stress (GPa)	Depth of Orthogonal Shear (mm)	Maximum Tensile Stress (GPa)
		(a)	Po	0.35 Po	0.5 a	0.42 Po	0.35 a	0.14 Po
0.5	40.0665	0.08886	2.42280961	0.847983363	0.04442931	1.01758004	0.03110052	0.33919335
1	80.133	0.11193	3.05395973	1.068885905	0.05596449	1.28266309	0.03917514	0.42755436
1.5	120.1995	0.12811	3.49685631	1.223899707	0.06405469	1.46867965	0.04483828	0.48955988
2	160.266	0.14099	3.8495266	1.347334309	0.07049455	1.61680117	0.04934618	0.53893372
2.5	200.3325	0.15186	4.14739375	1.451587813	0.0759323	1.74190538	0.05315261	0.58063513
3	240.399	0.16137	4.40779923	1.542729732	0.08068521	1.85127568	0.05647965	0.61709189
3.5	280.4655	0.16987	4.64068439	1.624239535	0.0849351	1.94908744	0.05945457	0.64969581
4	320.532	0.17759	4.85234133	1.698319466	0.08879705	2.03798336	0.06215793	0.67932779
4.5	360.5985	0.1847	5.04703464	1.766462125	0.09234903	2.11975455	0.06464432	0.70658485
5	400.665	0.19129	5.22780389	1.829731361	0.09564661	2.19567763	0.06695262	0.73189254
5.5	440.7315	0.19746	5.39690091	1.888915319	0.09873095	2.26669838	0.06911167	0.75556613
6	480.798	0.20327	5.55604588	1.94461606	0.10163351	2.33353927	0.07114346	0.77784642
6.5	520.8645	0.20876	5.70658601	1.997305103	0.1043789	2.39676612	0.07306523	0.79892204
7	560.931	0.21397	5.84959841	2.047359442	0.1069868	2.45683133	0.07489076	0.81894378
7.5	600.9975	0.21895	5.98595942	2.095085795	0.10947323	2.51410295	0.07663126	0.83803432
8	641.064	0.2237	6.11639271	2.140737447	0.11185142	2.56888494	0.078296	0.85629498
8.5	681.1305	0.22826	6.24150363	2.18452627	0.11413243	2.62143152	0.0798927	0.87381051
9	721.197	0.23265	6.36180428	2.226631499	0.1163256	2.6719578	0.08142792	0.8906526
9.5	761.2635	0.23688	6.47773221	2.267206273	0.11843894	2.72064753	0.08290726	0.90688251
10	801.33	0.24096	6.58966453	2.306382586	0.12047933	2.7676591	0.08433553	0.92255303

Table D1, Contact stresses for the upper drive steel ball and planetary ceramic ball

Lever Arm Load (Kg)	Contact Force (N)	Contact Radius (mm)	Peak Compressive Stress (GPa)	Maximum Shear Stress (GPa)	Depth of Max: Shear (mm)	Orthogonal Shear Stress (GPa)	Depth of Orthogonal Shear (mm)	Maximum Tensile Stress (GPa)
		(a)	Po	0.35 Po	0.5 a	0.42 Po	0.35 a	0.14 Po
0.5	40.0665	0.09419	2.15613546	0.75464741	0.04709678	0.90557689	0.03296774	0.30185896
1	80.133	0.11865	2.71781605	.951235619	0.05932451	1.14148274	0.04152716	0.38049425
1.5	120.1995	0.1358	3.11196383	1.08918734	0.06790044	1.30702481	0.04753031	0.43567494
2	160.266	0.14945	3.42581635	1.199035724	0.07472693	1.43884287	0.05230885	0.47961429
2.5	200.3325	0.16098	3.69089782	1.291814238	0.08049116	1.55017709	0.05634381	0.5167257
3	240.399	0.17106	3.92264096	1.372924336	0.08552942	1.6475092	0.0598706	0.54916973
3.5	280.4655	0.18007	4.12989287	1.445462506	0.09003447	1.73455501	0.06302413	0.578185
4	320.532	0.18826	4.31825313	1.511388597	0.09412829	1.81366632	0.0658898	0.60455544
4.5	360.5985	0.19579	4.49151691	1.57203092	0.09789352	1.8864371	0.06852546	0.62881237
5	400.665	0.20278	4.65238923	1.628336229	0.10138908	1.95400347	0.07097236	0.65133449
5.5	440.7315	0.20932	4.80287405	1.681005918	0.10465861	2.0172071	0.07326102	0.67240237
6	480.798	0.21547	4.94450223	1.730575782	0.10773543	2.07669094	0.0754148	0.69223031
6.5	520.8645	0.22129	5.07847269	1.77746544	0.11064564	2.13295853	0.07745195	0.71098618
7	560.931	0.22682	5.20574398	1.822010391	0.11341012	2.18641247	0.07938709	0.72880416
7.5	600.9975	0.23209	5.32709598	1.864483593	0.11604584	2.23738031	0.08123209	0.74579344
8	641.064	0.23713	5.44317272	1.905110452	0.11856681	2.28613254	0.08299677	0.76204418
8.5	681.1305	0.24197	5.55451292	1.944079521	0.12098476	2.33289542	0.08468933	0.77763181
9	721.197	0,24662	5.6615723	1.981550306	0.12330961	2.37786037	0.08631673	0.79262012
9.5	761.2635	0.2511	5.76474026	2.01765909	0.12554983	2.42119091	0.08788488	0.80706364
10	801.33	0.25543	5.8643524	2.052523339	0.12771273	2.46302801	0.08939891	0.82100934

Table D2, Contact stresses for the upper drive steel ball and planetary steel ball

Lever Arm Load (kg)	Contact Force (N)	Contact Radius (mm)	Contact Radius (mm)	Peak Compressive Stress (GPa)	Maximum Shear Stress (GPa)	Depth of Max: Shear (mm)	Orthogonal Shear Stress (GPa)	Depth of Orthogonal Shear (mm)	Maximum Tensile Stress (GPa)
		(a)	(b)	Po	0.35 Po	0.65 b	0.47 Po	0.4 b	0.14 Po
0.5	40.065	0.12561	0.0784543	1.94120563	0.67942197	0.050995	0.91236665	0.0313817	0.27176879
1	80.13	0.15822	0.0988234	2.44689628	0.8564137	0.064235	1.15004125	0.0395294	0.34256548
1.5	120.195	0.18109	0.1131093	2.801754262	0.98061399	0.073521	1.3168245	0.0452437	0.3922456
2	160.26	0.1993	0.124481	3.08432106	1.07951237	0.080913	1.4496309	0.0497924	0.43180495
2.5	200.325	0.21467	0.1340831	3.322978441	1.16304245	0.087154	1.56179987	0.0536332	0.46521698
3	240.39	0.22811	0.1424759	3.53162075	1.23606726	0.092609	1.65986175	0.0569904	0.4944269
3.5	280.455	0.24012	0.1499805	3.718213193	1.30137462	0.097487	1.7475602	0.0599922	0.52054985
4	320.52	0.25104	0.1568	3.887797157	1.360729	0.10192	1.82726466	0.06272	0.5442916
4.5	360.585	0.26108	0.1630721	4.043789501	1.41532633	0.105997	1.90058107	0.0652289	0.56613053
5	400.65	0.2704	0.1688951	4.188625595	1.46601896	0.109782	1.96865403	0.067558	0.58640758
5.5	440.715	0.27912	0.1743415	4.324109658	1.51343838	0.113322	2.03233154	0.0697366	0.60537535
6	480.78	0.28733	0.1794669	4.451619933	1.55806698	0.116653	2.09226137	0.0717868	0.62322679
6.5	520.845	0.29509	0.1843148	4.572235822	1.60028254	0.119805	2.14895084	0.0737259	0.64011302
7	560.91	0.30246	0.1889199	4.686820341	1.64038712	0.122798	2.20280556	0.0755679	0.65615485
7.5	600.975	0.30949	0.1933105	4.796075627	1.67862647	0.125652	2.25415554	0.0773242	0.67145059
8	641.04	0.31622	0.1975099	4.900581502	1.71520353	0.128381	2.30327331	0.079004	0.68608141
8.5	681.105	0.32267	0.2015378	5.000822984	1.75028804	0.131	2.3503868	0.0806151	0.70011522
9	721.17	0.32887	0.2054106	5.09721038	1.78402363	0.133517	2.39568888	0.0821642	0.71360945
9.5	761.235	0.33484	0.2091423	5.190094254	1.81653299	0.135943	2.4393443	0.0836569	0.7266132
10	801.3	0.34061	0.2127453	5.279776768	1.84792187	0.138284	2.48149508	0.0850981	0.73916875

Table D3, Contact stresses for the upper drive steel cone (apex angle 109.4°) and planetary ceramic ball.

Lever Arm Load (kg)	Contact Force (N)	Contact Radius (mm)	Contact Radius (mm)	Peak Compressive Stress (GPa)	Maximum Shear Stress (GPa)	Depth of Max: Shear (mm)	Orthogonal Shear Stress (GPa)	Depth of Orthogonal Shear (mm)	Maximum Tensile Stress (GPa)
		(a)	(b)	Po	0.35 Po	0.65 b	0.47 Po	0.4 b	0.14 Po
0.5	40.065	0.13312	0.0831365	1.728551759	0.60499312	0.054039	0.81241933	0.0332546	0.24199725
1	80.13	0.16768	0.1047212	2.178845355	0.76259587	0.068069	1.02405732	0.0418885	0.30503835
1.5	120.195	0.19192	0.1198596	2.494829596	0.87319036	0.077909	1.17256991	0.0479438	0.34927614
2	160.26	0.21121	0.1319099	2.74644196	0.96125469	0.085741	1.29082772	0.052764	0.38450187
2.5	200.325	0.2275	0.1420851	2.958955064	1.03563427	0.092355	1.39070888	0.056834	0.41425371
3	240.39	0.24174	0.1509788	3.144741168	1.10065941	0.098136	1.47802835	0.0603915	0.44026376
3.5	280.455	0.25448	0.1589312	3.31089291	1.15881252	0.103305	1.55611967	0.0635725	0.46352501
4	320.52	0.26605	0.1661577	3.461899405	1.21166479	0.108003	1.62709272	0.0664631	0.48466592
4.5	360.585	0.27669	0.1728042	3.600803206	1.26028112	0.112323	1.69237751	0.0691217	0.50411245
5	400.65	0.28657	0.1789746	3.729772894	1.30542051	0.116334	1.75299326	0.0715899	0.52216821
5.5	440.715	0.29581	0.1847461	3.850415042	1.34764526	0.120085	1.80969507	0.0738984	0.53905811
6	480.78	0.30451	0.1901774	3.963956908	1.38738492	0.123615	1.86305975	0.076071	0.55495397
6.5	520.845	0.31273	0.1953146	4.071359649	1.42497588	0.126954	1.91353904	0.0781258	0.56999035
7	560.91	0.32054	0.2001945	4.173391742	1.46068711	0.130126	1.96149412	0.0800778	0.58427484
7.5	600.975	0.32799	0.2048471	4.270678405	1.49473744	0.133151	2.00721885	0.0819389	0.59789498
8	641.04	0.33512	0.2092972	4.363735941	1.52730758	0.136043	2.05095589	0.0837189	0.61092303
8.5	681.105	0.34195	0.2135654	4.452996237	1.55854868	0.138818	2.09290823	0.0854262	0.62341947
9	721.17	0.34853	0.2176693	4.538824653	1.58858863	0.141485	2.13324759	0.0870677	0.63543545
9.5	761.235	0.35486	0.2216238	4.621533348	1.61753667	0.144055	2.17212067	0.0886495	0.64701467
10	801.3	0.36097	0.2254418	4.701391383	1.64548698	0.146537	2.20965395	0.0901767	0.65819479

Table D4, Contact stresses for the upper drive steel cone (apex angle 109.4°) and planetary steel ball.

Lever Arm Load (kg)	Contact Force (N)	Contact Radius (mm)	Contact Radius (mm)	Peak Compressive Stress (GPa)	Maximum Shear Stress (GPa)	Depth of Max: Shear (mm)	Orthogonal Shear Stress (GPa)	Depth of Orthogonal Shear (mm)	Maximum Tensile Stress (GPa)
		(a)	(b)	Po	0.35 Po	0.65 b	0.47 Po	0.4 b	0.14 Po
0.5	46.24	0.14123	0.0724393	2.158030821	0.75531079	0.047086	1.01427449	0.0289757	0.30212431
1	92.48	0.1779	0.0912467	2.720205169	0.95207181	0.05931	1.27849643	0.0364987	0.38082872
1.5	138.72	0.20361	0.1044373	3.11469942	1.0901448	0.067884	1.46390873	0.0417749	0.43605792
2	184.96	0.22408	0.1149371	3.428827841	1.20008974	0.074709	1.61154909	0.0459748	0.4800359
2.5	231.2	0.24137	0.123803	3.694142332	1.29294982	0.080472	1.7362469	0.0495212	0.51717993
3	277.44	0.25648	0.1315524	3.926089183	1.37413121	0.085509	1.84526192	0.0526209	0.54965249
3.5	323.68	0.26999	0.1384816	4.133523284	1.44673315	0.090013	1.94275594	0.0553926	0.57869326
4	369.92	0.28226	0.1447782	4.322049123	1.51271719	0.094106	2.03136309	0.0579113	0.60508688
4.5	416.16	0.29355	0.1505695	4.495465211	1.57341282	0.09787	2.11286865	0.0602278	0.62936513
5	462.4	0.30403	0.155946	4.656478939	1.62976763	0.101365	2.1885451	0.0623784	0.65190705
5.5	508.64	0.31384	0.1609749	4.80709605	1.68248362	0.104634	2.25933514	0.0643899	0.67299345
6	554.88	0.32307	0.1657073	4.948848731	1.73209706	0.10771	2.3259589	0.0662829	0.69283882
6.5	601.12	0.33179	0.1701835	5.08293695	1.77902793	0.110619	2.38898037	0.0680734	0.71161117
7	647.36	0.34008	0.1744355	5.210320119	1.82361204	0.113383	2.44885046	0.0697742	0.72944482
7.5	693.6	0.34799	0.1784895	5.3317788	1.86612258	0.116018	2.50593604	0.0713958	0.74644903
8	739.84	0.35555	0.182367	5.447957578	1.90678515	0.118539	2.56054006	0.0729468	0.76271406
8.5	786.08	0.3628	0.186086	5.559395647	1.94578848	0.120956	2.61291595	0.0744344	0.77831539
9	832.32	0.36977	0.1896619	5.666549145	1.9832922	0.12328	2.6632781	0.0758647	0.79331688
9.5	878.56	0.37649	0.1931075	5.76980779	2.01943273	0.12552	2.71180966	0.077243	0.80777309
10	924.8	0.38297	0.1964343	5.869507495	2.05432762	0.127682	2.75866852	0.0785737	0.82173105

Table D5, Contact stresses for the upper drive steel cone (apex angle 90°) and planetary ceramic ball.

Lever Arm Load (kg)	Contact Force (N)	Contact Radius (mm)	Contact Radius (mm)	Peak Compressive Stress (GPa)	Maximum Shear Stress (GPa)	Depth of Max: Shear (mm)	Orthogonal Shear Stress (GPa)	Depth of Orthogonal Shear (mm)	Maximum Tensile Stress (GPa)
		(a)	(b)	Po	0.35 Po	0.65 b	0.47 Po	0.4 b	0.14 Po
0.5	46.24	0.14966	0.0767696	1.921578405	0.67255244	0.0499	0.90314185	0.0307078	0.26902098
1	92.48	0.18852	0.0967013	2.422156097	0.84775463	0.062856	1.13841337	0.0386805	0.33910185
1.5	138.72	0.21577	0.1106804	2.773426165	0.97069916	0.071942	1.3035103	0.0442722	0.38827966
2	184.96	0.23746	0.1218078	3.053135975	1.06859759	0.079175	1.43497391	0.0487231	0.42743904
2.5	231.2	0.25578	0.1312038	3.289380328	1.15128311	0.085282	1.54600875	0.0524815	0.46051325
3	277.44	0.27179	0.1394163	3.495913087	1.22356958	0.090621	1.64307915	0.0557665	0.48942783
3.5	323.68	0.2861	0.1467597	3.680618924	1.28821662	0.095394	1.72989089	0.0587039	0.51528665
4	369.92	0.29911	0.1534328	3.848488251	1.34697089	0.099731	1.80878948	0.0613731	0.53878836
4.5	416.16	0.31108	0.1595703	4.002903381	1.40101618	0.103721	1.88136459	0.0638281	0.56040647
5	462.4	0.32219	0.1652682	4.14627506	1.45119627	0.107424	1.94874928	0.0661073	0.58047851
5.5	508.64	0.33258	0.1705977	4.280389265	1.49813624	0.110888	2.01178295	0.0682391	0.5992545
6	554.88	0.34235	0.175613	4.406610303	1.54231361	0.114148	2.07110684	0.0702452	0.61692544
6.5	601.12	0.3516	0.1803568	4.526006664	1.58410233	0.117232	2.12722313	0.0721427	0.63364093
7	647.36	0.36039	0.184863	4.639432637	1.62380142	0.120161	2.18053334	0.0739452	0.64952057
7.5	693.6	0.36876	0.1891593	4.747583261	1.66165414	0.122954	2.23136413	0.0756637	0.66466166
8	739.84	0.37677	0.1932686	4.851032493	1.69786137	0.125625	2.27998527	0.0773074	0.67914455
8.5	786.08	0.38446	0.1972099	4.950260449	1.73259116	0.128186	2.32662241	0.078884	0.69303646
9	832.32	0.39184	0.2009995	5.045673288	1.76598565	0.13065	2.37146645	0.0803998	0.70639426
9.5	878.56	0.39896	0.2046512	5.137618027	1.79816631	0.133023	2.41468047	0.0818605	0.71926652
10	924.8	0.40584	0.2081768	5.226393775	1.82923782	0.135315	2.45640507	0.0832707	0.73169513

Table D6, Contact stresses for the upper drive steel cone (apex angle 90°) and planetary steel ball.

Appendix E

ELASTO-HYDRODYNAMIC LUBRICATION (EHL)

The lubricated RCF tests conducted in the modified four ball machine relied on the lubricant regime to either partially or completely separate the contacting surfaces. The non-conformal contact between the upper drive rolling element and the three driven planetary balls indicates that the elastic deformation of the contacting surfaces will significantly effect the lubrication regime. This effect of elastic deformation is understood by the Elasto-Hydrodynamic Lubrication (EHL) which has been an area of research ever since the work done by Dowson (1966) and Archard and Kirk (1960). These researches have resulted in more precise definition of this lubrication regime which takes account of the properties of the lubricant as well as the material of the contacting bodies. The numerical solutions of this complex problem are based on the dimensionless groups and many results have been published which vary slightly. Jacobson (1991) have given the following expression of the hard EHL as a result of there investigations. However, it should be appreciated that the relation between the various dimensionless groups were found experimentally and the solutions should be considered approximate for coating materials:

$$H_{min} = 3.63\ U^{0.68}\ G^{0.49}\ W^{-0.073}(1-e^{-0.68k}) \quad \ldots\ldots\ldots\ldots \text{(E1)}$$

where:

H_{min} = minimum film thickness

U = dimensionless speed parameter = $(\eta_o \mu / E^{"} R_x)$ ..... (E2)

G = dimensionless material parameter = $(\xi\ E^{"})$ .....(E3)

W = dimensionless load parameter = $(F/E^{"}R_x^2)$ .....(E4)

k = dimensionless ellipticity parameter = $(R_y/R_x)^{2/\pi}$ .....(E5)

(η_o = viscosity at atmospheric pressure, μ = mean surface velocity in the direction

of motion, E^{*} = effective elastic modulus, R_x = effective radius in x direction, R_y = effective radius in y direction, ξ = pressure viscosity coefficient, F = normal load)

For simplicity reasons the calculations in this work have been based on the assumption of the Young's modulus of coating as 524 GPa and the Poisson's ratio of the coating material as 0.22. The following parameters are used in the calculation of the dimensionless groups:

η_o = 0.02 Ns/m^2 (Exxon-2389 lubricant)

η_o = 0.19 Ns/m^2 (Hitec-174 lubricant)

μ = 1.5 m/s (rolling element drive ball and cone with apex angle 109.4°)

μ = 1.8 m/s (rolling element drive cone with apex angle 90°)

E^{*} = 322 GPa (steel planetary balls)

E^{*} = 420 GPa (ceramic planetary balls)

$R_x = 3.175 \times 10^{-3}$m (rolling element drive ball and cone with apex angle 109.4°)

$R_x = 2.46 \times 10^{-3}$m (rolling element drive cone with apex angle 90°)

$\xi = 3.0 \times 10^{-8}$ m^2/N (approximated value for Exxon-2389)

$\xi = 4.0 \times 10^{-8}$ m^2/N (approximated value for Hitec-174)

k = 1.0 (rolling element drive ball)

k > 1 (rolling element drive cone)

The λ value, which is defined as the ratio of minimum film thickness (H_{min}) to the RMS value of the surface roughness (Rq) can thus be calculated using the equation

$$\lambda = \{H_{min}/(R^2_{qd}+R^2_{qp})^{0.5}\}$$

(R^2_{qd} is the RMS surface roughness of the drive rolling element and R^2_{qp} is the RMS surface roughness of the planetary ball)

The value of R^2_{qd} can vary from 0.06~0.12μm for various coatings and the value of R^2_{qp} is generally 0.013~0.015 μm for steel and ceramic lower balls. These are two dimensional surface roughness parameters and should be considered as approximate values since the measured values can vary for different cutoff lengths and the roughness filter used in the measurement. The calculations are based on the

values of R^2_{qd} as 0.07 μm and R^2_{qp} as 0.015 μm.

Inserting the values of these variables in the above equation following values of λ can be established for various contact configurations. Figure E1 shows some of these results for the contact configurations of the upper drive ball and cone for the two lubricants.

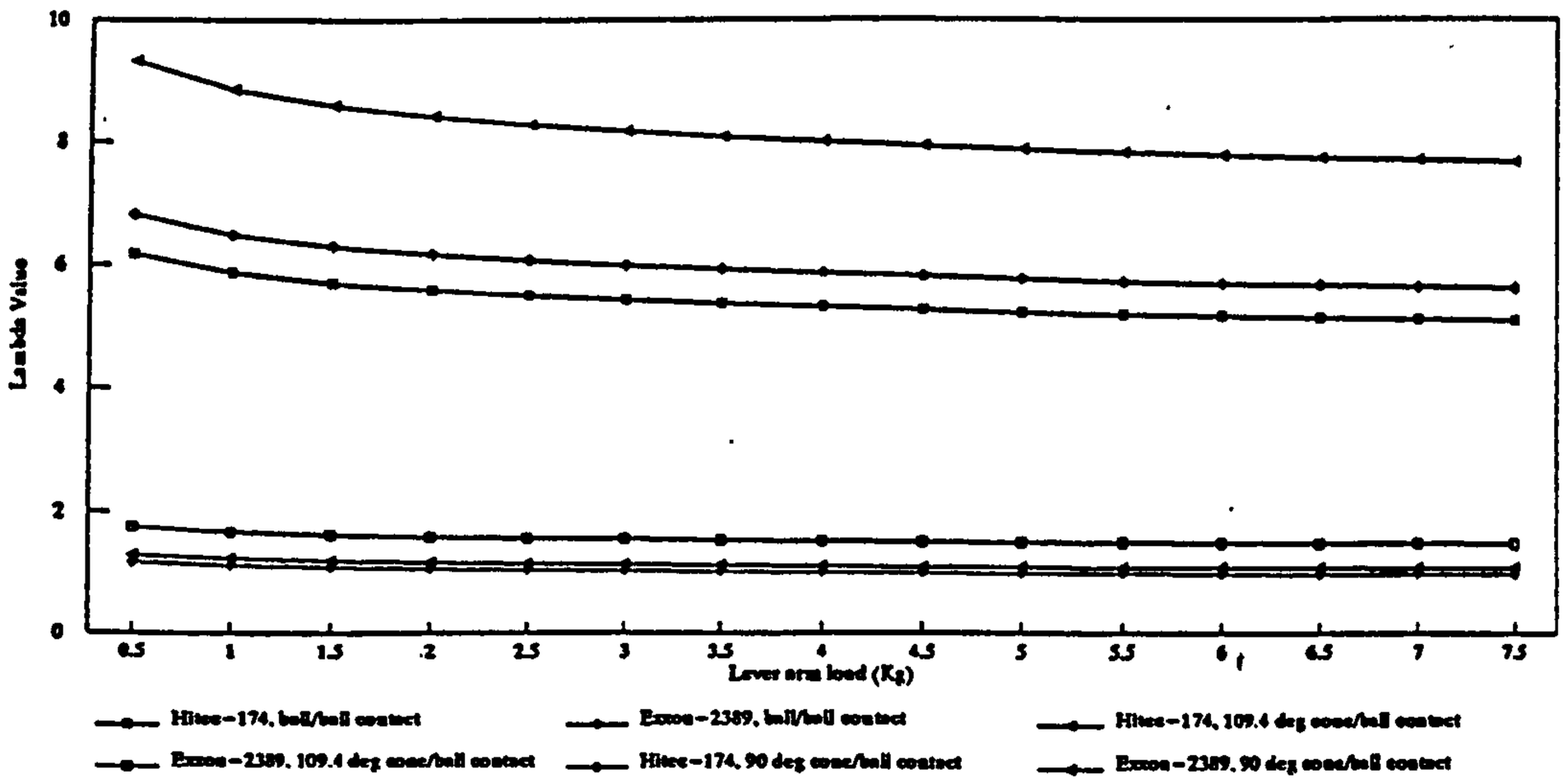

Figure E1, λ values for various contact configurations with varying load at spindle speed of 4,000 rpm.

The above figure (E1) shows the variations in λ values for the various contact configurations. The higher values of λ for the test lubricant Hitec-174 are mainly due to the higher viscosity of the lubricant. The variations in λ values for the drive ball and cone contacts are due to the changes in contact geometry which effects the contact load, surface speed and the ellipticity parameter (k).

It should be appreciated that in the above analysis approximated values of ξ are used for the test lubricants and $E^{"}$ and for the case of coated rolling elements. An analysis

was thus performed to study the effect of these approximations on the sensitivity of λ values. The result of the analysis revealed that for a 50% change in the value of ξ under the given test conditions the variation in λ value was less then 28%. Similarly for a change in the value of $E^{"}$ by 75 % under the given test conditions effects the ξ value by less then 6%. Similarly the effect of variation in the values of poisson's ratio (50%) was very mild (2%). Although the approximate values of ξ and $E^{"}$ are not thought to vary by such significant amounts as used in the above analysis the analysis revealed that the λ value was more sensitive to other parameters like η_o, μ and, R_{qd}.

Appendix F
INITIAL STUDIES

F1.1 Introduction

This appendix describes the work done prior to the work presented in this thesis to access the effect of coating material on the RCF performance of thermal spray coatings. The reader is referred to Ahmed et. al, (1997) and Hadfield et. al, (1995) for details of the work. This study addresses the Rolling Contact Fatigue (RCF) performance of WC-Co and Alumina (Al_2O_3) coatings deposited by the D-Gun (SDG 2040) process . The performance and failure mode of these coatings thus provided a feedback for the optimization of these coatings.

F1.2 Coated Cone Test Elements

Detonation gun sprayed tungsten carbide coatings are well known for their extremely high resistance against sliding wear, abrasion and fretting (Vuoristo et. al, 1993). A high impact kinetic energy of coating particles was utilised using a super D-Gun (SDG 2040) to spray two different types of coatings. Tungsten carbide (WC-15%Co) and aluminium oxide (Al_2O_3) were sprayed on M-50 bearing steel substrate. Properties such as hardness, corrosion resistance, wear resistance, and adhesive strength are the major attractions in the selection of these coating materials. The selection of substrate material as M-50 steel was based on its high tempering temperature and good combination of toughness/hardness for rolling contact fatigue applications.

The substrate shape for the rolling elements during this study was a 14.5 mm diameter cone with an apex angle of 90°. The substrate material was sand blasted prior to the coating process to assist the mechanical bonding between the coating and the substrate material. Table F1 describes some of the physical properties of the two coating materials obtained from the coating supplier data sheet. Physical properties of thermal spray coatings like modulus of elasticity, Poisson's ratio, adhesive strength etc. vary significantly not only by changing the parameters

controlled during the coating process but also with the method of measurement. Hence the listed values should only be used to provide an estimate of these physical properties, as the actual valués may vary.

The test cones were sprayed to an initial thickness of 100 μm which were ground and polished to achieve an average coating thickness of 70 μm. Owing to the porosity of the sprayed coated material the final surface finish achieved on these samples using conventional methods was 0.1 μm to 0.2 μm R_q. These surface roughness values are taken using a Talysurf series with step motor transfer table from Rank Taylor Hobson Ltd. The cutoff used was 0.8 mm with a Gaussion type roughness filter.

F1.3 Test Conditions and Experimental Test Results

A modified four ball machine described in appendix A, was used to conduct the RCF tests in conventional steel ball bearing (steel lower balls) and hybrid ceramic bearing configurations (ceramic lower balls). Two test lubricants were considered for the testing program. B.P. Hitec-174 is a high viscosity paraffin hydrocarbon lubricant which has a kinematic viscosity of 200 c.s.°C at 40°C and 40 c.s.°C at 100°C. This lubricant was not commercially available. Exxon-2389 is a synthetic lubricant which has a kinematic viscosity of 12.5 c.s.°C at 40°C and 3.2 c.s.°C at 100°C. RCF tests were conducted at a spindle speed of 1450 rpm with 185 N load applied to the cup assembly. The Elasto-Hydrodynamic Lubrication (EHL) minimum film thickness calculations for these lubricants under the given test conditions were made using the following relation by Hamrock and Dowson [12]:

$$H_{min}=3.63\ U^{0.68}G^{0.49}W^{-0.073}(1-e^{-0.68k}) \quad \text{----------(F1)}$$

where H_{min} is the minimum film thickness, U is the dimensionless speed parameter, G is the dimensionless materials parameter, W is the dimensionless load parameter, k is the dimensionless elipticity parameter. The EHL results indicated that the ratio

of the minimum film thickness to average roughness (λ) was $\lambda < 3$ and $\lambda < 1.5$ for the Hitec-174 and Exxon-2389 test lubricants respectively. Analysis was also carried out to establish the effect of material parameters on the H_{min}. This analysis revealed that there was less than 3% change in the value of H_{min} if the data for the Young's modulus and Poisson's ratio of the test cone are changed from steel to the coating material.

	Tungsten carbide (WC-15Co)	Aluminium oxide (Al_2O_3)
Hardness Hv300 (kg/mm^2)	1150	1000
Adhesive strength (kg/mm^2)	7.0	6.3
Porosity (%)	1.0 (max.)	2.0 (max.)
Young's modulus (kg/mm^2)	22500	9800
Coefficient of thermal expansion (1/C°)	8.5×10^{-6}	6.7×10^{-6}

Table F1, Physical properties of the coating material

Table F2 represents the RCF test results at a lever arm load of 2 kg and spindle speed of 1450 rpm, in terms of the contact configuration, lubricant and the time to failure. The test results are not intended for use as a basis for statistical fatigue life prediction, but as an indication of the coating performance and failure mode in various tribological conditions. The RCF tests at 7500 rpm did not last more than three minutes and are not included in table F2. The contact stresses represented in table F2 were based on the uncoated case of the rolling elements. The details of the magnitude and location of the shear and tensile stresses can be appreciated from appendix D.

Test No	Coating Material	Contact Load (N)	Average coating thickness (μm)	Lower balls	Contact stress* (GPa)	Contact width (mm) (b)	Depth of max: shear (0.65b) (μm)	Maximum shear stress (Gpa)	Lubricant	Time to Failure (minutes)
AF1	WC-15%Co	185	70	steel	3.05	0.12	80	1.07	Exxon-2389	60
AF2	WC-15%Co	185	70	steel	3.43	0.11	75	1.20	Hitec-174	69
AF3	Al_2O_3	185	70	steel	3.05	0.12	80	1.07	Exxon-2389	56
AF4	Al_2O_3	185	70	steel	3.43	0.11	75	1.20	Hitec-174	10
AF5	WC-15%Co	185	70	ceramic	3.05	0.12	80	1.07	Exxon-2389	187
AF6	WC-15%Co	185	70	ceramic	3.43	0.11	75	1.20	Hitec-174	33
AF7	Al_2O_3	185	70	ceramic	3.05	0.12	80	1.07	Exxon-2389	0.2
AF8	Al_2O_3	185	70	ceramic	3.43	0.11	75	1.20	Hitec-174	7.4

* UNCOATED CASE

Table F2, Rolling contact fatigue test results.

F1.4 Surface Observations

Figure F1 shows Scanning Electron Microscope (SEM) observations of a failed tungsten carbide coated cone (test AF1). In this case the coated cone was tested in the Exxon 2389 lubricant in contact with steel lower balls. Figure F1(a) shows the overall failed area and the failure mode of severe delamination. It is important to appreciate that there is no significant wear track on the periphery of the cone ie the specimen failed before any significant wear track was formed. It indicates that the failure of the coating was much more dependent on sub-surface effects rather than surface effects. The width of the delamination was approximately 1.5 mm wide. It is interesting to see edge cracks 1 mm to the left of the delamination area (figures F1(b) - F1(d)). Furthermore, the edge cracks are on the edge of the wear track which is near to the cone apex angle, ie the edge subjected to higher contact stress. These edge cracks may initiate fatigue failure and are thought to be caused by tensile stresses located at the contact surface edge. In the case of the aluminium oxide coatings there was no evidence of edge cracks on the surface.

Figure F2 shows the delamination failed tungsten carbide cone rotated to view the delamination cliff edges. The image in figure F2(a) shows the cliff edge towards the rolling direction where a crack at the base is evident. Here the failure depth was approximately 40 μm compared with a mean coating thickness of 75 μm. This implies that the fatigue failure occurs within the tungsten carbide coating and not de-bonding from the substrate. The Electron Probe Microscope Analysis (EPMA) of the exposed delamination failure also revealed that the de-bonding was through the coating material. This behaviour was different from the case of aluminium oxide coatings where the coating de-bonded from the substrate material. The image in figure F2(b) shows the failure initiation from the rolling direction. Here the delamination failure depth is significantly reduced.

A typical flake-like wear debris is shown in figure F3. It can be seen that the dimensions of this debris are approximately 1.2 x 0.6 mm. The top edge in figure F3(a) shows that the smooth polished surface is relatively intact. The underside of the debris (figure F3(b)) shows the surface of the delaminated surface.

Figure F4 represents the SEM micrographs typical results for ceramic coating. In these tests, the coating delaminated from the coating substrate interface. This behaviour was also confirmed by the EPMA analysis. A section of coating was also studied which revealed the same result. Figure F4(a) shows the overall failed area, whereas figure F4(b) gives some details of the failed area.

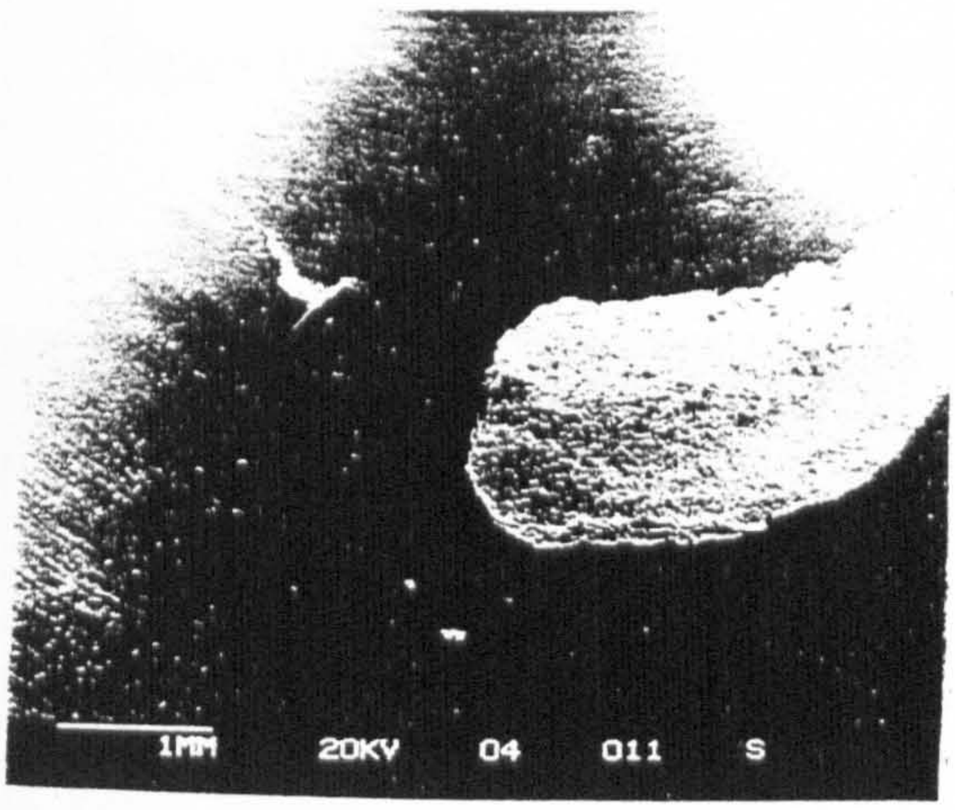

(a) overall view of failed area.

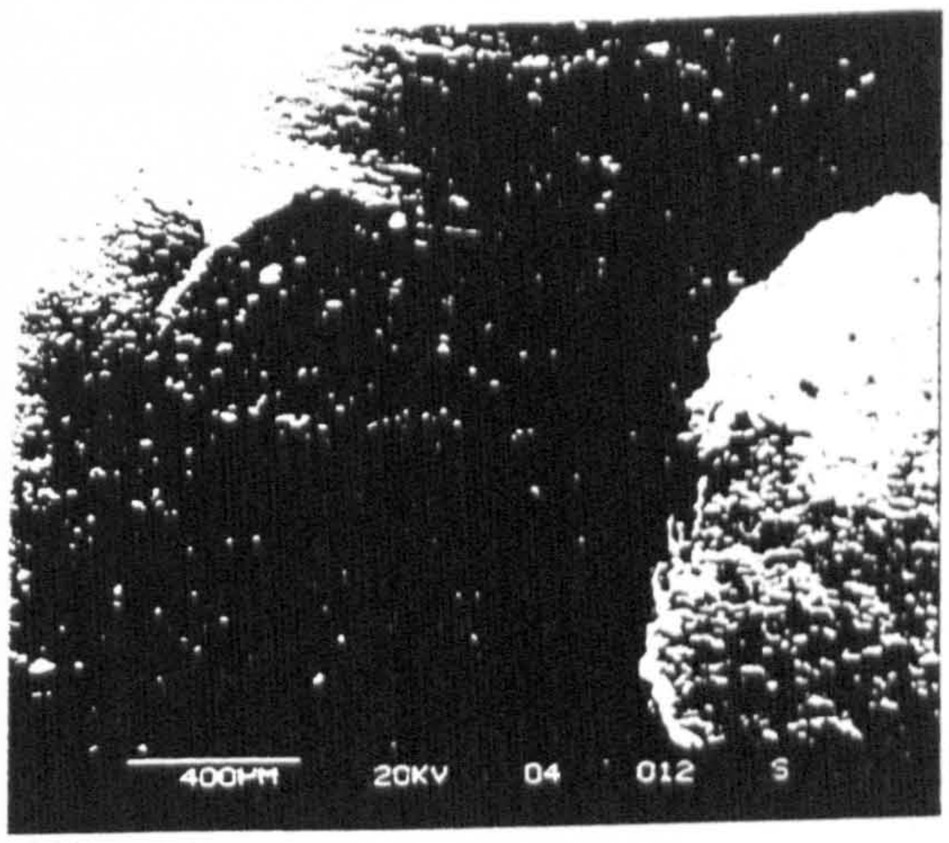

(b) edge cracks.

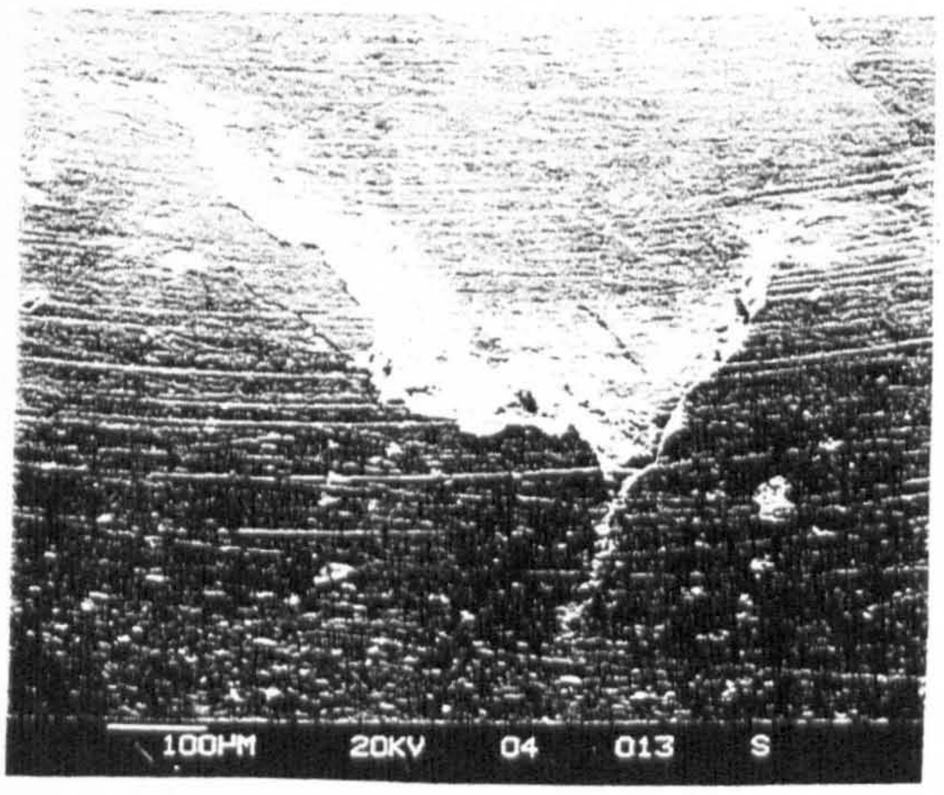

(c) edge crack detail.

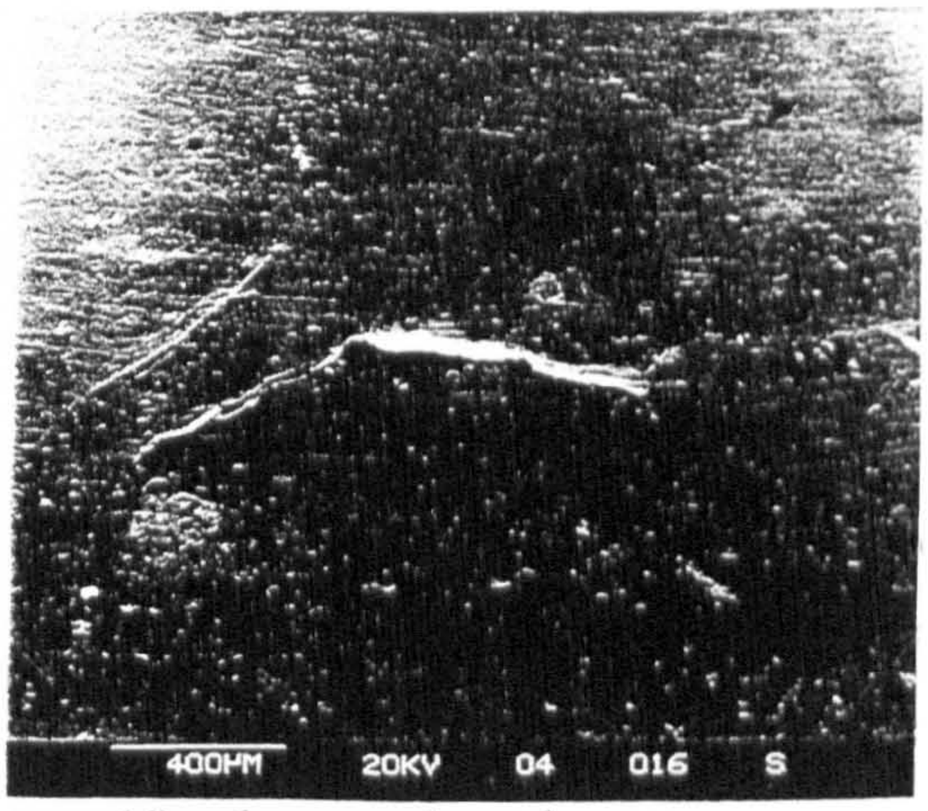

(d) edge crack end

Figure F1, Surface observations of tungsten carbide/steel contact (Exxon-2389)

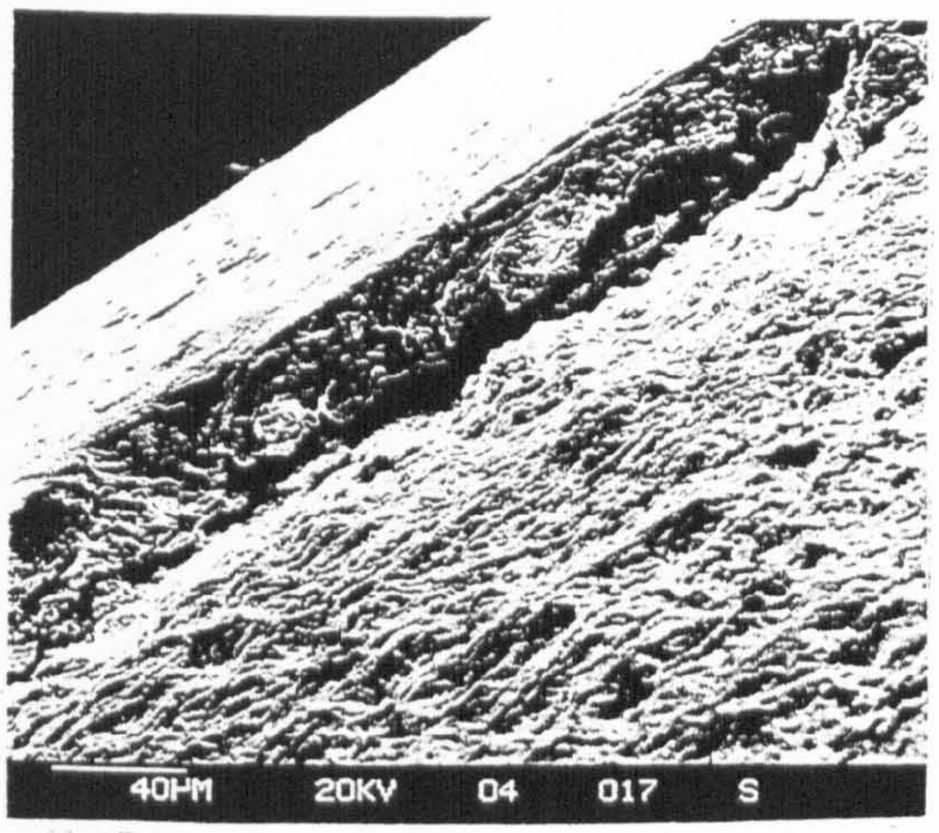

(a) cliff edge

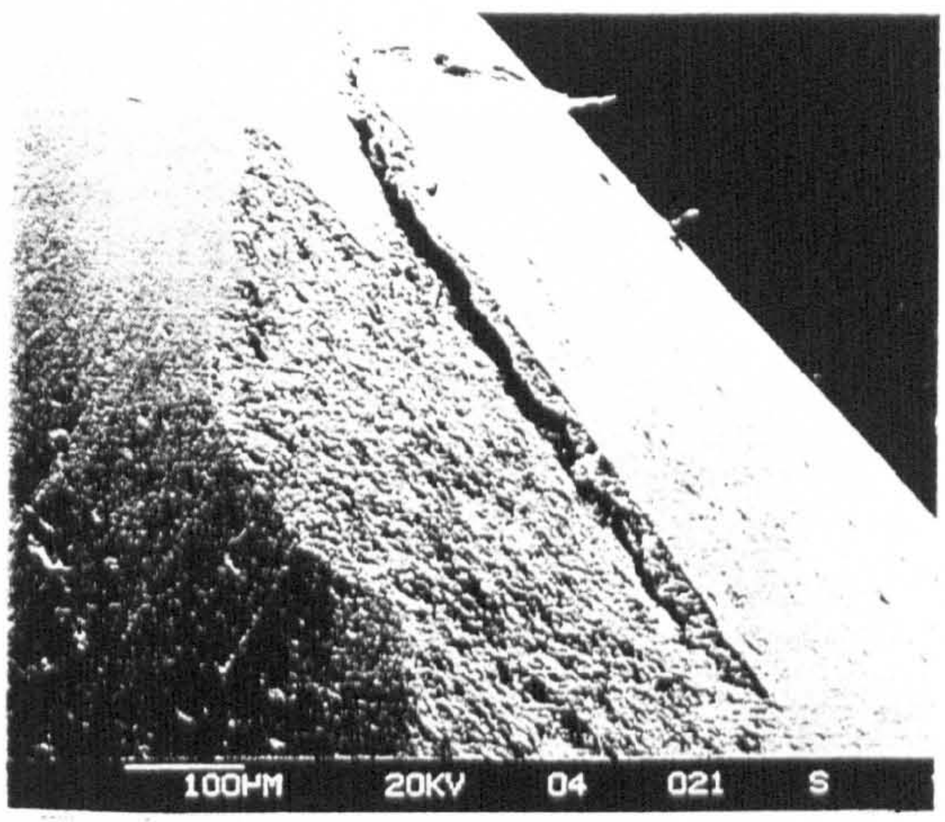

(b) cliff edge (initiation)

Figure F2, Delaminated edge of tungsten carbide/steel contact (Exxon-2389)

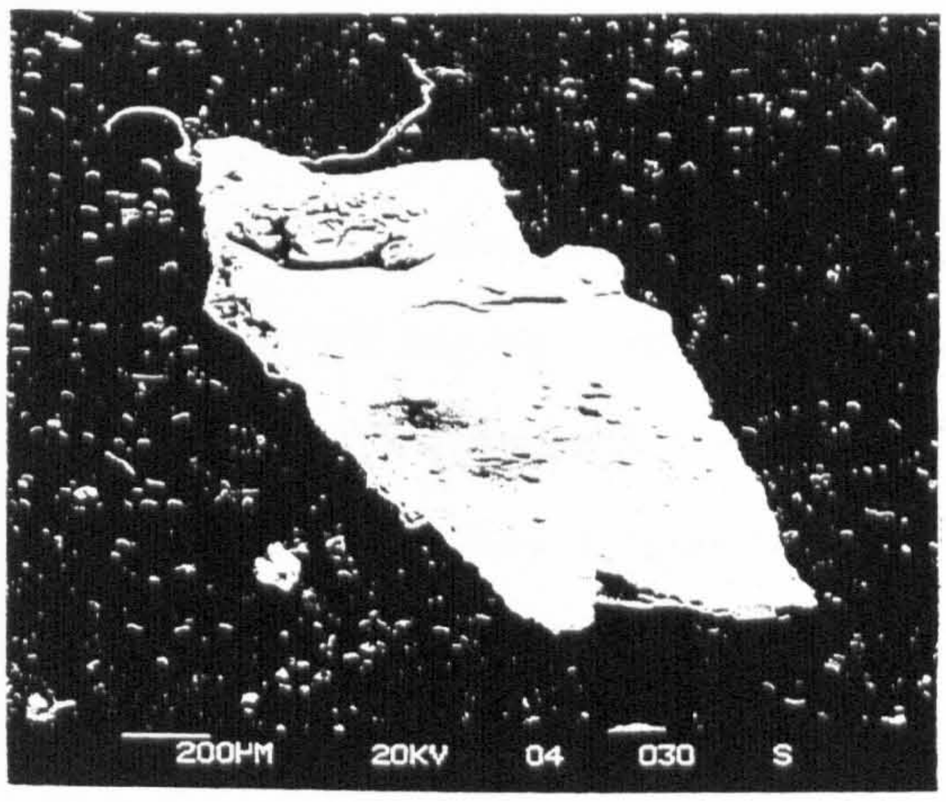

(a) debris (top surface)

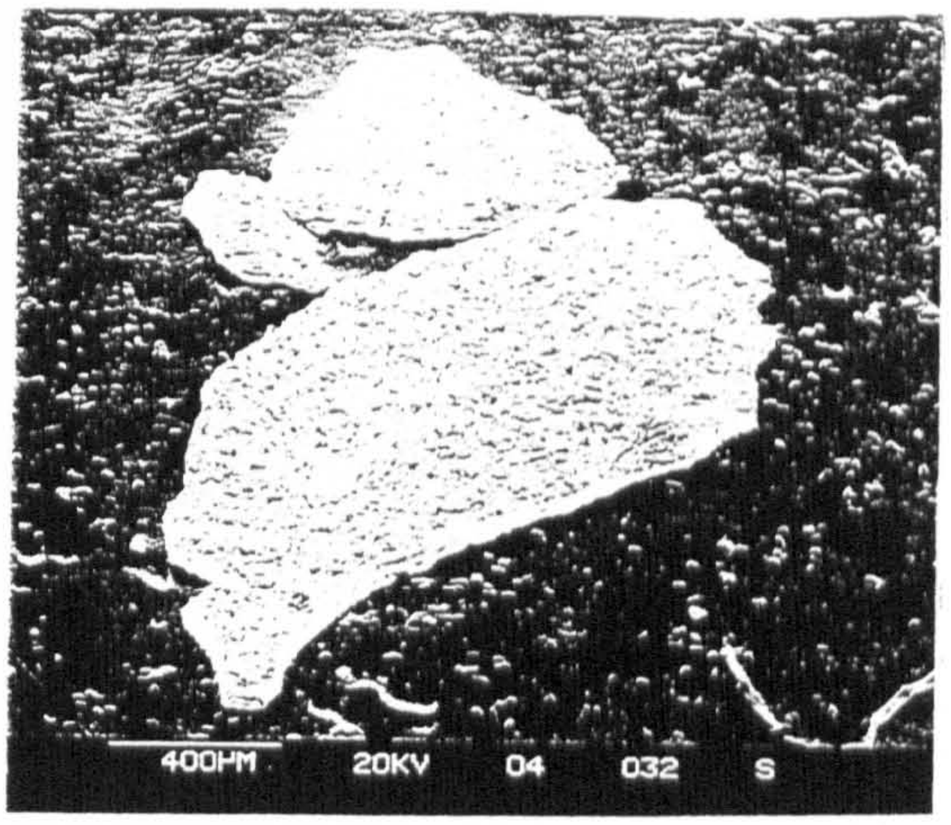

(b) delaminated surface

Figure F3, Debris from tungsten carbide/ceramic contact (HiTec-174)

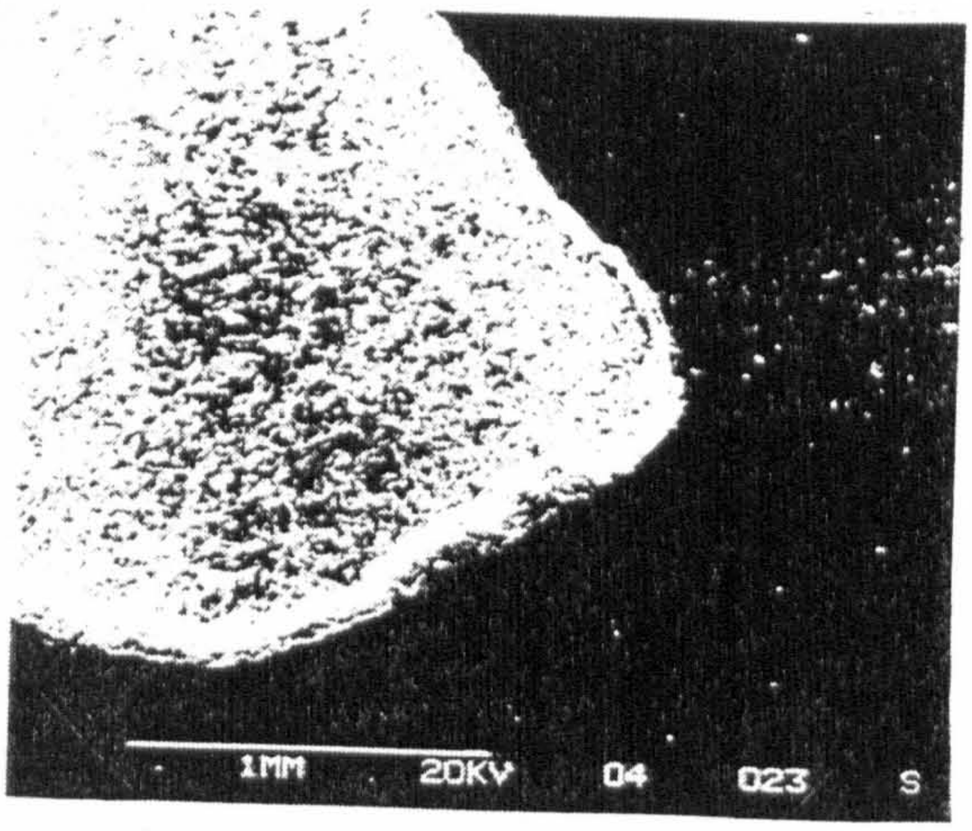

(a) overall view of failed area

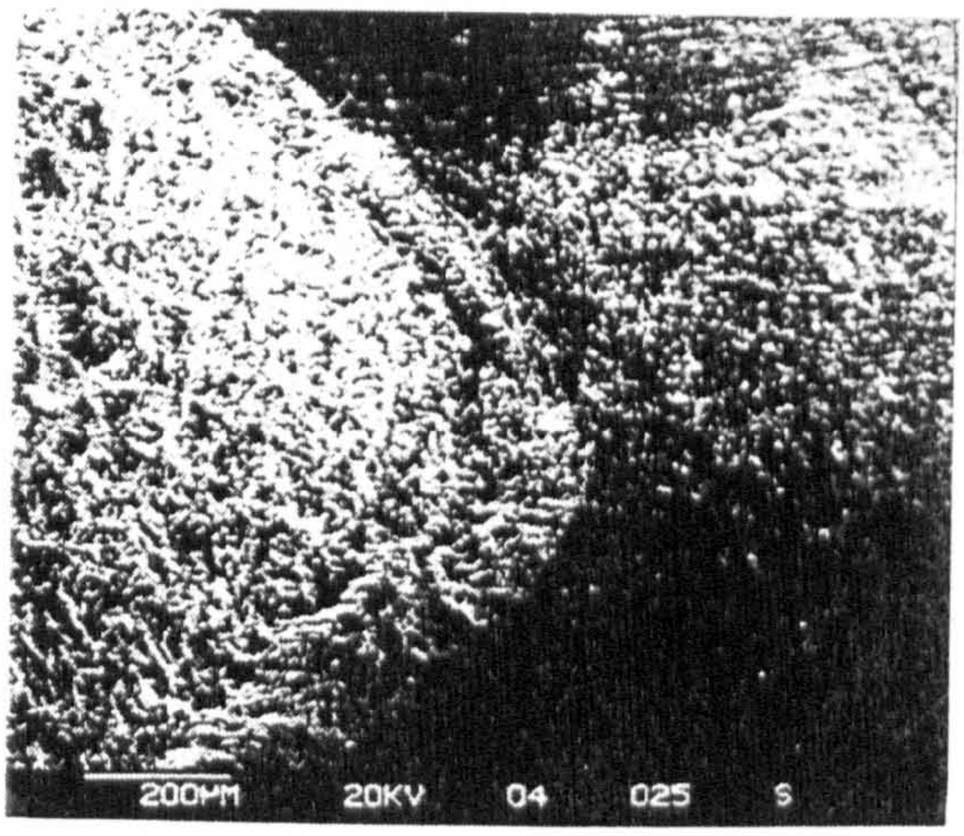

(b) delamination failure.

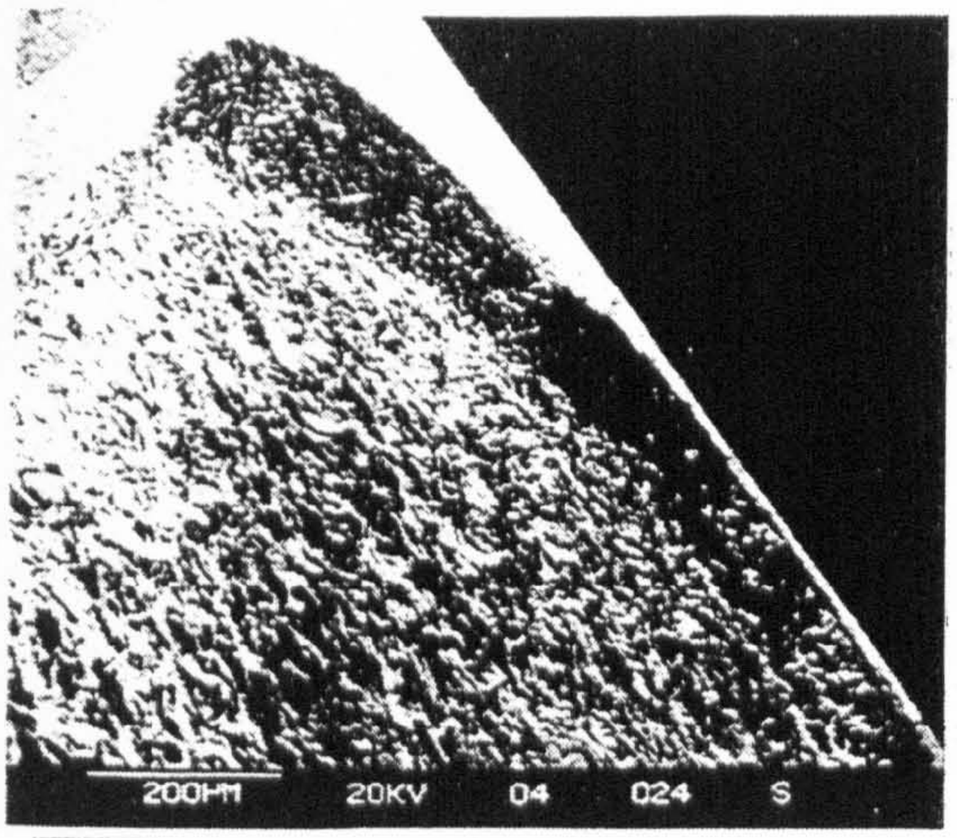

(c) failed area

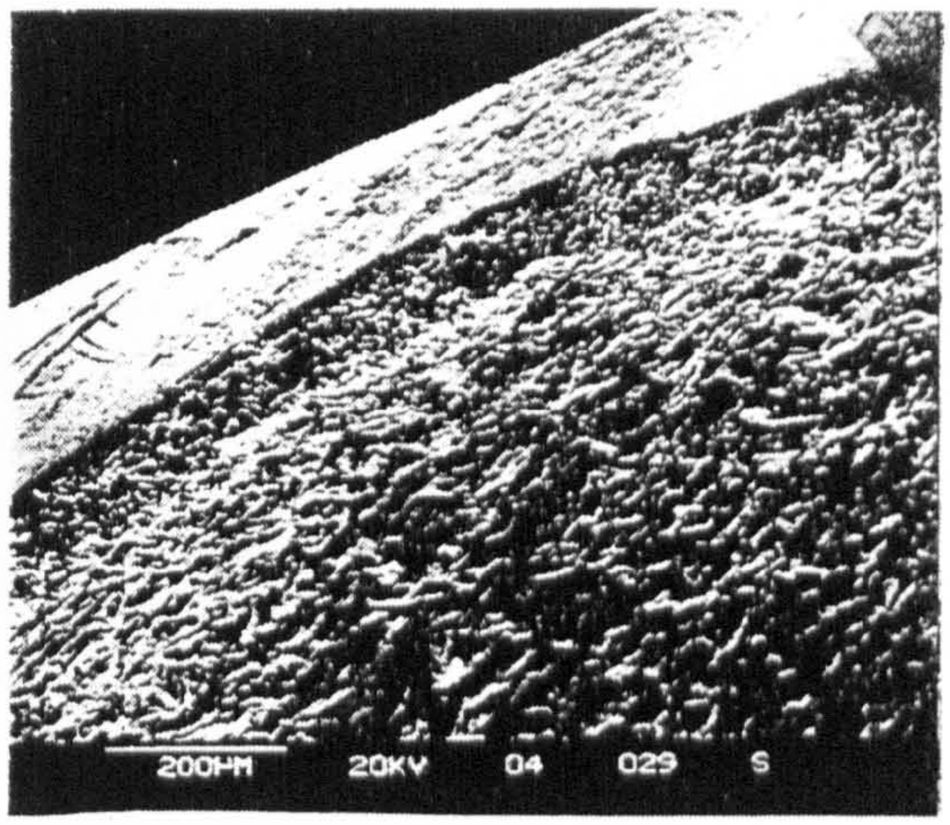

(d) delamination failure

Figure F4, Surface observations of Aluminium oxide/steel contact (Hitec-174)

F1.4 Microhardness Measurements

A Leitz miniload 2, Vickers, knoop and scratch hardness tester was used to measure the micro-hardness of the coating and substrate at different geometrical locations. The surface exposed after grinding the tip of the cone (for thickness measurements) was utilised for these measurements. The surface was polished using diamond particles to attain a smooth flat surface for the microhardness measurements. Preliminary measurements on the microhardness of the rolling elements using a variety of loads ranging from 50 p to 400 p, revealed that a load of 100 p for the substrate and 300 p for both the coating types provided consistent results. Twenty measurements on a typical cone revealed an average micro hardness of the WC-Co coating as 1200 Hv and Al_2O_3 coating as 1050 Hv, whereas the substrate hardness was 658 Hv. These values were averaged after neglecting the maximum and minimum reading values. The location of these hardness measurements can be appreciated from the figure F5. The major objective of this analysis was to investigate the variation in hardness of the coating and the substrate. The tests revealed that the hardness of the coating varies from 1100 Hv to 1300 Hv, while that of the substrate varies from 625 Hv to 725 Hv. Microhardness tests on the planetary steel balls at 100 p load showed an average microhardness of 850 Hv.

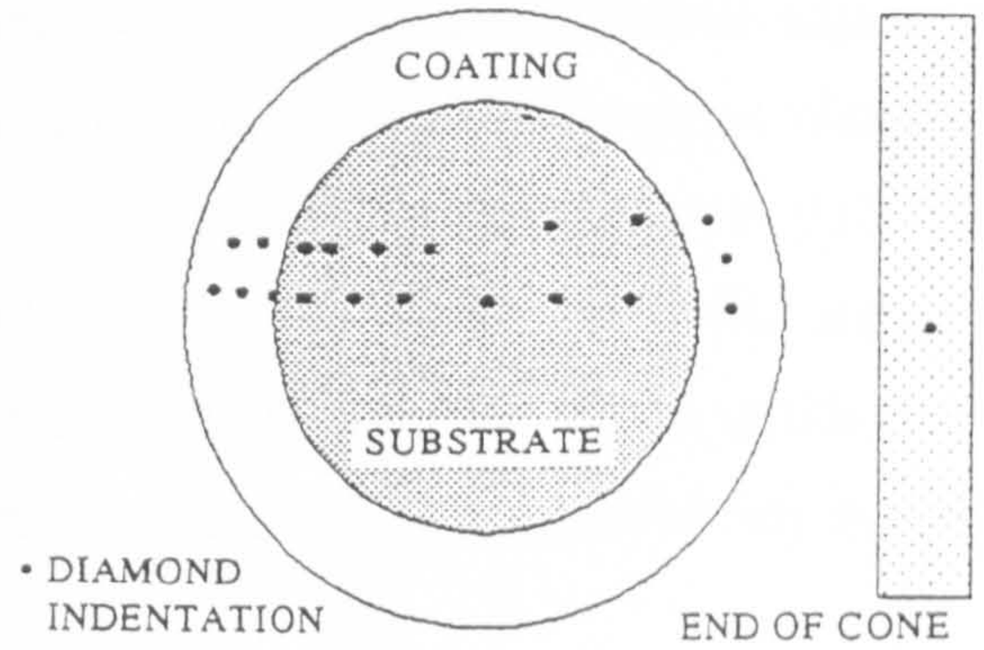

Figure F5, Location of microhardness measurements.

F1.6 Residual Stress

Spalling and cracking of the coating could have been due to high residual stresses in the coatings. Hence an attempt to measure the residual-stress of the test cones was made using an X-ray-diffraction technique. Although the measurement depth using this process is not large the process was selected because of its ability to measure complex sample shapes and also because of the non-destructive nature of the technique. The $\sin^2\psi$ method which measures the crystal inter-atomic distance was employed. A detailed explanation of this method is given by Farrahi et. al, (1991). The failed tested cones did not give satisfactory residual stress measurement results due to small diffraction peaks even after several repeated attempts. It was postulated that either the crystallisation of the D-Gun coatings was not good, or the grain size was not large which can be due to the parameters controlled during the thermal spraying process. It is probable that the coating material changed to a non-crystal material due to the quick cooling in the thermal spray process.

F1.7 Discussion

The first observation from table F2 was that the coated cones did not perform well in terms of durability or time to failure. Tests with uncoated M50 steel cones under the same conditions were suspended without failure after surpassing the coated cone cycles to failure. Secondly, the tungsten carbide coated cones generally performed

better than the aluminium oxide in all test configurations.

The third observation from these results is that the coated cones in contact with steel lower balls generally compare well with the results from contact with ceramic lower balls. This fact may be due to the higher contact stress with ceramic material due to the increase of elastic modulus ie. 207 GPa (steel) to 310 GPa (silicon nitride), as well as the increased hardness of ceramic balls. One surprising result was the tungsten carbide coated cone in contact with silicon nitride lower balls lubricated with Exxon 2389. In this case the time to failure reaches over 180 minutes.

The extent of retained WC in a Co matrix generally represents the wear resistance of WC coatings. This is dependent upon the spraying method and the parameters during the spraying eg particle size, type of powder used, velocity of spray, surrounding atmosphere and the substrate temperature. Cryogenic fracture study of plasma spray WC coatings by George et. al, (1995), revealed that these coatings not only have significant porosity but also secondary phase particles and lack of fusion. Vuoristo et. al, (1993) have shown that there was a dominant change in coating microstructure ie improved quantity of retained WC, if coarser coating powders are used. Also finer powders result in undesirable coating phases but have the advantage of low porosity levels. The delamination failure of these coatings can be thought to be as a result of these porosity/microcracks and secondary phases, ie voids due to a plastic flow of matrix around hard particles. Kesharam et. al, (1993) have also reported a delamination behaviour of the WC-Co coatings by D-Gun in a test configuration for radial and thrust bearings. Another reason for the delamination of the coatings could be the location of shear stresses at the depth of failure and, the difference in elastic properties of the coating and the substrate for coating substrate interfacial failures. The rolling friction can also alter the shear stress depth, although no measurements were made to specifically measure the value of rolling friction for these coatings, previous studies have shown that the value of rolling friction was very low. The role of residual stress can also be significant. It is interesting that the λ-value is higher for the tests with Hitec-174 lubricant, but the average time to failure was less. Although the reason for this was not verified, it can be thought to be as a result of either a chemical reaction between the coating and lubricant

(additives in lubricant) or a hydrostatic pressure build-up due to fluid entrapment. Several other factors such as subsurface cracking can also be considered.

The micro-hardness measurements showed a variation in the Vickers hardness throughout the coating section. It is in accordance with the analysis presented by Lin et. al, (1993). The micro-hardness tests on the planetary balls indicate that the average micro-hardness of the substrate was approximately 200 Hv lower than that of the standard bearing steel used for the planetary balls. It can actually degrade the performance of the coating by not supporting the coating, since the performance of the coating is a combination of coating and substrate.

The Al_2O_3 coatings where the failure was at the interface specifically suffer from thermal and mechanical mismatch between the coating and substrate. This difference seemed less intense for WC-Co coatings where the failure was not at the interface. The Al_2O_3 failed due to the poor adhesive strength whereas in the case of WC-Co coatings the cohesive strength of the coating needed improvement. Since the difference in coefficient of thermal expansion between the substrate and the coating is larger for Al_2O_3 coatings in comparison to WC-Co coatings the residual stress build-up at the interface can be large for Al_2O_3 coatings. The change in coating thickness can cause the maximum shear stress to move towards the interface and coating can fail by peeling from the substrate. A solution could be to use either HIP method or heat treatment, although other coating methods like HVOF can also be investigated.

The coatings also suffer from low shearing strength, since the tests conducted at high speeds of 7500 rpm the coatings time to failure was less than a minute for contact stress of 5.8 GPa. The failure mode remained as delamination. This also narrowed the possibility of any possible lubricant entrapment mechanism to assist coating delamination since the lubricant will require some time to due to inertia forces to penetrate in crack and ultimately propagate it to result in coating delamination.

REFERENCES

Ahmed, R. & Hadfield, M. "Rolling contact fatigue behaviour of thermally sprayed rolling elements", Surface and coatings technology, **82**, 176 - 186 (1996).

Ahmed, R. & Hadfield, M. "Rolling contact fatigue performance of detonation gun coated elements", Tribology international, **30 (2)**, 129 - 137 (1997).

Aramaki,H., Shoda,Y., Morishita,Y. and Sawamoto., "The Performance of Ball Bearings with Silicon-Nitride Ceramic Balls in High Speed Spindles for Machine Tools", J. of Tribology, **110**, 693-698 (1988).

Arata, Y. "Thermal spraying-current status and future trends" , ISSN 1241-3074 (1995).

Archard, J. F. & Kirk, M. T. "Lubrication at point contacts", Royal society **261-A**, 532-549 (1960).

Bidwell, J. B. "Rolling contact phenomenon",Elsevier publishing company, New York, (1962).

Bower, A. F. "The influence of crack face friction and trapped fluid on surface initiated rolling contact fatigue cracks", Trans of ASME, **110**, 704-711 (1988).

Brandt, O. C. "Mechanical properties of HVOF coatings", Journal of Thermal Spraying **4**, 147-152 (1995).

Bush, J. J., Grube, W. L., & Robinson, G. H. "Microstructural and residual stress changes in hardened steel due to rolling contact", Rolling contact phenomena, 365-399 (1962).

Chao, K. K., Saba, C. S., & Centers, P. W. "Effects of lubricant borne solid debris

in rolling surface contacts", Tribology transactions, **39(1)**, 13-22 (1996).

Chen, Q., Hahn, G. T., Rubin, C. A., & Bhargava, V. "The influence of residual stresses in rolling contact mode II driving force in bearing raceways", Wear, **126**, 17-30 (1988).

Chen, W. T. "Computation of stresses and displacements in a layered elastic medium", Internatioanl journal of engineering science, **9**, 775- (1971).

Clark, J. C. "Fracture tough bearings for high stress applications", Proc. 21st Joint Propulsion Conference, Paper AIAA-85-1138 (1985).

Cole, S. J., & Sayles, R. S. "A numerical model for the contact of layered elastic bodies with real rough surfaces", Transactions of ASME, **114**, 334-340 (1992).

Cullity B. D. 1978 Elements of X-ray diffraction, Addison-Wesley publishing company.

Dill,J.F., Gardos,M.N., Hintermann,H.E. and Boving,H.J. "Rolling Contact Fatigue Evaluation of Hard Coated Bearing Steels", ASLE Publication 230-240 (1984).

Djabella, H. & Arnell, R. D. "Finite element analysis of the contact stress in an elastic coating on an elastic substrate", Thin solid films, **213**, 205-209 (1992)

Djabella, H. & Arnell, R. D. "Finite element analysis of contact stress in elastic double-layer systems under normal load", Thin solid films, **223**, 98-108 (1993a).

Djabella, H. & Arnell, R. D. "Two-dimensional finite element analysis of elastic stress in double-layer systems under combined surface normal and tangential loads", Thin solid films, **226**, 65-73 (1993b).

Djabella, H. & Arnell, R. D. "Finite element comparative study of elastic stresses in single, double layer and multilayered coating systems", Thin solid films, **235**, 156-162 (1993c).

Djabella, H. & Arnell, R. D. "Finite element analysis of elastic stresses in multilayered systems", Thin solid films, **245**, 27-33 (1994).

Dowson, D. & Higginson, G. R. "Elasto-lydrodynamic lubrication", Pergamon press, (1966).

Fauchais, P. "Advances in thermal spraying", (Short course), ASM International, (1993).

Farrahi, G. H., Markho, P. H. & Maeder, G. "A study of fretting wear with particular reference to measurement of residual stress by X-ray diffraction". Wear **148**, 249-260 (1991).

George,F. Vander Voort, "A Layman's View of Plasma Spray Coating Metallography" Structure 8-13 (1995).

Gill, S. C. "Residual stress in plasma sprayed deposits". PhD thesis, Gonville and Caius college Cambridge, U. K (1993).

Goddard, K. N., & MacIsaac, B. D. "Use of oil borne debris as a failure criterion for rolling element bearings", Lubrication emgineering, **51(6)**, 481-487 (1995).

Greving, D. J., Rybicki, E. F., & Shadley, J. R. "Through-thickness residual stress evaluations for several industrial thermal spray coatings using a modified layer removal method", Journal of Thermal Spraying **3**, 379-388 (1994a).

Greving, D. J., Shadley, J. R., & Rybicki, E. F. "Effects of coating thickness and residual stresses on the bond strength of ASTM C633-79 thermal spray coating test

specimens", Journal of Thermal Spraying **3**, 371-378 (1994b).

Gudge, M., Rickerby, D. S., Kingswell, R., & Scott, K. T. "Residual stress in plasma metallic and ceramic coatings", Conference proceedings, National Thermal Spray Conference, Long Beach, Calafornia USA, 331-337 (1990).

Gupta, P. K., & Walowit, J. A. "Contact stress between an elastic cylinder and a layered elastic solid", Transactions of ASME, 250-257 April (1974).

Hadfield, M., Stolarski, T. A., & Cundill, R. T. "Failure mode of ceramics in rolling contact". Proc. R. Soc Lond. A **443,** 607-621 (1993).

Hadfield, M., Ahmed, R., & Tobe, S. "Rolling contact fatigue of thermal spray coated cones", Conference proceedings, International Thermal Spray Conference, Kobe Japan, 1097-1102 (1995).

Harris,. "Rolling bearing analysis", ISBN 0-471-79979-3 (1984).

Harvey, M. D. F., Sturgeon, A. J., Blunt, F. J., & Dunkerton, S. B. " Investigation in to the relationship between fuel gas selection, wear performance, and microstructure of HVOF sprayed WC-Co coatings", International thermal spray conference, Japan, 471-476 (1995).

Hills, D. A., Sackfield, A., & Uzel, A. R. "Stress concentrations in tractive rolling", Paper VII(ii), Leeds Lyon Symposium on Tribology, 171-178 (1985).

Irving, R., Knight, R. & Smith, R. W. "The HVOF processes", Welding journal, 25-30, July (1993).

Jacobson, B. O., "Rheology and elastohydrodynamic lubrication, Baker & Taylor (1991).

Johnson K. L. "Contact mechanics", Cambridge university press (1985).

Kapoor, A., & Johnson K. L. "Effect of changes in contact geometry on shakedown of surfaces in rolling/sliding contact", International Journal of Mech. sciences **34(3)**, 223-239 (1991).

Kapoor, A., & WilliamsJ. A. " Shakedown limits in rolling-sliding point contacts on an anisotropic half space, Tribology International **191(1-2)**, 256-260 (1996).

Kawase, R., & Tanaka, K. "Study on elastic constant and residual stress measurements during ceramic coatings", Conference proceedings, National Thermal Spray Conference, Long Beach, Calafornia USA, 339-342 (1990).

Keshavan, M. K. and Kembaiyan.K.T. "Wear Characterization and Practical Applications of Thermal Spray Coatings in Drilling Applications", Conference Proceedings, National Thermal Spray Conference, Anaheim, CA, USA, 635-641, (1993).

Kingswell, R., Rickerby, D. S., Scott, K. Y., & Bull, S. J. "Comparison of errosive wear behaviour of the vacuum plasma sprayed & bulk alumina", NTSC-90, California, USA, 179-185 (1990).

Knight, R., & Smith, R. W. "Residual stress in thermally sprayed coatings", Conference proceedings, National Thermal Spray Conference, Anaheim, California, USA, 607-612 (1993).

Kreye, H. "High velocity flame spraying-process and coating characteristics", Plasma Technic, 39-47 (1991).

Kruger, V., & Bartz. W. J. "Comparison of different ball fatigue test machines and significance of test results to gear lubrication", Rolling contact fatigue performance testing of lubricants, 137-159 (1977).

Kudinov, V. V., Pekshev, P. Yu., & Safiullin, V. A. "Forming of the structure of plasma-sprayed materials, High temperature dust laden jets, 381-418 (1989).

Kuroda, S., Fukushima, T., & Kitahara, S. "Significance of the quenching stress in the cohesion and adhesion of thermally sprayed coatings". Conference proceedings, International Thermal Spray Conference, Orlando, Florida USA, 903-909 (1992).

Lee, J. D., Ra, K. T., Hong, K. T., Hur, S. K. "Analysis of deposition phenomena and residual stress in plasma spray coatings", Surface and coatings technology, **56**, 27-37 (1992a).

Lee, K. S., Jinn, J. T., & Earmme, Y. Y. "Finite element analysis of a subsurface crack on the interface of a coated material under a moving compressive load", Wear, 155, 117-136 (1992b).

Lin, C. K and Berndt, C. C. "Microhardness Variations in Thermally Sprayed Coatings", Conference Proceedings, National Thermal Spray Conference, Anaheim, CA, USA, 561-568, (1993).

Lin, C. K., & Berndt, C. C."Measurement and analysis of adhesion strength for thermally sprayed coatings", Journal of thermal spraying technology, **3(1)**, 75-104 (1994).

Lin, C. K., Leigh, S. H., & Brendt, C. C., "Investigation of plasma sprayed materials by vickers indentation tests", Conference proceedings, International Thermal Spray Conference, Kobe Japan, 903 -908 (1995).

Littmann, W. E., Winder, R. L. "Propagation of contact fatique from surface and subsurface origins", ASME transactions, 624-636 September (1966)

Lucek,J.W. "Rolling Wear of Silicon Nitride Bearing Materials" ASME, 90-GT-

165, Presented at the Gas Turbine and Aero-Engine Congress and Exposition, Brussels, Belgium, June 11-14, (1990).

Makela, A., Vuoristo, P., Lahdensuo, M., Niemi, K. and Mantyla, T., "Rolling Contact Fatigue Testing of Thermally Sprayed Coatings", Conference Proceedings, Thermal Spray Industrial Applications, 759-764, (1994).

Maschio, R. D., Sgavo, V. M., & Rigoni, F. "Measurement of metal ceramic adhesion by indentation technique in thick TCB's2, ITSC-92, ISBN 0-87170-443-9, 947-952 (1992).

Mcpherson,R., "The Structure and Properties of Plasma Sprayed Alumina Coatings", Alumina conference, Parague, August, (1990)

Morishita, T., Kuramochi, E., Whitfield, R. W. & Tanabe, S. "Coatings with compressive stress", Conference proceedings, International Thermal Spray Conference, Orlando, Florida USA, 1001-1004 (1992).

Muro, H., Tsushima, N., & Nunome, K. "Failure analysis of rolling bearings by X-ray measurement of residual stress", Wear, **25**, 345-356 (1973).

Mutasim, Z. Z. & Smith, R. W. "Vacuum plasma spray deposition of WC-Co", NTSC-90, California, USA, 165-170 (1990).

Nakahira, H., Tani, K., Miyajima, K., & Harada, Y. "Anisotropy of thermally sprayed coatings", Conference proceedings, International Thermal Spray Conference, Orlando, Florida USA, 1011-1017 (1992).

Nakajima, A & Mawatari, T. "Surface durability of thermal sprayed WC cerment coating in lubricated rolling/sliding contact", World Tribology Congress, (1997).

Nieminen, R., Vuoristo, K., Niemi, K., & Mantyla, T. "Rolling contact fatigue

characteristics of thermal spray coatings", National thermal spray conference, Houstan, USA, 651-657 (1995).

Ohmori,A., "Thermal Spraying, Current Status and Future Trends", Conference Proceedings, Kobe, Japan, May (1995).

Ostojic, P., & Mcpherson, R. "Indentation toughness of plasma sprayed coatings", Materials forum, **10(4)**, 247-255 (1987).

Palmgren, A. "Ball and roller bearing engineering, S. K. F. Co, Holland (1945)

Pomeroy, R. J. & Johnson, K. L. "Residual stresses in rolling contact", Journal of strain analysis, **4(3)**, 208-218 (1969).

Provot, X., Burlet, H., Vardavoulias, M., Jeandin, M., Richaed, C., Lu, J., & Manesse, D. "Comparative studies of microstructures, residual stress distribution and wear properties for HVOF and APS WC-Co coatings of Ti6Al4V", Conference proceedings, National Thermal Spray Conference, Anaheim, Calif USA, 159-166 (1993).

Rhys-Jones,T.N., "The use of thermally sprayed coatings for compressor and turbine applications in aero-engines", Surface and Coatings Technology, **42**, 1-11 (1990).

Richard, C., Lu, J., Flavenot, J. F., Beranger, G., & Decomps, F. "Study of Cr_2O_3 material & characterization by an interfacial test on coating substrate adherence", NTSC-92, ISBN 0-87170-443-9, 11-17 (1992).

Soda, N. & Yamamaota, T. "Effect of tangential traction and roughness on crack initiation/propagation during rolling contact, ASLE transactions, **25(2)**, 198-204 (1981).

Sahoo, P., "High Performance Wear Coatings-the Quest Continues", Powder Metallurgy International, **25**, 73-78 (1993).

Sayles, R. S. "Debris and roughness in machine element contacts: some current and future engineering implications", Journal of engineering tribology, **209(3)**, 149-172 (1995).

Schwarzer, N., Djabella, H., Richter, F., & Arnell, R. D. " Comparison between analytical and FEM calculations for the contact problem of spherical indentors on layered materials", Thin solid films, **270**, 279-282 (1995).

Sproul,W.D., Graham,M.E., Wong,M. & Rudnik,P.J., "Reactive Unbalanced Magnetron Sputtering of the Nitride Coatings of Ti, Zr, Hf, Cr, Mo, Ti-Al, Ti-Zr, and Ti-Al-V on 440C Steel", Surface and Coatings Technology, **61**, 139-143 (1993).

Sun, Y., Bloyce, A., & Bell, T. " Finite element analysis of plastic deformation of various TiN coating/substrate systems under normal contact with a rigid sphere", Thin solid films, **271**, 122-131 (1995).

Tabor, D. "Proc. Roy. Soc. London, Paper A 229, 198 (1955).

Thom,R., Moore,L., Sproul,W.D. and Chang,T.P. "Rolling Contact Fatigue Tests of Reactively Sputtered Nitride Coatings of Ti, Zr, Hf, Cr, Mo, Ti-Al, Ti-Zr, and Ti-Al-V on 440C Steel", Surface and Coatings Technology, **62**, 423-427 (1993).

Tobe, S., Kodama, S. and Sekiguchi, K., "Rolling Fatigue Behaviour of Plasma Coated Steel", Conference Proceedings, Surface Engineering International Conference, Tokyo, Japan, 35-44 (1988).

Tobe,S., Kodama,S. and Misawa,H. "Rolling Fatigue Behaviour of Plasma Sprayed Coatings on Aluminium Alloy", Tokyo Metropolitan University, 2-1-2, Fukazwa, Setagaya-Ku, Tokyo, Japan, **158** (1990).

Tobe, S., Kodama, S. and Misawa, H., Conference Proceedings, Thermal Spray Research and Applications, 171-178 (1991).

Tobe, S., Misawa, H., Akita, K., & Fujinawa, G. "Strain analysis by X-ray diffraction technique and lamella structure of APPS and LPPS coatings", Conference proceedings, International Thermal Spray Conference, Orlando, Florida USA, 1005-1010 (1992).

Tourret,R and Wright,E.P., "Rolling Contact Fatigue: Performance Testing of Lubricants", Int. Symp., I.Petroleum, October 1976, London, Heyden & Son Ltd, (1977).

Tucker, Jr, R. C. "Structure property relationship in deposits produced by plasma spray & detonation gun techniques", Journal of vacuum science & technology **11**, 725-734 (1994).

Tyfor, W. R., & Beynon, J. H. "The effect of rolling direction reversal on fatigue crack morphology and propagation", Tribology International, **27(4)**, 273-282 (1994).

Vuoristo,P., Niemi,K., Makela,A. and Mantyla,T. "Spray Parameter Effects on Structure and Wear Properties of Detonation Gun Sprayed WC+17%Co Coatings", Conference Proceedings, National Thermal Spray Conference, Anaheim, CA, USA, 173-178 (1993).

Warnock, F. V. & Benham, P. P. "Mechanics of solids and strength of materials", Pitman Press, Bath (1965).

Way, E. "Pitting due to rolling contact", Journal of applied mechanics, **2**, A49-A58 (1935).

Wei,R., Wilbur,P.J. and Kustas,F.M. "A Rolling Contact Fatigue Study of Hard carbon Coated M-50 Steel" Transactions of ASME, **114**, 298-303 (1992).

Wei,R., Wilbur,P.J., Liston,M.J. and Lux, G. "Rolling Contact Fatigue Wear Characteristics of Diamond-Like Hydrocarbon Coatings on Steels", Wear 558-568 (1993).

Wira,K., Lin,C.W., and Loh,N.L., "Micro-Structure and Wear Properties of Arc Sprayed Tungsten Carbide Coatings", International Thermal Spray Conference, Kobe, Japan, 465-470 (1995)

Wong, S. K., & Kapoor, A. 1995 The effect of hard and stiff overlay coatings on the strength of surfaces in repeated sliding. Tribology International, **29(8)**, 503-506 (1996).

Yanke, S. J. & Paletka, P. J. "Effect of plasma spray processing variations on particle melting & splat spreading of hydroxylapalite and alumina", Journal of thermal spraying **2**, 271-283 (1993).

Yoshida, M., Tani, K., Nakahira, A., Nakajima, A., and Mawatari, T., Conference Proceedings, International Thermal Spray Conference, Kobe, Japan, 663-668 (1995).

Zaretsky, E. V., Parker, R. J., & Anderson, W. J. "A study of residual stress induced during rolling contact", Trans ASME, Journal of lubrication technology, **91F**, 314-319 (1969).

BIBLIOGRAPHY

Bertagnolli, M. Marchese, M., & Jacucci, G. "Modelling of particles impacting on a rigid substrate under plasma spraying conditions", Journal of thermal spray technology, **4(1)**, 41-49 (1995).

Beshish, G. K., Florey, C. W., Worzala, F. J., & Lenling, W. J. "Fracture toughness of thermal spray ceramic coatings determined by the indentation technique", Journal of thermal spray technology, **2(1)**, 35-38 (1993).

Dykhuizen, R. C. "Review of impact and solidification of molten thermal spray droplets", Journal of thermal spray technology, **3(4)**, 351-361 (1994).

Engineering Science Data Units, "ESDU 84017", (1984)

Eschnauer, H. R., & Knotek, O. "Complex carbide powders for plasma spraying", Thin solid films, **45**, 287-294 (1977).

Fukanuma, H. "Porosity formation and flattening model of an impinging particle in thermal spray coatings", Journal of thermal spray technology, **3(1)**, 33-44 (1994).

Gator Guard coatings, Sermatech technical services, Pennsylvania, USA.

Herman, H. "Plasma sprayed coatings", Scientific American, 79-83, September 1988.

Mathews, Coatings tribology, 1995.

McPherson, R., & Shafer, B. V. "Interlamella contact within plasma-sprayed coatings", Thin solid films, **97**, 201-204 (1982).

Modified Four Ball Machine, User Manual, 1980.

Montavon, G., Sampath, S., Berndt, C. C., Herman, H., & Coddet, C. "Effects of vacuum plasma spray processing parameters on splat morphology", Journal of thermal spray technology, **4(1)**, 67-74 (1995).

Moreau, C. Gougeon, P. & Lamontage, M. "Influence of substrate preparation on the flattening and cooling of plasma-sprayed particles", Journal of thermal spray technology, **4(1)**, 25-33 (1995).

Nerz, J., Kushener, B., Rotolico, A. "Microstructural evaluation of tungsten carbide-cobalt coatings", Journal of thermal spray technology, **1(2)**, 147-151 (1992).

PAFEC, user manual, 1990.

Pawlowski, "The science and engineering of thermal spray coatings", ISBN 0-471-95253-2 (1995).

Price, M. O., Wolfla, T. A., & Tucker, J. R. "Some comparative properties of laves-and carbide-strengthened coatings deposited by plasma or detonation gun", Thin solid films, **45**, 309-319 (1977).

Safi, S., Herman, H. "Microstructural investigation of plasma-sprayed aluminum coatings", Thin solid films, **45**, 295-307 (1977).

Suh, N. P. "An overview of the delamination theory of wear", Wear, **44**, 1-16 (1977).

Timoshenko, S. P. & Goodier, J. N. "Theory of elasticity, ISBN 0-07-Y85805-5, (1988).

Vardelle, M., Vardelle, A., & Fauchais, P. "Spray parameters and particle behaviour relationships during plasma spraying", Journal of thermal spray technology, **2(1)**, 79-91 (1993).

Wilms, V. H. S. "The microstructure of plasma sprayed coatings", PhD Thesis, SUNY at Stony Brook, (1978).